Electrohydrodynamic Air Movers for Thermal Management

Nels E. Jewell-Larsen

A dissertation
submitted in partial fulfillment of the
requirements for the degree of

Doctor of Philosophy

University of Washington
2012

Reading Committee:
Alexander V. Mamishev, Chair
Mani Soma
Stephen W. Montgomery
Joseph T. Dibene II

Program Authorized to Offer Degree:
Department of Electrical Engineering

University of Washington

Abstract

Electrostatic Fluid Accelerators for Thermal Management

Nels E. Jewell-Larsen

Chair of the Supervisory Committee:

Associate Professor Alexander V. Mamishev
Department of Electrical Engineering

Electrohydrodynamic (EHD) air movers are uniquely positioned to become a key emerging air mover technology to compete with mechanical rotary fans in the next generation of ultrathin consumer electronics thermal management, due to their form factor flexibility, low height capability, flow rates, and silent operation. However, as is true of many emerging technologies, EHD driven thermal management lacks the development of fundamental scaling and design rules, robust and mature design tools, and proof-of-concept demonstration of small-scale EHD systems for thermal management, which are needed to progress to the commercial sector. This dissertation, broken roughly into four parts, attempts to move EHD thermal management a step forward towards commercial application. The first, presents the development of design theory investigating the fundamental factors of pressure generation in EHD systems, transduction efficiency, and device scaling. The second presents a coupled-physics EHD numerical model and its results that take into account charge generation, charge transport, electrostatics, fluid dynamics, and heat transfer. The third presents simulations and experiential work focused on the development of a proof-of-concept meso/micro-scale

EHD air mover for jet impingement forced convection cooling. The forth presents a proof-of-concept EHD thermal management solution embedded in a commercial notebook computer, demonstrating the ability to integrate an EHD thermal system into a modern notebook computer. Finally, key future efforts required to bring EHD thermal management technology to a successful commercial application are reviewed.

TABLE OF CONTENTS

Page

LIST OF FIGURES

Figure Number Page

LIST OF TABLES

Table Number Page

ACKNOLEDGMENTS

Over the past decade, I have been blessed to have had the opportunity to conduct my undergraduate and graduate research under the direction of Professor Alexander Mamishev, Director of the Sensors Energy and Automation Laboratory (SEAL) in the Department of Electrical Engineering at the University of Washington. I would like to thank Professor Mamishev for always pushing and demanding the best in many different aspects of my work. I would also like to thank him for allowing and enabling me to pursue work with other research and development groups within the academic world and outside of it..

I would also like to express my gratitude to my thesis committee members, Dr. Igor Krichtafovitch, Dr. Steve Montgomery, Dr Ted Dibene, Professor Mani Soma, and Professor Richard Shi for their contributions of thoughts, advice, and time as committee members.

The advantage of having focused on a technology for a decade is that you have a chance to work with and share ideas with a large number of individuals, teams, corporations, and institutions. It is impossible to list everyone involved, but I want to recognize key individuals that supported or contributed to the presented work. As for almost all things, it is impossible to operate in isolation, and I want to credit many of the individuals below for their contribution to the development of this work. Thank you.

I would like to thank Tessera Technologies and the Silent Air Cooling Group, for their support and assistance. I am especially grateful for the thoughts, ideas, and support from Dr. Ken Honer, Dr. Hongyu Ran, Dr. Yan Zhang, Dr. Gustavo Joseph, Dr. Guilian Gao, Matt Schwiebert, Ron Goldman, Wilbur Lau, Craig Mitchell, and Liam Gouge. I look forward to our future collaboration.

Similarly, I would like to thank Kronos Air Technologies, with special thanks to Dr. Igor Krichtafovitch, Dr. Sergey Karpov, Vladislav Korolyov, Karl Winkler, and Rich Tusing. Specifically I would like to thank Dr. Sergey Karpov for his collaboration over the years in the development of the EHD model.

I would also like to thank Intel Corporation, and the Power and Thermal Technology Laboratory, with specific thanks to Steve Montgomery, Ted Dibene, and Tomm Aldridge.

As the cofounder of this project within SEAL a little over 10 years ago in the winter of 2000, I would like to thank Fumin Yang for many hours of work and conversations that we shared during the very early stages of this project. I would also like to thank Chi-Peng Hsu who worked as my partner on this project for several years and contributed significantly to our efforts in realizing a microfabricated EHD device.

Numerous experiments and simulations in this thesis were done by several talented undergraduates under my supervision, and I would like to thank them all for their contributions. I also would like to express my gratitude to all of the other graduate and undergraduate members of SEAL whom I talked and joked with, and with whom I have spent untold hours. Special thanks go to the graduate students I had the opportunity to share the lab with including, Dr. Mike Hegg, Dr. Xiaobei Li, Dr. Kishore Sundara-Rajan, Dr. Bing Jiang, Dr. Min Wang, and Gabe Rowe.

I would also like to thank my parents, Steve and Susan Jewell-Larsen, and brother and sister, Lee and Tess Jewell-Larsen, for their support and encouragement through the many years. In addition, I would like to thank my wonderful wife Jennifer for her continued support, and our in vivo son for providing additional motivation to wrap up this manuscript.

Financial support has been provided by Tessera Technologies, Kronos Air Technologies, Intel Corporation Enterprise Platform Group, the Grainger Foundation Graduate Fellowship program, and the Army Research Office Grant # DACA42-02-0023. Additional student support was provided by the American Public Power Association Demonstration of Energy-Efficient Developments (APPA DEED) Program with the assistance of Seattle City Light Corporation. Undergraduate research scholarships were funded by the University of Washington Mary Gates Research Training Grant, the Washington NASA Space Grant Consortium, and the Electrical Energy Industrial Consortium.

DEDICATION

This thesis is dedicated to my wife and son, Jennifer and Liam.

Chapter 1. Introduction

The work presented in this dissertation is motivated by the ever increasing need for improved methods and technologies for thermal management that enable the ever evolving electronics industry to continue its march towards more capable and smaller form factor applications. This dissertation is a study in the design, modeling, and integration of small scale electrohydrodynamic (EHD) air movers for forced convection heat transfer application. This work is based on publications [1-15] by the author.

1.1 Introduction to electrohydrodynamic air movers for thermal management

Electrohydrodynamic (EHD) air movers at their heart are simple devices consisting of a sharp and blunt electrode separated by an air gap and connected to a power supply to apply a voltage across them. When a sufficient electric potential is applied between them, usually on the order of kilovolts, ions are generated at the sharp electrode and accelerated in the electric field and through the air gap to the blunt electrode where they are deionized. As the ion stream passes through the air gap it transfers momentum to the surrounding air inducing airflow. The result is a solid state air mover that can be used to generate airflow, which can, in turn, be used in applications where airflow generation or perturbation is desired. This method of direct electrical to mechanical transduction enables a very dynamic and flexible air mover, with the ability to be silent, change flow magnitudes and directions rapidly, and operate in form factors incompatible with other air movers that require rotating or otherwise oscillating high speed moving parts. It is also possible to condition the airflow within the EHD air mover through particulate charging and precipitation out of the air.

Electrohydrodynamic (EHD) air movers have been examined for use in such applications as air propulsion [16-18], solid-fluid boundary layer modification [19-25] thermal management [3, 4, 13, 14, 26-33], electro-acoustics [34-36], particulate removal [37, 38], and dehumidification [37, 39, 40] among many others. Transition from the

understanding of underlying physical principles of EHD air movers to the design of practical devices spans many decades of prior research over many different fields and applications. These efforts have led to the discovery of numerous applications for EHD based technology, of which many are just starting to become a reality with recent research and development efforts worldwide.

EHD air movers are uniquely positioned to become the dominate emerging air mover technology to compete with mechanical rotary fans in the next generation of ultrathin consumer electronics devices, due to their form factor flexibility, small size, and silent operation.

The results of this dissertation are applicable primarily to the evaluation and design of EHD air movers as an alternative to or collaboration with traditional rotary fans for thermal management; however, developments from this work may be applied to the EHD field in general.

1.2 Advantages and disadvantages of EHD air movers for thermal management

EHD air movers are uniquely positioned to become the dominate emerging air mover technology to compete with mechanical rotary fans in the next generation of ultrathin consumer electronics devices, due to their form factor flexibility, small size, and silent operation. EHD air movers do have drawbacks including the need for high voltage generation, ozone management, and intrinsically lower pressure head generation than their mechanical fan counterparts. The discussion below reviews a few of the major advantages and disadvantages of EHD blowers in comparison to other air mover technologies.

1.2.1 Advantages of EHD air movers for thermal management

1.2.1.1 Thin profile capability

One of the most important advantages of EHD blowers is the ability to scale to fit in thin profile applications where conventional mechanical fans function poorly or not at

all. The absence of moving parts to generate airflow allows the EHD blowers to have total device thickness at the millimeter level and if microfabrication processes are used even thinner systems can be conceived of.

1.2.1.2 Flexible form factor

In comparison to mechanical rotary fans, which have rotating parts that require the fans to be circular in form, an EHD air mover requires only rough line of sight between emitter and collector electrodes enabling a wide range of possible cross sections and form factors. As an example, the device can be a designed to be a small square block in form and impinge a jet of air for local hot spot cooling in a remote area within a system or can be used as a long and thin rectangular solid format that spans an edge of a system that would otherwise be unused.

1.2.1.3 Low acoustic emission

EHD air movers are generally powered with a DC voltage that results in a near static electric field and ion current with time. The resulting pressure rise is therefore also static and gives off no or negligible acoustic energy within the audible range. To the extent that the EHD drive voltage is not DC, an acoustic signature will be present at the frequency of the AC component. This can be taken advantage of by using this effect to create loud speakers for music, noise cancelation, alerts, or other applications.

1.2.1.4 High mass flow rate

Synthetic jets and piezoelectric fans among other emerging airflow technologies have stayed in the emerging status for many decades. This has been due in a large part to their inability to produce significant net flow through a system, which is essential for cooling of a system. EHD blowers can provide flow rates similar or greater to mechanical fans in thin form factors with modest system flow restriction.

1.2.1.5 Boundary layer disruption

EHD body forces can be used to generate net flow as a primary air mover, or be used as a secondary air mover to boost and or mix airflows to reduce the fluid and

thermal boundary layer to enhance cooling. In the case where the thermal exchange surface is also the ion collecting surface of an EHD air mover, it is possible to impart momentum to the air within the boundary layer region to reduce its size and improve heat transfer.

1.2.2 Disadvantages of EHD blowers for thermal management

1.2.2.1 Pressure head

Flow rates for EHD air movers can be designed to meet or exceed the open flow rates for thin form factor mechanical fans, however, the maximum practical pressure head of an EHD blower will typically be lower than that of a mechanical centrifugal blower due to the nature of airflow generation. An EHD system uses ions traveling through a sea of neutral air molecules to entrain flow and provide backpressure, whereas a mechanical fan uses a solid blade to impart momentum to the airstream, which offers greater resistance and ultimately higher backpressure.

1.2.2.2 High voltage operation

To initiate and sustain a corona discharge process to generate ions in an EHD blower, the electric field in the area of ion creation must exceed the dielectric strength of air, which at standard conditions is approximately three kilovolts per millimeter. For most practical devices, this requires an operating voltage greater than a kilovolt and often multiple kilovolts. As most electronic applications do not have an existing power supply suitable to directly power an EHD air mover, a compact high voltage power supply must be included as part of the EHD system design.

High voltage safety in an EHD air mover is always an important consideration, and careful design and engineering are required to meet necessary safety standards. However, the low power and resulting electrical current required for most EHD driven thermal systems make safe design relatively simple.

1.2.2.3 Ozone generation

EHD air movers require corona discharge for ion generation, and ozone is created as a byproduct of the ion generation process in an oxygen environment. Ozone can be an irritant at high concentrations and damaging to some materials, therefore, many EHD air mover applications must include various ozone mitigation strategies such as use of ozone catalysts to convert the O_3 back to O_2 before exiting the device.

1.2.2.4 Reliability considerations

The absence of high speed rotating parts removes many of the reliability issues that plague long term operation of mechanical fans. However, both mechanical fans and EHD blowers share the issue of dust ingress, where dust buildup in the air mover and thermal exchange surfaces reduces blower performance and heat transfer. EHD blowers however, will capture particulates at a higher rate and must devote extra design effort to deal with it. EHD blowers also have unique reliability challenges relating to their sharp emitter electrode, which must be fabricated out of select materials to avoid corrosion and contaminate adhesion from the plasma environment around the emitter. The emitter electrode is also prone to build up of silica deposits over time from chemical vapor deposition within the corona plasma, which requires periodic removal for long term operation.

1.3 Scientific and Engineering Challenges

The research work presented in this dissertation has several scientific and engineering challenges, which can be broadly classified into several categories detailed below.

1.3.1 Design of EHD blowers

As with many technologies, the basic function can be described in a brief paragraph but the design complexity for real world applications is significant. The basic design rules and numerical modeling tools that are standard in a developed technology

like mechanical fans were largely absent at the time the author began research in this area.

The function of an EHD blower has many highly coupled and nonlinear parameters including electric field magnitude and profile, charge generation rate and transport, and resulting airflow, which make design and modeling challenging. Analytical models are only possible for the most simplified geometries and idealized assumptions, and their usefulness for design of real world applications are greatly limited. Finite element modeling has the ability to achieve much greater accuracy and usefulness. However, modeling accuracy is heavily dependent on the assumed boundary conditions, method of accounting for and modeling charge generation, among others, which can limit accuracy in cases where these quantities are difficult to estimate.

In the last decade, significant progress has been made in numerical modeling and design understanding, part of which is included in this dissertation work, but it still lags behind that of mature air mover technologies such as mechanical fans.

1.3.2 Miniaturization of EHD blowers

The body of research that has investigation EHD air movers through time has spent the vast majority of it focused on large macro scale devices and systems due to the relative ease of design and fabrication. Key benefits are achieved by going to meso and micro scale systems including reduced operating voltage and the ability to address applications requiring small form factor systems. However, the system design becomes more complicated due to increased sensitivity to device geometry, elevated current and space charge densities, and greater demands of component material properties, among other factors.

1.3.3 Integration of EHD thermal management systems within real-world electronic applications

The path from bench top curiosity and proof-of-concept experiment to integration in a commercial product is non-trivial, and is often the largest body of work in the continuum of technology development. The successful integration of an EHD air mover

requires multiple engineering challenges including the design of a compact EHD air mover that meets pressure and flow rate levels for adequate heat removal for a given system, design of the system-flow path and impedance to optimize the heat transfer, design of a compact high voltage power supply capable of stepping up voltages required for EHD operation, and develop and implement methods to mitigate ozone and provide long term reliability.

1.4 Scope of dissertation

Figure 1.1 shows the scope of this dissertation in visual format. This dissertation is a study into the design theory, miniaturization, modeling, and implementation of EHD air movers for thermal management applications such as consumer electronics. The process of EHD blower design is a balancing act between the performance requirements, application boundary conditions, and the common and unique engineering challenges related to EHD technology. This dissertation strives to develop a better understanding of EHD design tradeoffs and scaling, provide tools for performance estimation, and demonstrate the feasibility of small-scale EHD air blowers for thermal management. In addition, the dissertation aims to develop a better understanding of real-world challenges in the integration of EHD based thermal management into real-world systems such as consumer electronics.

Theory and design: In the realm of theory and design, this dissertation attempts to develop a better understanding of the fundamental scaling principles for EHD air movers, to reduce the design complexity from manipulation of complex fundamental equations to basic design rules easily used in real-world blower design. Much as the classic "fan laws" reduced the complexities of the system of equations which describe fan operation into a set of simple equations that could be used for first level design guidelines, this dissertation attempts to provide the analog for EHD blowers. In addition to device scaling, the dissertation attempts to develop a universal figure-of-merit that can be used to optimize the transduction efficiency based on the knowledge of the electric field and charge distribution, which can allow for optimization without the need to solve the often numerically intensive fluid dynamics solution for each stage of optimization. Also

included, is a discussion of the loss mechanisms present in EHD air mover systems and their impact to device scaling, which is critical in the understanding and development of paths for future optimization.

Numerical Modeling: In the evolution of a technology from lab curiosity to real world application, it is critical to develop the ability to predict performance of a design and optimize aspects that are difficult, time consuming or not feasible to observe through experimental investigation. In this light, this dissertation presents a model using the finite element method utilizing peeks empirical correlation for charge generation and the full set of governing equations for EHD driven flow. In addition, conductive and convective heat transfer equations are included to enable heat transfer estimation. The model is validated against experimental observations for electrical, fluid dynamic, and heat transfer predictions.

Miniaturization: As is true for many technologies, the ability to reduce the scale of EHD air movers opens up new applications and design possibilities not achievable at larger sizes. This is especially true for EHD air movers in the field of heat transfer, with the majority of the thermal solution market focused on consumer electronics, which demand small and ever shrinking form factors. As such, this dissertation attempts to communicate the capabilities and challenges of small-scale EHD devices for heat transfer enhancement through the numerical and experimental investigation of several meso-scale EHD designs.

Development for commercial application: The road from bench top curiosity to commercial product launch is long, and its full path is outside the scope of this dissertation. However, this dissertation does attempt to present the opportunity for EHD air movers as a replacement for mechanical fans in thin form factor electronics, and demonstrates a proof-of-concept thermal solution in a functional commercial notebook. In addition, it reviews the major challenges on the path to successful integration of an EHD thermal management system in consumer electronics applications and presents paths and some tools to that aim.

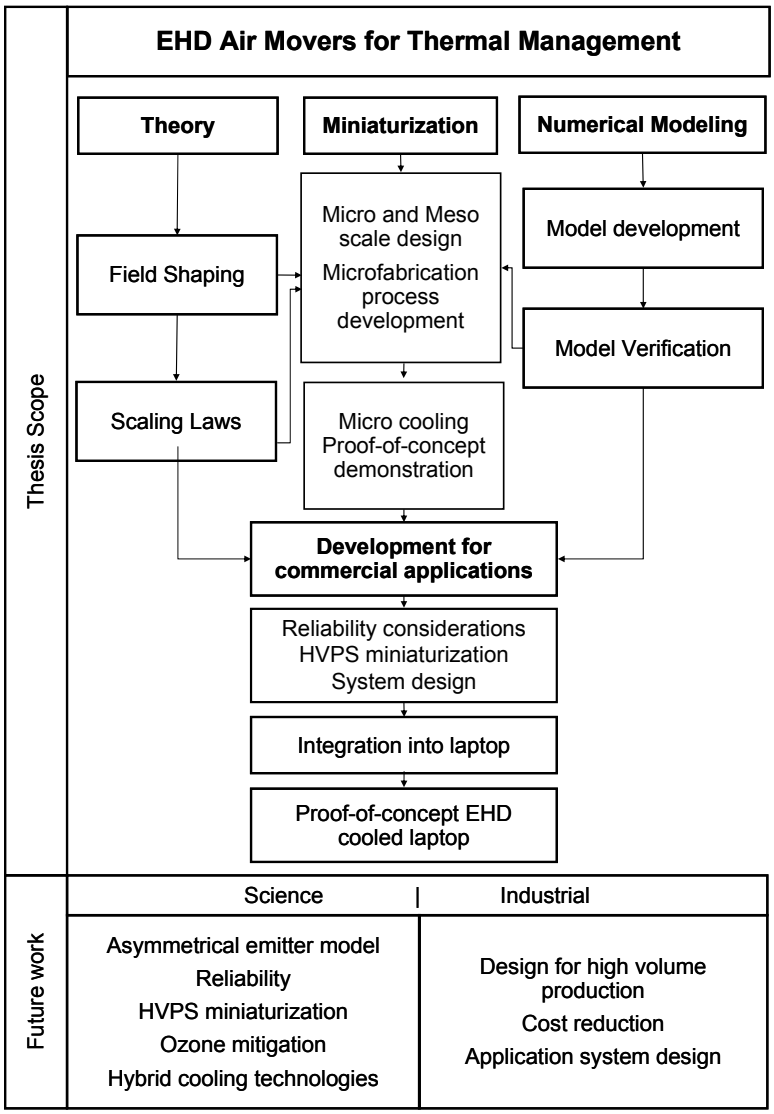

Figure 1.1. *Scope of dissertation and future work.*

1.5 Contributions of the dissertation

The dissertation makes four major contributions. First, it develops methodologies and design knowhow that can be used in design of EHD air movers for improved performance and to scale performance with device size. The majority of existing academic literature focused on single designs or modifying geometry for improved performance rather than focusing on the underlying principles of EHD air flow to derive

general figures-of-merit and scaling laws. Such know-how is critical in the design and optimization of EHD air movers for commercial and industrial applications.

Second, it presents a validated numerical model that can aid in the design and optimization of EHD based thermal systems. Although the basic operation of EHD airflow can be described in a brief paragraph, the design complexity for real world applications is significant. The basic design and numerical modeling tools that are standard in a developed technology like mechanical fans were largely absent at the time the author began research in this area. This dissertation has helped to move that area forward.

Third, it presents the first published demonstration of a functional microfabricated EHD forced convection cooling device known to the author. The dissertation discusses the methodology and process to design and fabricate small scale EHD systems as well as the challenges and opportunities of micro and meso-scale EHD systems for thermal management.

Forth, it presents the first published fully EHD cooled laptop known to the author, demonstrating the compatibility and potential for EHD based thermal management in thin form factor consumer electronics applications. The dissertation discusses many of the design considerations and hurtles for integrating in a laptop application.

Chapter 2. Thermal management background and motivation

2.1 Introduction to thermal management in microelectronics

The problem of thermal management in microelectronics is at the center of attention of academia, government agencies, and industry worldwide. Rapid development of microelectronics has led to an immense component density. Within this decade the size of a single transistor gate will decrease below 15 nm. This, in turn, will amplify the already existing problem, which is that each semiconductor component emits heat associated with the electrical resistance, leading to larger heat flux from the same surface area.

Formally, maximum operational thermal limits of most IC electronics systems were governed by critical transistor junction temperature maximums, that if exceeded lead to system malfunction, reduced longevity, or, at the extreme, complete device failure. However, as the human interaction with electronics systems become more intimate with the widespread use of mobile electronics, further demands are placed on the thermal solutions in order to maintain comfortable skin temperatures and maintain junction temperatures well under their maximum values in order to reduce leakage and thus improve battery life.

Effective and efficient thermal management is now increasingly critical to the electronics industry to satisfy the escalating market demand for faster, smaller, lighter, reliable, and cost-efficient products.

The thermal industry has responded with the development and implementation of many novel thermal solutions that are now used across a broad range of electronics or targeted for specific market segments, such as servers, workstations, desktops, notebooks, or ultra-mobile devices such as pads and smart phones. Ultimately, the aim of all thermal solutions is the same, namely to maintain device component and system temperatures within an acceptable range by removing heat energy from the system. However, the thermal requirements and system constraints vary widely leading to the need for a multitude of technologies to address the varied need, ranging from low heat flux devices around 10 W/m^2K using natural convection based solutions, to high heat flux devices in

the range of 1000 W/m^{2}K to 10000 W/m^{2}K using liquid jet impingement and or direct contact phase change cooling systems. The heat transfer capabilities of different heat transfer modes and technologies are shown in Figure 2.1.

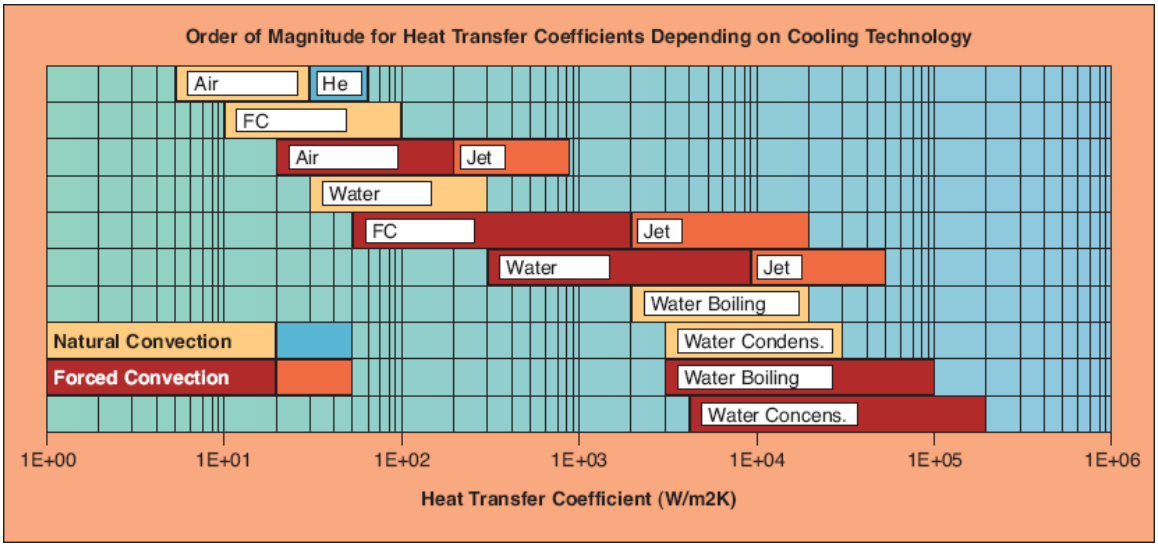

Figure 2.1. *Ranges of heat transfer coefficients for different heat transfer technologies and modes [41].*

Although a wide range of heat transfer rates are possible, the vast majority of electronics applications to date use natural or forced convection air cooling, even though conventional air based thermal management system cooling capabilities are often a bottleneck in device performance. The continued use of air cooling is largely due to the ease of design and relatively low cost of implementation, as well as the requirement of most devices to ultimately dissipate heat to the air environment around them. Other technologies such as liquid and phase-change based cooling, among others, continue to fill niche applications were high thermal dissipation rates are required and cost is elastic. Notably, as the alternative (non-air) cooling technologies mature, reducing both their design barriers and implementation cost, more and more of them will be adopted into larger market niches, such as liquid and phase change cooling into server thermal management systems and the use of phase change heat pipes in laptops, which is now almost ubiquitous. However, for the large majority of applications, especially consumer products, air cooling is likely to play a dominate thermal management role due to its design flexibility, and lower cost relative to alternatives.

Typical thermal management systems consist of several cooling sub subsystems that may include heat spreaders, thermal interface materials (TIM), heat transport devices, and heat exchangers, as shown in Figure 2.2 and Figure 2.3. The heat spreaders act to transport heat from hot spots to a larger thermally conducting surface. Thermal interface materials provide high thermal conductivity connections between different components of the thermal solution, and heat transport devices such as phase-change heat pipes, liquid coolers, peltier devices, and vapor chambers among others, work to efficiently transport heat away from its source to a heat exchanger where the heat can be removed from the system. The primary function of the heat exchangers, e.g. heat sinks, is to minimize the thermal resistance from the thermal system to the air, otherwise known as the airside thermal resistance.

Generally, the airside thermal resistance is minimized by creating the maximum effective surface area to which heat is transferred, in order to be carried away by the external cooling medium to the ambient, while at the same time delivering heat to the heatsink in a uniform fashion to reduce spreading resistances and improve the temperature uniformity of the outgoing air. Forced convection air cooling relies on an efficient exchange of heat at the solid-fluid boundary layer to achieve maximum heat transfer rates and, ultimately, lower thermal resistance between the hot surface being cooled and ambient air.

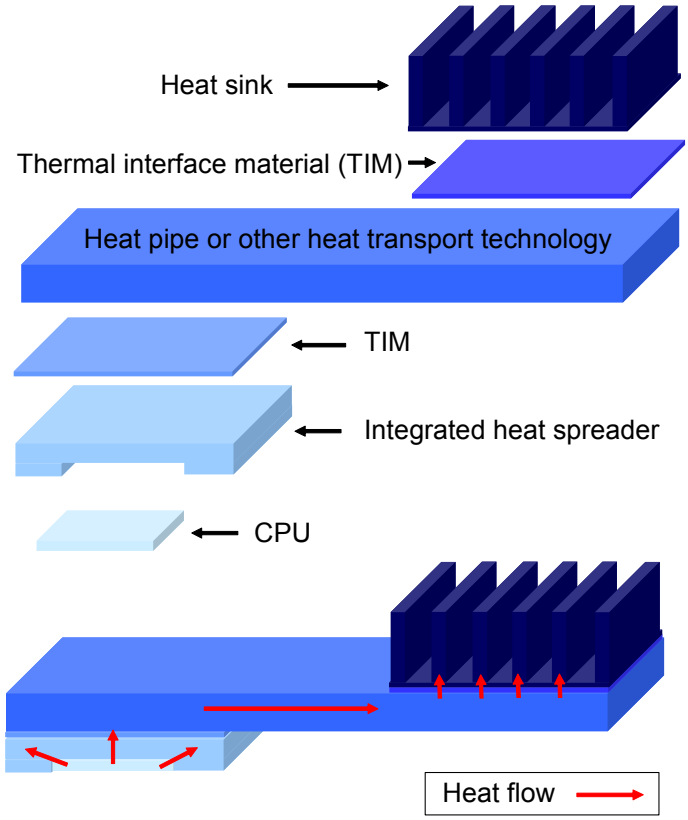

Figure 2.2. *Generic notebook thermal management stack-up and heat flow from the CPU silicon die to the ambient air.*

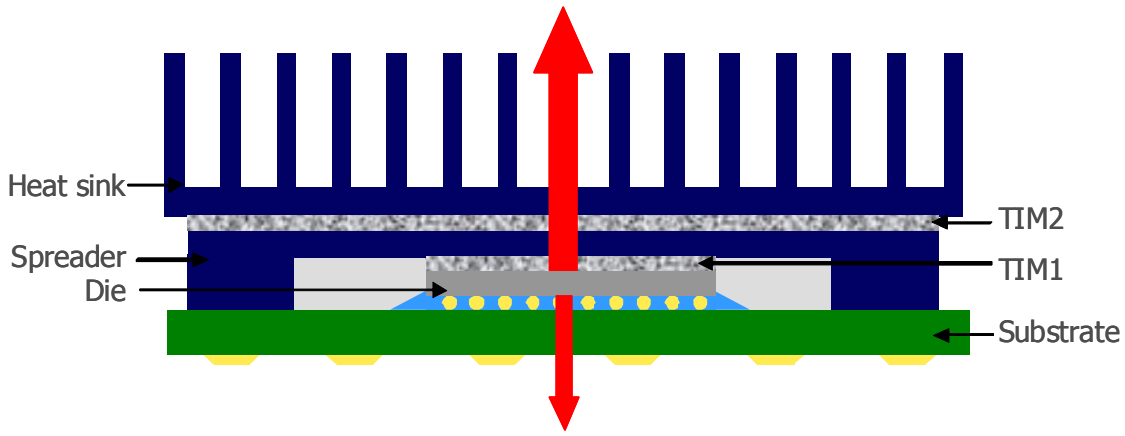

Figure 2.3. *Generic desktop thermal management stack-up and heat flow from the CPU silicon die to the ambient air and substrate.*

The effect of the fluid boundary layer δ on the airside thermal resistance Ψ_{sa} for forced convection is shown below in Figure 2.4.

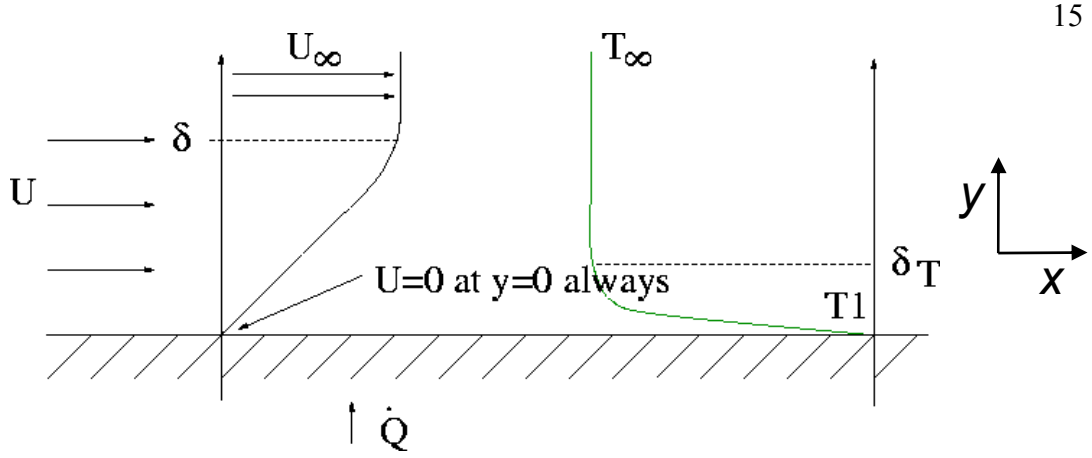

Figure 2.4. *Large air-side thermal resistance Ψ_{sa} is created by poor heat conduction through the fluid boundary layer δ, which forms a thermal boundary layer δ_T that reduces the temperature gradient and thus the heat flux to the fluid.*

The heat flux between the solid fluid boundary Q' is equal to the product of the thermal conductance of the interface k and the temperature gradient at the interface.

$$Q' = -k \left. \frac{\partial T}{\partial y} \right|_{y=0} \tag{2.1}$$

A temperature gradient is formed by lossy conduction of heat through the low velocity fluid near the solid-fluid interface that makes up the fluid boundary layer. As a result, a thermal boundary layer δ_T is formed, and the temperature gradient at the interface can be approximated by

$$\left. \frac{\partial T}{\partial y} \right|_{y=0} \cong \frac{T_\infty - T_1}{\delta_T} \tag{2.2}$$

where T_∞ is the ambient fluid temperature and T_1 is the temperature at the thermal exchange surface. Thus, the airside thermal resistance Ψ_{sa} is proportional to the size of the fluid boundary layer.

$$\psi_{sa} \equiv \delta_T \equiv \delta \tag{2.3}$$

Relatively high airside thermal resistances plague conventional forced convection cooling systems, to the point that the airside thermal resistance is often the largest thermal resistance component in the thermal stake up, Figure 2.5, which is largely due to non-ideal convective heat transfer through the solid-fluid boundary layer. Beyond being

the bottleneck in thermal performance, the airside thermal solution, including the heatsink, fan, and air duct/vent, contributes significant volume and mass to the overall device compared to the heat sources to which they are designed to cool. It is therefore critical to improve the efficiency of the airside cooling in order to continue the trend of device miniaturization and performance enhancement.

The total thermal resistance of the air cooled heatsink can broken into two basic components. One is associated with the conduction of heat from the compact heat source to the heatsink fins; the second is associated with heat convection from fin surface to the air. The heat convection rate on the fin surface is

$$Q' = h(T_s - T_a) \tag{2.4}$$

where h is the convection heat transfer coefficient and T_s and T_a are respectively the average heatsink surface and average air temperature. The total heat removal from the heatsink Q by the air flow is

$$Q = \dot{m} c_p (T_{out} - T_{in}) \tag{2.5}$$

where $\dot{m}$ is the mass flow rate, C_p the heat capacity of air and T_{out} and T_{in} are the average air temperature at the exit and inlet of the heatsink, respectively. From the equation, a higher h value is needed to increase the fin heat transfer rate. On the other hand, to increase the total heat dissipation, we need to increase both the mass flow rate $\dot{m}$ and the average exit temperature T_{out}. With a fixed fan curve, the flow rate can be increased by reducing the system flow resistance, and T_{out} can be maximized by keeping the hot air next to the fin surface and the cold air in the middle of the channel well mixed before leaving the heatsink. However, many applications set maximum allowable outlet temperature T_{out} which ultimately limit the benefit from increasing h without a further increase in flow rate.

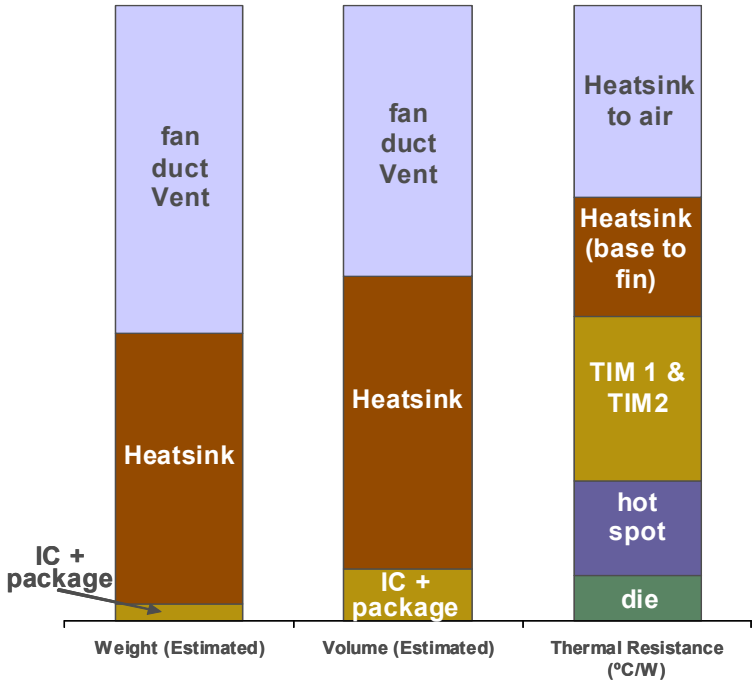

Figure 2.5. *Plot showing the relative weight, volume, and thermal resistance of the airside thermal solution in a generic forced convection air cooling system. Figure adapted from Intel IDF 2007.*

Emerging technologies to improve air cooling efficiency fall into three general categories: heatsink structure optimization [42-45], use of high thermal conductivity materials [46, 47], and innovative air moving technologies [5, 48-52]. Examples in the first category includes metallic and non-metallic foams, micro scale fabricated textured surfaces, and stretched extrusions of powdered metal [48]. The objective in these is to increase the ratio of surface area to volume there by increasing the heat that can be removed in a given volume. However, the tradeoff is increased pressure loss due to friction through the small channels. Foamed materials work well for small heat sinks, but when the heatsink get larger and deeper, the impact of pressure drop based losses can significantly influence the efficiency. Other directions have been to reduce flow restriction or enhance turbulence mixing by optimizing heatsink fin structures by going to straight fins, cubic pin fins, pyramids, dimples, porous tunnels, etc. [44], and to stagger heatsink fins [42].

Although it is likely that gains in TIM and heat transport materials and technologies will continue to be made, they will largely be incremental and will further

push airside cooling as the major thermal bottleneck in consumer electronics. As the combined heatsink rotary fan assembly has now reached a high degree of maturity, it is also unlikely to see major gains in performance and capability. Thus, major future improvement in air cooling will likely be driven from advancements in air movers, which will in turn lead to a wave of innovation in heatsink structure and material optimization based on the novel performance characteristics of future air movers and their integration into new applications that stretch the limits of the thermal technologies today.

2.2 Rotary fans for microelectronics forced convection cooling

Most current cooling solutions employ rotary fans to produce airflow through the heat exchanger to enable adequate convection heat transfer. In fact, the mechanical fan is for all practical means the sole method of active air movement for forced convection cooling in use today due to its reasonable transduction efficiency, low cost, and robust operation, which is the result of over a hundred years of technology optimization and specialization.

A set of simple but useful equations describe the scaling relationship of key rotary fan performance metrics with changes in rotor size and speed. These "Fan Laws", shown below, ignore loss mechanisms; effectively assuming fan electrical to mechanical transduction efficiency stays constant with changes in fan size and aspect ratio. Although the Fan Laws have proven valid over a wide range of device parameters, they breakdown as loss mechanisms become significant as fans move to smaller and thinner form factors to address the thermal needs of ever shrinking electronic devices.

$$G = w\, d^2 h \tag{2.6}$$

$$p = w^2 d^2 h^0 \tag{2.7}$$

$$P = w^3 d^4 h \tag{2.8}$$

where G is the output flow rate of the fan, p is the back pressure, P is the power output of the fan, and the fan rotational speed, diameter, and height are respectively w, d, and h.

The major losses reported in small scale fans are due to the transition from turbulent to laminar boundary layers at the rotors, which significantly impacts the transduction efficiency from the rotor to the air and causes a decrease in fan performance.

It has been proposed that due to boundary layer effects the efficiency of similar fans scale at a rate of $1/x^{1/2}$ where x is the scaling rate [53]. In addition to transduction losses at the rotor from boundary layer effects, limitations to aspect ratios in centrifugal fans, the most common rotary fans used in thin form factor electronics, also exist, making it impractical to simply reduce the z height of the fan but otherwise maintain performance as predicted by the Fan Laws. The design point where aspect ratio limitations take affect is where the area of the outlet of the rotor becomes less than the area of the inlet orifice of the fan, which happens when the height of the rotor becomes less than one quarter the fan inlet orifice diameter [54]. After that point, losses in efficiency and performance rise significantly, effectively limiting fan aspect ratios as illustrated in Figure 2.6. Therefore, at a constant rotational speed, as the fan aspect ratio becomes smaller, smaller pressure rise and smaller flow rate are expected, although the fan's power consumption decreases as well. The smaller pressure rise and smaller flow rate results in lower heat transfer removal ability than expected based on the fan laws.

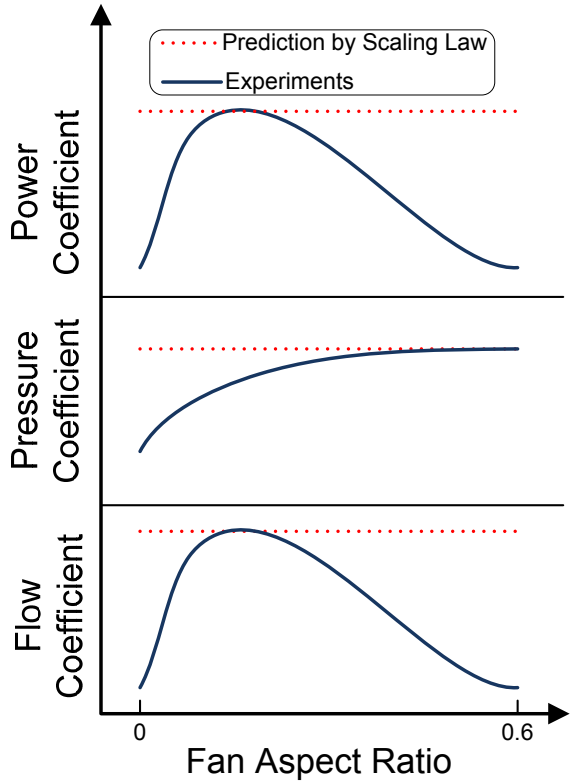

Figure 2.6. *Fundamental limits of the miniaturized rotary fan in terms of flow coefficient, pressure coefficient, and power coefficient at constant rotational speed [54].*

Figure 2.6 shows the impact of fan aspect ratio reduction to flow, pressure, and the resultant kinetic power delivered to the air. Here the aspect ratio is the height of the rotor divided by the diameter of the fan. In practice, if you had a given fan and wanted to keep all dimensions congruent but reduce the height you would get a decrease in the aspect ratio as defined in Figure 2.6. The dotted line represents the predicted performance relative to the fan scaling laws and the blue curve shows the measured performance for a range of fans with varying fan aspect ratio. Walsh et al. showed that for aspect ratios below approximately 0.08 fan performance dropped off quickly. Of course, the fan aspect ratio related losses can be avoided by shrinking the diameter of the fan with a decrease in height, but as both pressure and flow rate change with the square of the diameter, a reduction in diameter quickly leads to significant performance loss.

Beyond transduction losses increasing as fans shrink, the cost and reliability become larger issues as the challenge to produce low cost reliable miniature fan motors, rotors, and flutes for smaller fans increase. In the design of low aspect ratio thin fans bearing failure is an ever increasing challenge as the effective lever arm of the fan blade increases for decreasing fan aspect ratio, which in turn makes it difficult to maintain the relative position of the fan rotor to the fan case with gyroscopic forces induced by rapid tilting or motion of the notebook or other mobile electronics product they are designed for. In addition, acoustics become significant due to the need for higher rotor speeds for the smaller fans which can ultimately limit the fan performance due to acoustic bounds even if reliable high speed devices can be made [55]. There is also a trend to increasing the number of fans in a system to compensate for the limited performance of thinner fans, however, this requires more footprint and volume within a given application for the thermal management solution, provides more rotating mechanical parts to fail, and can lead to unpleasant audible beat frequencies from interference between the multiple fan acoustic emissions.

Further, there are inherent limitations to rotary fans design flexibility beyond z height limitations due to the necessity of high-speed rotating parts, which therefore necessitate a circular cross-section that cannot easily be coinhabited by other thermal

elements such as a heatsink. In addition, the use of rotating members introduces vibration, acoustics, and gyroscopic forces to the system.

For all these reasons, the search for a novel air movement technology has been taken up and several of the emerging air mover technologies are presented in the following subchapter.

2.3 Review of emerging airside cooling technologies

2.3.1 Synthetic jet

A synthetic jet is formed by periodic suction and ejection of fluid out of an orifice bounding a cavity by the time periodic motion of a diaphragm, as plotted in Figure 2.7. Unlike conventional jets, synthetic jets are "zero-mass-flux" in nature and produce a fluid flow with finite momentum that neither adds or remove mass to the system, and therefore can consume less energy than a blower, which require net mass flux. The output of a synthetic jet can produce a high velocity periodic jet pulses that can produce high levels of forced convection when impinging on a surface. These jets are ideally suited for spot cooling at the package and heat sinks levels, and with better COP than rotary fan [56]. Synthetic jets can also be used in conjunction with fans in a form known as fan augmentation. The periodic formation of vortex structures enhances turbulence and increases the convection coefficient at the boundary layer, while the mechanical fan produced net mass flux flow. In addition, flow entrainment formed by the synthetic jet can reduce flow bypass from the channel, thereby improving the cooling effectiveness with the same amount of air flow. The result is that the system fans may operate at lower RPM, resulting in longer useful life for the fan, reduced fan acoustic noise and system power consumption [56]. Another benefit of synthetic jets is the lack of rotational parts and the failure mechanisms related to them. A synthetic jet still necessitates a moving diaphragm and therefore will have mechanical failure modes associated with the diaphragm, but less severe, enabling reliability and life of operation greater than rotary fans [57].

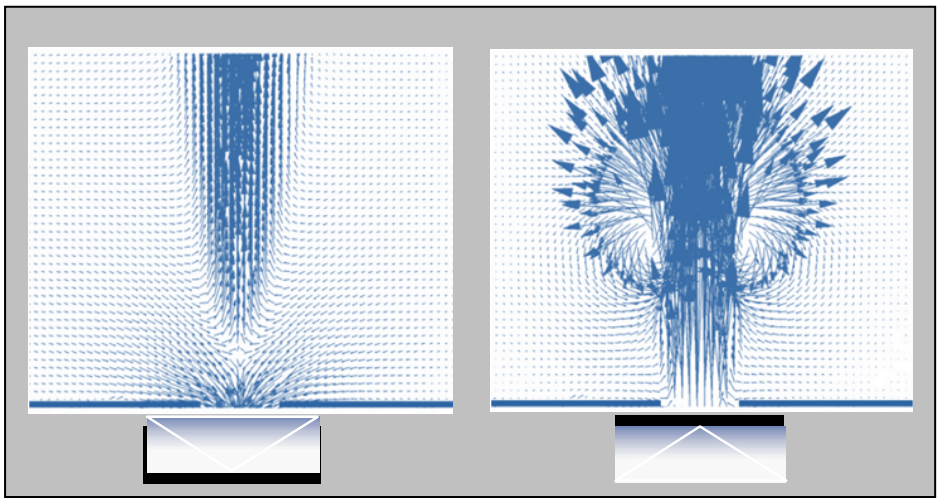

Figure 2.7. *(left) Particle Image Velocimetry of a SynJet formed from an orifice bounding a cavity. Air is slowly drawn into the SynJet on the diaphragm down-stroke, then the air pulse is rapidly expelled on the diaphragm upstroke (right). Figures adapted from presentation by Nuventix [56].*

However, the functional dependence of flow rate and pressure on size and frequency of diaphragm vibration scale similarly to the fan law. Flow rate reduces when the device is miniaturized. Because it does not generate net mass flux and high pressure, it may not be suitable for applications such as laptops, where the main purpose of the air cooling system is to remove heat from the chassis rather than boost h locally. Its preferred application is in relatively open environments such as LED cooling, or as fan augmentation in server and desktop applications. In particular, the long operating life of the synthetic jet device fits well with the LED lighting application, which can require continuous operation for more than ten years.

2.3.2 Piezoelectric fans

A piezoelectric fan, also known as a piezo fan, shown in Figure 2.8, consists of a piece of piezoelectric material bonded to a flexible cantilever beam. Under an alternating electric potential, the beam vibrates back and forth and generates air flow much in the manner that a paper fan would produce airflow when held in the hand and rotated up and down at the wrist. Efficiency of the air mover is maximized when driven at the resonance of the cantilever beam.

Piezo fans consume very little power and offer enhanced heat transfer versus natural convection. The piezoelectric fan has the advantages of low acoustic noise and power consumption. However, acoustics and vibration can be an issue when used at high oscillation frequencies. When the blades are intertwined between heatsink fins, the unsteady stream flow reduces the boundary layer and enhances convection [58].When used as a fan enhancement, it brings improvement in convection at no or low base airflow through the heatsink. Since, by itself, it generates a small amount of net airflow, its application is limited to low power applications or localized cooling of low power components. Compared with other air moving technologies, the major advantage of piezoelectric fans is the potential for low cost and low power consumption.

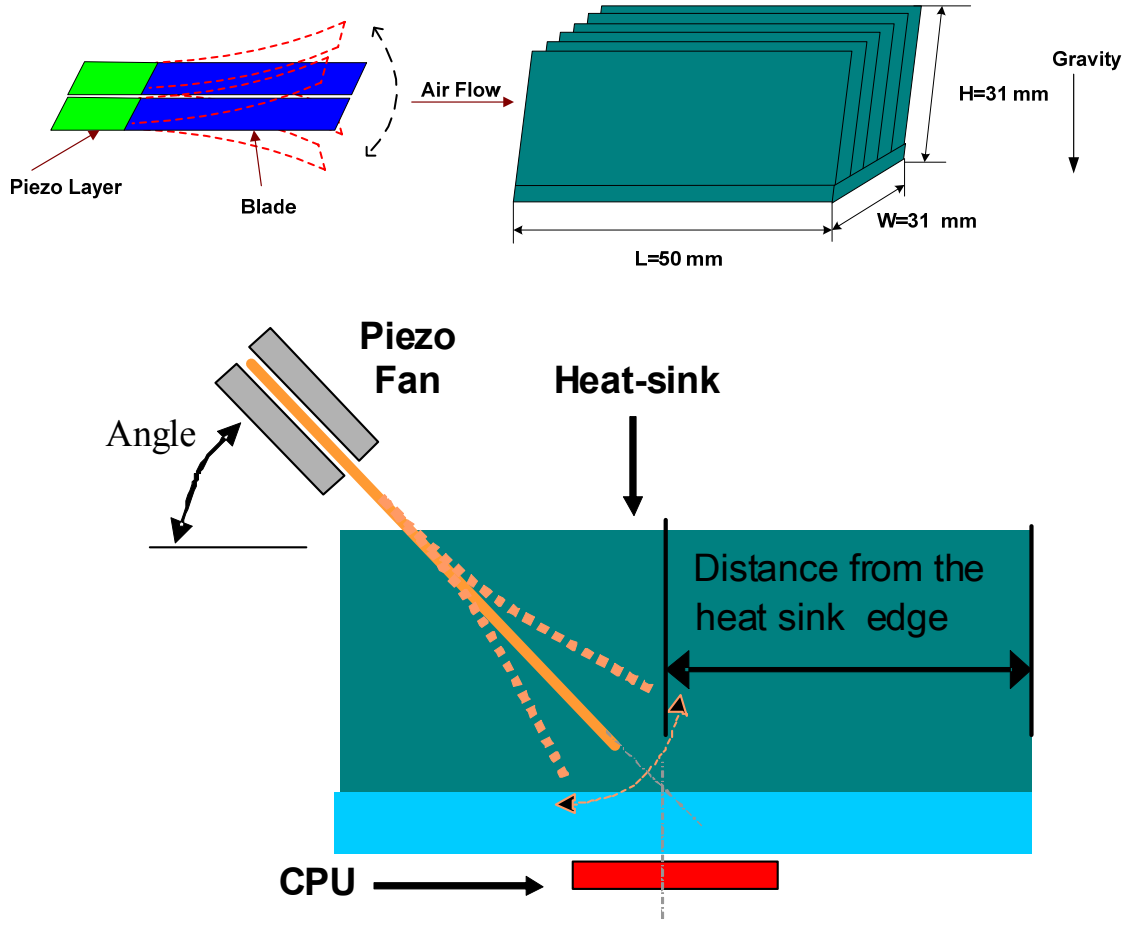

Figure 2.8. *Heatsink cooled with Piezoelectric fan. (top), the piezo fans are placed in front of a heat sink; (bottom), many piezo blades are interwoven between the heat-sink fins very close to the surface of the fins, the thermal boundary layer is disturbed by the proximity of the blade increasing heat transfer [51].*

2.3.3 Summary

For the objective of developing a technology to replace the mechanical fan, neither piezoelectric fans nor synthetic jets can move enough air in a small package to meet the cooling requirements of most consumer electronics today. However, one or both may become valuable thermal enhancers for a primary air mover technology in the future, and both have attributes well suited for applications like LED lighting cooling, which will be an important market in the coming years.

2.4 Chapter summary

The world of electronics and heat transfer are intimately linked, and more and more the latter is defining what is possible of the former. For many groups of applications, such as notebooks, the minimum satisfactory performance level requires more heat generation than can be comfortably removed through passive cooling, making active cooling required.

Forced air cooling has been the dominate active cooling method for consumer electronics, and will be for the foreseeable future, due to the relative ease of transferring heat to the surrounding environment, compared to methods relying on liquid, phase change, or other heat transfer technologies.

The progression of consumer electronics to ever thinner and smaller form factors is compounded with the changing use models that put computing applications closer and closer to the user. These changes have driven the requirements for thin and quiet thermal solutions to a level that has not been seen before. Further, these trends suggest that the demand for thin and silent thermal solutions will only increase from the requirements seen today.

Mechanical fans, which have been for all intensive purposes are the only commercial technology used for forced convection air cooling to date, are struggling to meet the new requirements for thin form factor and silent operation, and recent studies suggest that fundamental barriers exist in their evolution to ever thinner and quieter form factors without significant compromises to performance and reliability. Thus, a vacuum

has been created, generating a desire for alternative air movers applicable to the future generations of thin and silent consumer electronics.

Several emerging airside cooling technologies exist today that are being reevaluated, after having been in and out of the thermal research labs over the last few decades, including synthetic jets and piezoelectric fans. However, both suffer from limited net airflow generation and, in some cases, acoustic noise. Since net airflow is the primary factor in setting maximum heat transfer out of a system, low net airflow generation capability make neither synthetic jets of piezoelectric fans an obvious candidate for mechanical fan replacement in most consumer electronics computing applications.

With no obvious technology for mechanical fan replacement for future consumer electronics applications with existing technologies, the market is open and in search for new thermal management solutions.

Chapter 3. EHD background and state of the art

3.1 Basic operation of electrostatic fluid accelerators

The mechanism of corona-induced ionic wind propulsion is illustrated in Figure 3.1. Gas molecules near the corona discharge region become ionized when a high intensity electric field is applied between a high tip curvature corona electrode and a low tip curvature collector electrode. In the case of a wire or rod electrode, the radius of curvature of the cross-section along the diameter of the wire or rod electrode is equivalent to the tip curvature of a needle electrode. The ionized gas molecules travel towards the collector electrode, colliding with neutral air molecules. During these collisions, momentum is imparted from the ionized gas to the neutral air molecules, resulting in the movement of gas towards the collector electrode. The operating voltage range for corona discharge lies between the corona onset and air gap breakdown voltage [59]. Corona induced airflow is possible with both a positive and negative voltage. In general, selection of polarity depends on a large number of factors, which include electrode material, device geometry, ozone generation constraints, fluid composition, and others.

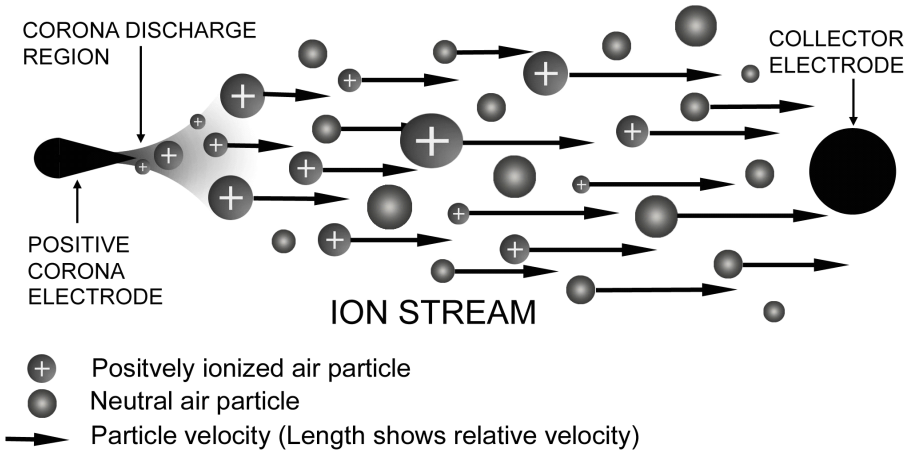

Figure 3.1. *Ion stream of a DC electrostatic air pump, where a high voltage is applied between the corona and collector electrodes.*

3.2 Fundamentals of corona discharges in air

3.2.1 Positive corona discharge

The ionization process for a direct current (DC) positive corona is well understood and described in Figure 3.2 [60-66]. A high positive electric potential is applied to the high tip curvature corona electrode. The relatively low tip curvature collector electrode is grounded or set to a lower potential. Free naturally occurring electrons in close proximity to the electrodes are accelerated towards the corona electrode by the electric field. In the plasma region, tens to hundreds of microns from the corona electrode surface, the electric field intensity reaches a critical level. In the region where the critical field exists, collisions of electrons and neutral gas molecules in the ionization region result in electrons breaking free of the neutral air molecules. This process creates free electrons and positive ions, which in turn are accelerated by Coulombic forces and produce more pairs of free electrons and positive ions. This process is known as the electron avalanche, which is described mathematically in sub-section 3.2.3. Free electron and ion pairs are also produced through a photoionization process. Photons are emitted from excited electrons as they decay into lower energy levels in the plasma of the corona discharge. The emitted photons collide with the surrounding air molecules, causing an ionization event on impact, creating additional free electron-ion pairs. The combination of photoionization and electron avalanche ionization processes is responsible for the stable plasma found in a corona discharge since the photoionization continually seeds additional avalanches which in-turn create more photoionization events, and so on. In dry air, O_2+ and N_2+ are the major charge carriers. The ionization region from a positive corona is characterized by a uniform, dim, bluish-purple glow along the electrode surface, shown in Figure 3.3, on the left.

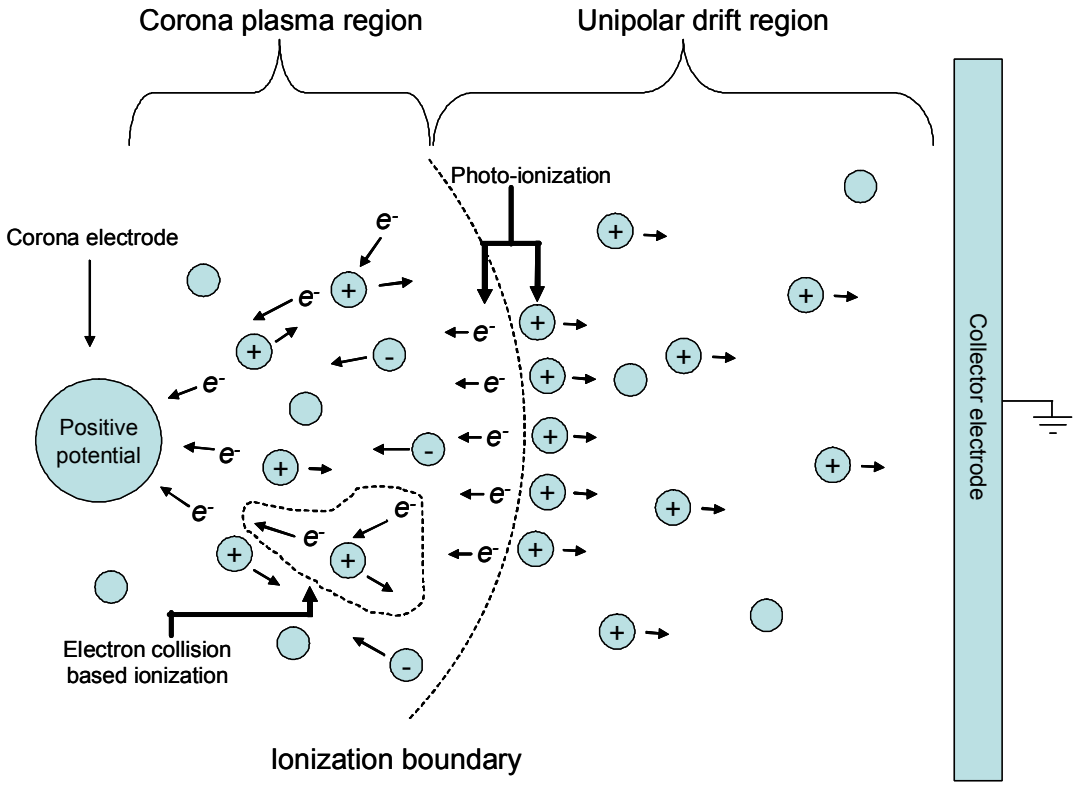

Figure 3.2. *Model of a positive corona discharge [66].*

Free electrons may also attach to electronegative gas molecules, such as O_2, forming negative ions, or they may recombine with positive ions. In other words, the net ionization rate is reduced by both electron attachment and recombination. Near the corona electrode, electrons have average energies high enough to sustain net ionization, however, as the distance from the corona electrode surface increases, the rate of ionization decreases and the rate of attachment and recombination increases. The location where the rate of ionization and combined rate of attachment and recombination are equal is the location of the ionization and plasma region boundary, as shown in Figure 3.2. Outside the corona plasma region, the field strength is insufficient to produce collision-induced electron-ion pairs. In this area, only ions of the same polarity as the corona electrode exist in significant number. The unipolar ions are propelled from the edge of the corona region towards the collector electrode. Any negative ions remaining within the corona region will be drawn towards the corona electrode and into the plasma region. Due to the lower tip curvature of the collector electrode, the electric field is relatively

weak compared to the region near the corona electrode and no ionization occurs in its vicinity.

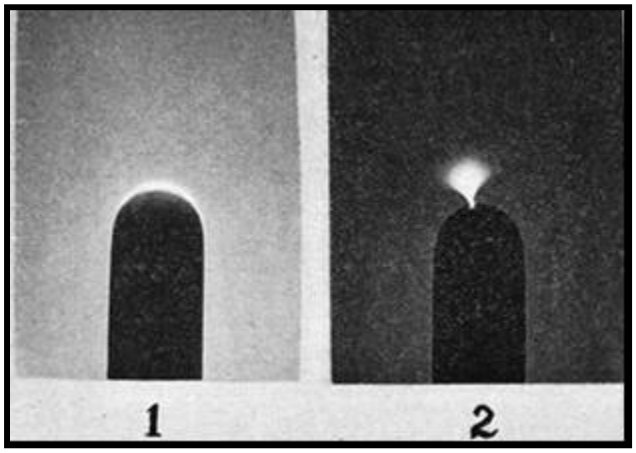

Figure 3.3. *Visual difference between a positive corona discharge and a negative corona discharge* [67]. *Positive and negative polarity coronas are shown in 1 (left) and 2 (right) respectively.*

3.2.2 Negative corona discharge

The ionization process for a DC negative corona is illustrated in Figure 3.4. The mechanisms giving rise to a negative corona are similar to those for a positive corona [60-62, 64, 66, 68-70]. A high negative potential is applied to the corona electrode and the collector electrode is grounded or set at a higher potential. Similar to a positive corona scenario, naturally occurring electrons in the air initiate the electron avalanche process. However, unlike the positive corona scenario, the secondary electrons in a negative corona are produced primarily by photo-emission from the corona electrode surface [68, 71]. The production of electrons by photo-emission from the corona electrode depends partially on matching the energy of emitted photons to the work function of the corona electrode material. If the photon is of low energy compared to the work function of the electrode material, it will be unable to overcome the work function of the electrode and release an electron from the corona electrode surface. Therefore, material selection has an impact on a negative corona discharge [72] where as it has minimal impact for positive coronas. In the ionization region, production of free electrons by electron collisions with air molecules is greater than recombination and attachment of electrons to neutral electronegative gas molecules, like O_2. At some distance from the

corona electrode surface, the attachment and recombination rate becomes equal to or greater than the ionization rate, marking the outer edge of the ionization region.

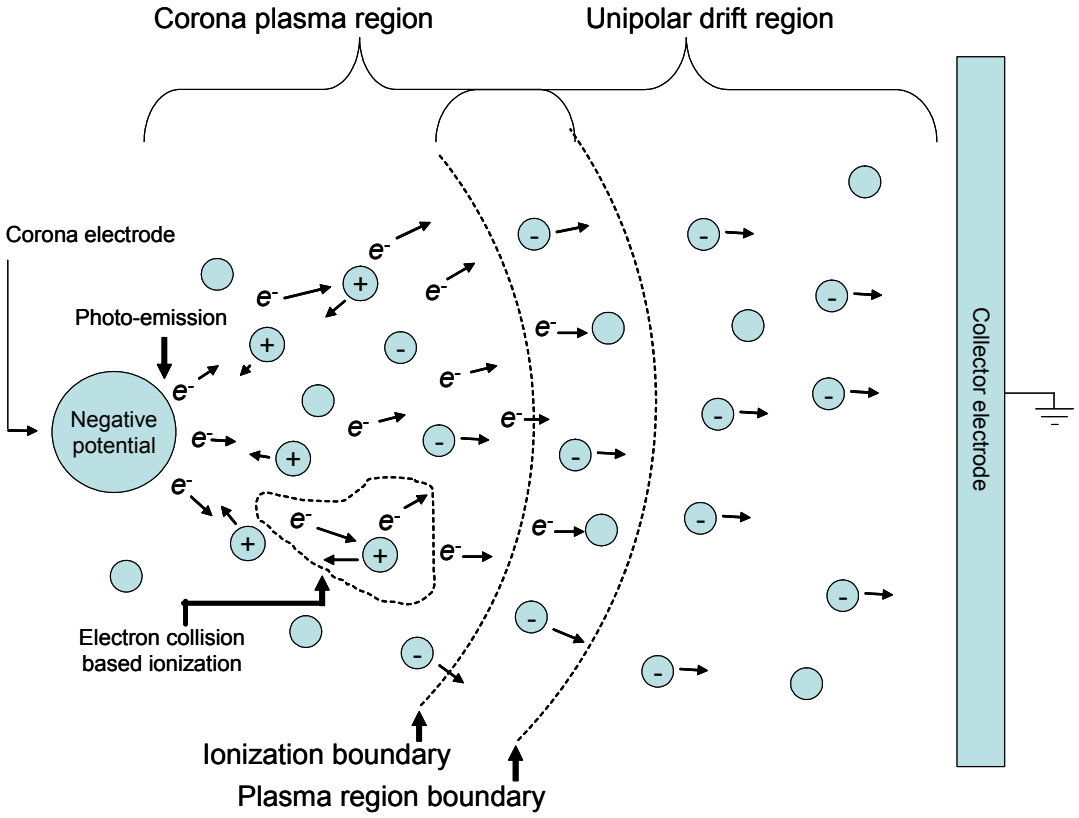

Figure 3.4. *Model of a negative corona discharge [66].*

Unlike the positive corona case however, electrons are propelled outside the ionization region where they bombard other neutral air molecules. This bombardment can drive certain chemical reactions. The electron bombardment outside of the ionization region creates a larger volume in which reactions can occur than compared to the positive corona case. This larger reactive volume in negative coronas is responsible for up to an order of magnitude increase in ozone generation rates over those generated in positive coronas [66]. The negative corona visually takes the form of brush-like bluish-purple discharges that are discontinuous along the electrode, as shown in Figure 3.3, on the right. The brush or tuff-like discharges of a negative corona are characterized by intermittent Trichel pulses, which can reach frequencies of 2×10^5 Hz [73]. Unlike positive coronas, negative coronas are only found in electronegative gases, such as oxygen, water vapor, and carbon dioxide. A negative corona will not occur in pure gases

with no or very low affinity for electrons, such as nitrogen, hydrogen, helium, and argon [66].

3.2.3 Analytical description of an electron avalanche process

Townsend [74] investigated the ionization process and expressed the electron ionization in differential equation form as

$$dn = \alpha n dx \tag{3.1}$$

where dn is the incremental increase in the number of electrons produced by n electrons moving a distance dx in the electric field. The coefficient α varies with the gas properties and density and is a function of the electric field strength. For a uniform electric field and corona discharge conditions, α is a constant and (3.1) can be integrated to

$$n = n_0 e^{\alpha x} \tag{3.2}$$

where n_0 is the number of free electrons at x equal to zero.

In a more general case, where the field varies with x, making α a function of x

$$n = n_0 e^{\int_0^x \alpha dx} \tag{3.3}$$

In addition to ionizing molecules based on high energy collisions, electrons can also attach to many neutral molecules to form negative gas ions. This happens more readily for electronegative elements, such as halogens, oxygen, and sulfur, which are deficient in electrons in their outer electron shells and therefore have high electron affinity. Gases such as Cl_2, CCl_4, HF, O_2, SO_2, and SF_6 are strongly electronegative and act as effective electron traps in gas discharges [70]. Electron attachment can significantly reduce electron ionization by removing free electrons from the system that would otherwise seed additional electron avalanche events. Electron attachment can be expressed as

$$n = n_0 e^{-\eta x} \tag{3.4}$$

where η is the coefficient of attachment, which is a function of gas properties and the electric field strength. Combining (3.3) and (3.4) yields the value of n for a uniform field

$$n = n_0 e^{(\alpha-\eta)x} \tag{3.5}$$

At low electric fields, η exceeds α, and the number of electrons declines with distance. At the threshold value E_T where $\eta = \alpha$, n remains constant. For $E > E_T$, α exceeds η, and the number of electrons increases with distance.

3.2.4 Qualitative current-voltage relationship

The high electric field intensity required for EHD operation is generally created by applying an electric potential between two electrodes. The corona onset voltage is defined as the magnitude of the voltage that causes the field intensity in the vicinity of the corona electrode tip to exceed the critical value needed to start a corona plasma. Below this voltage, no discharge occurs and no current between the two electrodes exist. After the potential exceeds the onset voltage, current is present in the air in the form of a space charge consisting of ions traveling between the two electrodes, as illustrated in Figure 3.5. A further increase in voltage leads to an exponentially increasing current, followed by a spark-over, which marks the electrical breakdown across the electrode separation gap.

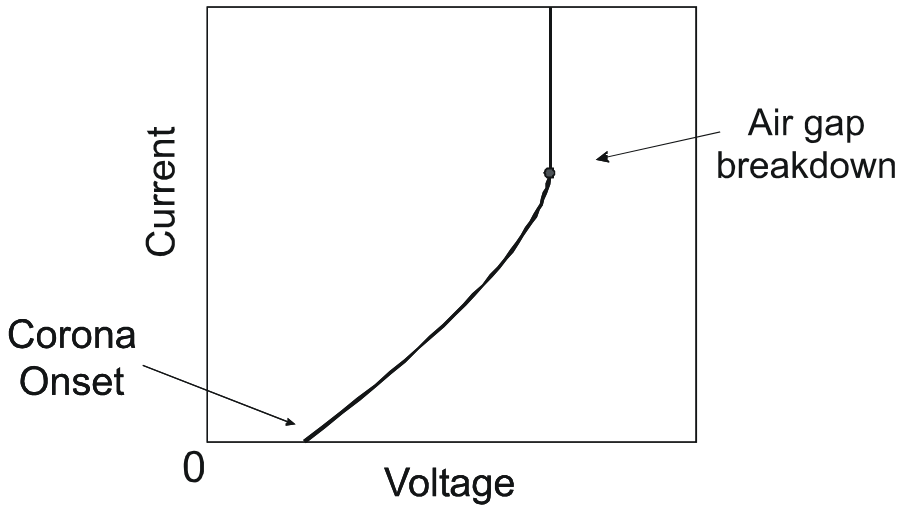

Figure 3.5. *Corona current-voltage relationship.*

3.2.5 Theoretical current-voltage relationship

The current-voltage relationship of a corona discharge is a function of several variables which include: gas composition, temperature and pressure, electrode geometry, corona to collector voltage polarity, electrode surface roughness, and particles suspended within the gas [70]. Equations can be analytically expressed for concentric cylinder and sphere electrode geometry, but for most other cases, the relationship can only be approximated numerically or determined experimentally.

Poisson's equation, which governs all electrostatic phenomena is [75].

$$\nabla^2 V = -4\pi\rho \tag{3.6}$$

where ρ is the space charge density and V is the electric potential.

In cylindrical coordinates, assuming axial symmetry, the voltage is constant in θ and φ, therefore, equation (3.6) reduces to

$$\frac{d^2V}{dr^2} + \frac{1}{r}\cdot\frac{dV}{dr} + 4\pi\rho = 0 \tag{3.7}$$

where ρ is the space charge density, given by

$$\rho = \frac{i}{2\pi rKE} \tag{3.8}$$

where i is the corona current, K is a constant, and

$$E = -\frac{dV}{dr} \tag{3.9}$$

Combining the three previous equations, results in

$$rE\frac{dE}{dr} + E^2 - \frac{2i}{K} = 0 \tag{3.10}$$

This equation can be integrated to:

$$E = -\frac{dV}{dr} = -\sqrt{\left(2i/K\right) + \left(C^2/r^2\right)} \tag{3.11}$$

where C is the constant of integration.

Integrating (3.11) gives

$$V = C\log\left(\frac{\sqrt{C^2 + \left(2ia^2/K\right)} + C}{\sqrt{C^2 + \left(2ib^2/K\right)} + C}\right) \tag{3.12}$$

The constant of integration C may be calculated from (3.11) by using the boundary condition at the outer radius of the plasma region near the wire. The electric field magnitude at this point is E_0 and the corresponding radius is r_0. Knowing E_0 and r_0, C can be expressed as

$$C = r_0\sqrt{E_0^{\,2} - (2i/K)} \tag{3.13}$$

Using the value of C from (3.13), the current-voltage relationship can be expressed as

$$V = r_0 E_0\left\{\log\frac{a}{b} + 1 - \sqrt{1 + \left(2i/K\right)\cdot\left(b^2/E_0^{\,2}r_0^{\,2}\right)} + \log\frac{1 + \sqrt{1 + (2i/K)\cdot(b^2/E_0^{\,2}r_0^{\,2})}}{2}\right\} \tag{3.14}$$

where a is the diameter of the corona wire, b is the diameter of the hollow cylindrical shaped collector electrode, r_0 is the outer radius of the plasma region around the wire, and E_0 is the corona initiation field strength at this point.

According to Peek's law, E_0 can be estimated by

$$E_0 = 30 f\delta(1 + 0.30\sqrt{\delta/a}) \tag{3.15}$$

where

$$\delta = \frac{T_0}{T}\cdot\frac{P}{P_0} \tag{3.16}$$

In equation (3.16), T_0 is the absolute room temperature ($293K$), P_0 is the normal atmospheric pressure (760 mmHg), and T and P are the actual temperature and pressure of the air. In (3.15), f is a roughness factor of the wire, which decreases when the wire is rough, marred, or specked with dust. The parameter f is usually between 0.5 and 0.7 for dirty, scratched wire. Corona initiation field strength E_0 is also a function of gas density [70] and composition.

Corona initiation field strength is determined solely by the geometry of the corona electrode and the physical properties of the gas in which the corona is being formed. Corona onset voltage, on the other hand, is set by the design of both corona electrode and corona to collector electrode distance. It can be calculated through (3.14) for a pair of concentric cylindrical electrodes by setting $i = 0$ and $r_0 = a$

$$V_0 = aE_0 \log\frac{b}{a} = 30\,fa\delta(1 + 0.30\sqrt{\delta / a})\log\frac{b}{a} \tag{3.17}$$

3.2.6 Electrical conduction in different states of matter

Electrical conduction in gas differs fundamentally from conduction in a solid or liquid. In solid and liquid conductors, electrons move in a lattice structure or between atoms loosely bound to each other. When an electric field is applied to a solid or liquid conductor, it is relatively simple for electrons to move through the medium assuming that free carriers exist, compared to the same matter in a gas phase. For example, in metal solids such as copper, electrons in the conductance band act as free charge carriers moving through the material with little resistance. Matter in a gaseous state, on the other hand, is composed of mostly neutral molecules separated from each other in space without free electrons and ions under normal conditions. Gas density is on the order of 10^{19} molecules per cm^3 at one atmosphere, which is approximately three orders of magnitude lower than matter in a solid or liquid phase. The large distance between gas molecules and the lack of abundant charge carriers cause gases to be good electrical insulators. In the case of a cold plasma, like corona discharge, conduction between emitter and collector electrodes occurs through the ionization of individual gas molecules and then transportation of those ions through space to the collecting electrode. As the corona discharge current increases, the density of free charges within the gas increases, and the conductivity increases. A corona discharge is only one form of electrical conduction in gases; others include sparks, arcs, streamers, and other plasmas [70].

3.3 History and state of the art

3.3.1 History

The first experimental observations of corona wind were reported in the 1700's [76]. Many pioneers of electricity, including Newton, Faraday, and Maxwell, studied this phenomenon [77-79] and one of its first uses was likely that of self-propelled spinning wheel used as an entertainment piece for aristocrats who dabbled in the sciences in the 1800's. Rigorous fundamental studies were conducted by Stuetzer [80], who investigated ion conduction in both liquids and gases, and Robinson [81], who investigated corona wind pressure, electric parameters, and efficiency under varying pressure and conditions. The more recent investigations of corona propulsion focused on heat transfer [3, 4, 11, 13, 14, 23, 26-31, 33, 82, 83], boundary layer modification [19-21, 23, 24, 84], acoustic transduction [34-36] air sterilization [85], and dehumidification [39, 40, 86].

3.3.2 Experimental investigations into EHD enhanced thermal management

One of the earliest references of EHD driven flows utilized for enhanced convection heat transfer is a patent by Burke in 1931 [87] that presented a new method for reducing the fluid boundary layer and increasing heat transfer along the heated surface of a metal exhaust flue by creating a recirculating EHD flow within the flue. Early investigation into EHD based heat transfer was also conducted by Velkoff in the early 1960's [88] investigating heat transfer enhancement through EHD driven fluid boundary layer modification. While other early studies investigated the use of EHD driven flows to cool a secondary surface, Robinson, in 1968, [89] proposed using the high velocity around the corona electrode itself to enhance the thermal transfer from the coronating surface, reporting heat transfer enhancement of up to six times. Mizushina et al. [90] obtained an increase in heat transfer coefficients up to 2.5 times with air flowing in a circular tube in the laminar regime. Velkoff and Godfrey [91] analyzed a low-velocity air-flow along a heated flat plate, obtaining a maximum heat transfer enhancement of 3.5 times. The corona electrodes were an array of fine wires, positioned

in parallel with the main flow path. Ohadi et al. [92] examined the turbulent flow of air in a circular duct, with two high-voltage thin wire electrodes placed longitudinally in the proximity of the pipe axis, obtaining a heat transfer augmentation of 2.6. Molki et al. [93] conducted a numerical and experimental investigation of airflow in a square duct, with the corona electrode situated at the centerline along the primary flow and channel axis. A maximum heat transfer enhancement of a factor of 2 was observed at the entry region of the channel and a factor of 3.4 was observed for the fully developed flow. Franke and Hogue [27], studied the effect of corona wind on the heat transfer coefficient from a heated horizontal cylinder. The corona wind was directed toward the lower region of the grounded cylinder by placing either a positively charged single-wire emitter (0.1 and 0.32 mm in diameter) or multi-point emitter parallel to and directly below the heated cylinder. A jet of air from a wedged-shaped plenum was also directed at the cylinder to compare its effect with that of the corona wind, giving similar results, suggesting that the flow could be modeled like an impinging jet. Franke and Hogue [27] found that heat transfer rates were increased as much as six times the free convection rate by corona winds (the free convection heat transfer coefficient was found to be 7.7 W/m^2 K). For a given emitter, the heat transfer rate varied with emitter current. Compared with the stretched-wire emitter, the multi-point emitter was more effective in increasing heat transfer rates at a given power level.

A majority of the heat transfer investigation to date have been focused on heat transfer from macro-scale tubes and ducts, due to the obvious application for heat transfer in large industrial and commercial applications. However, several studies have investigated heat transfer in the macro-scale point-to-plane or wire-to-plane regimes. Owsenek et al. [29] studied the effect of corona wind on the enhancement of free convection, with a needle to plate geometry in air. The heat transfer coefficient was derived from the measured surface temperature distribution with an infrared camera. Local heat transfer coefficients greater than 65 W/m^2K were measured, which indicates an enhancement of more than 25:1 over natural convection (a value of 2.5 W/m^2 K was measured for the natural convection coefficient). Owsenek and Seyed-Yagoobi [94] employed a wire to horizontal plate geometry, and studied the effect of the corona wind

on the enhancement of the free-convection, heat transfer coefficient. For a wire located 4 cm above the plate, with a 20 kV operation voltage, they recorded an enhancement of more than four times in the heat transfer coefficient, just below the electrode wire. When the wire was located two centimeters above the plate and, with a 12.6 kV operation voltage, the corresponding heat transfer enhancement was found to be more than eight times natural convection.

Many previous EHD enhanced heat transfer investigation at the macro-scale have been conducted with heat transfer enhancements ranging from two to twenty five times natural convection heat transfer rates and convection heat transfer coefficients up to 65 W/m^2K have been achieved. However, relatively little or no work has gone into the investigation of meso-scale EHD devices for thermal management. Here meso-scale is being used to describe the size scale between macro and micro, generally in the region of millimeters to hundreds of microns. This thesis presents one of the first investigations into heat transfer from meso-scale EHD air mover devices.

3.3.3 Modeling of EHD driven airflow

Although the basic principles of EHD operation have been long understood, there are relatively few examples of successful designs of practical devices. An overwhelming majority of the existing electrostatic air propulsion devices have simple electrode geometry, convenient for theoretical development and modeling, but are sub-optimal in terms of air speed, backpressure, efficiency, and longevity [95-97]. Significant room for EHD air mover technology evolution exists on the path towards practical devices and applications.

A major limiting factor to the evolution of novel and useful EHD air mover technology has been in the ability to accurately model processed systems for practical geometries required for real world applications. Below is a concise review of the evolution of EHD modeling including major governing phenomena such as electrostatics, ion (space charge) transport, charge generation, and fluid dynamics.

In the presence of space charge, the electric potential distribution is governed by Poisson's equation (3.6), which is a linear equation for a given charge density

distribution. However, for unipolar charge currents the charge density distribution is not simply deducted because it is coupled to the electric field profile. The mathematical system describing unipolar ionic charge currents with coupled electric potential and charge density is inherently nonlinear. Solutions by analytical means are limited to a few cases where the problem configurations are highly symmetric such that the mathematical system can be reduced to an ordinary differential equation, as is the case for concentric cylinders or spheres [98]. In general, for all practical applications numerical methods are required and with the advent of modern microprocessors, numerical modeling is commonplace. Some early modeling approaches used the finite-difference method for coupling charge transport and electric field [99], however to enable convenient computation with non-uniform mesh in complicated and sharp geometries, a finite-element method has been widely adopted in solving Poisson's equation [100]. Commonly the method of characteristics is used for solving charge transport since by neglecting diffusion effects the charge transport equation for determining charge density is of the hyperbolic type [101]. However, for improved accuracy by accounting for charge diffusion the finite-element method has been successfully used [102].

Modeling of the corona discharge plasma itself is rarely conducted in modeling of EHD devices due to the complexity of the ionization process, which includes impact ionization, photoionization, and photo-emission processes within the corona discharge region. Several attempts have been made using a simplifying subset of possible ionization reactions, which appear to correlate well qualitatively with experimental evidence. However due to the large number of potential ionization reactions, high speed interactions requiring small time steps, and highly coupled interactions, the computational requirements are immense even with simplified one-dimensional models [65]. Therefore, such an approach at this time can be useful for detailed study of some physical corona processes, but generally not yet as a design or optimization tool in engineering applications. Numerical models have been created to predict ion and electron bombardment driven chemical reactions in the corona discharge plasma region, however they generally rely on empirical correlations for corona electrode current densities and

corona onset conditions or experimentally derived corona electrode current densities as input to the model [66, 103-105].

In nearly all models not investigating chemical processes, the ionization region which lies within the corona plasma is ignored and boundary conditions based on empirical correlations for charge generation in coronas such as Peek's equation are used to predict the critical corona onset field and thus the corona electrode current density [98, 102]. In cases where current densities can be determined experimentally, the estimation of charge generation can be ignored and supplemented with empirical data.

The modeling of EHD flow is done through the coupling of Coulombic force being applied to the ions as a body force on the fluid in which the ions reside. As described in detail in Chapter 5.1, this coupling is done with application of Coulombic force as a body force parameter in the Navier-Stokes equations. Using this approach, relatively good agreement between simulated and measured airflow velocities has been achieved using both finite-volume and finite-element methods to solve the fluid dynamic problem [106, 107].

3.3.4 State of art in modeling of EHD driven forced convection heat transfer

Only a few examples of numerical models for EHD based heat transfer are found in the literature with many of them appearing in the last several years [93, 108, 109]. One of the first models developed for EHD based enhanced convection heat transfer was by Mathew et al [28] for a two-wire-to-duct electrode arrangement. The study investigated the heat transfer enhancement in a duct with EHD generated cross flows. More recent studies have also been focused on using EHD cross flows for heat transfer enhancement in other macro-scale channels and along banks of tubes [30, 108, 109]. To date, EHD based forced convection models have generally neglected the modeling of charge generation, and used simplistic forms of space charge transport that neglect ion movement due to convection and diffusion. In addition, previous modeling efforts lack rigorous validation of the modeling efforts in terms of electrical and fluid dynamic parameters.

3.3.5 Progress in miniaturization of electrostatic air pumps

The application of electrostatic air pump technology to micro/meso-scale devices is a relatively new direction in this field, with some of the first discussions on the topic appearing less than five years ago [3, 14, 84, 110]. Recently there have been several attempts to develop proof-of-concept devices, aimed in the direction of thermal management of microelectronics, at both Purdue University and the University of Washington. The recent move to the micro-scale has driven the field to complete a deeper analysis of the scaling effects of corona discharge, field emission, and air breakdown for small electrode gaps and high electrode tip curvatures [111-115].

3.4 Chapter summary

Over three hundred years have elapsed since the first documented discovery of EHD driven air movement with a corona discharge ion source. Since that time, corona discharge has been examined for a wide variety of uses with a small sub set of those focused on EHD driven airflow. In that time, a fundamental understanding of the underlying physics has been developed and documented. Although analyzed extensively for applications such as xerography and air purification, which focus on corona discharge based charging rather than air movement, most efforts in developing EHD based air movers have been academic curiosities, rather than focused research efforts leading to technology commercialization. The area of forced convection heat transfer with EHD driven airflow received little attention or development before the last two decades, with most of the documented work occurring in the last. The majority of reported heat transfer work has focused on heat transfer enhancement through mixing of existing flows, and relatively little attention has been given to purely EHD driven flows for forced convection cooling until very recently, especially for the application of cooling electronics.

Commercialization efforts for forced convection EHD cooling have been even more recent, with relatively little public data available to form an exact timeline, but perhaps starting with collaborative efforts between the University of Washington and

Kronos Air technologies, and then later joined by collaborative efforts between Purdue University and Thorrn Micro systems. Tessera Technologies took over research and development efforts from Kronos and continues to work toward commercialization of EHD cooling for the notebook market and perhaps others. Thorn has changed their name to Ventiva after receiving venture funding and is rumored to be working in the LED cooling space. In addition, there are rumors of other companies working on EHD technology, mainly in Asia, probably in response to development and marketing efforts of the technology by Tessera and Ventiva. To date the author is not aware of a commercial EHD thermal management product on the market, but given recent development efforts, it would not be surprising to see one in the near future.

Chapter 4. Theoretical investigation of EHD driven air movers

4.1 Key metrics in EHD transduction

Electrohydrodynamic flow is generated by work done on charged particles by electric fields that then transfer momentum to the surrounding fluid. There are several key metrics in this transduction of electrical to mechanical energy and the resulting flow, which will be reviewed in this subchapter.

It is useful to look at a unit volume within the drift region of an EHD device to understand the transduction of energy and its limits. In an EHD system, force is applied to the fluid by the Coulombic forces applied to the ions within the fluid by the electric field. The force applied to a unit volume can be written as

$$dF = qEdV \tag{4.1}$$

where dF is the force exerted on the unit volume dV, q is the space charge density, and E is the electric field strength within dV. This gives the EHD force density. Notably the maximum force density is limited by the maximum charge density and electric field strength that can be achieved without dielectric breakdown, which are dependent on device geometry and fluid properties. Further, for similar geometries, but at varying scale, the maximum values for q and E are predominantly dependent on the material properties of the working fluid, and as such, the total force and thus work that can be applied to the fluid will scale with size, or rather to some extent with the active volume of the device.

dF can be broken into

$$dV = Adx \tag{4.2}$$

The pressure can be defined as:

$$P = \frac{F}{A} \tag{4.3}$$

4.1.1 Scaling of maximum pressure rise

To illustrate the scaling effects of the EHD induced pressure rise within an electrostatic air pump, a simplified pump geometry is used, where the electric field is assumed to be parallel between the corona and collector electrodes. This situation would be approximately true if many wire-to-rod pairs were aligned in parallel with each other. The electric field would be non-uniform near the corona and collector electrodes, but nearly uniform towards the center of the electrode separation, as depicted in Figure 4.1. For simplicity, the remainder of this derivation will assume that the electric field is parallel between the corona and collector electrode array, as shown in Figure 4.2 [116].

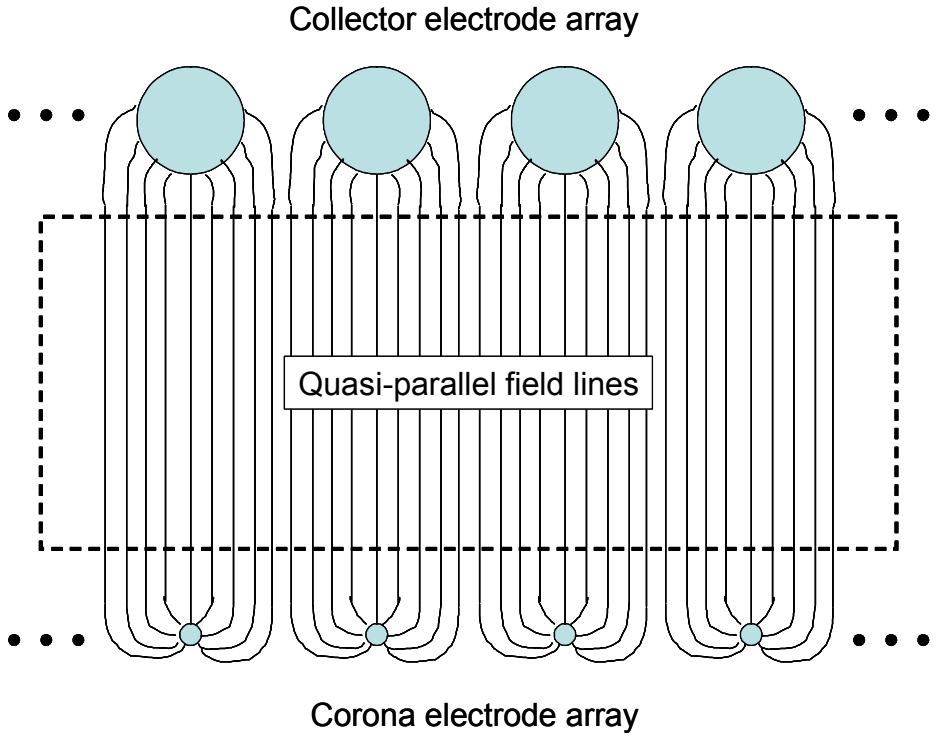

Figure 4.1. *Wire-to-rod array displaying quasi-parallel fields in the inter-electrode region.*

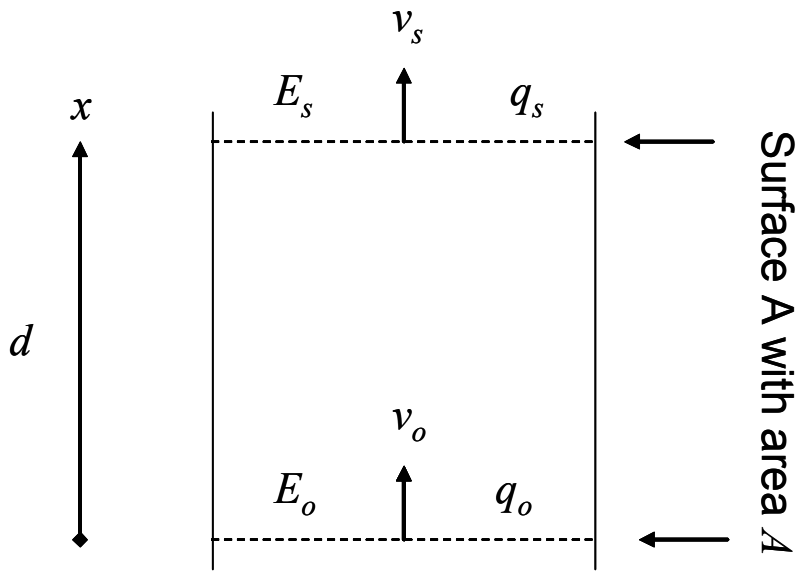

Figure 4.2. *Simplified model of a parallel array wire-to-rod electrostatic air pump.*

For the model shown in Figure 4.2, d is the corona-collector electrode separation distance and A is the area of the collecting electrode surface A. E_0, v_0, and q_0 are the electric field strength, ion velocity, and charge density, respectively, at the corona electrode array. E_s, v_s, and q_s are the electric field strength, ion velocity, and charge, density, respectively, at the collector electrode array.

The current passing through surface A is given by:

$$I = qAv \tag{4.4}$$

where I is the current passing through A; q is the charge density; A is the area of surface A, and; v is the velocity of the ions, where v is equal to:

$$v = kE \tag{4.5}$$

where k is the mobility coefficient of the ions (space charge) and E is the electric field strength. Gauss's law gives:

$$\frac{dE}{dx} = \frac{q}{\varepsilon_0} \tag{4.6}$$

where ε_0 is the electrical permittivity of free space. Substituting (4.6) into (4.4) and solving for E results in:

$$EdE = \frac{I}{\varepsilon_0 Ak} dx \tag{4.7}$$

Integrating (4.7) gives:

$$E = \sqrt{E_0^2 + \frac{2I}{Ak\varepsilon_0}} \tag{4.8}$$

Solving for current in (4.8) to obtain current in terms of the electric field strength and setting x equal to the corona-collector electrode separation distance d:

$$I = \frac{Ak\varepsilon_0 \left(E^2 - E_0^2\right)}{2} \tag{4.9}$$

To find the maximum current, E is set to its maximum value just short of dielectric breakdown E_c, and E_0 is set to zero, giving:

$$I_{\max} = \frac{Ak\varepsilon_0 E_c^2}{2} \tag{4.10}$$

The maximum pressure is found by the following:

ΔP can be arrived at by solving (4.4) for q, substituting and integrating:

$$\Delta P = \frac{Id}{kA} \tag{4.11}$$

The maximum pressure will occur when E is equal to E_c and E_0 is zero for **Figure 4.2** or I is equal to I_{max} (4.10) for (4.11), both giving:

$$\Delta P_{\max} = \frac{\varepsilon_0 E_c^2 d}{2} \tag{4.12}$$

The maximum force can be obtained by multiplying (4.12) by the collecting area:

$$F_{\max} = \frac{\varepsilon_0 A E_c^2 d}{2} \tag{4.13}$$

It is important to note that the maximum pressure is both a function of the separation gap of the corona and collector electrodes and the intrinsic properties of the dielectric fluid, which define E_c. The maximum force density exerted by the electric field on an ion within the pump is independent of size because it is a function of E_c. However,

the net force and ultimately work applied by the EHD blower is a function of the separation gap.

4.2 Sources of transduction efficiency loss within corona based EHD generated flows

In all air movement technologies there exist transduction loss mechanisms that limit the maximum achievable air movement efficiency for a given technology. The loss mechanisms often scale with physical size, limiting the practical scale for a given technology. Although a detailed review of all loss mechanisms is outside of the scope of this dissertation, this chapter presents an overview of loss mechanisms relevant to corona driven EHD airflows, as many are unique from other common air mover technologies.

The major sources of transduction losses in and an EHD AIR MOVER can be broken down to six major loss types, including ionization losses within plasma, ion to bulk flow coupling loss, losses due to non-parallel electric fields and non-uniform space charge sources, fluid flow resistance loss, deionization/ion-bombardment loss on collectors, and power supply losses. A brief review of these loss mechanisms follow.

4.2.1 Ionization process within corona plasma

During the ionization process within the plasma region around the emitter electrode, ions and electrons are accelerated towards and away from the emitter. In the process, ionization and deionization events occur, resulting in various losses such as light emission, heat generation, and an assortment of chemical reactions. Many of these losses are associated with electron or ion interactions with themselves or other airborne constituents.

The larger the plasma cross sectional size, the larger the path length of a given ion or electron through the plasma, and the higher the probability it will participate in a loss causing event. Therefore, if EHD scaling is done so as to maintain the plasma size around the emitter, the ionization losses should scale relatively constant with size. This would be true in the case of a wire-to-plate EHD blower configuration, where the length of the wire

and plate were either reduced or increased, but the cross sectional geometry of the device remained constant. However, if geometry were scaled such that the plasma region is reduced, by increasing the ionization losses per ion generated would be expected to decrease.

The change of plasma size affects the relative loss from the generation of a single ion, however, if geometry is scaled such that the current to voltage relationship changes, more or less ions, current, will be required for a given power delivered to the airflow. In the case where the distance between emitter and collector was increased, less current per unit voltage would be creating, reducing the ionization losses for the system.

4.2.2 Ion/bulk flow coupling

Air pressure and flow are generated by the collision of ions traveling from the emitter to collector electrodes. As the ions travel, the electric field accelerates the ions until they hit another air molecule, where their momentum is then passed onward. However, because the ions will not always collide with another air molecule at the desired angle, the kinetic energy transferred will not be perfectly aligned with the direction of the electric field. This causes the air molecules to move in directions orthogonal to the direction of the electric field, which leads to an increase in the average random kinetic energy of the fluid, but not necessary an increase to the net flow.

This loss should be independent of device scaling since it is a fluid level effect. However, the loss will depend on the fluid properties, with the loss reducing as the electrical ion mobility reduces.

4.2.3 Non-uniform electric fields and space charge distributions

An ideal EHD blower would generate a plane of charge between two plates, parallel to that charge plane, and then bias the plates to create a uniform electric field between them. In such a configuration, it would be possible to generate a uniform force between the plates, since the charge density and field strength would be constant within the air gap. This would represent the ideal EHD blower design for transduction

efficiency; however, it is not practical to achieve with a corona discharge as an ion source.

A corona discharge, by its nature, is required to have a non-uniform electric field in order to achieve a local dielectric breakdown of the air in the region around the corona wire, without a breakdown of the air across the entire air gap between the corona and collector electrodes.

The non-uniform electric field creates losses in two ways. The first source of the loss is due to the forces exerted on the ion that are not aligned with the intended direction of the flow. Therefore, the component of the electric field vector at any point that is orthogonal to the direction of flow reduces efficiency. The electric field's non-uniformity between the emitter and the collector determines the energy losses and energy efficiency. The second source of loss is highly related to the first loss. The space charge or ions are generated in a very concentrated area, which causes the body force on the fluid near the emitter to be large relative to elsewhere in the system. The non-uniform body force creates losses by locally accelerating the air around the emitter, which can lead to recirculation zones in an EHD blower, and non-uniform pressure profiles.

These losses should remain constant with the scaling effect as long as the geometry of the devices is similar, e.g., all components of a device are scaled by the same ratio including the emitter.

4.2.4 Other loss factors

Fluid flow resistance is common among all air movers, and is not discussed here in detail, but is an important loss factor that becomes increasingly important as systems shrink.

During the ion deionization process where a charge carrier passes through the surface of the collector to deionize the carrier air molecule, a current forms through the collector surface. Any electrical resistance to the deionization current will result in power dissipation at the surface and thus loss in efficiency. Notably, a similar loss is seen at the emitter surface. Given a constant surface conductivity and a constant current density over the collector, the losses should be independent of scaling.

Generation of the high voltage required to operate EHD systems, will be required for most EHD applications, and will incur losses in the process. Although not technically a transduction loss, power supply losses are an important loss factor to be considered in any EHD system. In general, as the total power delivered goes down the maximum achievable efficiency decreases, and as the required operating voltage increases, the maximum achievable efficiency decreases.

4.3 Electric field shaping for EHD device performance optimization

4.3.1 Summary

This study was conducted for the purpose of optimizing device characteristics through the control of the electric field distribution between the emitter and collector electrode of an EHD system. Previous efforts to optimize ionic wind pumps concentrated on geometric modifications of the device design, investigating the effect of collector electrode orientation with respect to the corona electrode and its influence on the field line geometry and air flow efficiency [117]. The influence of geometry and distributed voltage on pump performance was investigated by the author in [3]. Although that study demonstrated enhanced pump performance, it did not include an exploration into the optimal electric field distribution. Further advancements in pump performance require taking into consideration the effects of space charge and collector surface voltage distributions in order to find optimum device parameters. Simulations were performed for multiple collector electrode voltage distributions. A method to quantify the change in pump electric field optimization between different voltage distributions is presented. The influence of space charge on pump performance is also discussed. Experimental studies were conducted using the distributed voltage collector electrode method investigated in the modeling section and results are presented.

4.3.2 Numerical Simulations

The selection of governing equations for the numerical simulation of ionic wind pumps depends on the desired degree of accuracy and the relative importance of physical processes that take place during the device operation. This study focuses on a first-order approximation. The ionic wind pump is modeled in the electroquasistatic regime. The simulator solves Poisson's equation, $\nabla^2\phi = -\rho/\varepsilon_0$ where ϕ is the electric potential, ρ is the charge density, and ε_0 is the dielectric permittivity of free space. The space charge distribution is also postulated in a quasistatic regime, based on generally accepted charge

distributions in corona devices [18]. The air dynamics, charge dynamics, and the charge generation in the corona region are considered secondary effects and are not included in the model. The modeling methodology used here is a precursor to the more detailed and fuller model presented later, but is adequate for the scope of the investigation in this chapter.

The purpose of the following numerical simulations is to compare the figures of merit for a classic and optimized geometry. This analysis develops better understanding of the effects of different design approaches on the overall device performance.

For reference purposes, the calculation of important dimensionless parameters for this system follows. Reynolds number is defined as [118, 119]:

$$Re = \frac{LU_0}{\nu_f} \tag{4.14}$$

where U_0 = 1 m/s is the characteristic velocity of the fluid and L = 0.01 m is the characteristic length of the device. Matsuda number is defined as [118, 120, 121]:

$$Md = \frac{\varepsilon_0 E_0^2 L^2}{\rho_f \nu_f^2} \tag{4.15}$$

where $\varepsilon_0 = 8.85 \cdot 10^{-12}$ F/m is the dielectric permittivity of free space, $E_0 = 3 \cdot 10^6$ V/m is the characteristic electric field intensity, ρ_f = 1.29 kg/m^3 is density of the fluid, and ν_f = $1.56 \cdot 10^{-5}$ N·s/m^2 is the kinematic viscosity of the fluid (air). EHD number is defined as [118, 121, 122]:

$$E_{hd} = \frac{eN_{io}E_0^2 L^3}{\rho_f \nu_f^2} \tag{4.16}$$

where $e = 1.6 \cdot 10^{-19}$ C is the elementary charge, $N_{io} = 1.6 \cdot 10^{14}$ m^{-3} is the number density of the charges.

With these parameters, Re = 573, Md = $2.8 \cdot 10^6$, and E_{hd} = $8.1 \cdot 10^{10}$. We are observing a laminar flow with a strong influence of electric field forces and a moderate influence of dielectric forces. Note that in a conventional analysis for electrostatic precipitators, the Matsuda number is compared to the square of the Reynolds number to determine the relative significance of the secondary flow (ionic wind flow) to the primary

flow due to an externally created pressure difference. In case of this study, however, the airflow is not due to an external pressure difference, and the value for U_0 is determined empirically.

4.3.2.1 Figure-of-merit concept

The figure-of-merit (FoM) calculations act as a metric to compare quantitatively efficiency of different pump designs and different voltage distributions for a given design. Corona pumps utilize Coulombic forces on ions induced by electric fields to generate airflow. For a two-dimensional model, the force vector applied to an ion within the pump can be broken down into two components, one component in the direction of intended airflow, x, and the second orthogonal to intended airflow, y. The greater the ratio of the x to y directional components, the greater the expected efficiency is of the system.

Electric field E_x and E_y component magnitudes are multiplied by a unit charge ρ converting them to Coulombic force values, f_x and f_y. The f_x and f_y values are integrated separately along specified discrete horizontal lines within the pump channel. A ratio is taken of the F_x and F_y scalars giving the figure-of-merit value f_m shown below (4.17).

$$f_m = \frac{F_x}{F_y} = \frac{\iint_A \rho \cdot |E_x| \, dxdy}{\iint_A \rho \cdot |E_y| \, dxdy} \tag{4.17}$$

The double integral in (4.17) is taken over the area enclosed by the collector electrodes in the cross-section of the simulation space. The non-capitalized variable f represents the force at a given point, whereas the capital F represents the integral value of all point forces.

The purpose of the figure of merit is to decouple the charge density distribution and the electric field distribution in the evaluation of device geometry. The main reason for this approach is the desire to design multi-stage pumps where the charge at a given stage is injected from the outside and not necessarily generated at the corona electrode.

4.3.2.2 Classic geometry

Simulations for the classic wire-to-rod geometry were conducted with Ansoft Maxwell EM 2-D electrostatic field solver [123].

4.3.2.2.1 Simulation specification and boundary conditions

The simulation space was broken down into five subdomians as follows: the surrounding air environment, two insulating Teflon (ε=2.1) walls in parallel to form an air channel, a conductive collector electrode at the downstream end of the air channel, the region falling between the two Teflon support structures where a space charge was defined for this simulation and finally, a conductive corona electrode at the upstream end of the air channel.

The simulation boundary conditions were as follows: The perimeter of the simulation space was set to a balloon boundary condition setting the electrical charge to zero at infinity. A positive potential of 10 kV was applied to the corona electrode and ground to the collector electrode. Space charge was included in the simulation to account for the electric field generated from the ion stream passing between corona and collector electrodes. When simulating with a space charge, a charge density of 10^{-4} C/m^3 was placed along a line between the corona tip and the collecting electrode, decreasing linearly to zero at the surface of the Teflon channel wall on either side of the channel. The space charge value used was adapted from corona pump space charge calculations conducted by Colver et al. [18], and therefore no specific corona current is specified in the simulations. This space charge magnitude and distribution approximate the actual values. A coupled-field simulation taking into account fluid dynamics and space charge would have been more accurate, but is viewed by the authors as unnecessarily complex for the purpose of this study. The simulations shown in Figure 4.3 through Figure 4.5 used the preceding boundary conditions without a space charge and Figure 4.6 used the preceding boundary conditions with an applied space charge.

The electric field distribution was calculated in the simulation space. The pump air channel is then divided into 45 horizontal segments in the vertical direction. Each of the segments can be seen as the individual horizontal lines within the force vector plots in Figure 4.3 through Figure 4.6. Along each segment, a horizontal line orthogonal to the direction of airflow is drawn. Along each line, the x and y electric field vector magnitudes are extracted to be used in FoM pump efficiency comparison calculations.

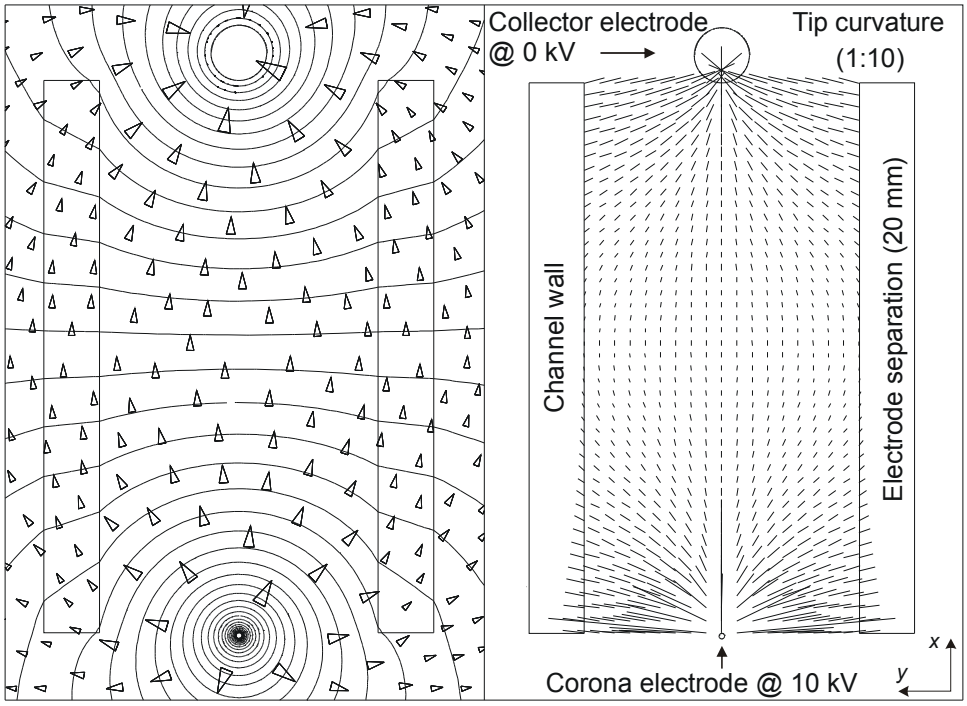

(a) (b)

Figure 4.3. *Numerical simulation of the classic wire-to-rod geometry with: (a) equipotential lines and electric field shown as arrows scaled logarithmically with the field magnitude; (b) calculated Coulombic force vectors within pump channel used to compute the FoM value. The distance between corona and collector electrode is 20 mm, the ratio of electrode radii is 1:10, and the FoM is 18.16.*

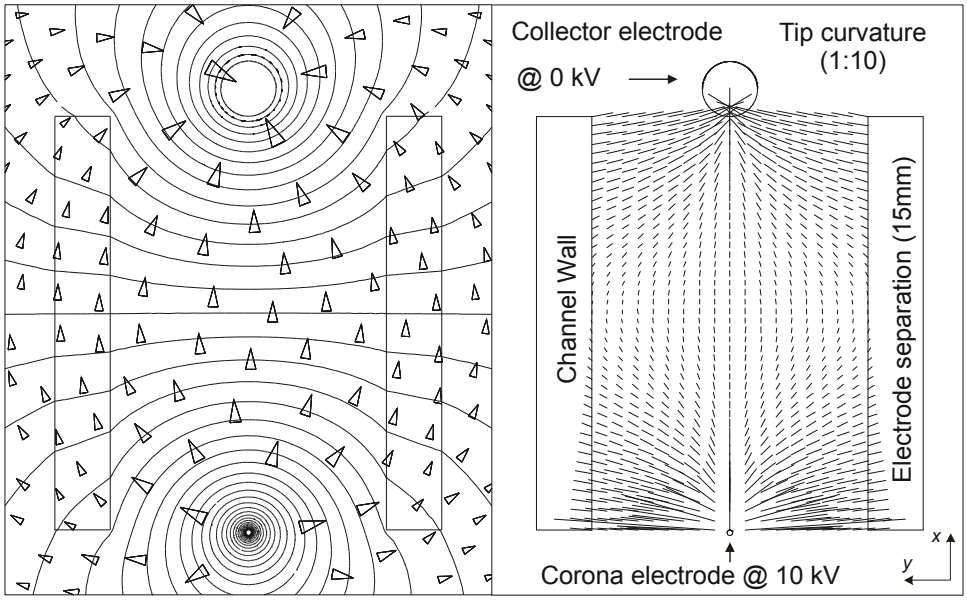

(a) (b)

Figure 4.4. *Numerical simulation of the classic wire-to-rod geometry with: (a) equipotential lines and electric field shown as arrows scaled logarithmically with the field magnitude; (b) calculated Coulombic force vectors within pump channel used to compute the FoM value. The separation distance between the corona and collector electrode is 15 mm, the ratio of electrode radii is 1:10, and the FoM is 18.13.*

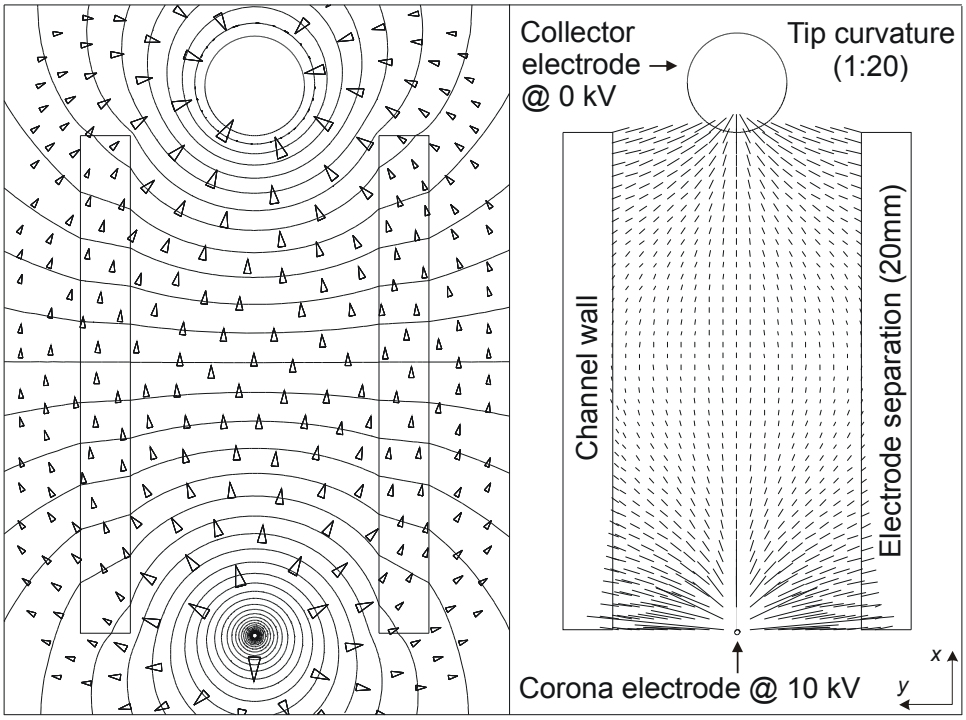

(a) (b)

Figure 4.5. *Numerical simulation of the classic wire-to-rod geometry with: (a) equipotential lines and electric field shown as arrows scaled logarithmically with the field magnitude; (b) calculated force vectors within pump channel used to compute the FoM value. The separation distance between corona and collector electrodes is 20 mm, the ratio of electrode radii is 1:20, and the FoM is 32.8.*

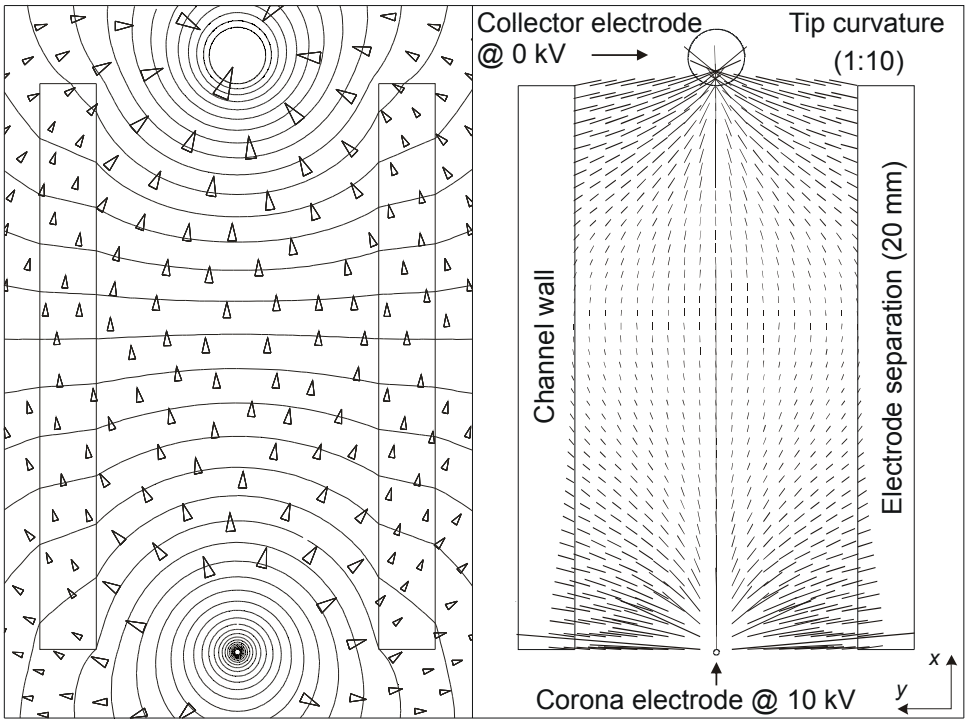

(a) (b)

Figure 4.6. *Numerical simulation of the classic wire-to-rod geometry with space charge: (a) equipotential lines and electric field shown as arrows scaled logarithmically with the field magnitude; (b) calculated Coulombic force vectors within pump channel used to compute the FoM value. The separation distance between corona and collector electrodes is 20 mm, the ratio of electrode radii is 1:10, and the FoM is 18.16.*

4.3.2.2.2 Classic geometry simulation results

A control simulation, shown in Figure 4.3, is used as the baseline design, with a 20 mm separation distance between the corona and collector electrodes and a ratio of corona and collector electrode radii of 1:10. Figure 4.4 and Figure 4.5 show how the change of one design parameter from the baseline case shown in Figure 4.3 affects the field distribution and, consequently, the FoM. Figure 4.6 shows the effect of space charge on the FoM for the classic geometry. Specifically, Figure 4.4 shows a wire-to-rod model with a 15 mm separation distance between the corona and collector electrodes and Figure 4.5 shows a model with a ratio of corona and collector electrode radii of 1:20. These two variations of the baseline wire-to-rod model illustrate several important design features. The FoM increases slightly as the separation increases for the models shown in Figure 4.4 and Figure 4.3. This is an expected result, since as the channel width decreases relative to the electrode separation distance the channel contains fewer of the outer

electric field lines. In a wire-to-rod regime, the farther the field line is from the center line between the two electrodes the greater its curvature and thus its orthogonal component. It should also be noted that the proposed FoM described in this paper is not dependent on the feature size, but only on the relative proportions of the design elements. The figure-of-merit would remain approximately the same for a microfabricated device built to the proportions of the macro prototype. The FoM for the model shown in Figure 4.5 is dramatically larger, than that for Figure 4.3, due to a strong contribution of field components in the region immediately below the collector electrode. Figure 4.7 shows a nearly linear increase of the FoM with the corona to collector electrode radii ratio. In the extreme, the FoM approaches infinity for a pair of guarded parallel-plate electrodes (assuming existence of corona discharge and/or space charge in the region).

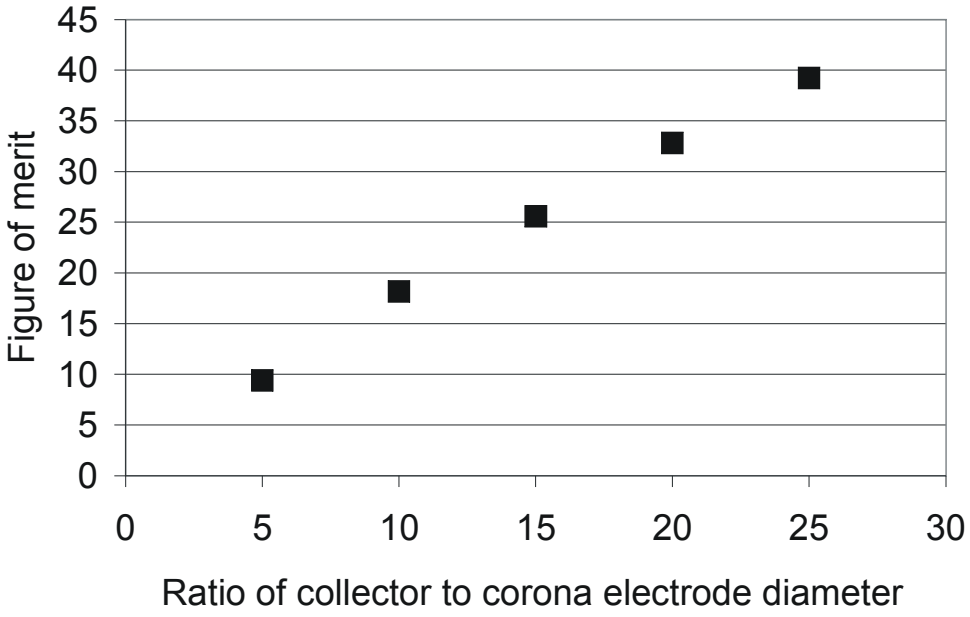

Figure 4.7. *Relationship between the figure-of-merit (FoM) and ratio of corona to collector electrode radii has a positive near linear relationship for increasing electrode radii from numerical simulations with 20 mm electrode separation.*

A more accurate estimate of device performance should take into account fluid dynamics. A first order approximation is used in this investigation to account for air resistance due to the collector electrode. The air resistance compensation is calculated by defining a region directly upstream of the collector electrode and then removing all x-directed force vector components within that region before calculating the FoM. Although approximate, the author feels the compensation method should be adequate to

observe basic trends. Figure 4.8 illustrates the relative importance of fluid dynamics. The "Compensated" curve shows a linear decrease in the FoM as the separation between the corona and collector electrode increase. The electric field near the collector electrode is higher than the average electric field within the channel. Since the air resistance compensation removes the x-directed electric field components near the collector electrode, the impact of the compensation increases when the electrode separation distance grows relative to the channel width. However, if no compensation is applied, the FoM slowly increases with increased separation. The effect of space charge on the FoM was found to be negligible for the classical geometry, with a difference of only 0.003 in FoM between models with and without an applied space charge, shown in Figure 4.6 and Figure 4.3 respectively. The above analysis of canonical electrode shapes helps developing intuition for interpreting the results of numerical simulations of optimized geometry, presented next.

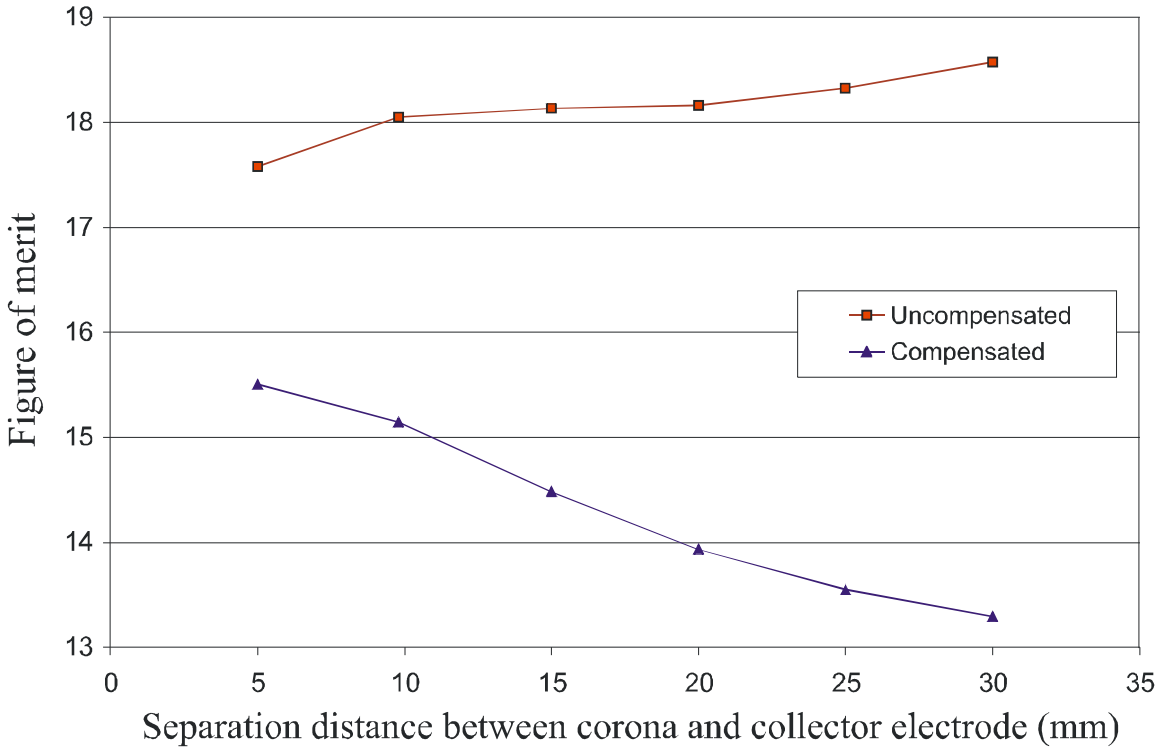

Figure 4.8. *Relationship between the figure-of-merit (FoM) and separation distance between electrodes, with and without air resistance compensation.*

4.3.2.3 Optimized geometry

Figure 4.9 shows the sharp-edge-to-parallel-plane geometry chosen for this study. The sharp-edge-to-parallel-plane configuration has several advantages over the classic point-to-plane and wire-to-rod geometries. This geometry enables the use of a thin collector electrode and substantially decreases air resistance. The sharp-edge-to-parallel-plane assembly utilizes a razor-like corona electrode, allowing for electrode wear without significant tip curvature degradation or structural fatigue. Corona electrode surface degradation from a wire-to-rod configuration is shown in Figure 4.10. Corona electrode degradation, which may include erosion and deposits on the electrode surface, may lead to non-uniform corona discharge and, thus to eventual device failure. The use of a sharp-edge corona electrode minimizes the impact of erosion, extending device life. The sharp-edge-to-parallel-plane regime decreases pump air resistance by moving the collector electrode from the main airflow path, as found in a wire-to-rod regime, to the sides of the main airflow path and the corona electrode. With the collector electrodes positioned at the sides of the airflow, it is possible to control the electric field as a function of distance along the collector electrode by applying a distributed voltage along the collector surface. Control over the electric field geometry makes it possible to control the distribution of the Coulombic forces acting on the ions within the pump, ultimately making possible the control of airflow profiles.

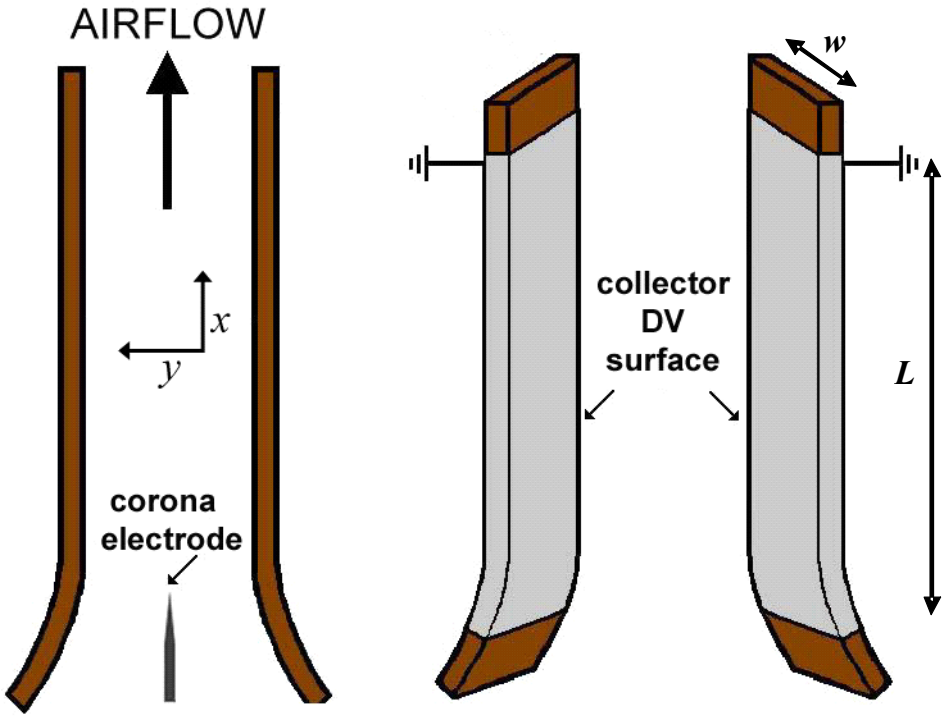

(a) (b)

Figure 4.9. *(a) side view of the corona pump structure; (b) a distributed voltage (DV) with a continuous voltage gradient generated along the collector electrode surface. A value of eight cm and two and a half cm were used for the collector surface length (L) and width (w) during experimental testing.*

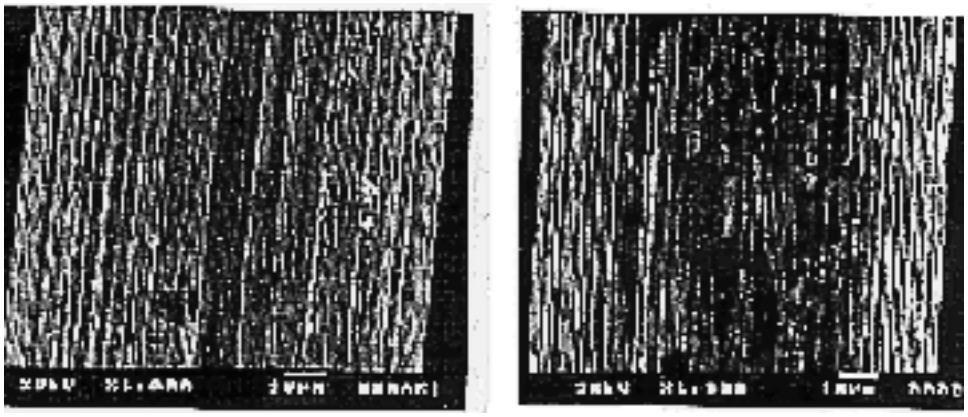

Figure 4.10. *SEM picture of corona electrode surface degradation in a wire-to-rod assembly.*

4.3.2.3.1 Simulation specifications and boundary conditions

Simulations for a sharp-edge-to-parallel-plane geometry were conducted with Ansoft Maxwell EM 2-D electrostatic field solver [123]. The simulation space was

broken down into five subdomains as follows: the surrounding air environment, an insulating support structure, a conductive collector electrode on the inner wall of the insulating support structure, the region falling between the two collector electrodes where a space charge was defined for this simulation, and finally, a conductive corona electrode.

The simulation boundary conditions were as follows: The perimeter of the simulation space was set to a balloon boundary condition setting the electrical charge to zero at infinity. A positive potential of 10 kV was applied to the corona tip. The potential applied to the curved collector electrode was modeled as a linear function from 0 volts at the top to a higher potential from (0.5 kV to 5 kV) at the bottom, nearest to the corona electrode. Space charge was included in the simulation to account for the electric field generated from the ion stream passing between corona and collector electrodes. When simulating with a space charge, a charge density of 10^{-4} C/m^3 was placed at the corona tip decreasing linearly by 10^{-5} C/m^3 per cm in the direction of airflow within the collector channel. The space charge value used was adapted from corona pump space charge calculations conducted by Colver et. al. [18], and therefore a corona current is not specified for the simulations. This space charge magnitude and distribution approximate the actual values. A coupled-field simulation taking into account fluid dynamics and space charge would have been more accurate, but is viewed by the authors as unnecessarily complex for the purpose of this study. The simulations shown in Figure 4.12 and Figure 4.13 use the above boundary conditions without an applied space charge and with a collector potential of zero and five thousand volts respectively. The simulations shown in Figure 4.14 and Figure 4.15 are the analogue to Figure 4.12 and Figure 4.13**.**

The electric field distribution was calculated in the simulation space. The pump air channel is then divided into 45 horizontal segments in the vertical direction. Each of the segments can be seen as the individual horizontal lines within the force vector plots in Figure 4.12 through Figure 4.15. Along each segment, a horizontal line orthogonal to the direction of airflow is drawn. Along each line, the x and y electric field vector magnitude is extracted to be used in FoM pump efficiency comparison calculations.

4.3.2.3.2 Optimized geometry simulation results

Corona pump optimization using a distributed voltage along the collector electrode was found to be feasible. A positive correlation between the calculated FoM and the magnitude of the voltage distributed along the length of the collector electrode is shown in Figure 4.11. As the voltage distributed over the collector increases from 0 V (Figure 4.12 and Figure 4.14) to 5 kV (Figure 4.13 and Figure 4.15), the equipotential voltage lines within the corona air pump channel become more horizontal, and the electric field, shown as arrows, becomes better aligned with the pump flow. All equipotential lines are separated by 416 V, which is calculated by dividing the total voltage drop between the corona and collector electrodes by 24, the number of equipotential lines for each plot. A collector distributed voltage increase from 0 V to 5 kV resulted in a FoM increase of 74.3%.

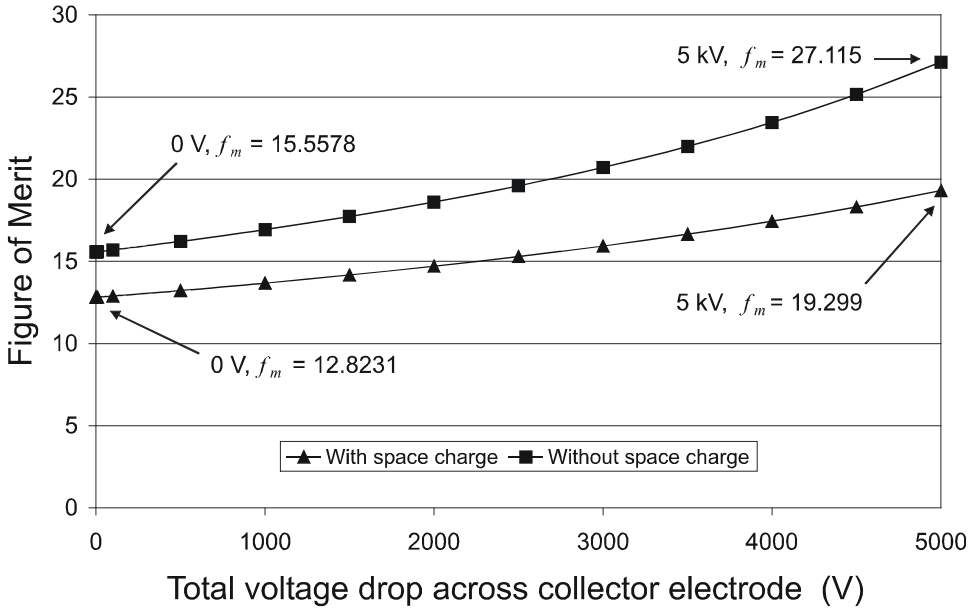

Figure 4.11. *Relationship between the figure-of-merit (FoM) and total voltage drop of distributed collector voltage, with and without space charge.*

The effect of space charge on the electric field can be seen best by comparing equipotential lines within the pump channel in Figure 4.13 and Figure 4.15. The equipotential field lines within the pump channel are nearly parallel to each other and orthogonal to pump flow in Figure 4.13, where no space charge is present. As space charge is introduced, Figure 4.15, it changes the electric field distribution, resulting in

more curved equipotential lines within the pump channel. The space charge is composed of the ions within the pump. Since all the floating charges outside the corona discharge region are of the same polarity as the corona electrode, they reduce the electric field magnitude in the areas around the corona electrode and in the region of ion flow.

The reduction of the electric field in these regions results in a smoothing or decreasing of the electric field around the corona tip and along the center of the channel. The resulting decrease in FoM caused by including space charge in the simulations is displayed in Figure 4.11, ranging from 17% to 28% for the lowest and highest distributed voltage, respectively.

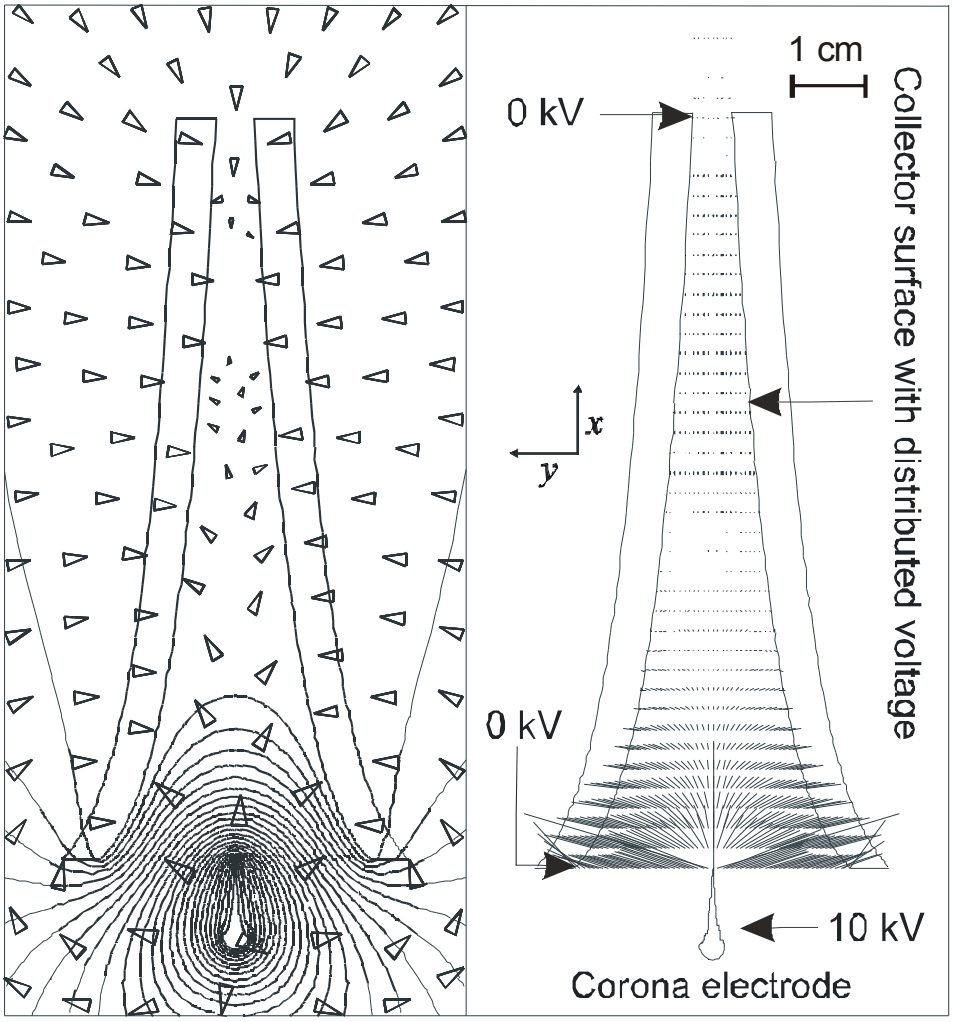

(a) (b)

Figure 4.12. *Simulation plots for a grounded collector electrode without an applied space charge: (a) equipotential lines and electric field shown as arrows scaled logarithmically with the field magnitude; (b) calculated Coulombic force vectors within pump channel used to compute the FoM value, 15.58 for this simulation.*

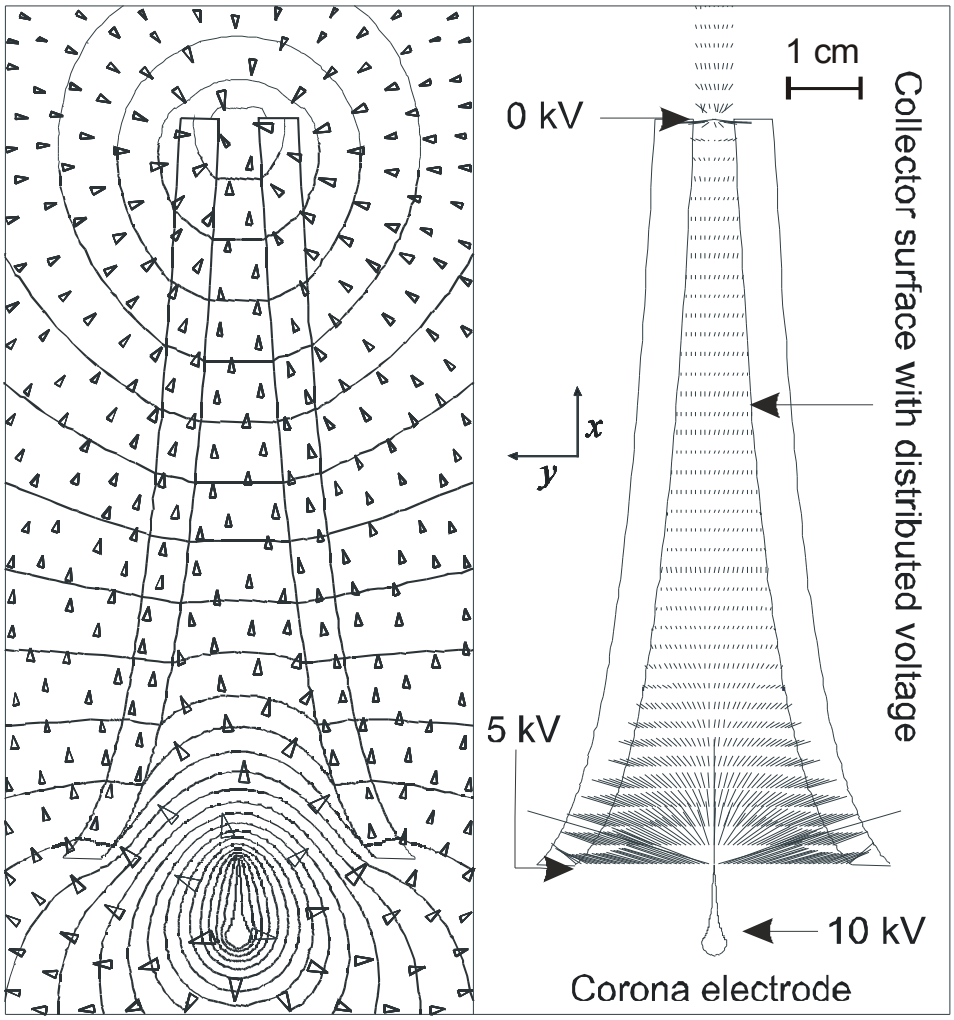

(a) (b)

Figure 4.13. *Simulation plots for a collector electrode distributed voltage of 5 kV without an applied space charge: (a) equipotential lines and electric field shown as arrows scaled logarithmically with the field magnitude; (b) calculated Coulombic force vectors within pump channel used to compute the FoM value, 27.12 for this simulation.*

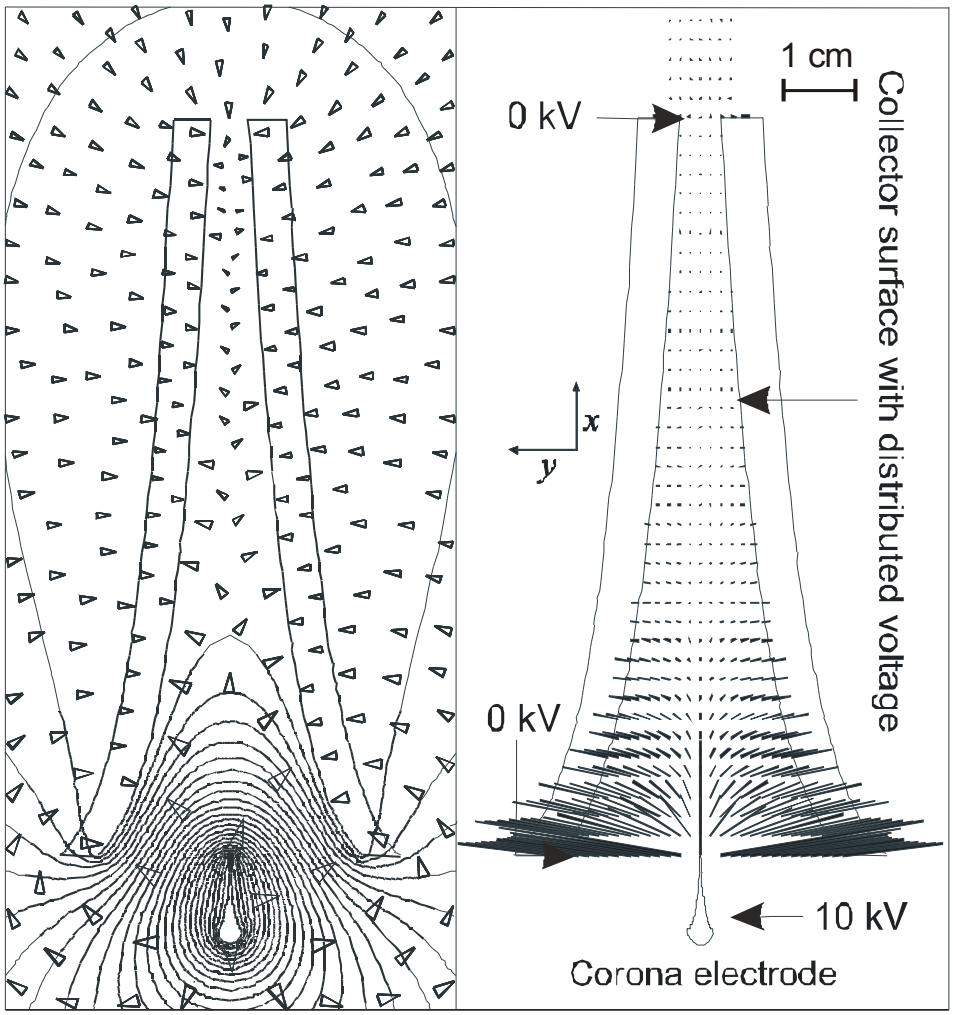

(a) (b)

Figure 4.14. *Simulation plots for a grounded collector electrode with an applied space charge: (a) equipotential lines and electric field shown as arrows scaled logarithmically with the field magnitude; (b) calculated Coulombic force vectors within pump channel used to compute the FoM value, 12.82 for this simulation.*

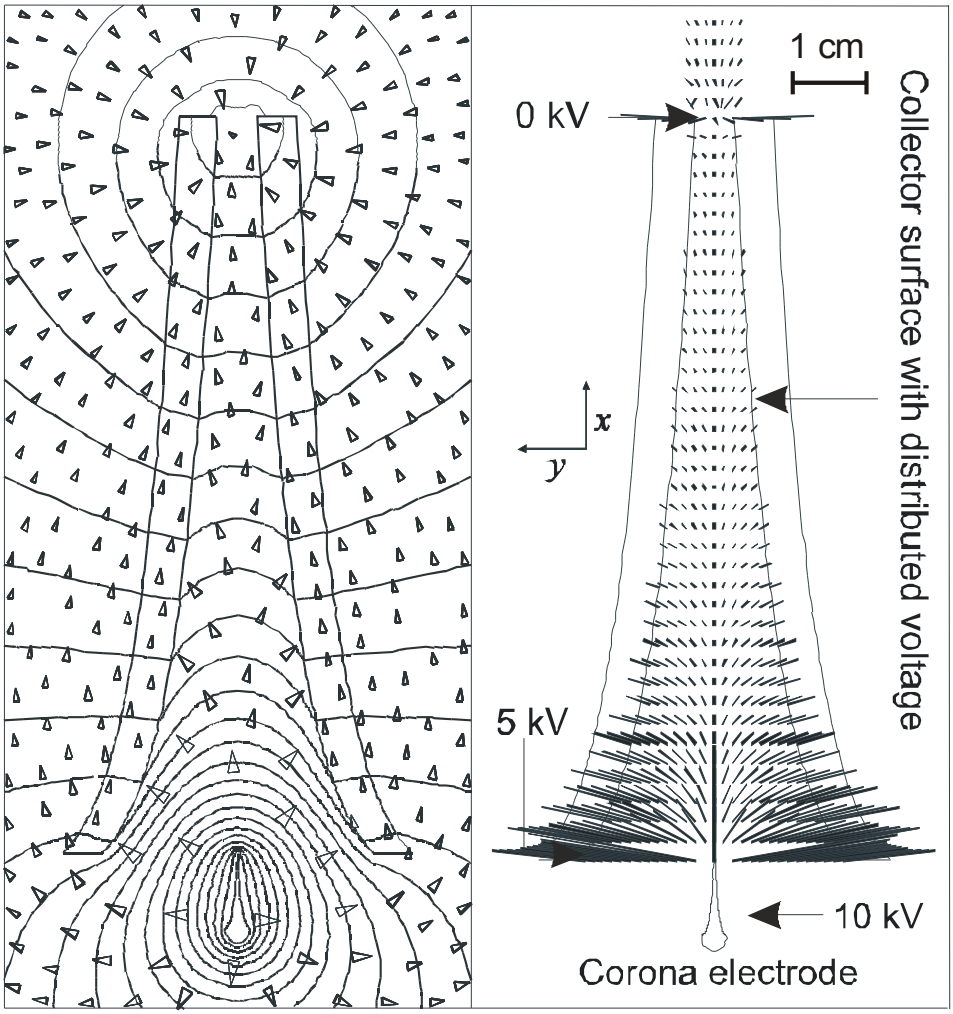

(a) (b)

Figure 4.15. *Simulation plots for a collector electrode distributed voltage of 5 kV with an applied space charge: (a) equipotential lines and electric field shown as arrows scaled logarithmically with the field magnitude; (b) calculated Coulombic force vectors within pump.*

4.3.3 Experimental results

The experiments presented here illustrate the performance of canonical and optimized geometries. Both designs use a single corona electrode. The canonical design has wire-to-rod geometry, and the optimized design employs curved electrodes shown in the optimization studies in the previous section.

4.3.3.1 Experimental setup

Figure 4.16 shows the photograph of the experimental setup for the canonical wire-to-rod geometry, which corresponds to the computer simulations in Figure 4.3, Figure 4.4, and Figure 4.5. The corona electrode was constructed from a steel wire with a diameter of 0.24 mm on a single axis translation table with 1 μm resolution. The collector electrode was built from a copper pipe with a diameter of 4.87 mm and uniform thickness of .95 mm on a second identical single axis translation stage for micro-precision placement. The corona electrode and collector electrode are placed parallel to each other with a total coronation length of 36.6 mm.

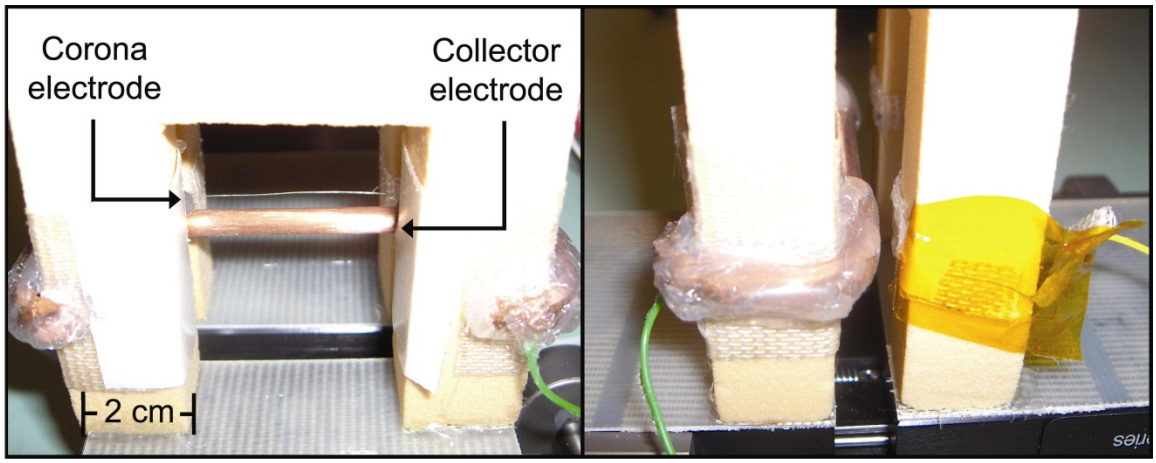

(a) (b)

Figure 4.16. *Front view (a) and side view (b) of the canonical wire-to-rod geometry experimental setup.*

Figure 4.17 shows the photographs of the experimental setup for the optimized geometry. The corona electrode was constructed from a high carbon steel razor, which provides a consistent tip diameter along its length. Teflon support bars insulate the collector electrodes from the device stand and provide a mechanical connection to the xyz-translation table for micro-precision placement. The electrodes were built using semi-conductive carbon-doped polyimide Kapton to form a constant voltage gradient along the collector displayed in Figure 4.9. The voltage distribution along the electrode is not only a function of surface conductivity, but also a function of space charge dynamics and hence of the ionic current distribution in the volume of the device. The design includes two collector electrode sheets symmetrical with respect to the razor-like corona

electrode and tapering towards the vertical axis. A value of 8 cm and 2.5 cm were used for the semi-conductive collector surface length (L) and width (w) respectively during experimental testing. Dimensions are shown schematically in Figure 4.9 and referenced in simulations in Figure 4.12 through Figure 4.15.

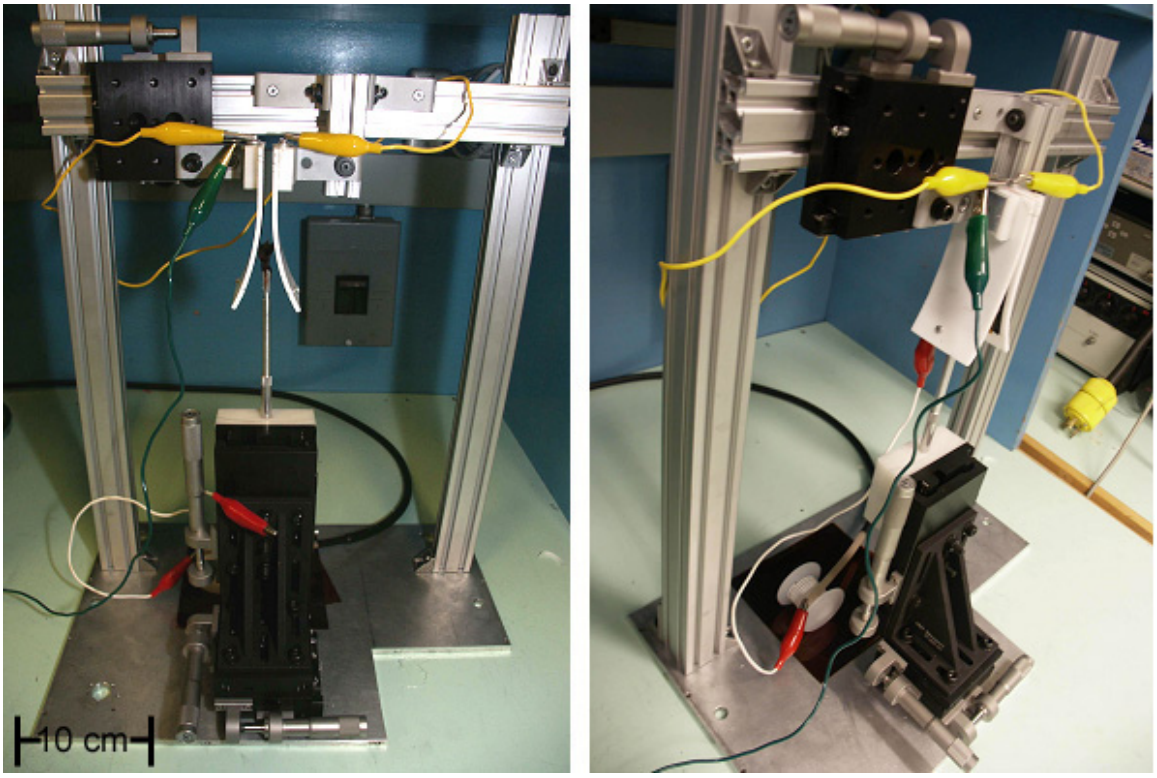

(a) (b)

Figure 4.17. *Front view (a) and side view (b) of the experimental setup using semi-conductive Kapton as the collector electrode.*

Power was supplied for both sets of experiments by a Hipotronics model R30B HV DC Power Supply. Voltages were confirmed with a Tektronix P6015 high voltage probe connected to an HP 54501A oscilloscope. Air velocity was measured using a hot wire anemometer based VELOCICALC PLUS 8386 airflow sensor with an accuracy of ±1.5% at the range of airspeeds measured. Data acquisition was done an in house LabView program which recorded data from the VELOCICALC PLUS 8386 at the rate of one reading per second.

4.3.3.2 Experimental results with canonical geometry

Figure 4.18 shows the measured speed of air for a range of corona voltage V_c from 6 kV to 12 kV. The air velocity v_a increased linearly with V_c at a slope of 0.6 m/(kV·s). The measured I-V curve is shown in Figure 4.19, displaying an onset voltage for this geometry at about 65% of the breakdown voltage, which means that a wide envelope is available for device operation. The air velocity profile in Figure 4.20 was measured in the y-direction across the collector electrode outlet of the geometry in Figure 4.3, with corona to collector electrode separation of 5 mm. Two peaks were detected in the proximity of the sides of the collector electrode, because the electrode obstructs the airflow.

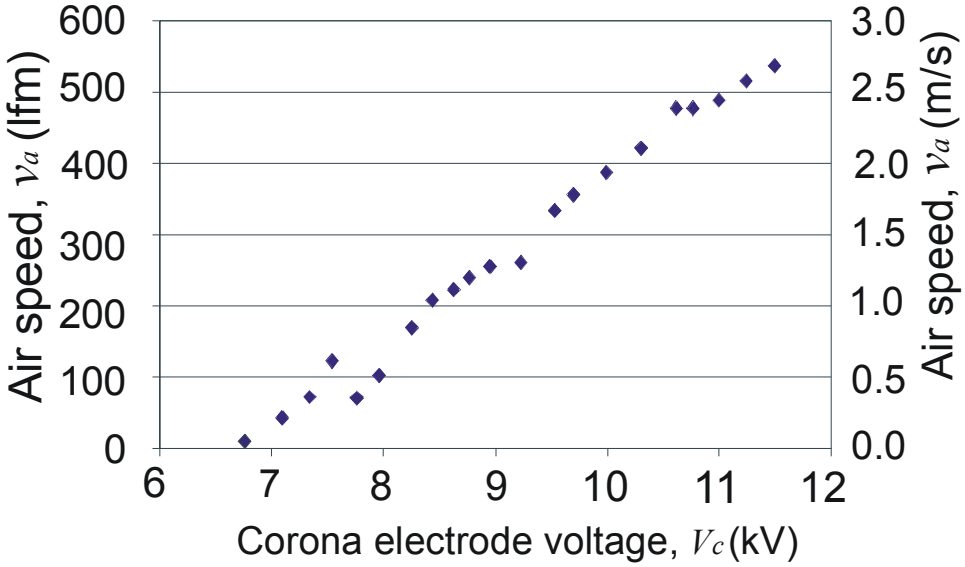

Figure 4.18. *Measured electrode voltage V_c versus air speed v_a at the outlet.*

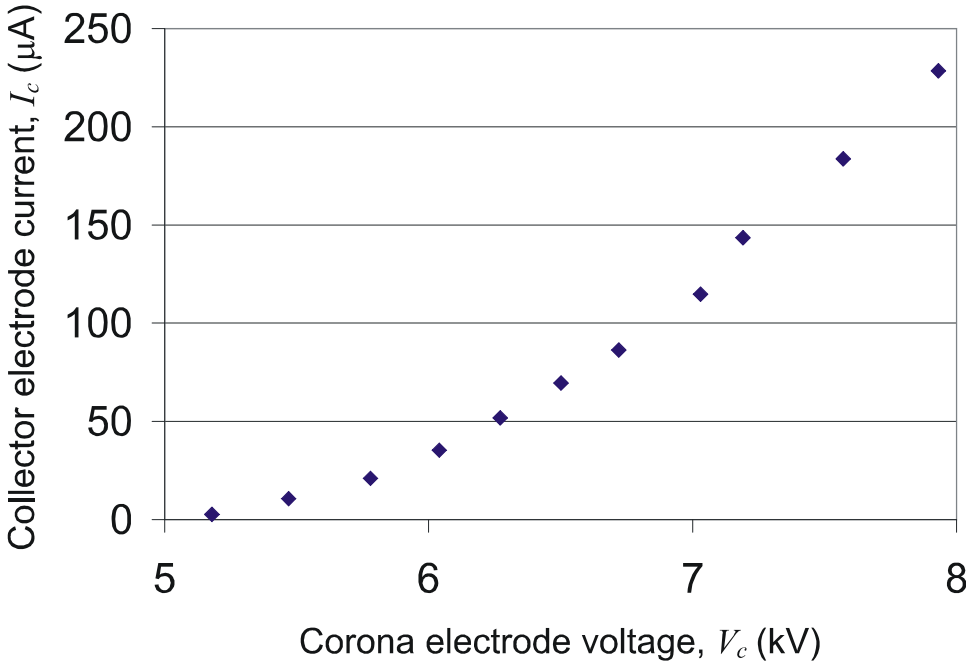

Figure 4.19. *Measured corona voltage V_c versus collector electrode current I_c exhibits an exponential dependence.*

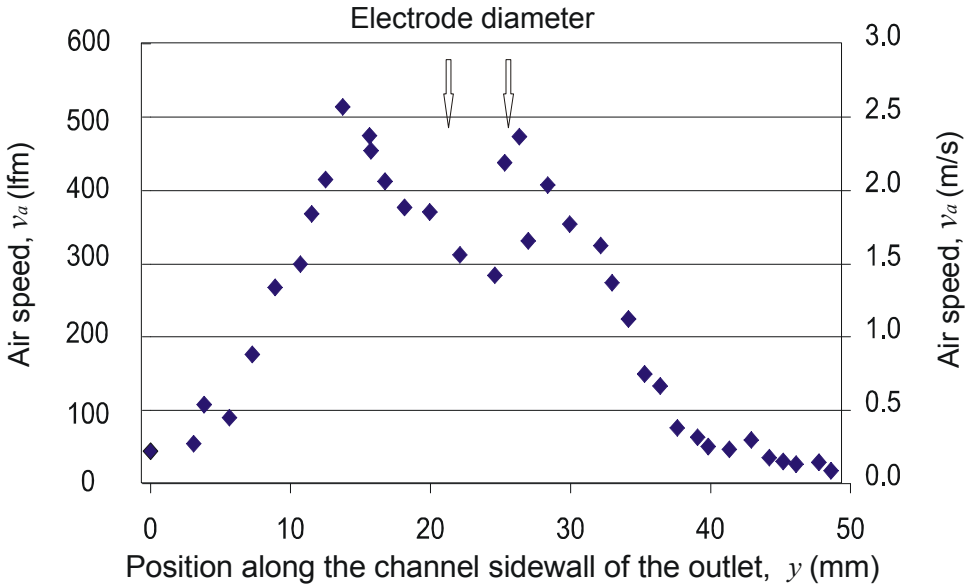

Figure 4.20. *Air speed profile along the sidewall from the outlet. Collector electrode is positioned between the two arrows shown on graph.*

4.3.3.3 Experimental results with optimized geometry

All subsequent data presented in this investigation is produced with the experimental setup displayed in Figure 4.17, which uses a semi-conductive 20 micron thick Kapton film for the collector electrode.

Figure 4.21 shows the measured I-V characteristic of the corona air pump. Beyond corona onset voltage, occurring at 5.2 kV, a collector current I_c from the corona electrode to the collector electrode was measured. In accordance with classical theory [81], I_c increases exponentially with the corona voltage V_c, corresponding to a logarithmic decrease in air resistance [81]. Figure 4.22 shows a detected measurable airflow beyond corona voltage V_c of 6 kV and air velocity v_a increased linearly with V_c at a slope of 1.5 m/(kV·s) up to the 9 kV potential and decreased to a slope of 0.5 m/(kV·s) above 9 kV. Stable peak air velocity was limited at a V_c of 11 kV due to dielectric breakdown at higher potential differences. The v_a vs. V_c relationship shown in Figure 4.22, Figure 4.23, and Figure 4.24 was achieved using semi-conductive Kapton collectors, which generate a non-optimized linear voltage gradient due to the inherent fixed film resistance leading to a continuous voltage drop across the film. With further optimization efforts, the optimized surface conductivity distribution will result in higher air velocities.

The air velocity profile shown in Figure 4.23 was measured in the y-direction across the collector electrode outlet shown in Figure 4.17. Two peaks are detected along the outlet directly above the corners of the corona electrode. These peaks are due to increased ion generation at the two ends of the blade-shaped corona electrode, caused by an increase in electric field intensity at the sharp corners.

Figure 4.24 illustrates an air velocity profile across the separation gap between the two collector electrodes. At the center of the outlet separation, the airflow reached a maximum velocity of about 4 m/s, or 800 linear feet per minute (lfm). Airflow measurements were taken at the top of the channel, four and a half centimeters upstream from the point of ion recombination, resulting in an airflow profile measurement showing significant air resistance at the sides and corresponding lower air velocities. Ongoing efforts are focused on decreasing the channel length in order to further improve the

airflow profile. An investigation is also being conducted to enable dynamic collector voltages. The dynamic voltage control can be used to realize optimized voltage distributions, determined by numerical modeling. Optimized voltage distributions will increase the ion acceleration period and inter-channel airflow control, resulting in a more uniform airflow profile across the channel.

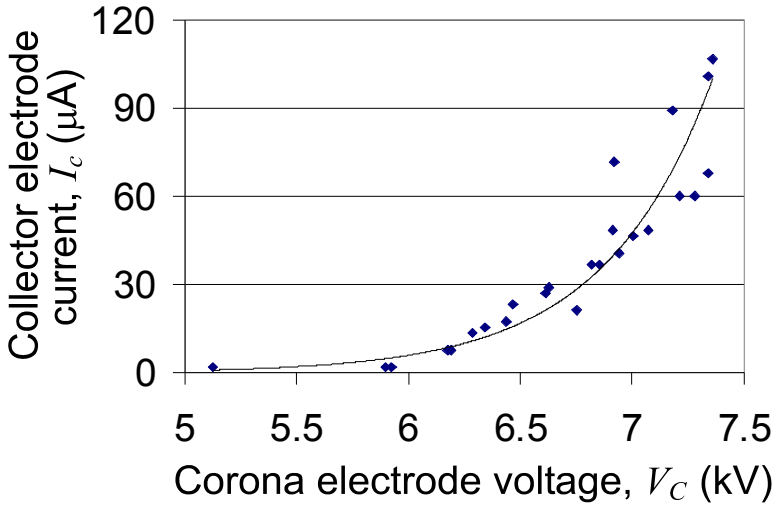

Figure 4.21. *Measured corona voltage V_c versus collector electrode current I_c exhibits an exponential dependence of approximately 3E-5e^{2Vc}.*

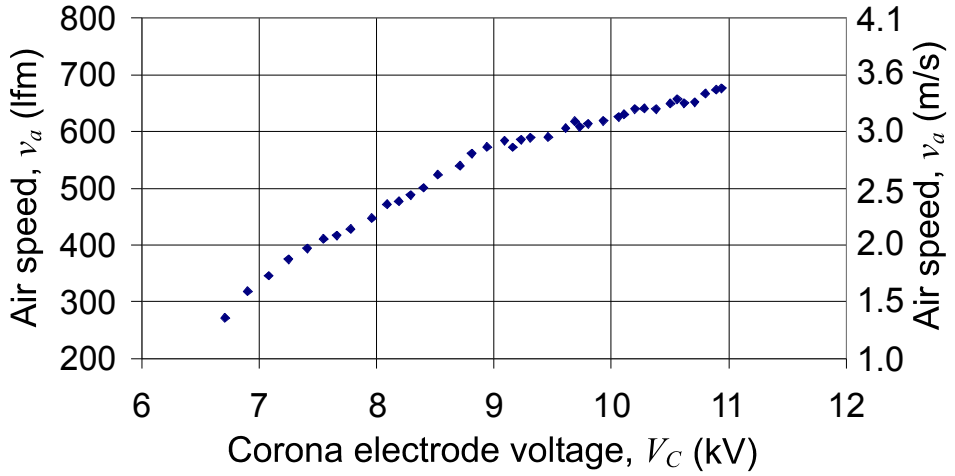

Figure 4.22. *Measured corona voltage V_c versus air speed v_a at the outlet.*

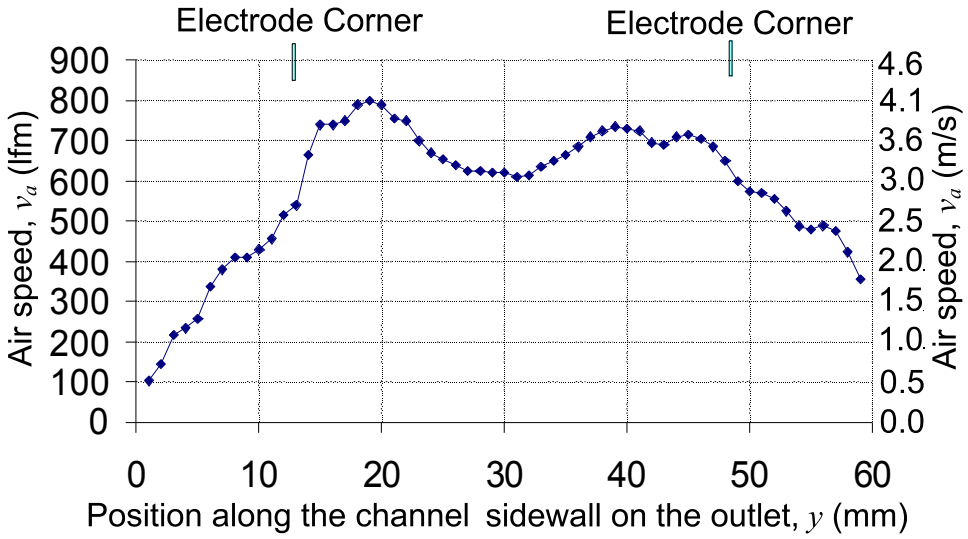

Figure 4.23. *Air speed profile along the sidewall from the outlet.*

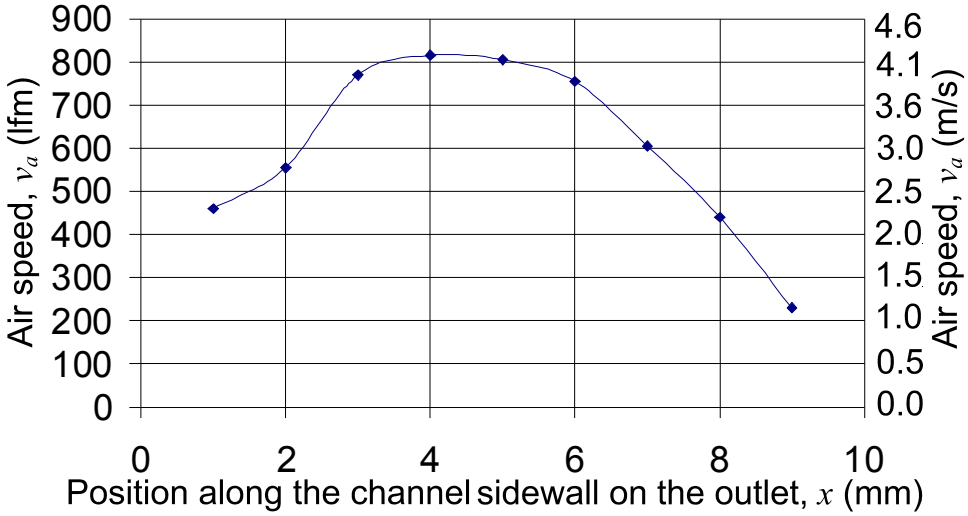

Figure 4.24. *Air speed profile across the 8 mm separation of the pump outlet.*

4.3.3.4 Performance comparison

By dividing the airflow rating in cubic cm per second (cm^3/sW) by the power consumption in watts, the pump efficiency can be determined. Following this definition, Figure 4.25 relates the corona voltage (V_c) to the pump efficiency. Airflow ratings were calculated from the peak air velocity multiplied by the cross-sectional area of the aperture.

Efficiency reached a maximum of 3776 cm^3/sW (8 CFM/W) at low air velocities and decreased exponentially with V_c approaching a limit of 142 cm^3/sW (0.3 CFM/W) at 11 kV.

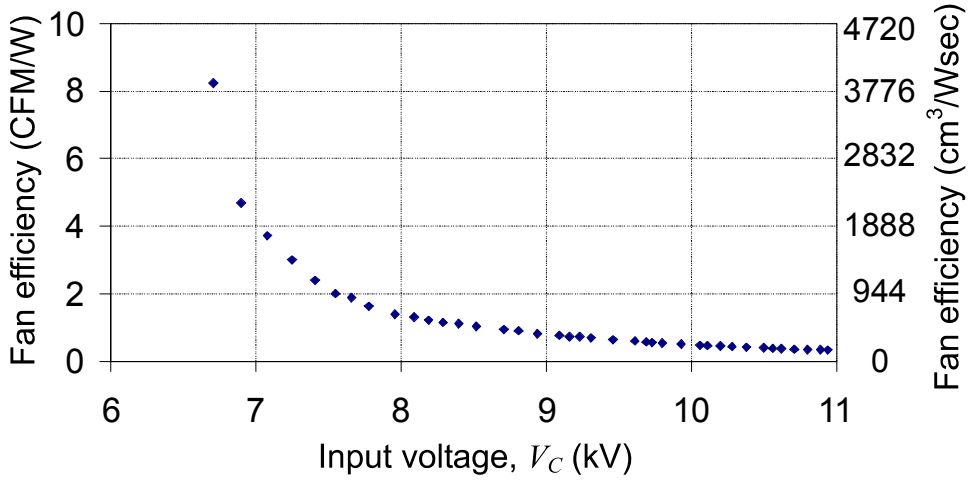

Figure 4.25. *Pump efficiency as a function of input voltage (V).*

Traditional computer cooling fan efficiency ranges from 1800 to 3600 cm^3/sW at various air velocities [124] as shown in Table 4.1. The corona air pump fabricated in this investigation lies within the range of efficiency for conventional fans while offering higher air velocities. The corona-generated airflow also has less vorticity, which leads to a quieter operation.

Table 4.1. *CPU rotary fan airflows and efficiencies.*

Pentium CPU fan	Fan Diameter (mm)	Airflow (lfm / m/s)	Efficiency (CFM/W / cm^3/sW)
Pentium II in desktop chassis	40	370 / 1.9	3.79 / 1789
Pentium II & III in tower chassis	50	568 / 2.9	6.67 / 3148
Pentium III in 1U server chassis	50	663 / 3.4	7.78 / 3672
Pentium 4 in 1U server chassis	60	559 / 2.8	4.89 / 2308

4.3.4 Conclusions

Advantages of electrostatic fluid accelerators over traditional devices include elimination of moving parts, low noise, dynamic airflow profiles, versatile shapes and sizes, compatibility with chip and chip-level structures, and improved energy efficiency.

This study explores the possibility of building an electrostatic fluid accelerator for enhanced heat withdrawal from microelectronic devices and MEMS. The analysis is also applicable to other air management tasks, such as ventilation, filtering, and dehumidification achieved using electrostatic corona discharge.

A numerical optimization study of electrostatic fluid accelerators conducted here used the concept of figure of merit based on distribution of the electric field in the cross-section of the device. Device optimization through the application of a distributed collector voltage was shown to be possible. The effect of space charge on device performance was investigated.

In the experimental verification study, channel device geometry with a razor corona electrode was found to be a promising design for heat removal and for air propulsion. A prototype air pump of this kind has been built at the macro-scale for analysis of electrical and airflow properties. Experiments showed a near linear relationship between corona voltage and air velocity. At the center of the aperture separation, the airflow reached a maximum of 4 m/s at 11 kV, beyond which the dielectric breakdown occurred. The prototype electrostatic fluid accelerator efficiency was comparable to that of conventional rotary CPU cooling fans. At lower air velocities, the device efficiency was about 3776 cm^3/s (8 CFM/W).

The main challenges in the realization of practical electrostatic fluid accelerators include understanding of relative importance of design features, improved energy efficiency, sufficient airflow rates, and miniaturization of electrode structures. Future research directions include optimization of geometry and driving electronics; system integration; numerical simulation of the electrodynamics of moving media and space charge on a micro-scale; and micro-scale fabrication. Figure-of-merit efficiency calculations should be expanded to other corona based devices and coupled with simulations that take into account actual space charge distributions and fluid dynamics. Future work should also investigate the optimization strategy with more complex and dynamic distributed voltages in order to improve performance of electrostatic fluid accelerators, dehumidifiers, and other corona based devices.

4.4 Scaling laws for EHD air movers

Forced convection can be effective at removing heat to the ambient environment. However, considerable implementation challenges remain for cooling solution thicknesses below 6mm, where the height of rotary fans is a limiting factor. While scaling laws for fans have been previously reported in the literature, the scaling rules for electrohydrodynamic (EHD) air movers have not been widely studied. This chapter explores the impact of thickness, width, and input power on pressure and airflow of EHD air movers using coupled-physics modeling, with experimental validation of the results. Device thicknesses were in the 2 to 6 mm range, device widths in the 10 to 100 mm range, and input powers between 0.25W and 2.5W.

4.4.1 Scaling laws for rotary fans

Conventional mechanical fan scaling laws are well known and the basis for design of large-scale fans. These laws are summarized in Eqns. (4.18) to (4.20) and describe how the flow rate Q, pressure rise ΔP, and power consumption scale with key fan parameters such as rotation speed ω, fan diameter Φ, rotor blade height h, and fluid density ρ_{air} [54].

$$Q \propto [\omega]^1 [\phi]^2 [h]^1 \tag{4.18}$$

$$\Delta P \propto [\rho_{air}]^1 [\omega]^2 [\phi]^2 \tag{4.19}$$

$$Power = (\Delta P)(Q) \propto [\rho_{air}]^1 [\omega]^3 [\phi]^4 [h]^1 \tag{4.20}$$

Equations (4.18) to (4.20) can be rearranged and simplified to show their dependence on input power and height giving

$$Q \propto (Power)^{1/3} h^{2/3} \tag{4.21}$$

$$\Delta P \propto \left(\frac{Power}{h}\right)^{2/3} \tag{4.22}$$

As shown in Eqn. (4.21), fan flow rate should scale by $h^{2/3}$, leading to a reduction in flow rate with decreasing h. However, real world fan flow rates drop off faster, especially at small form factors, due to losses that include inlet, outlet and boundary layer

effects [54], low Reynolds number effects [53], and electromechanical efficiency losses related to scaling motor size [125].

Additionally, in order to achieve required airflow rates, thinner fans need higher rotor speeds or larger diameters, both of which increase noise and can ultimately limit performance due to acoustic bounds of a given application [55].

Finally, as fans are made thinner, reliable motor and bearing structures become more challenging and an increasing percentage of the overall thickness is needed for the air gap between the fan blades and the case, as well as the case itself. As part of this study multiple 6 mm commercial laptop fans were measured where the fan blade represented less than 50% of the overall fan height. Fan packaging is a mature area and significant reductions in packaging thickness are unlikely for 6 mm fan thicknesses. Moreover, further reduction in fan height will force a disproportionate percentage reduction in fan blade height compared to total fan height. Considerable challenges remain for the implementation of mechanical fans significantly thinner than 6mm.

4.4.2 Electrohydrodynamic air movement

EHD air movers operate by applying an electric potential between a pair of emitter and collector electrodes to create a corona discharge adjacent to the emitter. A sharp electric field gradient is required to ignite and maintain a corona discharge. Thus, the emitter must have a much smaller radius of curvature relative to the collector. The ions produced in the corona are accelerated by the electric field between the two electrodes and transfer momentum to intermediate neutral air molecules, resulting in a net airflow as shown in Figure 3.1 for a pin–rod configuration. By eliminating mechanical components such as rotating fan blades and bearings, EHD air movers can be made very thin while avoiding the acoustical, vibrational and wear-out issues that plague fans.

The performance of EHD air movers was studied by a combination of computational modeling and experimental validation in this chapter to develop basic scaling laws.

4.4.3 Ideal EHD scaling laws

In its simplest form, an ideal EHD air mover can be represented by a plane charge source at an electric potential V (an emitter), separated by a distance s from a fully-fluid-permeable, grounded collector, as depicted in Figure 4.26. In this idealized device the fluid is allowed to slip along the walls, eliminating boundary layer effects. The dielectric walls act as an electric symmetry condition and the device is therefore electrically equivalent to an infinite uniform field. In this configuration the electric field E is equal at all points between the source and the collector and all field lines are moving parallel to each other and orthogonal to the collector and charge planes.

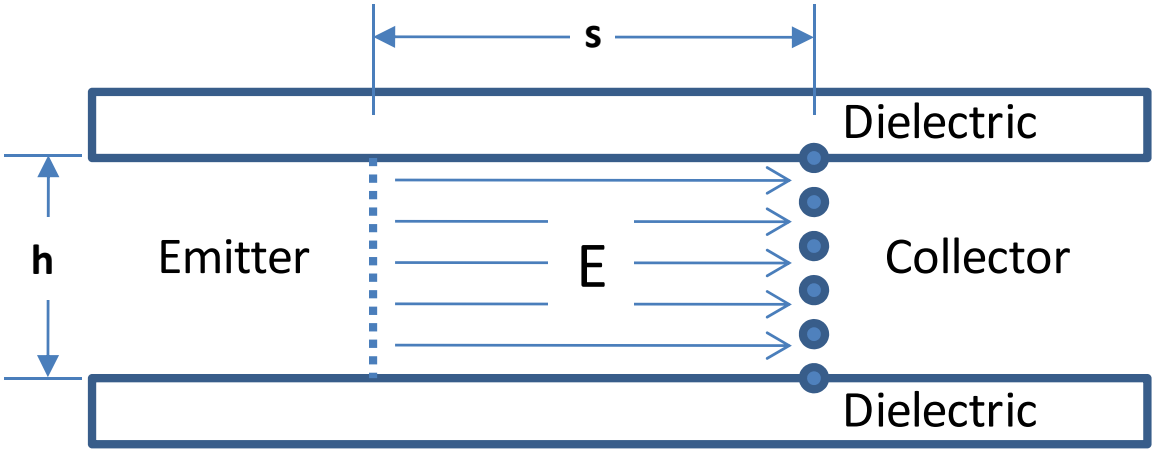

Figure 4.26. *Schematic of an idealized EHD air mover, with a plane charge source parallel to a fluid-permeable collector.*

Ions originating at the charge source are accelerated towards the collecting electrode in a straight path along the electric field lines. This flow of ions amounts to an electric current I, with the overall electric power of the device given by

$$Power = I\,V \tag{4.23}$$

The net body force acting on the air within the device—and therefore the pressure on the collector plane—is proportional to the total integrated force within the air gap which is equal to the product of the electric field strength and the total space charge within that volume

$$\Delta P \propto \int_{Vol} \rho \nabla V \tag{4.24}$$

where ρ is the space charge density. An ideal EHD device can hence be abstracted as a planar pressure source located between the charge source and the collector.

Applying Bernoulli's equation to a stream tube that connects a region far away from the inlet ($U_\infty = 0$) to the collector plane of an ideal EHD air mover, it holds that

$$\Delta P = \tfrac{1}{2}\rho_{air} U^2 \tag{4.25}$$

where U is the airflow velocity at the collector plane. The flow mechanical power W', is given by the product

$$W' = Q\,\Delta P = (whU)\left(\tfrac{1}{2}\rho_{air} U^2\right) = \tfrac{1}{2}\rho_{air}\, whU^3 \tag{4.26}$$

Assuming that a constant transduction efficiency relates the electric and mechanical powers ((4.23) and (4.26)), it follows that the flow in an EHD device scales as

$$Q \propto (Power)^{1/3}\, h^{2/3} \tag{4.27}$$

identical to the corresponding scaling for a mechanical fan, given by (4.21).

Combining (4.26) and (4.27) we obtain that the static pressure of an EHD air mover scales as

$$\Delta P \propto \left(\frac{Power}{h}\right)^{2/3} \tag{4.28}$$

identical to (4.22) for a mechanical fan. It should also be noted that although (4.28) was solved in terms of h and the device width was assumed to be constant, h can be substituted for the product of h and w, which is the cross section area of the ideal EHD air mover.

$$\Delta P \propto \left(\frac{Power}{Area}\right)^{2/3} \tag{4.29}$$

From an energy point of view, it is not unexpected that the ideal scaling laws obtained for both mechanical fans ((4.21) and (4.22)) and EHD air movers (. (4.27) and (4.28)) are identical. Both devices affect air motion by applying energy, drawn from electrical power, onto an area, be it the space between the collectors or the size of the impeller. Therefore, changes in flow and pressure follow the same energy considerations imposed by Bernoulli's equation.

4.4.4 *Practical reference geometry*

The geometry used for this study is shown in Figure 4.27. It includes two dielectric plates that define an airflow channel of width *w* and height *h*. An emitter wire 25 microns in diameter is held under tension and centered within the channel upstream of the collector electrodes. Collector electrodes protrude from the surface of each dielectric layer by 100 microns.

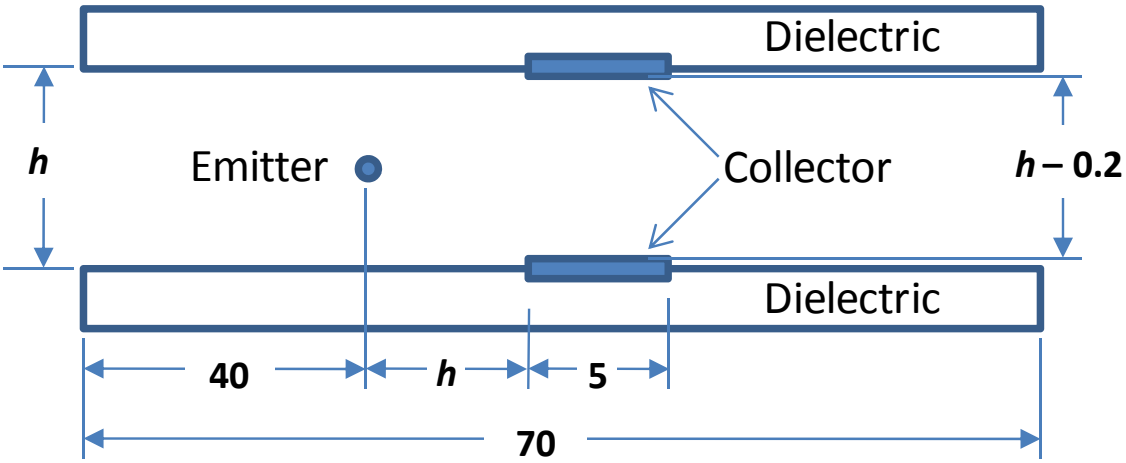

Figure 4.27. Cross-section of reference geometry. *The device projects into the page by a width W. Solid dielectric sidewalls define the edges. Geometric parameters detailed in* Table 4.2. *Dimensions in millimeters.*

Table 4.2. *Geometric parameters.*

Emitter diameter, *d*	25 μm
Device height, *h*	2, 4, 6 mm
Device width, *w*	10–100 mm

4.4.5 *Governing equations for EHD flow*

The EHD model used for this study was adapted from the authors' previously published modeling work [12] and it is described in depth elsewhere in this thesis, but is included here for convenience of the reader.

Electrohydrodynamic flow induced by corona discharge is described by the following equations. The electric potential V is governed by Poisson's equation

$$\nabla^2 V = -\frac{\rho}{\varepsilon_0} \tag{4.30}$$

where ρ is the space charge density and ε_0 is the dielectric permittivity of free space. The electric potential is defined from electric field intensity E as

$$\mathbf{E} = -\nabla V \tag{4.31}$$

Electric current in the ion drift zone is a combination of three effects: conduction (motion of ions under electric field relative to entire airflow), convection (transport of charges with airflow), and diffusion. Therefore, current density **J** is given by

$$\mathbf{J} = \mu_{\mathrm{E}}\mathbf{E}\rho + \mathbf{U}\rho - D\nabla\rho \tag{4.32}$$

where μ_{E} is the air ions mobility in an electric field, U is the velocity vector of airflow, and D is the diffusivity coefficient of ions. Current continuity condition gives the equation for current density

$$\nabla \bullet \mathbf{J} = 0 \tag{4.33}$$

The hydrodynamic part of the problem is described by the Navier–Stokes equations and momentum continuity equation for steady state incompressible air flow

$$\rho_{air}\mathbf{U}\cdot\nabla\mathbf{U} = -\nabla P + \mu\nabla^2\mathbf{U} - \rho\nabla V \tag{4.34}$$

$$\nabla\cdot\mathbf{U} = 0 \tag{4.35}$$

where ρ_{air} is the air density, P is the air pressure, and μ is the air dynamic viscosity.

The computational model was constructed using COMSOL Multiphysics, a commercial software package that performs equation-based multiphysics modeling for different physical processes by applying the finite element method to the system of partial differential equations. Space charge generation from corona discharge is modeled using Peek's equation and Kaptsov's assumption as described in [12, 59, 126]. The boundary conditions to the model are summarized in Table 4.3.

Table 4.3. *Model boundary conditions.*

Electrostatic boundary conditions	
Emitter electrode	0–10 kV
Collector electrode	0V
All dielectric channel and air surfaces	Symmetry
Inlet and Outlet	0V
Charge transport boundary conditions	
Charge density on emitter	Based on [12, 126]
Collector surfaces	$\nabla \rho = 0$
Dielectric surfaces	Symmetry
Navier–Stokes boundary conditions	
All solid surfaces	No-slip
Inlet boundary	Prescribed velocity
Outlet boundary	Zero pressure

4.4.6 Sample FEM modeling results

Example simulation results for EHD-driven flow are shown in Figure 4.28 for the case of a 2mm-thick EHD air mover at 1W input power. The top panel shows the electric field distribution in the channel from which the space-charge distribution is predicted (second panel). The electric field is strongest in the vicinity of the emitter, where ion generation occurs in the form of a corona discharge. Said ions travel toward the collector along the electric field lines. This results in a body force equal to the net Coulombic body force (shown in the third panel) on the fluid within the channel. The ions exchange momentum with neutral air molecules via collisions, and cause air flow in the direction of net body force, as shown in the bottommost panel.

Representative airflow results are shown in Figure 4.29 for 4 mm and 6 mm channels (top and bottom panels, respectively), following the same procedure as outlined above for the 2 mm device.

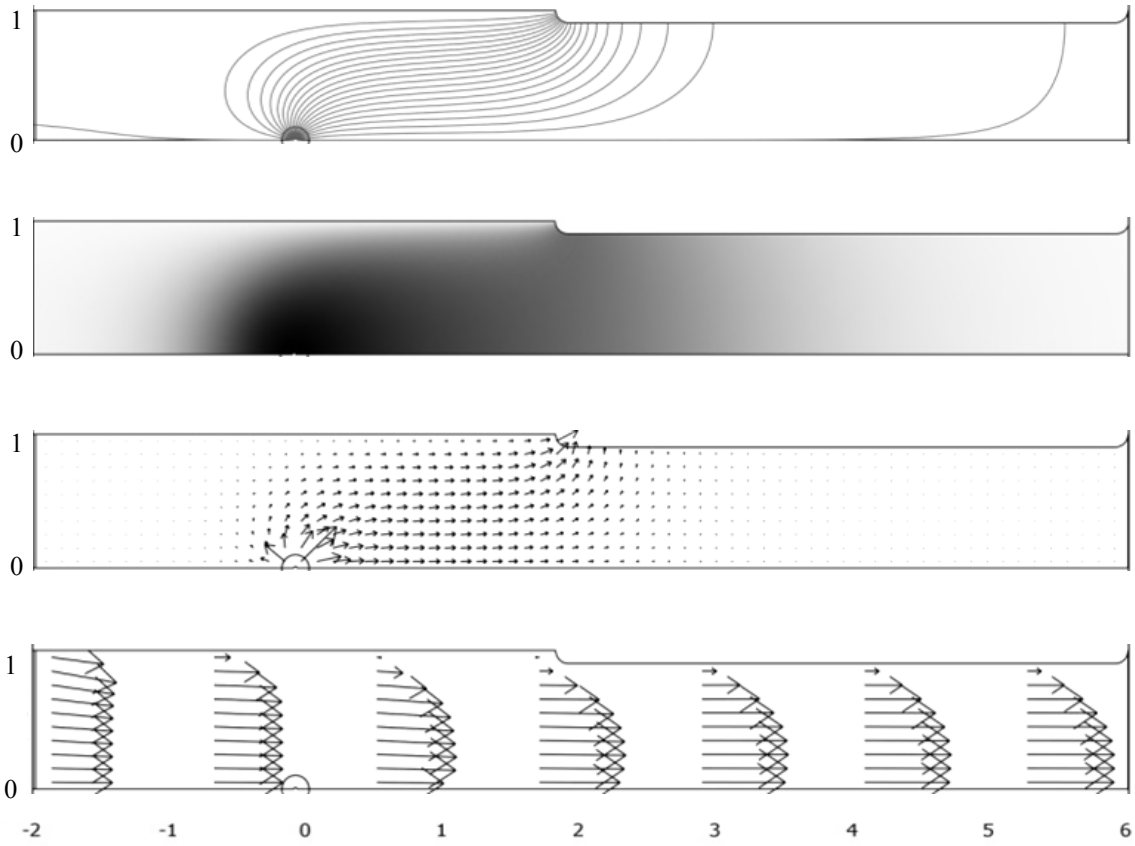

Figure 4.28. *Numerical results of 2 mm thick EHD air mover at 1 watt input power. From top to bottom, the panels show: the electric field lines; the relative space charge density as intensity plot; the coulombic body force as arrows proportional to force; and the Velocity field as arrows proportional to velocity. Duct dimensions in millimeters.*

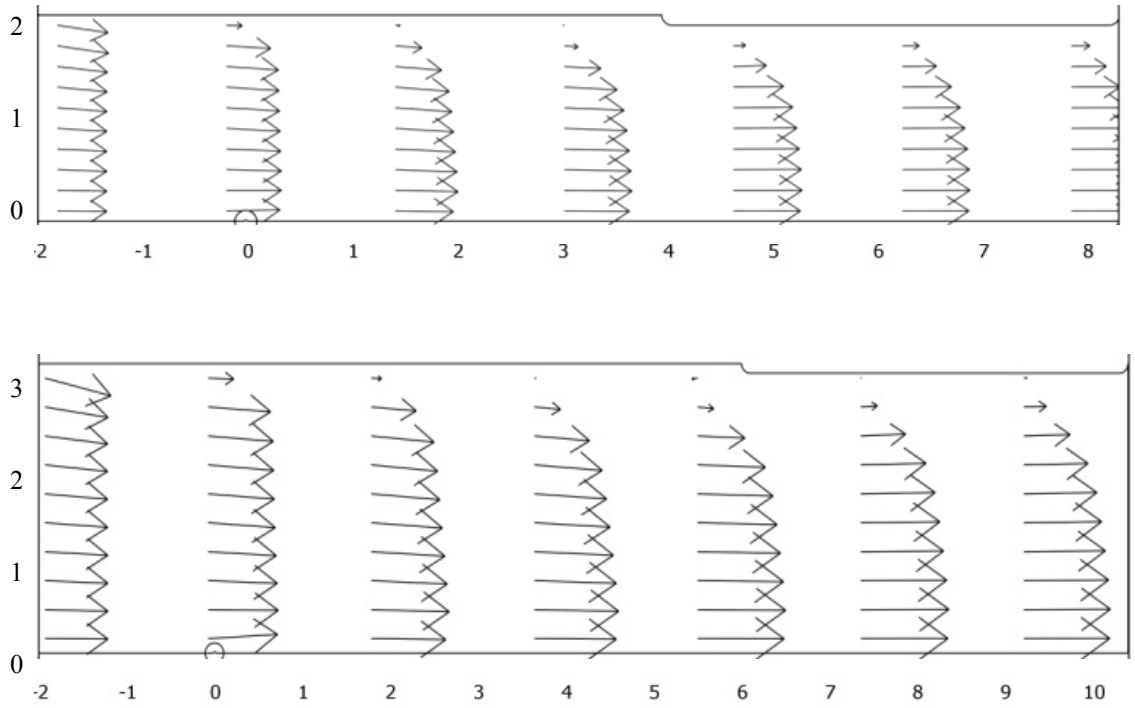

Figure 4.29. *Numerical results of 4 and 6 mm thick EHD air movers at 1 Watt input power. Velocity field as arrows proportional to velocity. Duct dimensions in mm.*

4.4.7 Experimental methods

The prototypes for each thickness were constructed from two sheets of acrylic. A groove was made into each of the two plates to accurately position the top and bottom collecting electrodes, which were made out of gold-plated aluminum to ensure simple soldering connections (see Figure 4.30).

A 25 μm-diameter emitter wire was suspended under tension halfway between the two plates and positioned upstream of the collector electrodes.

Dielectric sidewalls were used to seal the edges and set the spacing between the two plates. The width between the dielectric sidewalls was 100 mm. In order to achieve a lower width, a tight fitting piece of acrylic was inserted into the gap to block the flow in a portion of the channel. The acrylic piece had a cut-out that arrested the corona in that area as well so that no power was consumed in the inactive length.

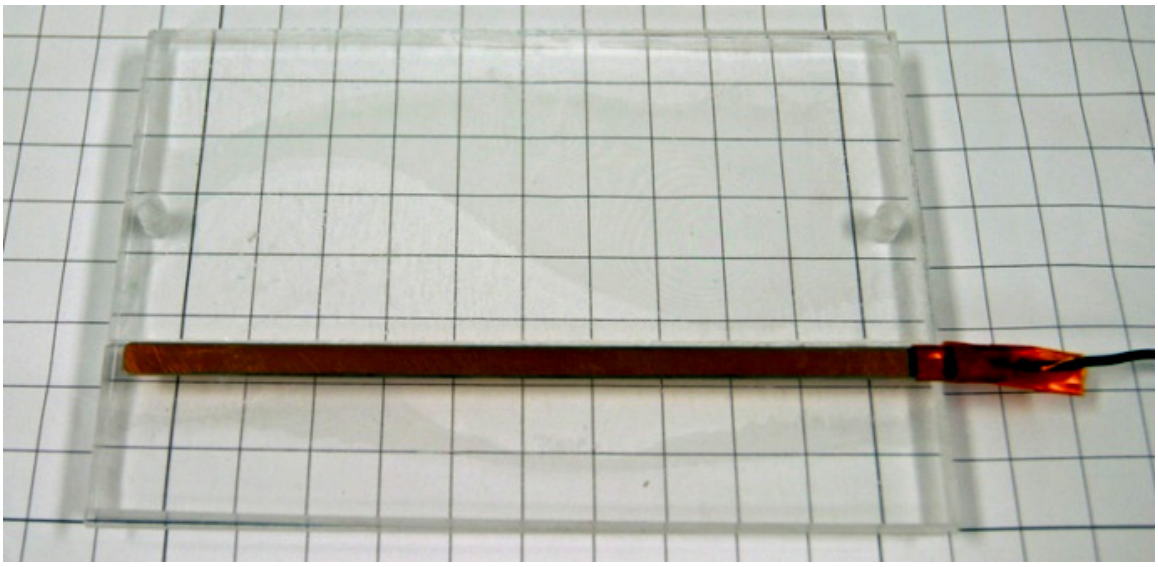

Figure 4.30. *Top half of experimental structure showing metal collector electrode on dielectric plate. The bottom half is a mirror image of the top. An emitter wire is suspended between the top and a bottom halves.*

4.4.8 Experimental airflow performance measurement procedure

The prototypes were affixed to a wind-tunnel to measure their airflow performance, shown in Figure 4.31. Hot-melt glue was used to seal the experimental structure to an acrylic face plate.

The relation between pressure and flow rate was determined by measuring the pressure across the EHD air mover when varying amounts of air were pulled through the system by the wind tunnel fan. A digital pressure gauge with 0.25 Pa resolution was used to read the pressure between the inlet and outlet of the EHD air mover. Flow rate was determined by an additional pressure gauge that measured the relative pressure drop across a calibrated nozzle through which all air flowed in the wind tunnel. The EHD air mover was powered using a precision Matsusada DC high-voltage power supply, and emitter voltage and current were monitored using precision digital multimeters with 1 mV and 10 nA resolution respectively and a one gigaohm input impedance high-voltage probe for the voltage measurement.

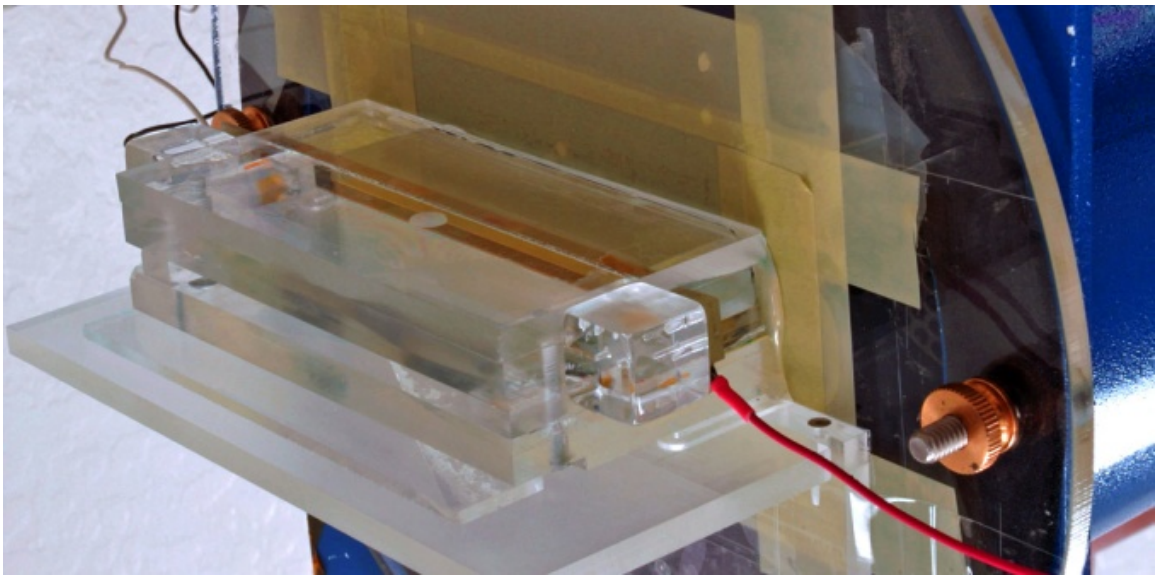

Figure 4.31. *Experimental device mounted to a wind tunnel for characterizing flow and pressure as a function of applied power. The duct in this particular device was 6 mm tall and 100 mm wide.*

4.4.9 Experimental and modeling scaling law results

The simulated and experimental EHD air mover flow rates as a function of input power for 100 mm wide 70 mm long ducts with thicknesses of 2 mm and 6 mm are shown in Figure 4.32. The pressures for these devices were simulated and measured experimentally. The results are presented in Figure 4.33. As expected, the experimentally measured pressures and flow rates were lower than simulated, as the latter assumed a perfectly sealed device with exactly uniform power density along the emitter and no duct side walls.

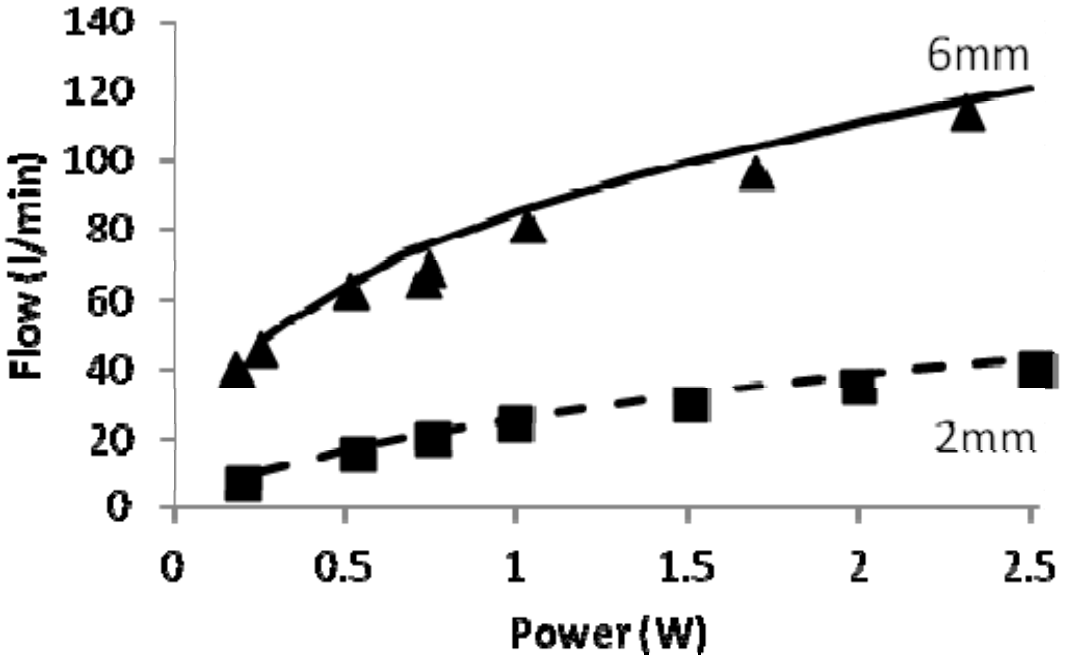

Figure 4.32. *Comparison of experimental and modeled results for airflow vs. input power for 2 and 6 mm thick EHD air movers with 100 mm wide by 70 mm long ducts.*

Figure 4.34 shows the simulated and experimentally measured mean outlet velocity, as a function of input power per unit length, of a 6 mm thick EHD air mover that is 70 mm long. The first measurement was taken with the channel width completely open to the full value of 100 mm. The second measurement was taken with half of the channel blocked by a tight fitting piece of acrylic. The acrylic plate contained a groove that surrounded the emitter wire over half the channel width and prevented the formation of a corona in that region. The acrylic piece also effectively reduced the fluidic channel to half its width. The results support the assertion that outlet velocity, which is proportional to flow rate, is a function of power per width on the emitter wire and validates the use of 2-D models for simulating performance.

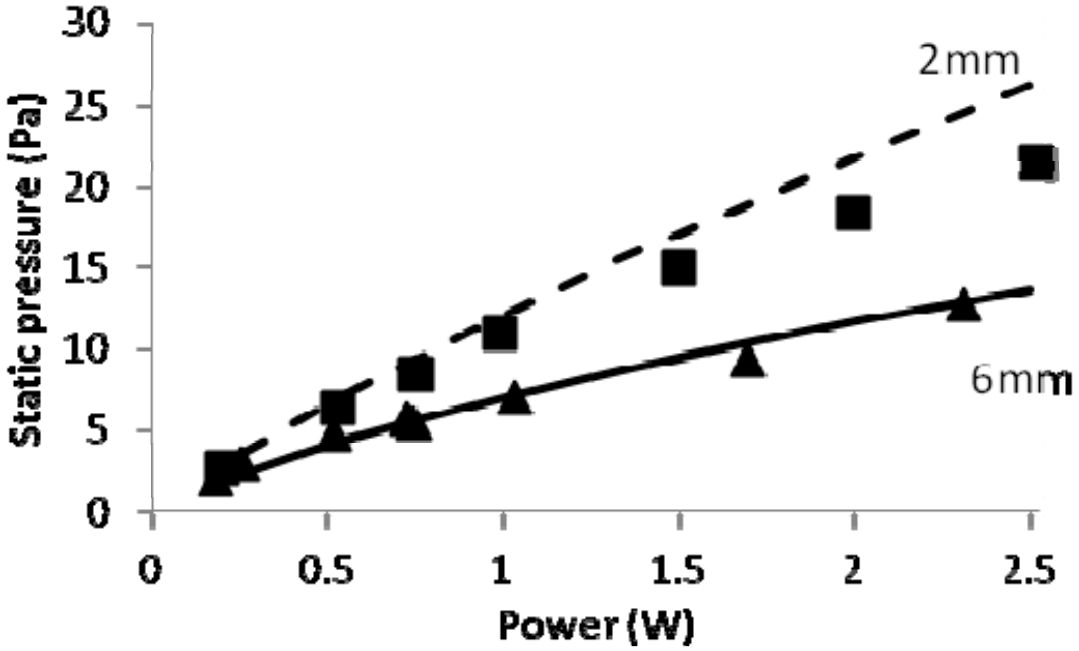

Figure 4.33. *Comparison of experimental and modeled results for stagnation pressure vs. input power for 2 and 6 mm EHD air movers with 100 mm wide by 70 mm long ducts.*

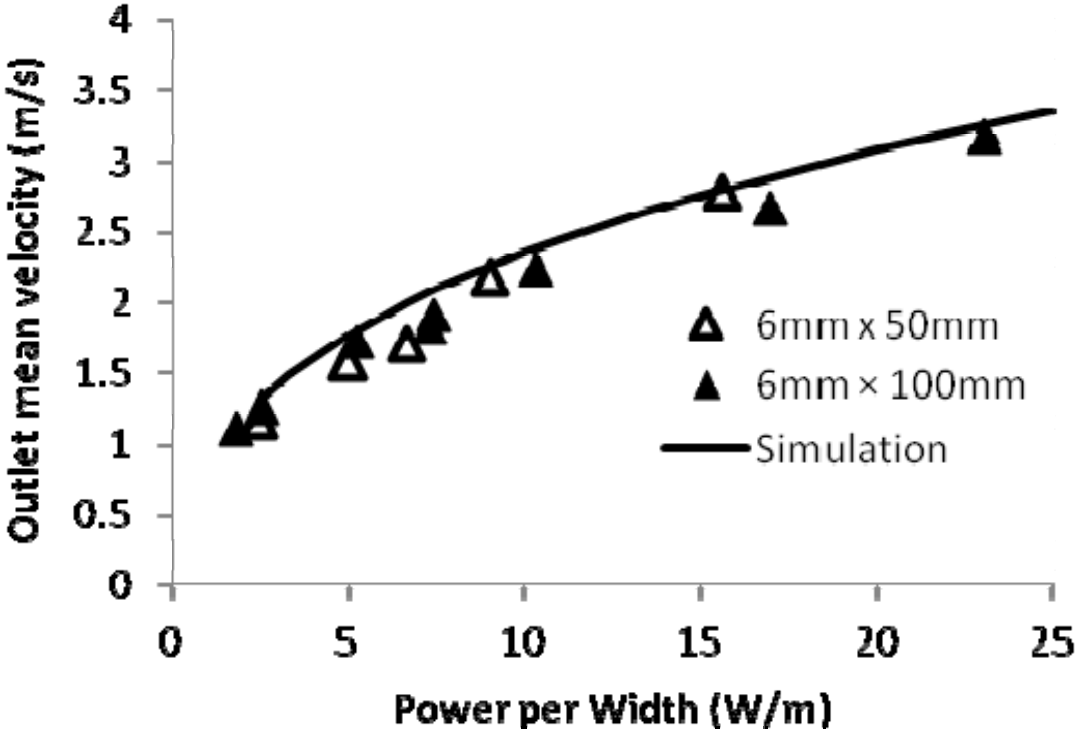

Figure 4.34. *Comparison of experimental and modeled average outlet velocity vs. power per-duct-width for 6 mm thick EHD air movers with 50 and 100 mm wide ducts.*

Fans are often characterized using a P-Q curve, which shows the pressure build-up that results when the flow is throttled. The equivalent curves are shown in Figure 4.35 for a 2 mm × 100 mm × 70 mm and a 6 mm × 100 mm × 70 mm (thickness × width × length) EHD air mover. The input power in each case was 1.5 W. Both experimental and simulated results are plotted and agree well with each other.

Unlike most air movers the flow resistance through an EHD air mover set within a channel is almost negligible since the emitter cross section is small compared to the channel height and the collecting electrodes can be made nearly flush to the channel surface. Therefore, it should be expected that the flow resulting from the pressure head developed by the EHD air mover can be predicted by representing the EHD as an ideal pressure source within the channel and calculating the flow required to generate a pressure drop equal to the EHD pressure head. The results of such a calculation are shown in Figure 4.36, where the lines show the numerically simulated flow rates and the symbols represent the flow rates calculated using Bernoulli's equation for pressure driven flow in a channel assuming an ideal pressure source in the duct equal to the numerically simulated stagnation pressures. There is good agreement between the simulated and calculated values suggesting that the ideal pressure source assumption is valid.

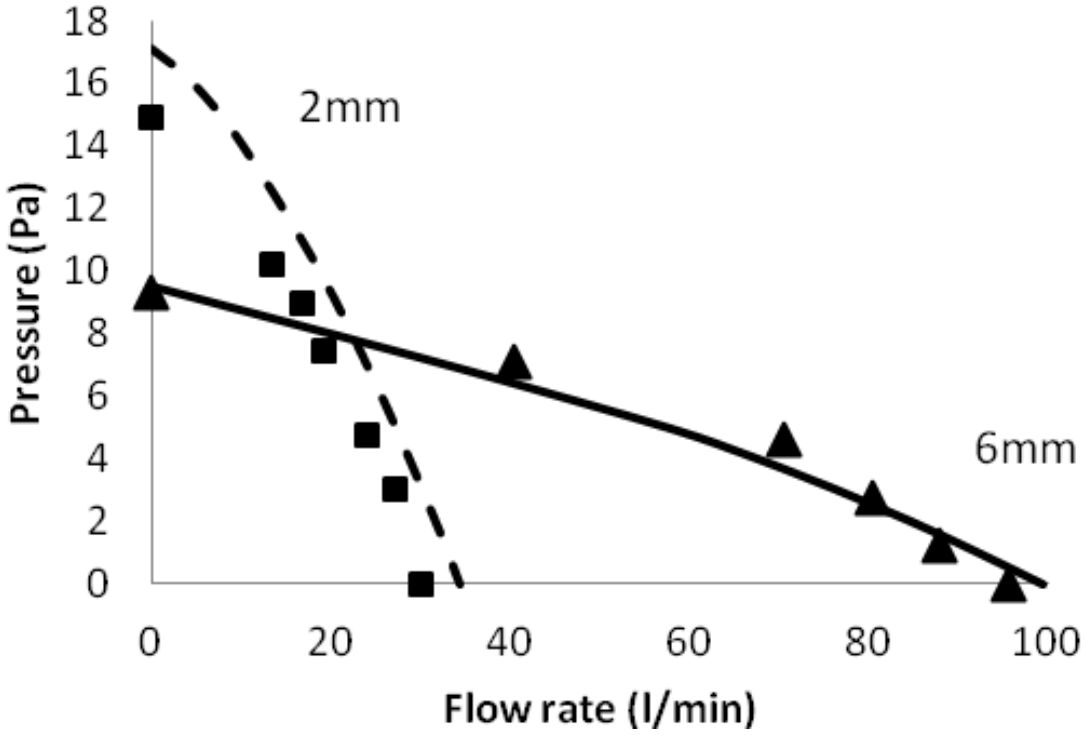

Figure 4.35. *Comparison of experimental and modeled fan curves at 1.5 watt input power flowing through 100 mm wide by 70 mm long duct for a 2 and 6 mm thick EHD air mover.*

In order to separate the performance of the EHD air mover itself from the long duct used in the experimental study, the results from Figure 4.35 were scaled to a 10 mm duct length, which approximates the required channel length for the EHD device alone. The scaling was done by calculating the flow through a 10 mm duct assuming the EHD was an ideal pressure source in a channel, as described above and verified in Figure 4.36. The results of the scaled P-Q curve for EHD air mover at 1.5 W input power in 100 mm wide by 10 mm long ducts with thicknesses of 2 mm and 6 mm are compared to numerical P-Q results for a short duct and are shown in Figure 4.37. The 2 mm EHD air mover flow rate increases approximately 30 % for the shorter duct length, while the 6 mm EHD air mover shows only a slight increase, which is expected due to the comparably low flow resistance of the 6 mm duct.

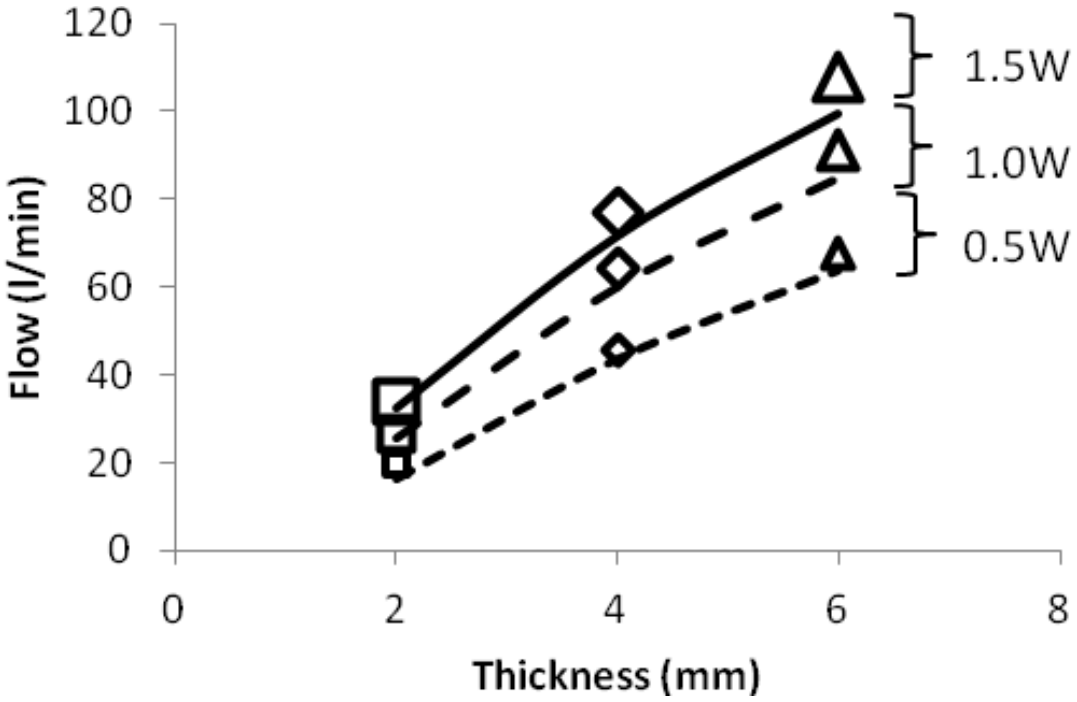

Figure 4.36. *Flow rate through a 100 mm wide 70 mm long duct as a function of thickness for three different power settings. The lines indicate numerically simulated flows. The symbols indicate what flow could be expected due to an ideal pressure source equal to the numerically simulated stagnation pressure level located within the duct.*

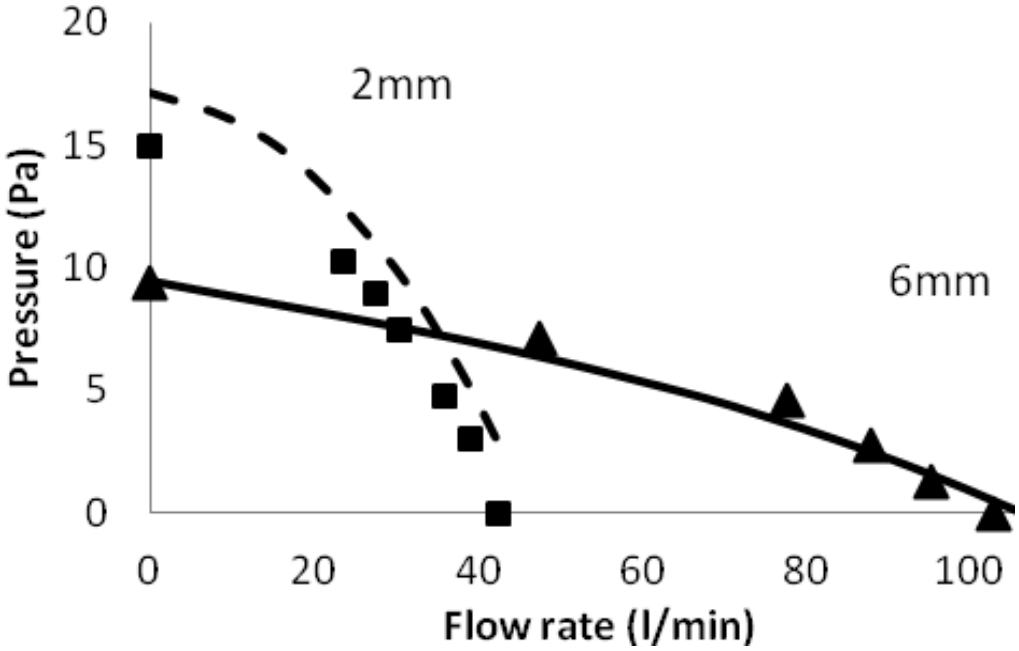

Figure 4.37. *Comparison of scaled experimental and modeled P-Q curves at 1.5 W input power flowing through a 100 mm wide by 10 mm long duct for a 2 and 6 mm thick EHD air mover.*

4.4.10 Scaling trends

The trends of airflow and pressure for the reference EHD air mover geometry are now compared to the ideal EHD air mover scaling laws. The EHD air movers were 100 mm wide, with lengths of 9, 11, and 13 mm for 2, 4, and 6 mm air mover heights, respectively. The simulated results were directly modeled for the stated channel lengths and the experimental flow results were scaled to the shortened lengths using the ideal pressure source method described earlier in the paper. Stagnation pressure is not affected by duct length and therefore did not need to be scaled.

The experimental flow results are plotted against a power density axis scaled per the ideal EHD air mover scaling law in Figure 4.38. Both the 2 mm and 6 mm air mover data fall along the same general line indicating that the practical reference geometry scales as the ideal case.

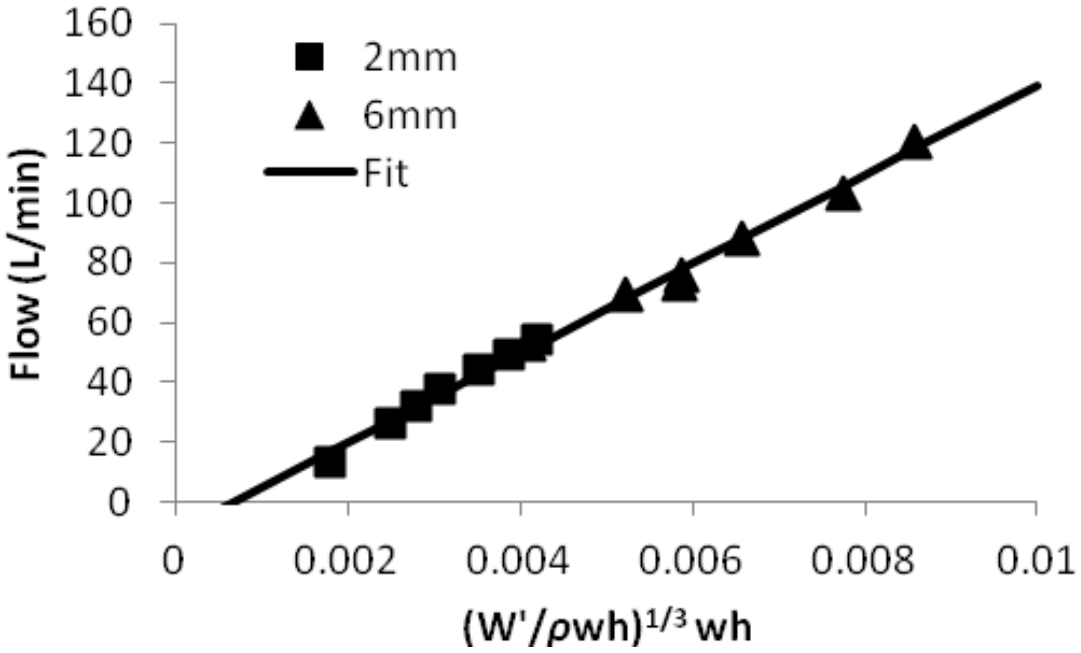

Figure 4.38. *Experimental flow rate vs. power density fit to ideal EHD air mover scaling law.*

The simulated pressure results in Figure 4.39 are plotted against a power density axis scaled per the ideal EHD air mover scaling law. As such, if the scaling law fits, the data from all channel heights should collapse onto a single straight line. Good agreement is seen for all air mover heights. Figure 4.40 shows a similar chart as Figure 4.39, but using experimental pressure results instead of simulation. The fit line is the same as in Figure 4.39. The 6 mm results correlate well, but the 2 mm results are lower than predicted. The deviation in the 2 mm simulated and experimental air mover pressure is likely due to emitter wire misalignment in the hand built prototypes causing a non-uniform pressure distribution across the channel. Emitter wire misalignment was also observed in the 6 mm device. However, due to the larger emitter to collector air gap the misalignments had less impact on pressure distribution across the channel and therefore more closely fit the expected scaling.

Unlike pressure, maximum flow rate is much less sensitive to emitter wire misalignment because the outlet velocity scales only as the cube root of power density.

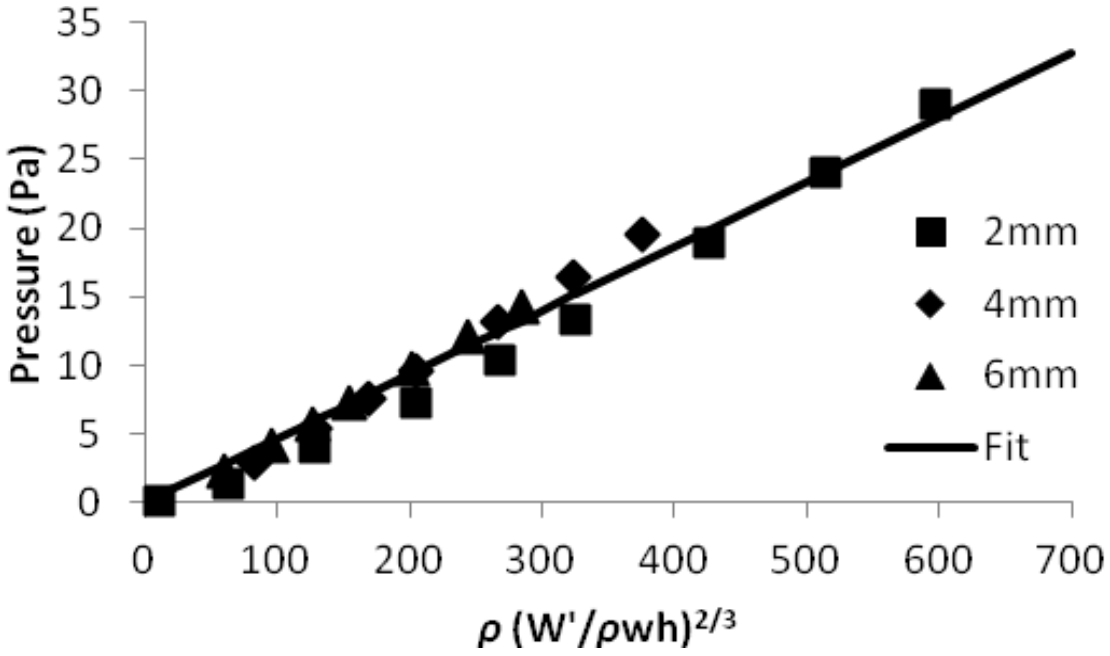

Figure 4.39. *Modeled stagnation pressure vs. power density fit to ideal EHD air mover scaling law.*

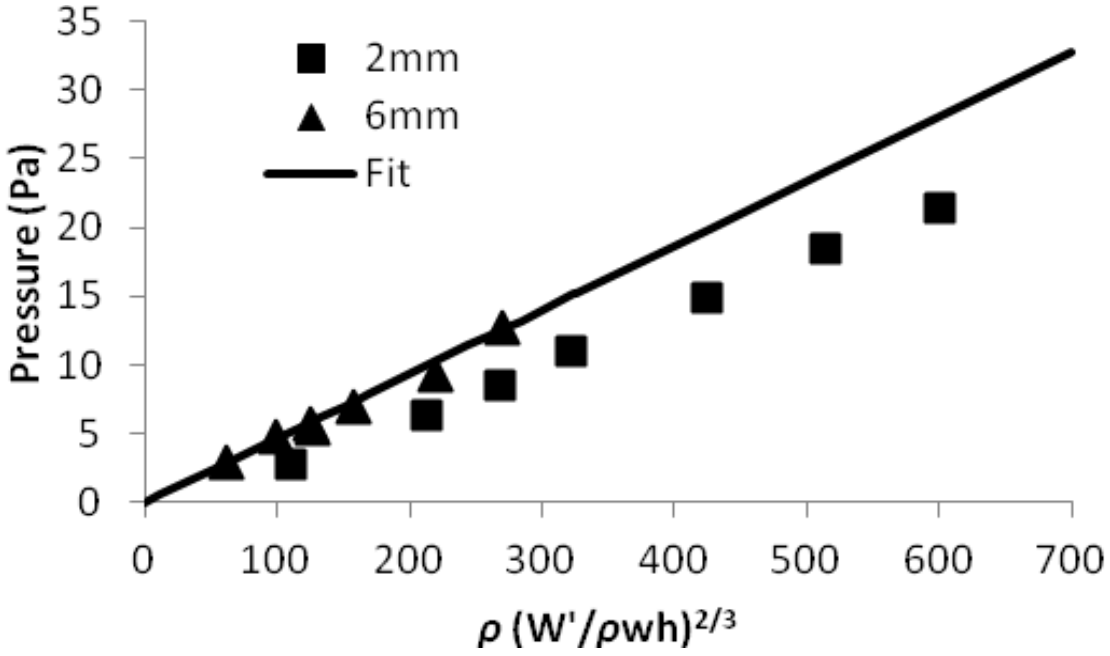

Figure 4.40. *Experimental stagnation pressure vs. power density fit to ideal EHD air mover scaling law.*

4.4.11 Scaling law conclusions

The static pressure in an ideal EHD air mover, where the ion source is a uniform plane of charge, scales as the power density raised to the two-thirds power.

The open air flow rate in an ideal EHD air mover scales as the product of the outlet area and the power density raised to the one-third power.

Outlet air velocity is uniform across the EHD air mover width, unlike a mechanical blower, which has a highly non-uniform outlet velocity profile. The EHD air mover would maximize heat transfer efficiency through a heatsink for a given flow rate due to the uniform outlet velocity.

4.4.12 Chapter summary

1. Practical EHD air movers with single wire emitters were modeled and demonstrated in the range of 2 mm to 6 mm thick.
2. The pressure and flow of the practical geometry scaled similarly to the ideal case.
3. The computational model was shown to predict pressure and flow characteristics that matched the measured results of prototype devices.
4. The airflow created by an EHD air mover within a duct can be predicted reasonably well by considering the device to be an ideal pressure source with no additional internal flow resistance beyond that of the duct. This is because the EHD air mover has little flow impedance of its own by virtue of its straight-through flow path. It also avoids the flow restriction of a plenum as commonly used above and below mechanical blowers.
5. Thinner devices produced higher pressure at a given input power than thicker devices, but lower open-air flow due to the increased flow restriction of the thinner duct.
6. Although the thinnest EHD air mover investigated in this study was 2 mm it is conceivable further miniaturization is possible without departing far from the ideal scaling laws.

Chapter 5. Modeling of electrostatic fluid acceleration systems

A numerical modeling approach for EHD driven convective heat transfer is presented in this chapter, including the set of governing equations and charge generation equations used in the model, and a description of the scope and limitations to the proposed model. A numerical model for a wire-to-grid EHD geometry is presented, followed by a model validation investigation, and concluding with a modeling study for meso-scale EHD forced convection cooling.

5.1 Governing equations for electrohydrodynamic flow

Electrohydrodynamic flow induced by corona discharge and the resulting heat transfer is described by the following equations. The electric potential V is governed by Poisson's equation

$$\nabla^2 V = -\frac{\rho}{\varepsilon_0} \tag{5.1}$$

where ρ is the space charge density and ε_0 is the dielectric permittivity of free space. The electric potential is defined from electric field intensity $\mathbf{E}$ as

$$\mathbf{E} = -\nabla V \tag{5.2}$$

Ion transport contributing to electric current in the drifting zone is a combination of three effects: conduction (motion of ions under electric field relative to bulk airflow), convection (transport of charges with airflow), and diffusion. Therefore, current density $\mathbf{J}$ is given by

$$\mathbf{J} = \mu_{\mathrm{E}} \mathbf{E}\rho + \mathbf{U}\rho - D\nabla\rho \tag{5.3}$$

where μ_{E} is the air ions mobility in an electric field, $\mathbf{U}$ is velocity vector of airflow, and D is the diffusivity coefficient of ions. Current continuity condition gives equation for current density

$$\nabla \bullet \mathbf{J} = 0 \tag{5.4}$$

The hydrodynamic part of the problem is described by the Navier-Stokes equations and momentum continuity equation for steady state incompressible air flow

$$\rho_A \mathbf{U} \bullet \nabla \mathbf{U} = -\nabla p + \mu \nabla^2 \mathbf{U} - \rho \nabla V \tag{5.5}$$

$$\nabla \bullet \mathbf{U} = 0 \tag{5.6}$$

where ρ_A is the air density, p is the air pressure, and μ is the air dynamic viscosity.

Heat transfer then can be described by thermal conduction and convention

$$q = \nabla \bullet \left(-k \nabla T\right) + \rho_A C_p \mathbf{U} \bullet \nabla T \tag{5.7}$$

where q is the heat generation from the corona discharge, k is the thermal conductivity of the medium, T is the temperature, and C_p is the specific heat capacity of air.

The system of equations (5.1, 5.4, 5.5, 5.6, and 5.7) is subject to appropriate boundary conditions described in detail in the following sections for the EHD forced convection heat transfer model investigated in this study.

5.2 Space charge generation model for corona discharge

Space charge generation by corona discharge in an EHD blower can be modeled by applying appropriate electrostatic and charge transport boundary conditions at the surface of the ionization zone. A description of the boundary conditions for space charge generation estimation is described in this section.

The air gap between corona and collecting electrodes can be divided into two regions, the ionization and drift zones. The ionization zone exists in close proximity to the corona electrode, in which air ionization occurs, and both positive and negative ions exist. The drift region, located between the ionization region and the collector electrode contains ions of a single polarity that have been driven out of the ionization region by the electric field. When the radius of the corona electrode is much smaller than the distance between corona and collecting electrodes, the ionization zone forms a nearly uniform sheath over the coronating region of the corona electrode surface. For the positive corona, the electric field strength E_e at the surface of a smooth corona electrode of radius R_e is given by Peek's empirical formula for air at standard conditions [59]

$$E_e = E_0 \left(1 + 2.62 \cdot 10^{-2} / \sqrt{R_e}\right) \tag{5.8}$$

where the corona electrode radius R_e is measured in meters and $E_0 = 3.16 \cdot 10^6$ V/m is the approximate breakdown (ionizing) electric strength of air at standard conditions. A more

general form of Peek's equation is described previously in Chapter 3.2.5. Thus, assuming the electrode tip radius is much smaller than the distance between corona and collecting electrodes, and therefore the electric field distribution can be approximated as concentric cylinders, the electric potential and electric field intensity inside the ionization zone are

$$V = V_{\mathrm{e}} - E_{\mathrm{e}} R_{\mathrm{e}} \ln \frac{r}{R_{\mathrm{e}}} \tag{5.9}$$

$$E = E_{\mathrm{e}} \frac{R_{\mathrm{e}}}{r} \tag{5.10}$$

where V_{e} is the voltage at the electrode surface, and V is the voltage at a radius r from the center of the corona electrode tip within the ionization region. At the boundary between the ionization and drifting zones, the electric field strength is equal to the breakdown electric field strength E_0. Using (5.9) and (5.10), the radius of the external surface of the ionization zone can be estimated

$$R_0 = R_{\mathrm{e}} E_{\mathrm{e}} / E_0 = R_{\mathrm{e}} \left(1 + 2.62 \cdot 10^{-2} / \sqrt{R_{\mathrm{e}}}\right) \tag{5.11}$$

The voltage drop through the ionization zone can be found by integrating the electric field strength from R_{e} to R_0. As the result, the voltage on the external boundary of the ionization zone is given by

$$V_0 = V_{\mathrm{e}} - E_{\mathrm{e}} R_{\mathrm{e}} \ln \frac{E_{\mathrm{e}}}{E_0} \tag{5.12}$$

At the external surface of the ionization zone, Kaptsov's assumption is used [126], which states that the ionization zone radius remains approximately constant with V_{e} once a stable corona is formed. This enables estimation of the surface charge density by specifying the electric field strength: $E = E_0$ at $r = R_0$. Therefore, space charge generation due to corona discharge can be calculated by prescribing voltage V_0 to the external surface of the ionization zone at a radius R_0 from the center of the corona electrode tip to satisfy Poisson's equation. The charge transport equation is similarly satisfied by applying a surface charge density at the external surface of the ionization zone such that the resulting electric field at that surface located at a radius R_0 is equal to

the breakdown field intensity E_0. The validity of Kaptsov's assumption has been shown to hold well by recent corona modeling efforts [104].

In the proposed method above, the surface of the ionization boundary is treated as the edge of the "black box" of the ionization zone and neither Poisson's equation or the charge transport equation are solved within it. This will lead to some error, as there is work conducted on the working fluid within the ionization zone that will be ignored, however the volume of the ionization zone tends to be small so the error is not expected to be large for most cases. Alternatively, another methodology is to include the region between the surface of the corona discharge emitter electrode to the surface of the ionization zone in the Poisson and charge transport calculations. This simplifies the model as it does not require setting up special treatment of the ionization boundary. This is especially true when the electric field is non-uniform around the emitter, such as the case of blade emitter or certain collector designs, which would require a non-circular ionization zone to be created in the numerical model, which can be time consuming to setup. However, by including the ionization region there will be error on the predicted work on the fluid, as the complexities of the plasma within the ionization zone are being reduced to a single polarity ion field. It is this author's experience that the inclusion or exclusion of the ionization zone gives little difference in the predicted results for most geometries, and therefore the use of either method can be valid, and both are used in the studies investigated within this thesis.

5.3 Limitations and scope of proposed EHD air mover model

The model presented in this chapter for EHD driven forced convection takes into account the critical components necessary for modeling corona discharge driven EHD flows in air and the resulting heat transfer including, charge generation, charge transport, fluid dynamics, conduction and convection heat transfer, and heat generation from the corona discharge. However, as all engineering models are approximations and only valid over specific ranges and domains, this model is no exception, and discussed below are limitations to the model segmented into relevant divisions.

5.3.1 Corona discharge and air breakdown

In the interest of creating a model for use as an engineering tool that only requires modest computational power, the underlying plasma physics of the corona discharge is not directly modeled, rather boundary conditions based on empirically derived formulas, such as Peeks equation, are used to approximate the charge generation from the underlying corona discharge. There are ongoing efforts to accurately model all of the impact ionization, photoionization, and photo-emission processes within the corona discharge region, however due to the significant complexity of the problem, this is still an ongoing area of research and at the time of this writing, and is not suited well for engineering design and optimization use. The use of empirical approximations for charge generation as used in this model requires that all areas within the model which generate corona must explicitly be defined by the user rather than automatically being recognized by the model. This makes it difficult to model complex geometry corona generation surfaces that have varying radius of curvature without sacrificing accuracy. In the event that a specific geometry makes charge estimation impractical, the model can still be used to estimate EHD blower performance by directly applying specific charge densities if they can be determined or estimated empirically.

Depending on electrode material and thus the work function of the corona electrode, field emission may have some impact on corona IV characteristics, since field emission can source free electrons which can trigger or enhance an electron avalanche process. However it is viewed in this model as a secondary effect and is not included. At small air gap separations near 40 micrometers and below, it has been shown that field emission is the main phenomena responsible for seeding electron avalanches [115], however this work investigates air gaps significantly larger.

Calculation of the breakdown or spark-over threshold of the air gap separating the corona and collector electrodes is not attempted in this model, and it is required of the user to estimate this outside of the model, or determine it experimentally.

In the proposed model the ion mobility is assumed to be constant throughout the modeling space, however, it has been shown that ion mobilities can fluctuate based on attachment of other molecules to the ion reducing the mobility. However, changes in ion

mobility due to attachment is generally not significant with ion traveling distances on the range of millimeters investigated in this study [127] making the constant mobility assumption a good approximation.

5.3.2 Fluid dynamics

The proposed model uses the steady-state incompressible form of the Navier-Stokes equations for estimation of fluid dynamics, which is capable of modeling fluid flow in the laminar regime though not adequate for turbulent flows. Due to the relatively low Reynolds number flows investigated in this study, modeling of turbulent flow is not necessary, though could become an issue for models with larger length scales or high externally applied airflow velocities. The Navier-Stokes equations assume a continuous homogenous fluid, therefore they do not properly model fluid flow were element dimensions are on the order of the mean free path of air molecules. Although the corona electrode tip may be on the border of the limit of the size scale in some of these models, the exact fluid flow profile surrounding the corona electrode is generally not critical to the model accuracy. Buoyancy flows are not accounted for in the model and will lead to a margin of error, however, at the temperature deltas of several tens of degrees and EHD induce airflows in several meters per second the error will be low.

5.3.3 Heat transfer

Conduction and convection are calculated in the proposed model but radiation heat transfer is ignored since the investigation focuses is on forced convection heat transfer at modest temperatures where heat transfer from radiation is insignificant.

A constant air thermal conductivity is assumed throughout the model, which is justified by the fact that convection is driving the heat transfer on the fluid side in the proposed model and the maximum temperature differences in the model are small.

5.3.4 Chemical processes and electrode degradation

Although outside the scope of this investigation and ignored in the proposed model, chemical vapor deposition of silica on the corona electrode and corona electrode

erosion and degradation through ion bombardment, oxidation, and other chemical processes are important design parameters for many EHD based applications, especially those focused on meso and micro scale designs. This affects the choice of component material properties and puts restrictions on useful device designs. Chemical processes within the corona plasma interact with the corona electrode but also with the components of the air itself, generating multiple byproduct species such as ozone and NO_x [128]. Ozone generation is often a critical parameter in EHD blower performance on the macro-scale since at high levels it can be toxic to humans and at moderate levels can speed oxidation and degradation of certain plastics and materials. Due to the small scale nature of the devices modeled in this investigation and small total corona plasma volume, generation of product gasses like ozone would be modest [72, 103, 105, 122].

5.4 Numerical modeling solvers and settings

The EHD-induced heat transfer was numerically modeled in FEMLAB, a finite element modeling suite, using the steady-state coupled physics modeling approach outlined previously using (5.1) through (5.12). The highly non-linear solver regime provided in FEMLAB was used for modeling due to the non-linearity of the charge transport and Navior-Stokes equations. The convergence criterion was set to a relative tolerance of 1.0E-6. The UMFPACK linear equation solver was chosen for its highly efficient direct solution of asymmetric systems, as well as general robustness.

5.5 Validation of EHD air mover model using wire-to-grid channel geometry

The wire-to-grid channel geometry was developed as a test bed in which to validate the EHD air mover numerical model. The wire-to-grid channel geometry was selected for its ease of modeling and fabricating as well as allowing for straightforward experimental measurement of EHD blower current and airflow, which was used to validate the numerical model. This section introduces the wire-to-grid channel EHD blower concept, then presents individually the experimental and numerical model

designs, numerical results, and concludes with a comparison and discussion of the numerical and experimental results.

5.5.1 Wire-to-grid channel EHD blower geometry concept

The wire-to-grid channel EHD blower geometry consists of three major components, a corona electrode, collecting mesh, and collecting side walls, as shown in Figure 5.1. The corona wire consists of a conductive wire with a constant radius of curvature along its length which is centered between and parallel to two conductive plates that make up the collecting side walls of the channel. A collecting mesh consisting of parallel conductive wire electrodes is placed within the channel downstream and parallel to the corona electrode and orthogonal to the airflow path. The electrodes in the collecting mesh are spaced close together such that the electric field intensity and gradient at their surface is reduced below the corona onset requirement, while at the same time creating only a low pressure drop to the airflow passing through the mesh.

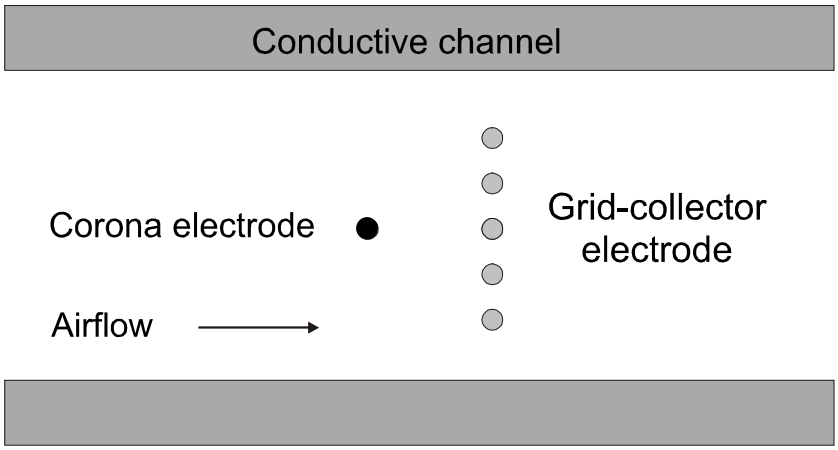

Figure 5.1. *Wire-to-grid channel EHD blower geometry concept, not drawn to scale.*

Physical measurement of average air velocity at the output of the channel is relatively simple since the air velocity is fairly uniform across the output of the channel, which would not necessarily be the case if the grid collector electrodes were replaced with a single or multiple rod of larger diameter. A channel geometry was chosen such that it enables simple measurement of the total volume of airflow produced from the EHD blower, which would be difficult in the case of an open system without a channel to confine the flow. The conductive channel geometry allows for maximum collection of

ions produced by the corona discharge by creating a large surface over which ion collection can occur, thus increasing the accuracy of corona current measurements during operation.

By utilizing a conductive channel, the boundary conditions at the surface of the channel are simplified. Had a dielectric surface been used for the channel, there would be ion deposition on the channel wall creating a surface charge that would have to be accounted for in the numerical model. Although such modeling is possible, it adds additional complexity and sources of error, which should be minimized for model validation purposes. The geometry was made symmetric about the horizontal plane parallel to and centered between the channel walls. The symmetry allows for solution of the numerical model by only solving half the domain space, reducing solution computation requirements and thus solver time.

5.5.2 Experimental model design and test procedure

5.5.2.1 Experimental model design

The wire-to-grid channel EHD blower geometry described in section 5.5.1 is shown to scale in Figure 5.2. The top and bottom collecting plates were constructed of flat rectangular aluminum bar stock with a cross-section width and length of 5 mm and 34 mm respectively, and an overall length of 30 cm. The corona and collecting electrode wires were held in place 10 mm from the outlet plane of the device by wire spacing structures attached to either end of the top and bottom collecting plates. The wire spacing structure was made from a PCB board ensuring accurate mutual and absolute placement of the corona and collecting wire electrodes relative to themselves and the collecting plates. Fourteen 100 um diameter tungsten collecting wires were strung 1 mm apart on center from the top to the bottom of the channel made by the collecting plates, creating a total channel gap of 15 mm. A single tungsten corona wire electrode of the same diameter was placed parallel to the collecting wires and centered between the collecting plates, with a total coronating wire length of 27.7 centimeters. The setup was designed to allow for two possible positions of the corona wire from the collecting wires of 5 mm and 9 mm. To ensure proper tensioning of the corona wire during operation, a spring based wire

tensioning system was used at one end of the channel. Proper tensioning of the corona wire electrode is critical in order to avoid oscillations of the wire during operation, and minimize bowing of the wire under electrostatic forces, both of which would modify the discharge characteristics of the device, reducing the congruency of the experimental and numerical models.

A dielectric termination transition block was used to minimize sharp E-field edge effects at the termination of the corona wire on either end of the channel and prevent premature dielectric breakdown between corona and collector electrodes. The termination transition blocks were fabricated from polycarbonate, consisting of a simple rectangular block with a single 3 mm hole bored through it in which the corona wire electrode was passed through and centered within.

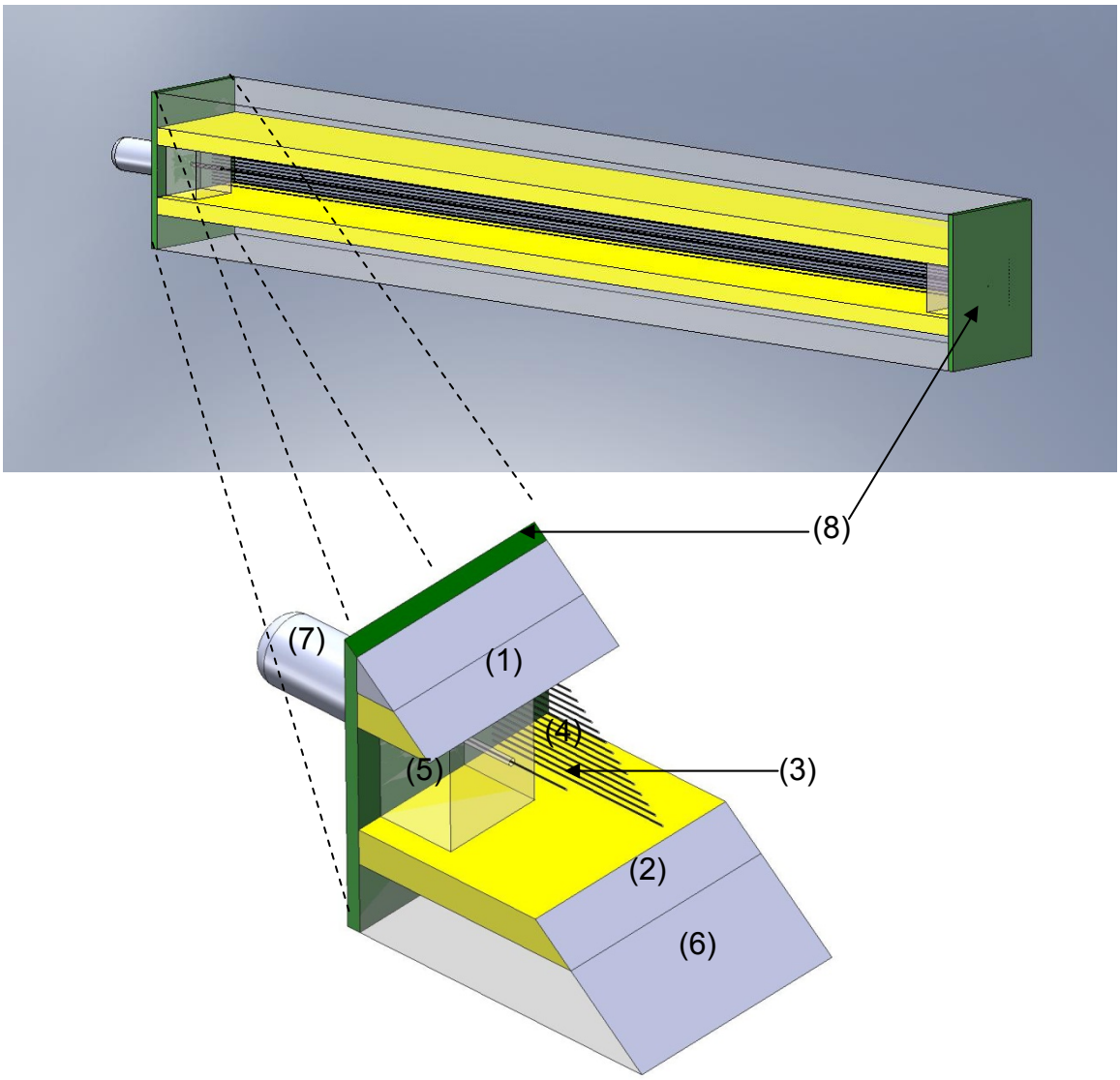

Figure 5.2. *3D CAD drawings of the wire-to-grid channel experimental model drawn to relative scale. Full model shown on top with cut away image shown below. 1) upper collecting electrode plate, 2) lower collecting electrode plate, 3) corona wire electrode, 4) collecting wire array electrodes, 5) dielectric corona wire termination transition blocks, 6) dielectric support structure, 7) corona wire electrode tensioning system, 8) wire spacing structure.*

A cross section of the wire-to-grid channel model design and critical design parameter are shown in Figure 5.3 and Table 5.1. The physical wire-to-grid channel model is shown in Figure 5.4.

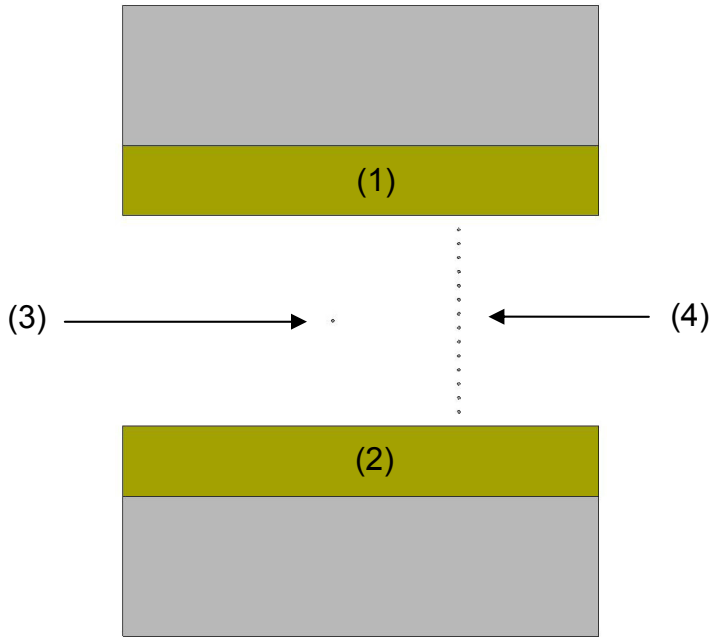

Figure 5.3. *2D cartoon cross section of wire-to-grid channel experimental prototype drawn to relative scale: 1) upper collecting electrode plate, 2) lower collecting electrode plate, 3) corona wire electrode, 4) collecting wire array electrodes.*

Table 5.1. *Experimental wire-to-grid channel prototype design parameters*

Static device parameter	**Value**
Channel height	15 mm
Active corona wire and channel length	277 mm
Channel depth	34 mm
Distance from collecting wire electrodes to output	10 mm
Corona electrode to channel electrode separation	7.5 mm
Vertical separation of individual collecting electrode wires	1 mm
Number of corona electrodes	1
Number of collecting wire electrodes in wire grid	14
Wire diameter of collecting grid wire electrodes	100 μm
Corona electrode wire diameter	100 μm
Variable device parameter	**Value**
Corona wire to collecting wire electrodes separation	5 or 9 mm

5.5.2.2 Experimental test setup and procedure

Current-voltage and output air velocity profile measurements were taken from the wire-to-grid channel EHD blower prototype using the experimental test setup shown in Figure 5.4. In operation, the corona electrode of the prototype was connected to the output of a positive polarity high voltage power supply, and the collecting plates and wires were connected to ground. Voltage and current measurements on the corona

electrode were measured using the built in current and voltage measurement capabilities of the Spellman SL high voltage power supply. All measurements were conducted in ambient air at room temperature and pressure.

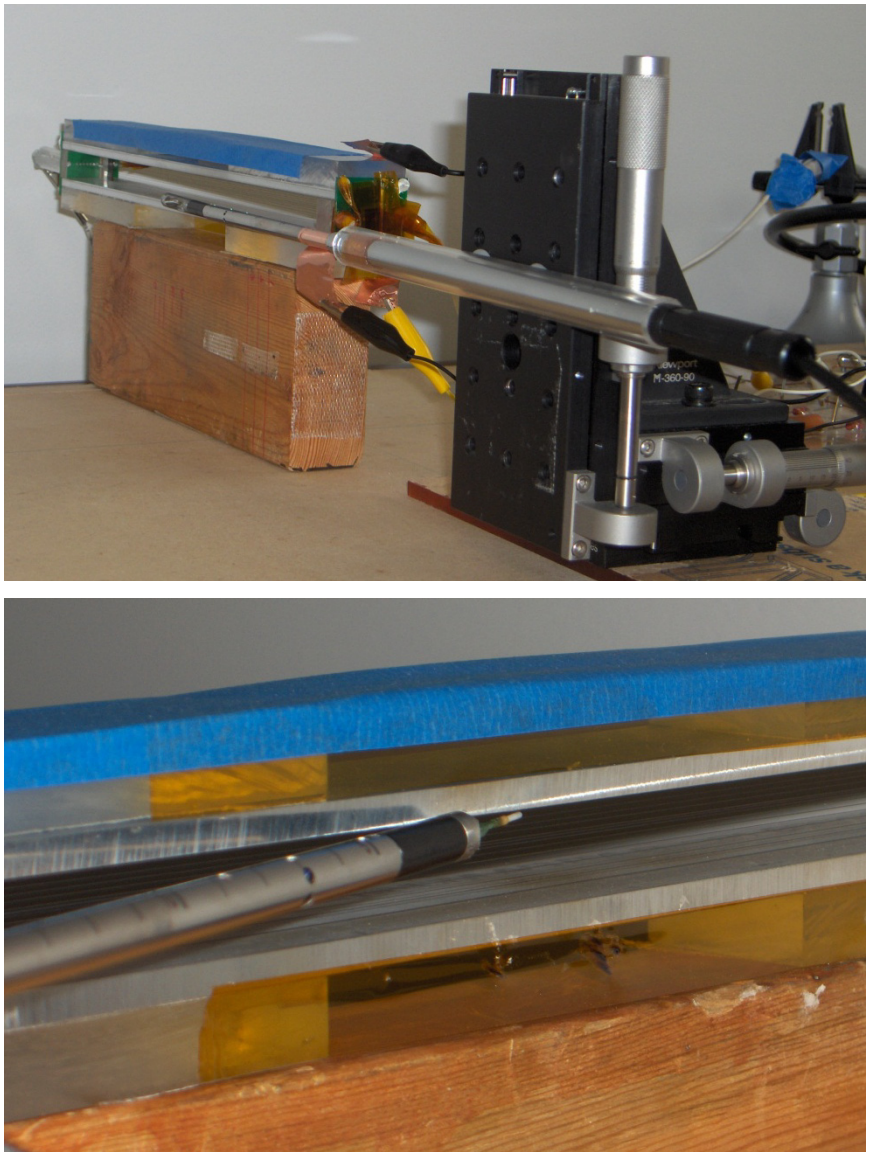

Figure 5.4. *Top shows picture of the experimental test setup for the wire-to-grid channel prototype current-voltage and airflow profile measurements. Prototype wire-to-grid channel EHD blower and stand, hot wire anemometer, and XYZ precision stage are shown, with high voltage DC power supply with and DAQ PC out of picture. Bottom shows close-up view of the channel output with hot wire anemometer.*

Airflow measurements were taken at the midpoint along the length of the prototype such that any fluid dynamic edge effects from the side walls at either end

would not impact the air velocity profile or magnitude at the point of measurement. At the midpoint of the device the airflow measurements were taken immediately inside the output of the device, and were taken from 1.5 mm from the top of the channel to 1.5 mm from the bottom of the channel at one or 1.5 mm increments. Measurements were taken no closer than 1.5 mm from the collecting plates due to size restriction of the anemometer probe. For each measurement point ten data samples were collected and averaged. Air velocity measurements were taken with a TSI Velocicalc Plus hotwire anemometer, and logged to a PC using a custom LabView program.

Although not shown in Figure 5.4, a solid wall separator was placed above the EHD blower prototype such that it would eliminate any possible direct recirculation path between the input and output of the device. However, it was found that the wall had no measurable impact on the air velocity profile or magnitude and was discarded. Smoke stream studies were also conducted to confirm that no direct recirculation was occurring around the top or sides of the device.

Current-voltage measurements and output air velocity measurements were taken for two corona wire to collecting wire array electrode separations, over a range of corona operating voltages. A detailed test procedure is shown in Table 5.2.

Table 5.2. *Experimental model test corona electrode operating voltages.*

Corona wire electrode diameter (um)	Corona to collector wire array electrode separation (mm)	Corona to collector electrode potential (kV)
100	5	4.5, 5 , 5.5, 6, 6.5, 7
	9	4.5, 5 , 5.5, 6, 6.5, 7, 7.5, 8

5.5.3 Numerical model solution domain and results

5.5.3.1 Numerical solution domain and boundary conditions

The wire-to-grid channel EHD blower numerical simulation space, subdomains, and boundaries, are shown in Figure 5.5, and the same space with mesh elements is shown in Figure 5.6. A single subdomain was used for the entire simulation space, which made up the inside of the channel, where the electrical, charge transport, and fluid

dynamic domain equations were solved, using the subdomain modeling parameter values shown in Table 5.3.

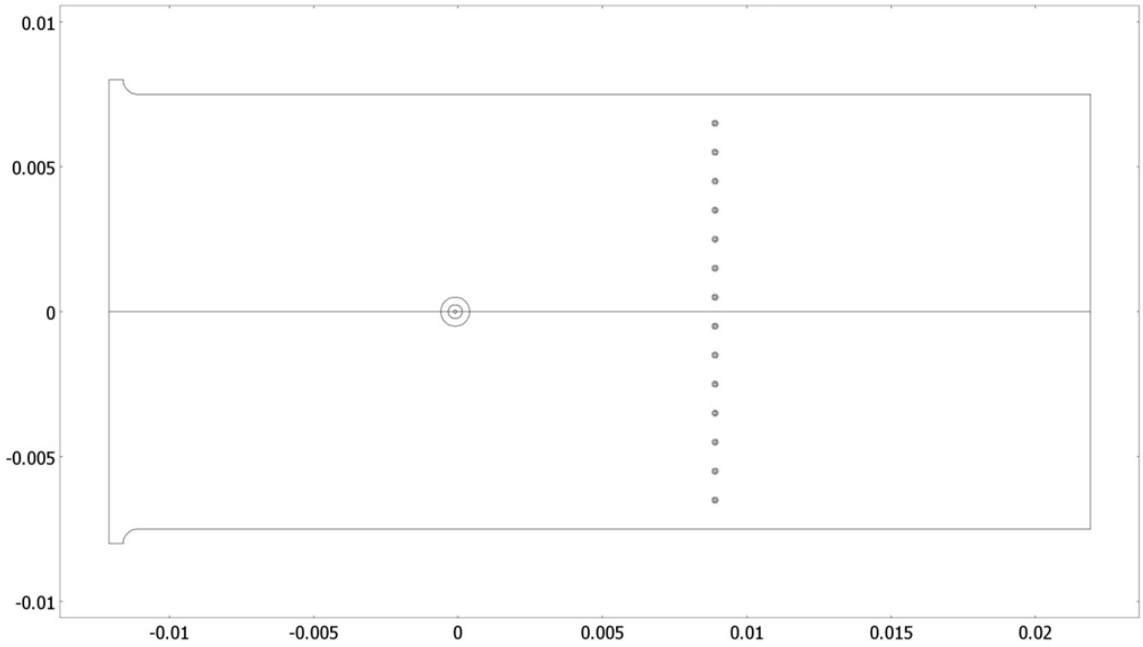

Figure 5.5. *Numerical solution domain of wire-to-grid channel EHD blower geometry. The corona electrode is represented by the smallest of the three concentric circles centered at (0,0). The two larger concentric circles were used to define mesh refinement but do not represent actual boundaries within the model.*

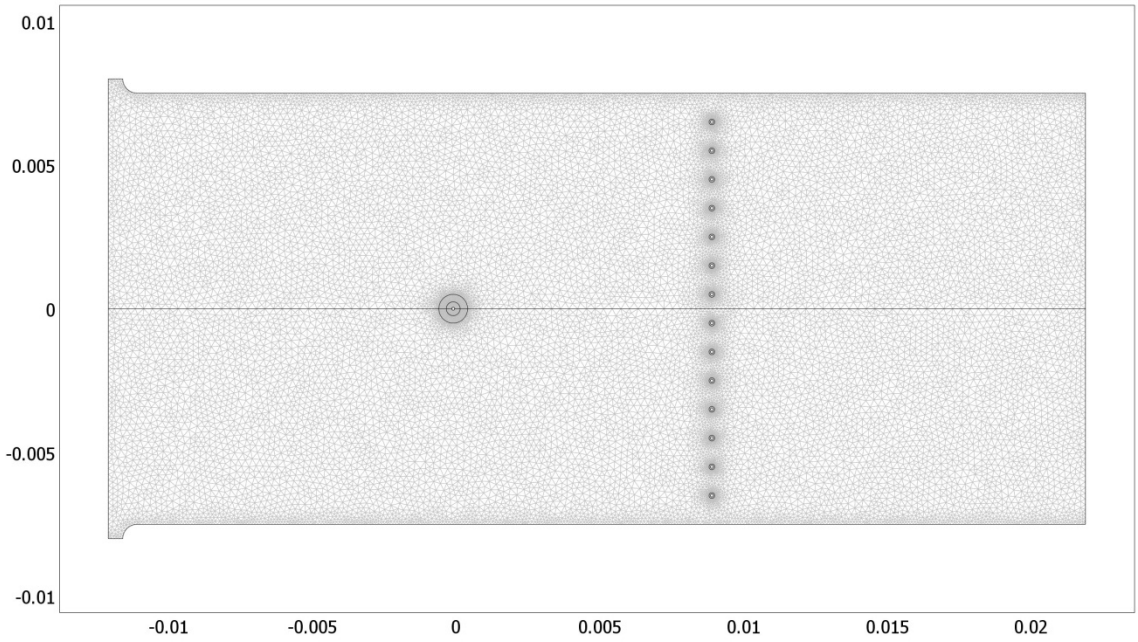

Figure 5.6. *Numerical solution domain of wire-to-grid channel EHD blower geometry, showing mesh elements, and distribution of mesh element density. Approximately 44 thousand mesh elements were used, with the highest density in areas of high electric field strength and space charge density.*

Table 5.3. *Sub-domain modeling parameter values used in FEM modeling.*

Modeling parameter	**Value**
Relative dielectric permittivity of air, ε_r	1
Charge diffusion coefficient, D	5.3×10^{-5} m^2/s
Ion mobility coefficient, μ_E	1.77×10^{-4} m^2/(Vs)
Density of air, ρ_{air}	1.23 kg/m^3
Dynamic viscosity of air, μ	1.8×10^{-5} Ns/m^2
Corona electrode to channel electrode separation	7.5 mm
Corona electrode to grid collector minimum separation	9 and 5 mm
Corona electrode radius	50 μm
Collecting grid wire electrode radius	50 μm

Boundary conditions applied to the numerical model, are shown in Table 5.4 and are as follows. For electrostatics, a constant positive DC voltage V_0 was applied to the corona wire surface, and zero volts were applied to the channel wall and surface of all collecting grid wires. The inlet and outlet boundaries were set to ground. For charge

transport, a space charge surface density is applied to the surface of the corona wire electrode, calculated using (5.8) to (5.10). A zero diffusive flux condition is imposed on all boundaries except for the external surface of the corona wire, where a charge density is imposed. The validity of this assumption is justified by the fact that the diffusion term is very small compared to the conduction term in (5.4) and can be set to zero at the boundaries with negligible effect [102, 129].

For fluid dynamics, a no-slip condition is applied to the surface of the channel, collecting grid wires, and corona electrode. Normal flow with pressure prescribed from Bernoulli's equation was used at the channel input air boundary, and an outlet-flow condition and zero pressure was prescribed at the outlet air boundary.

A schematic of the numerical simulation space along with the modeling mesh is shown in Figure 5.6. The numerical simulation space was descretized in approximately 44,000 triangular elements, with the element density being highest in the region around the corona electrode and in the areas of relative high space charge density and electric field intensity.

Table 5.4. *Boundary conditions used in FEM modeling.*

Boundary	Electrostatics	Charge transport	Fluid dynamics
Channel wall and collecting-grid wires	grounded	Charge gradient = 0	No-slip
Corona electrode	Voltage V_e and electric field intensity E_e	Surface charge density solved by model	No-slip
Channel inlet air boundaries	Grounded	Zero diffusive flux	Normal flow with pressure prescribed from Bernoulli's equation
Channel outlet air boundary	Grounded	Zero diffusive flux	Outlet-flow condition and zero pressure

5.5.3.2 Wire-to-grid channel numerical results

Numerical simulations results for the wire-to-grid channel geometry are presented for device electric field profile, charge distribution, air velocity field, onset voltage, current-voltage curve, and output average air velocity and profile. Surface plots of the investigated model for two separate corona to collection grid electrode separation are

shown in Figure 5.7 through Figure 5.12, and display the solutions to the three coupled physical phenomena modeled: electrostatics, charge transport, and fluid dynamics. The plots shown in Figure 5.7 through Figure 5.9 and Figure 5.10 through Figure 5.12 were generated with a corona to collector electrode spacing of 9 mm and 5 mm respectively and electric potential differences of 8 kV and 7 kV respectively.

The electric potential map, Figure 5.7, has the highest electric potential at the surface of the corona electrode with electric potential decreasing in magnitude from the edge of the corona electrode to the channel walls and collecting grid. The space charge, Figure 5.8, is distributed with highest density near the corona electrode and decreasing in all directions, with the charge density greater in the direction of the collecting wires than in the direction of the channel input. Charge flux stream lines are shown in white in Figure 5.8, showing greater charge flux in the direction of the collecting grid than towards the channel input. The traveling ion stream entrains airflow in the direction of the wire grid as shown in Figure 5.9, with the greatest air velocities in the region of greatest space charge density and field intensity around the corona electrode. For all surface maps shown in this section, the largest displayed magnitude values on the surface map are shown in red, and the lowest in dark blue, with other values following the color spectrum between red and blue.

For a 9 mm corona electrode to collecting grid spacing, the majority of the ion current travels to the top and bottom collecting electrodes rather than to the collecting grid, which is shown in Figure 5.8, by the large number of charge flux lines between the corona wire and the top and bottom plates. This is due to the fact that the electric field is stronger between the plates and the corona wire than between the grid and the corona wire, which is caused by the relative placement of the wire to the collecting electrodes and the potential on the electrodes. Since EHD driven airflow is induced by the net body force created by the electric field on the space charge within the fluid, it is the asymmetry in the applied body force in this case that creates the net air flow. Thus, in the 9 mm case, a large amount of the force exerted on the fluid is not contributing to the net flow. If the corona wire to collecting grid distance is reduced to 5 mm the asymmetry is increased, or rather there is an increase in ratio of forces in the direction of flow vs. those opposite and

orthogonal to the direction of flow. With a higher ratio of forces in the direction of flow, the 5 mm case would be expected to generate a greater flow rate than the 9 mm case, which is correctly predicted by the model and can be seen by comparing the velocity field surface maps in Figure 5.9 and Figure 5.12 and the average outlet velocities in Figure 5.16. Notably, even though the input power of the 5 mm case at 7 kV is 7/8 that of the 9 mm case at 8 kV, a higher maximum velocity and average velocity is seen in the 5 mm model.

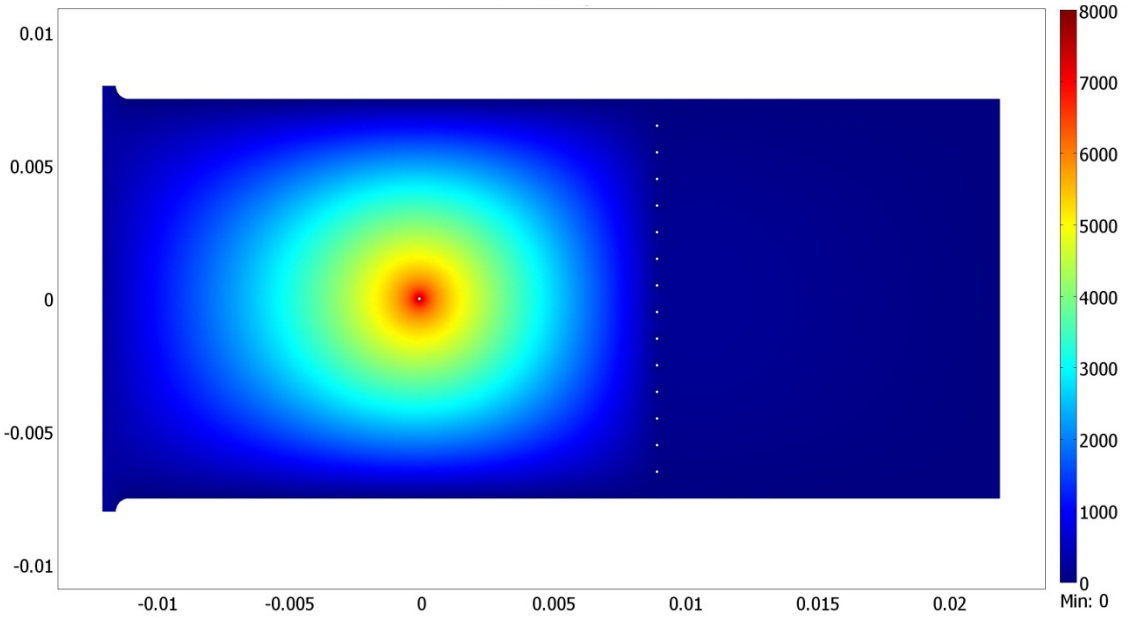

Figure 5.7. *Electric potential as surface map with units in volts for 9 mm corona to collector electrode separation and corona electrode voltage of 8 kV. Simulation space dimensions in meters.*

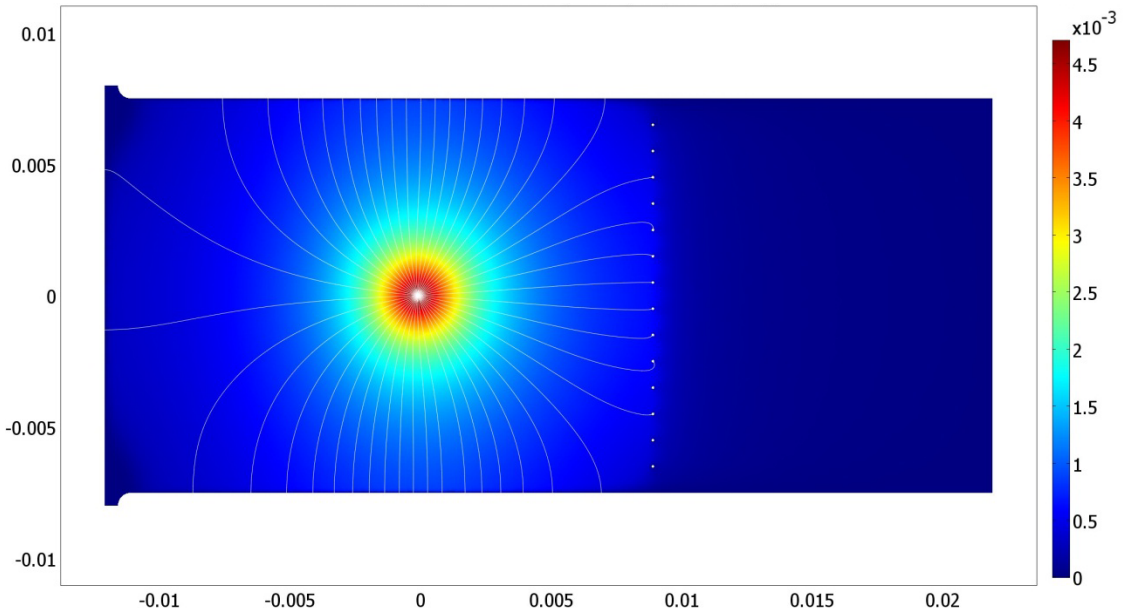

Figure 5.8. *Space charge density as surface map with units in C/m3 and space charge flux lines for 9 mm corona to collector electrode separation and corona electrode voltage of 8 kV. Simulation space dimensions in meters.*

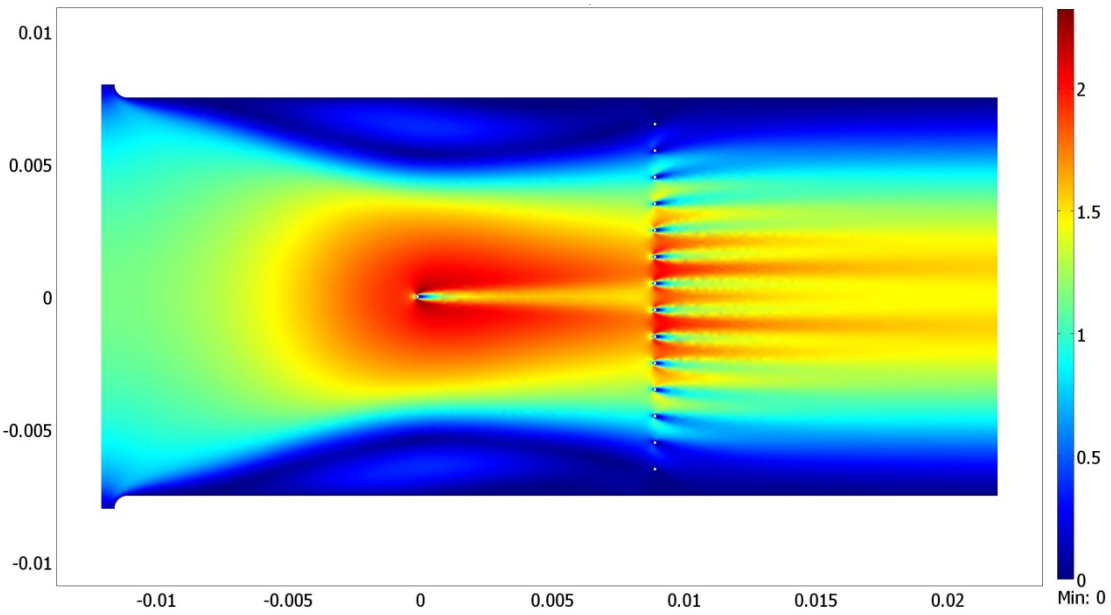

Figure 5.9. *Air velocity field as surface map with units in m/s for 9 mm corona to collector electrode separation and corona electrode voltage of 8 kV. Simulation space dimensions in meters.*

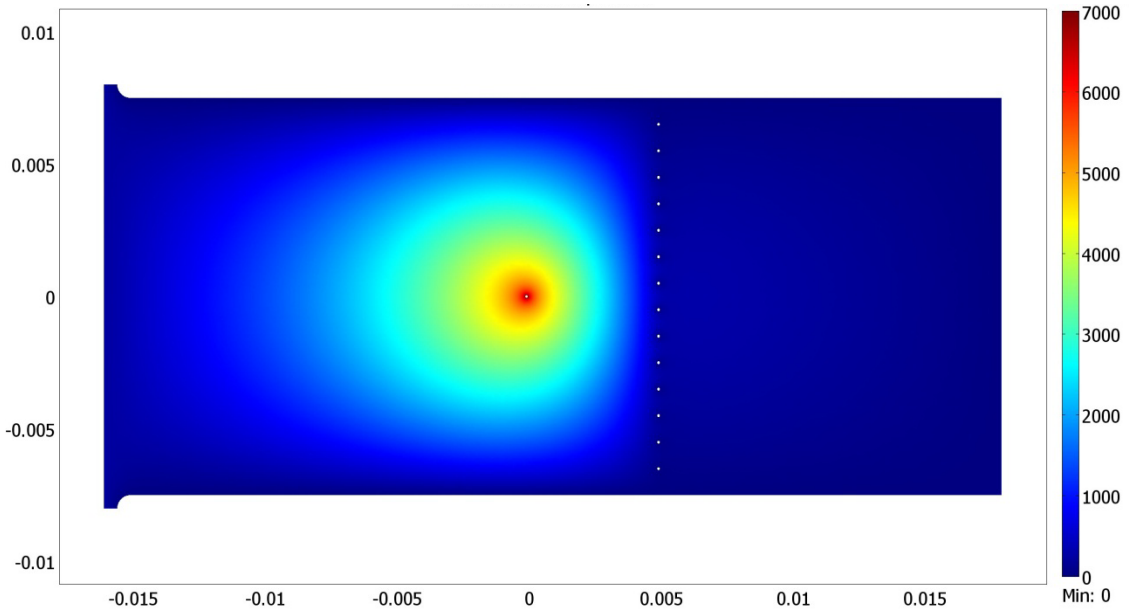

Figure 5.10. *Electric potential as surface map with units in volts for 5 mm corona to collector electrode separation and corona electrode voltage of 7 kV. Simulation space dimensions in meters.*

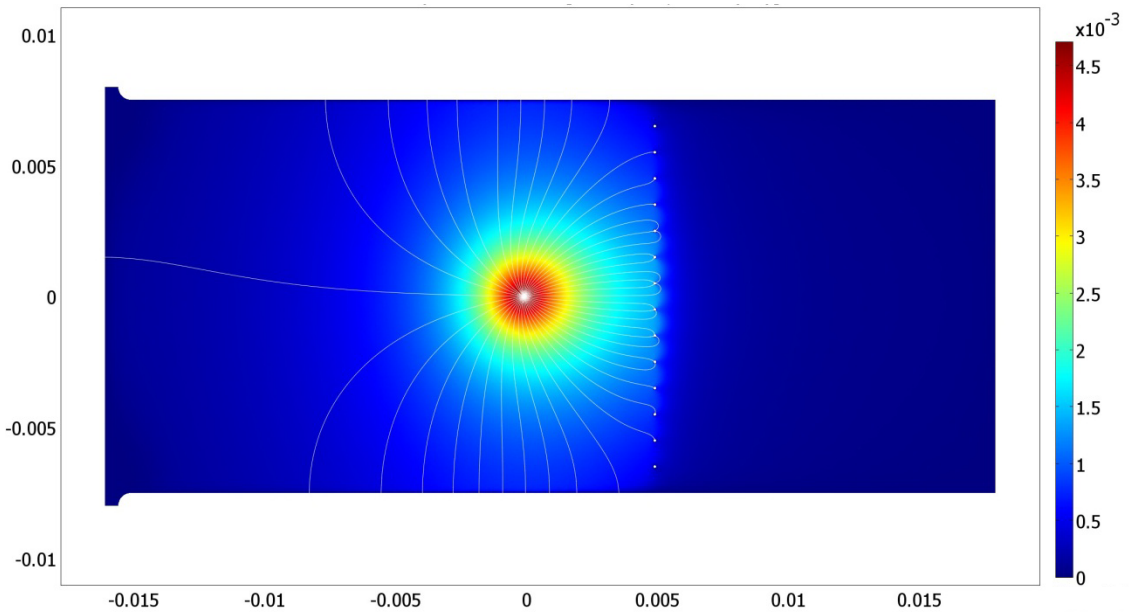

Figure 5.11. *Space charge density as surface map with units in C/m3 and space charge flux lines for 5 mm corona to collector electrode separation and corona electrode voltage of 7 kV. Simulation space dimensions in meters.*

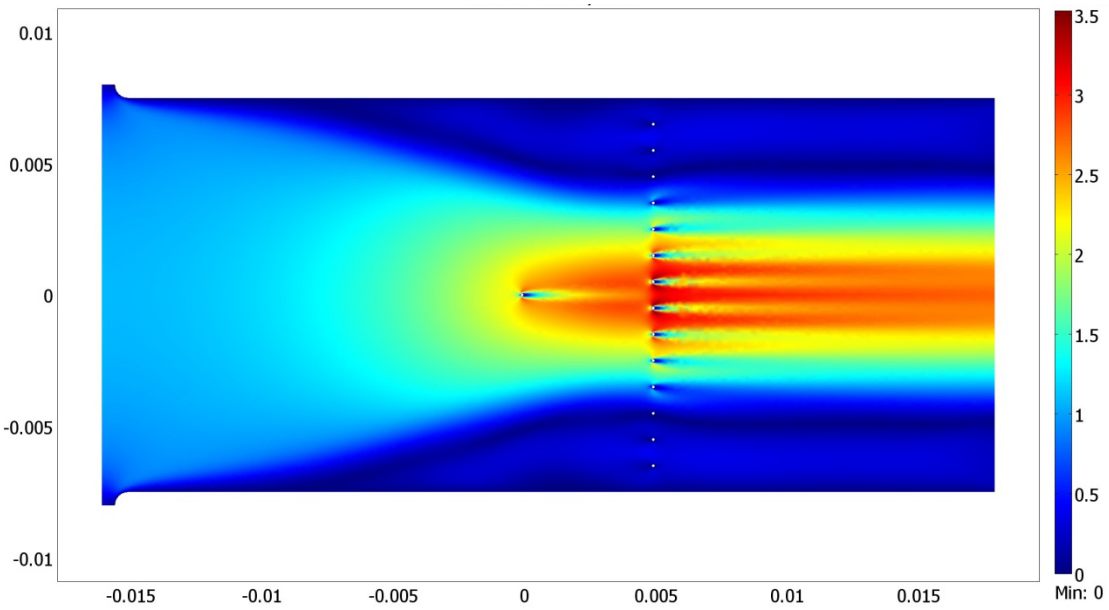

Figure 5.12. *Air velocity field as surface map with units in m/s for 5 mm corona to collector electrode separation and corona electrode voltage of 7 kV. Simulation space dimensions in meters.*

The corona ion current, I_c, leaving the ionization zone can be calculated by multiplying the ion current density, (5.3), by the area of the wire surface assuming the electric field at the surface of the corona electrode is equal to, E_p. A one-centimeter corona wire length was assumed for the current-voltage plots shown in Figure 5.13. The corona onset voltage V_0 for the 9 mm and 5 mm separations were 4.04 kV and 3.90 kV respectively. As expected, a lower onset voltage and larger dI_c/dV_e was predicted for the 5 mm separation, due to the larger field enhancement factor from the smaller air gap in the 5 mm case.

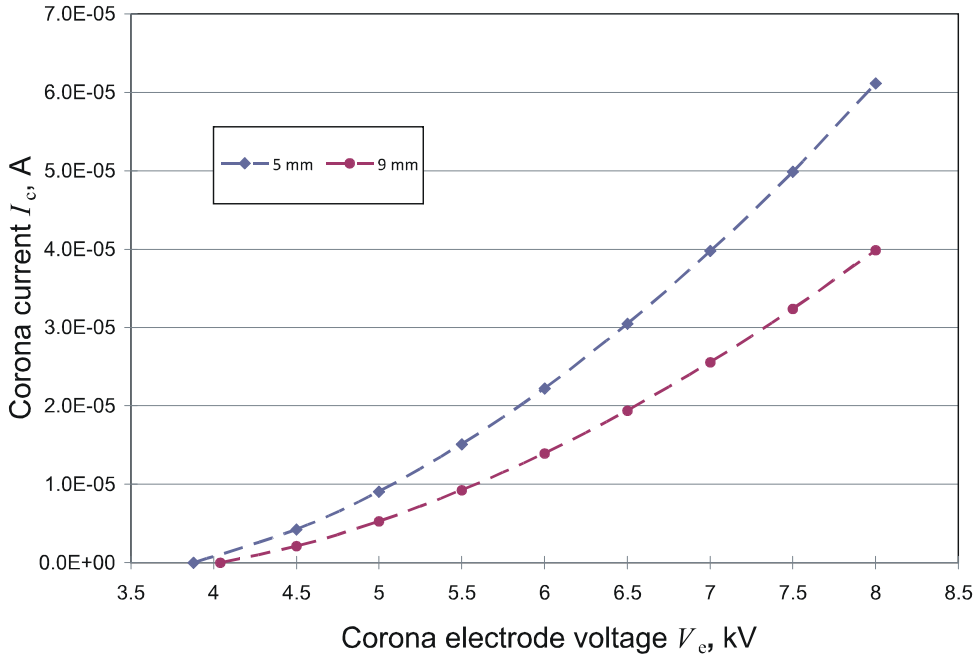

Figure 5.13. *Numerical corona current I_c vs. applied voltage V_e curves for 9 mm and 5 mm corona to collector grid electrode separations, assuming a 1 cm active corona wire length.*

The air velocity profile taken at the outlet of the device channel for 9 mm and 5 mm corona to collection grid separations, are shown respectively in Figure 5.14 and Figure 5.15 for corona electrode voltages from 4.5 kV to 8 kV with steps of 0.5 kV. (Notably, the model does not attempt to predict dielectric breakdown of the air gap, and in the 5 mm experimental model it was found that the corona current became unstable due to streamer activity at 7.5 kV, with breakdown occurring near 8 kV. Modeled EHD current and air flow results have been included for 7.5 kV and 8 kV for comparison of trends in this section, but should not be used for other purposes.)

Both the maximum air velocity magnitude at the outlet, Figure 5.14 and Figure 5.15, and average outlet air velocity, Figure 5.16, is shown to increase approximately linear with increasing operating voltage, which is consistent with experimental studies presented later in this thesis and results presented in literature [3]. The average air velocity for the 9 mm setup increases close to linearly with applied voltage from 4.5 kV to 8 kV, however, the 5 mm case is shown to increase at one slope between 4.5 kV and 5 KV and then roughly another slope from 5.5 kV to 8 kV. This abrupt change in slope can

be attributed to the recirculation zones that appear at either side of the channel in the 5 mm case at voltages of 5.5 kV and above, which reduce the net flow output slightly due to the recalculating flow. Comparing the 9 mm and 5 mm corona to collecting grid spacing output profiles, two significant differences exist, namely velocity magnitude and outlet profile shape. The outlet velocity magnitude is greater in the 5 mm case than the 9 mm case, which is due to two factors, the first because at given voltage a larger total body force is applied to the air for reasons described above, and the second because the 5 mm case has a greater ratio of forces being applied in the direction of flow. The larger velocity magnitudes can be attributed to a combination of these two factors. The difference in the outlet velocity profile shape as well as the recirculation regions at the channel edges in the 5 mm case, Figure 5.15, are due in part because of the focused body force generated by the 5 mm case, in comparison to the more diffuse body force generated in the 9 mm case, and also because the overall greater velocity magnitudes, which cause the flow to take a more exaggerated parabolic shape due to viscous forces at the side walls.

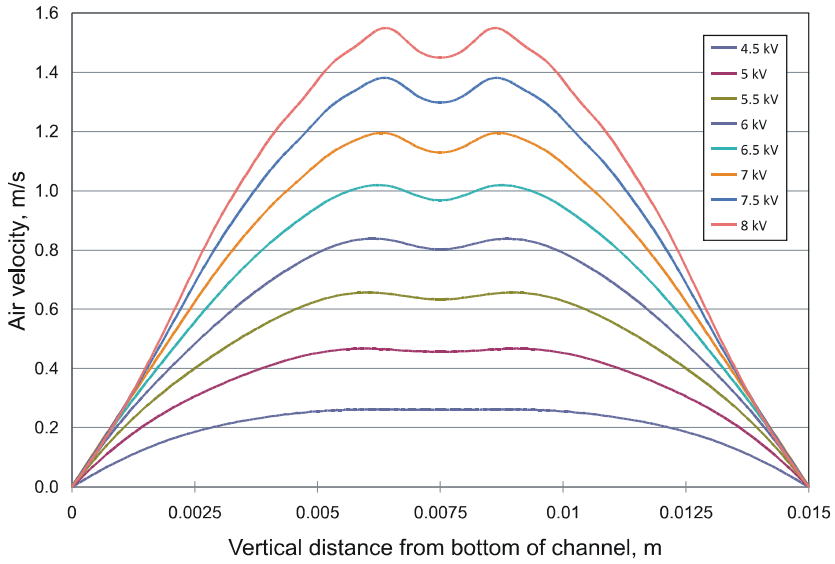

Figure 5.14. *Numerical air velocity profile curves taken at the outlet of the channel for a 9 mm corona to collector grid electrode separation. Curves for applied corona electrode voltages of 4.5 kV to 8 kV with steps of 0.5 kV.*

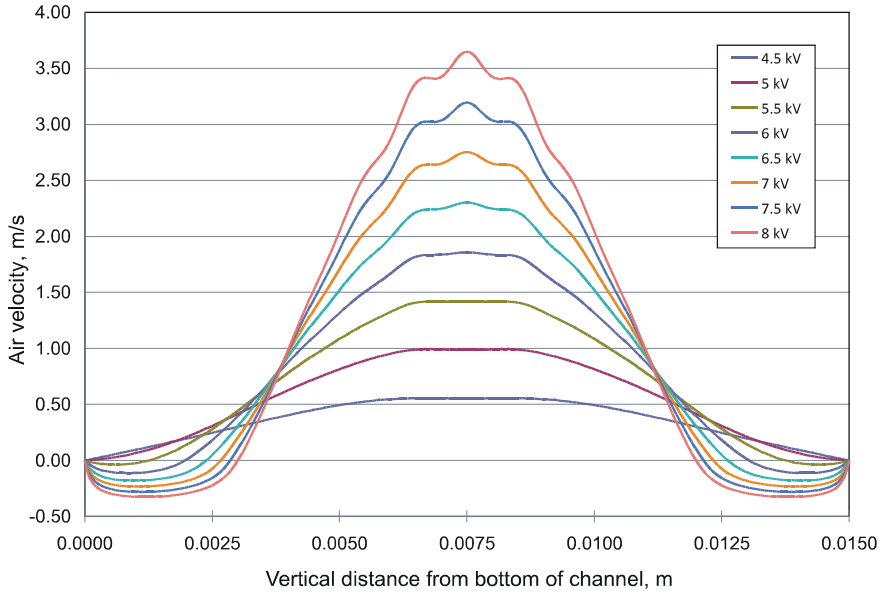

Figure 5.15. *Numerical air velocity profile curves taken at the outlet of the channel for a 5 mm corona to collector grid electrode separation. Curves for applied corona electrode voltages of 4.5 kV to 8 kV with steps of 0.5 kV.*

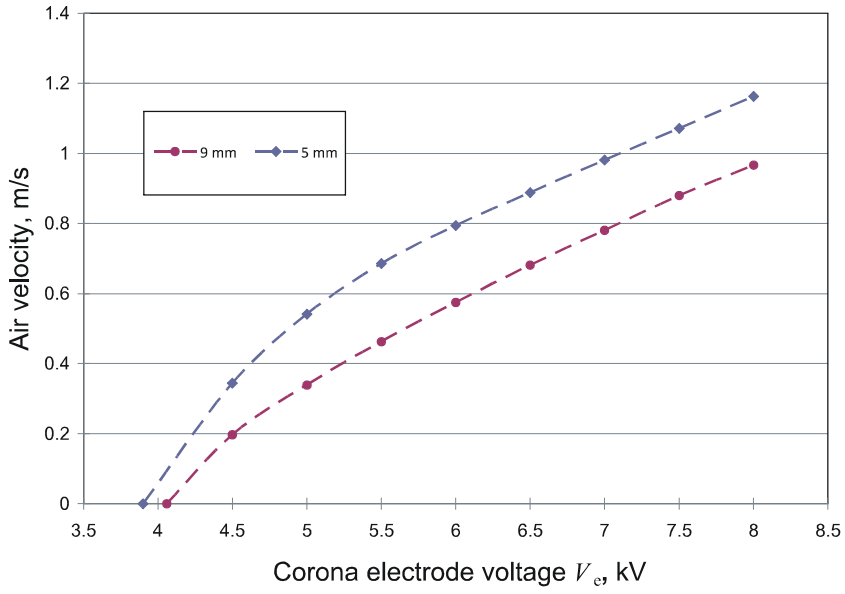

Figure 5.16. *Numerical average air velocity at the outlet of the channel as a function of applied corona electrode voltage for 9 mm and 5 mm corona to collector grid electrode separations.*

5.5.3.3 Summary of numerical test bed results

The numerical EHD modeling test bed created around a wire-to-grid channel EHD blower geometry, for two different corona wire electrode to collecting grid electrode separations, was successfully used to predict corona onset voltages, current-voltage curves, outlet airflow profiles and average velocities that will be compared against an equivalent wire-to-grid channel experimental EHD blower model in the following section. Beyond, predicting reasonably easily verifiable results such as outlet air velocities and corona currents, the model enables analysis of air gap electric field profile, space charge distribution and flux, and airflow patterns. All of which allow for "designer insight" into device operation and further improvement and optimization, which is what makes such a model a powerful and necessary tool in the development of next generation EHD technologies and devices.

5.5.4 Comparison and discussion of numerical and experimental wire-to-grid channel results

This section presents a comparison of results from the wire-to-channel EHD blower numerical model with results obtained from the wire-to-channel experimental model. In general, numerical results were found to agree well with experimental results, and are presented in the following order: corona onset voltage, current-voltage curves, average outlet airflow, and outlet air velocity profiles.

Experimental and numerical results for corona onset and current-voltage curves were found to be in good agreement with each other over the entire unipolar operating range of the experimental model, as shown in Figure 5.17. Notably, the unipolar operating range is being defined in this text as the EHD blower operating voltage range in which a stable corona exists and only ions of a single charge polarity exist in the drift zone. The unipolar range does not include the operating range near air gap breakdown where corona streamers and other pre arc bipolar plasmas exist. All experimental values shown in this section fall within the unipolar operating range of the device, since operating above that range creates ion neutralization within the drift region and opposing

EHD forces, which significantly decrease airflow, while at the same time the larger total current increase operating power.

In order to compare corona onset potentials between the numerical and experimental model, the criteria to determine corona onset has to be established. For this study, corona onset was defined as the operating voltage at which a total corona current of two microamperes was measured or calculated for the experimental and numerical models respectively. The value of two microamperes was chosen since it represented the lower bound of accurate current measurement capabilities by the high voltage power supply used. Numerical corona current calculations were conducted assuming the same coronating corona electrode length as the experimental model, which was 27.7 centimeters.

A comparison of the predicted vs. measured corona onset voltages for both the 9 mm and 5 mm corona electrode to collector grid electrode separations showed that the predicted corona onset voltages were within one percent of the measured values, with predicted and measured values being respectively 3.9 kV vs. 3.88 kV, and 4.04 kV vs. 4.06 kV for the 5 mm and 9 mm separations respectively.

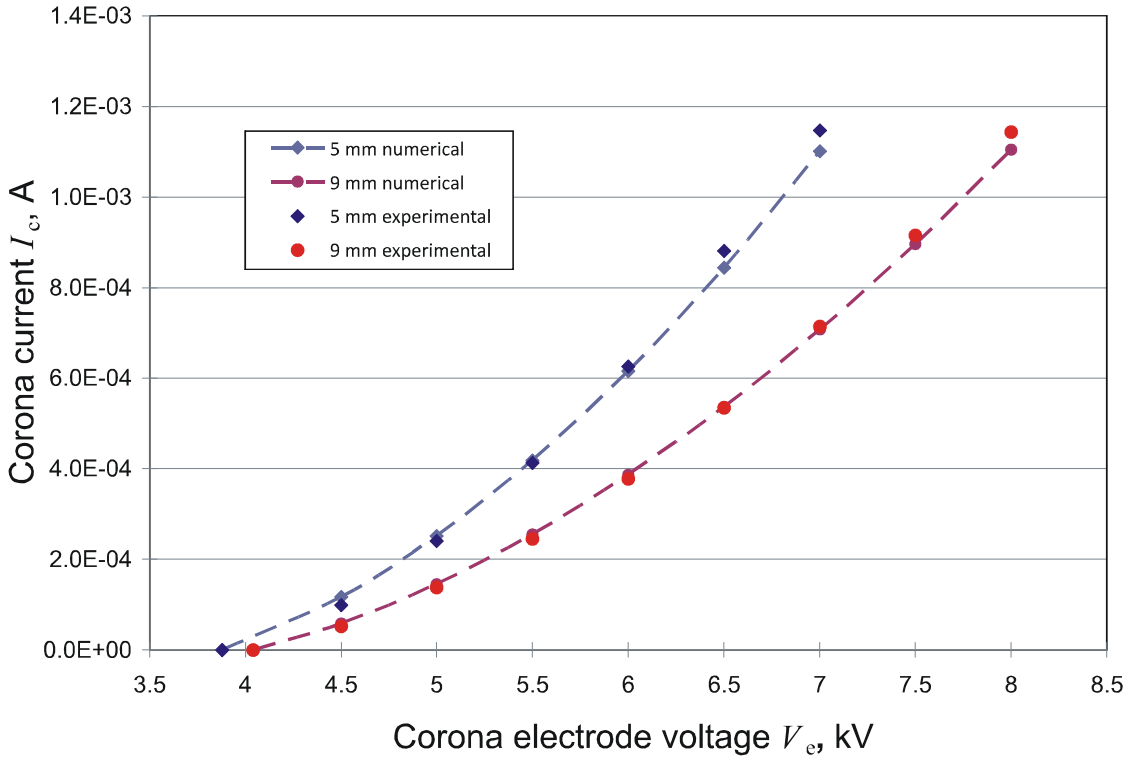

Figure 5.17. *Comparison of numerical and experimental corona current Ic vs. applied voltage V_e for corona electrode to collecting grid electrode spacing's of 5 mm and 9 mm. Numerical values for 9 mm and 5 mm are shown in purple circle and light blue diamond dotted lines respectively. Experimental values for 9 mm and 5 mm are shown respectively in red circles and dark blue diamonds.*

Corona current I_c was measured and calculated for discrete operating voltages at 0.5 kV intervals from 4.5 kV until 8 kV or until an operating potential was reached that had evidence of corona streamers or arcing. The maximum operating voltage before corona streamers was found for the 5 mm separation was 7 kV, and the 9 mm separation maintained a unipolar regime throughout the range up to 8 kV.

Predicted corona current I_c was found to agree well with experientially measured values for both 5 mm and 9 mm separations, with the maximum error for all points being less than five percent, for the 9 mm and 5 mm separations. The error rate is seen to be slightly higher for the 5 mm case than the 9 mm case, which may be due to the greater nonuniformity of the electric filed for the 5 mm case. The model asserts a constant surface charge density around the surface of the corona electrode, where as in reality the space charge density would vary as a function of the field intensity near the wire.

However, the model partly compensated for this by adjusting the surface charge until the average electric field at the surface is equal to E_e, rather than all points being equal to E_e. This causes a higher field to exist on the surfaces that would ideally have a higher charge density, and a lower field in places that would ideally have a lower charge density, thus the resulting charge flux from the surface takes into account the nonuniform field intensity around the corona electrode. Although this method appears to be a decent approximation as shown by the results in Figure 5.17, it is likely the cause of the larger error seen in the 5 mm case.

Numerical and experimental average airflow velocity measurements across the outlet of the channel for discrete operating voltages from corona onset to 7 kV for the 5 mm separation, and to 8 kV for the 9 mm separation are shown in Figure 5.18. In order to properly compare the average outlet airflow velocity from numerical calculations to the experimentally measured values, the average outlet numerical velocities were averaged over the same vertical channel region over which the experimental measurements were taken. Specifically, the numerical velocity values were averaged from 1.5 mm from the bottom of the channel up to 1.5 mm from the top of the channel, which was the same range over which the experimental measurements were taken. Notably, by removing the upper and bottom extremes of the channel velocity values from the average calculation, the adjusted average value is increased, which is seen when comparing values from Figure 5.18 to the full outlet channel velocity found in Figure 5.16. Therefore, the experimental average values presented in Figure 5.18 are similarly artificially high, and the actual full channel average outlet airflow velocities should be lower by a similar percentage as seen between values shown in Figure 5.18 and Figure 5.16.

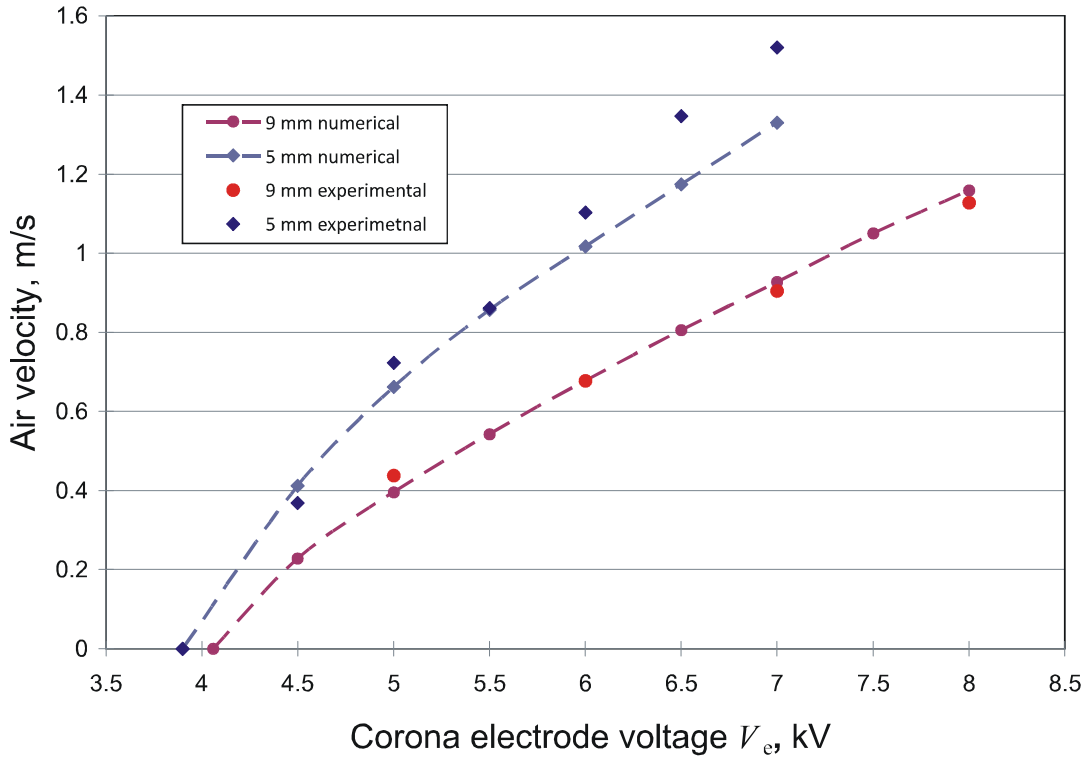

Figure 5.18. *Comparison of numerical and experimental average output air velocity vs. applied corona electrode voltage V_e for 9 mm and 5 mm corona electrode to collector grid electrode separations. Numerical and experimental air velocity values displayed were averaged over the center vertical 12 mm of the outlet of the channel, due to limitations in the experimental probe measurement capabilities. Numerical values for 9 mm and 5 mm are shown in purple circle and light blue diamond dotted lines respectively. Experimental values for 9 mm and 5 mm are shown respectively in red circles and dark blue diamonds.*

Good agreement is shown between the predicted and measured values for the 9 mm corona electrode to collecting grid electrode separation, with the maximum deviation being twelve percent at 5 kV and the average deviation being approximately eight percent for all points. The correlation between predicted and measured values was not as close as the 9 mm case, with the maximum deviation being six percent at 5 kV and the average deviation being approximately three percent for all points. The larger error in the estimated vs. measured values may be largely attributed to measurement error from the hot wire anemometer, and its inability to measure a true velocity vector rather than the absolute velocity magnitude that it does measure. Figure 5.15 shows that the numerical model predicts recirculation regions to occur at both the top and bottom of the channel

outlet, which causes a negative real velocity to exist along a portion of the outlet channel. Circulation regions were confirmed experimentally using smoke flow visualization, which revealed the existence of a recirculation region in the case of the 5 mm separation. When measuring the airflow profile with the hot wire anemometer probe, regions that had a real negative velocity with respect to intended channel flow would appear to have a positive velocity, and would cause an overestimation of average channel velocity. This measurement error is likely a significant contribution to the deviation seen between the predicted and measured average outlet air velocities. A comparison of the predicted and measured channel outlet air velocity profiles for the 9 mm and 5 mm corona to collector grid electrode separations, over a set of operating potentials, are shown respectively in Figure 5.19 and Figure 5.20. For Figure 5.19 and Figure 5.20, the numerical values are shown as absolute values, which are used since they should more accurately track the measured values from the hotwire anemometer, which they are plotted with. For both the 5.5 kV and 6.5 kV experimental outlet velocity curves shown in Figure 5.20, there are "humps" on ether end of the velocity curves that likely represent recirculation zones, and they roughly align with the "humps" in the numerical curves shown in the same figure. It is also seen that the correlation between the 9 mm case average airflow values are closer than in the 5 mm case where the recirculation regions exist, suggesting that it is reasonable to assume the error is due to magnitude versus vector velocity measurements of the outlet air profile.

The comparison of the predicted versus measured outlet profiles in Figure 5.19 and Figure 5.20 have relatively good correlation with each other; however, a shift of the maximum outlet velocity towards the top of the channel and higher maximum velocities for the experimental results compared to the numerical is seen. The maximum velocity peak shift is likely due to slight non-symmetries in the experimental model corona electrode placement for the 9 mm air gap setting, causing the airflow profile peak to shift 1 mm toward the top of the channel and distort the shape. The 5 mm air gap results do not exhibit the shift, suggesting that the error is in wire placement since it is the only fixture modification between measurements.

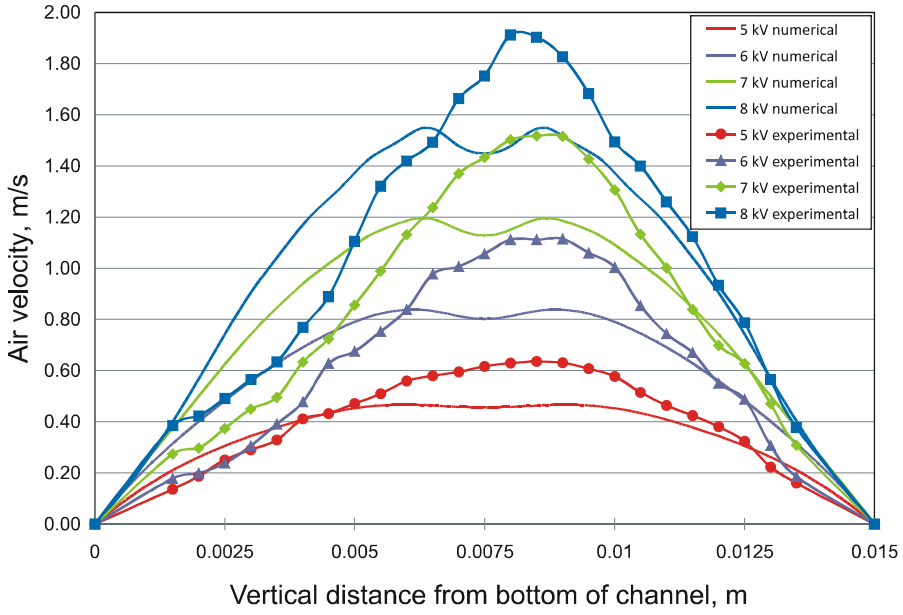

Figure 5.19. *Comparison of numerical and experimental outlet air velocity profiles for a 9 mm corona electrode to collector grid electrode spacing and applied voltage Ve from 5 kV to 8 kV in 1 kV steps. Numerical values are shown by line plots, and experimental values shown by line plots with markers. Line plots with the same color represent values taken at the same operating voltage.*

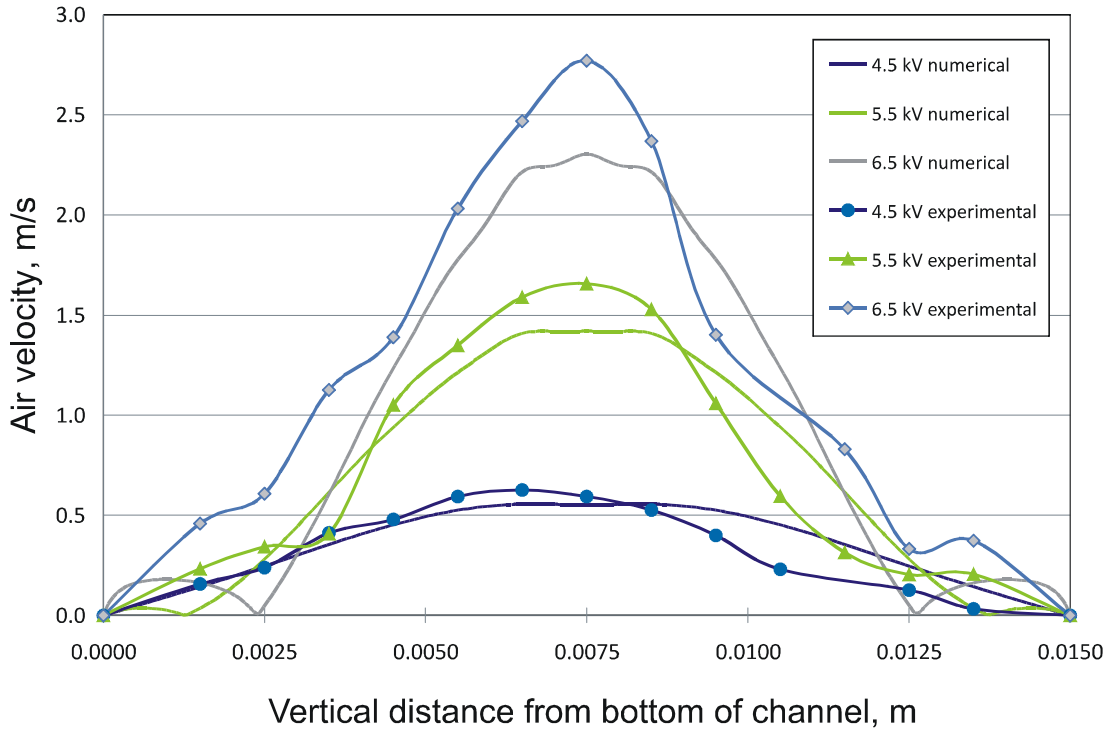

Figure 5.20. *Comparison of numerical and experimental outlet air velocity profile for a 5 mm corona electrode to collector grid electrode spacing and applied voltage Ve from 4.5 kV to 6.5 kV in 1 kV steps. Numerical values are shown by line plots, and experimental values shown by line plots with markers. Line plots with the same color represent values taken at the same operating voltage.*

5.5.5 EHD blower model verification summary

The numerical EHD modeling test bed was validated against an experimental model with substantially similar geometry. By comparison of numerical and experimental results, the numerical model was shown to predict electrical properties of the EHD system including corona onset voltages and current-voltage curves with an error of less than about five percent, and predict fluid dynamic properties including outlet airflow profiles and average velocities within an error of about ten percent.

Beyond absolute accuracy the model showed that it correctly predicted trends, electrical and fluid dynamic that make it a critical EHD air mover design tool. The primary motivation for the model development and validation was for flow generation for heat transfer applications, however, it is applicable to a range of other applications including, EHD air movers, precipitators, heaters, speakers, and others.

5.6 Cantilever-to-plane EHD blower geometry for jet impingement heat transfer

This sub-chapter presents numerical modeling results for a cantilever-to-plane EHD blower design for jet impingement forced convection spot cooling. The previous chapter introduced and validated the general EHD model that is adapted for used in this section with a new EHD blower geometry and focuses on heat transfer capability and effectiveness of a meso-scale EHD blower in a jet impingement configuration.

5.6.1 Numerical modeling of cantilever-to-plane EHD blower design

Although not described here in detail, the complete set of governing equations for the modeling effort in this study is given in Chapter 5.1.

Space charge generation by corona discharge in an EHD blower can be modeled by applying appropriate electrostatic and charge transport boundary conditions at the surface of the corona electrode surface, as described in depth earlier in this chapter. In this investigation the use of a complex corona electrode geometry makes accurate estimation of corona based charge generation through the use of Peek's equation and Kaptsov's assumption difficult. Therefore, experimental current-voltage data taken from a microfabricated meso-scale cantilever EHD blower of the same structure investigated in this paper, shown in Figure 5.21, was used to prescribe surface charge density at the surface of the coronating electrode such that the simulated current density was equal to the measured experimental current density at the coronating electrode surface. A detailed description of the meso-scale cantilever EHD blower fabrication and corona current measurement procedure can be found in Chapter 6.

5.6.2 Cantilever-to-plane EHD blower design

A high tip curvature cantilever beam suspended over a flat conductive thermal exchange surface, shown in Figure 5.21, was used as the basis for the EHD driven heat transfer modeled in this study. A DC voltage is applied between the corona electrode and

the conductive thermal exchange surface, creating a corona discharge at the lower tip of the cantilever. The ions generated by the corona are accelerated towards the thermal exchange surface creating an air jet along their path, resulting in forced convection thermal transfer from the substrate. The cantilever-to-plane EHD blower design, although not necessarily optimal for cooling, was chosen due to its relative ease of modeling as well as relative ease of micro-fabrication and experimental analysis with infrared imaging.

5.6.3 Numerical solution domain and boundary conditions

The three-dimensional cantilever EHD blower structure shown in Figure 5.21 can be approximated by the two-dimensional axial symmetric model shown in Figure 5.22, where the device is reduced to a single cross-sectional plane taken across the end of the cantilever where a line of axial symmetry bisects the tip of the corona electrode as depicted in Figure 5.22 (a) and (b). The simplified two-dimensional model makes a number of assumptions, including rounding cantilever tip cross-section corners, and effectively ignoring the electric field and fluid dynamics contribution by the rest of the cantilever structure. However, these approximations will lead mainly to second order effects in air jet shape. The corona electrode cross-section was made to be 400 μm in height with a top and bottom radius of curvature of 50 μm and 25 μm respectively, which corresponds to measured values from the equivalent microfabricated experimental model structure described in detail in the experimental section within this chapter. The modeling equations and methodology used for this study are described in Sub-chapter (5.1).

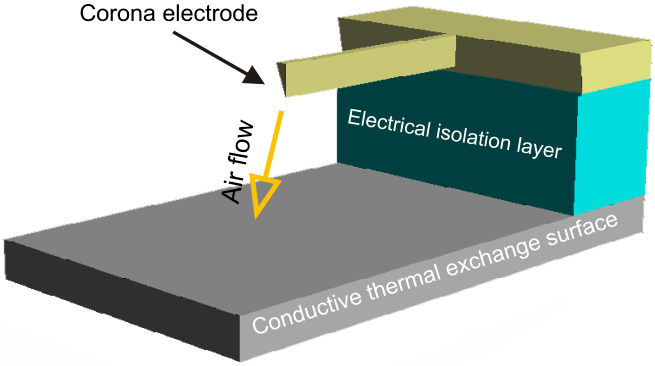

Figure 5.21. *Diagram of cantilever EHD blower structure and operation. The ion stream generated by the corona discharge is propelled towards the surface of the collecting electrode entraining an air jet in its path that impinges on the surface cooling it.*

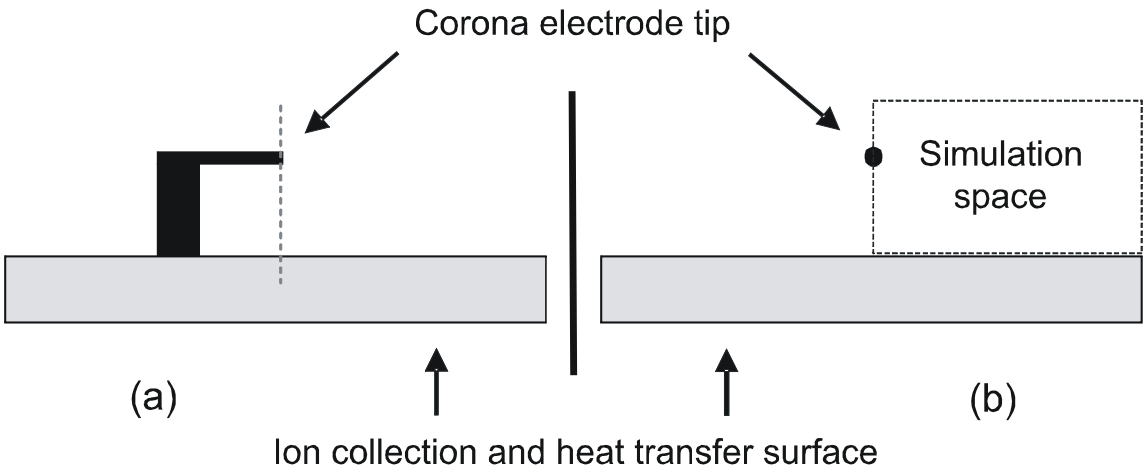

Figure 5.22. *Two cross-section views of the EHD blower are shown in (a) and (b). The dashed line in (a) shows the location of the plane of cross-section that is displayed in (b). The simulation space used to model the EHD blower is shown in (b) with the line of axial symmetry going through the center of the corona tip cross-section. Model dimensions are not drawn to scale.*

The numeric simulation space, subdomains, and boundaries are shown in Figure 5.23. A single domain was used for the entire simulation space, which made up the air gap between the corona and collector electrodes as well as a region above the corona electrode. The domain size was selected to be 7 mm in z and 20 mm in r.

The electrostatic, charge transport, fluid dynamic, and heat transfer domain equations were solved within the simulation domain using modeling parameter values shown in Table 5.5. Boundary conditions applied to the numerical model, are shown in Table 5.6 and are as follows. For electrostatics, a constant positive dc voltage V_e was

applied to the corona electrode surface, and zero volts were applied to the substrate/thermal exchange surface, which acted as the collector electrode. All other boundaries were set to an absorbing boundary condition (ABC). For charge transport, a space charge surface density is applied to the surface of the corona electrode, calculated using experimental data from the microfabricated EHD device presented in the experimental section of this chapter. A zero diffusive charge flux condition is imposed on all boundaries except for the surface of the corona electrode. The validity of this assumption is justified by the fact that the diffusion term is very small compared to the conduction term in (5.4) and can be set to zero at the boundaries with negligible effect [102, 129].

For fluid dynamics, a no-slip condition is applied to the surface of the substrate and corona electrode, normal flow with pressure prescribed from Bernoulli's equation was used at the upper air boundary, and an outlet-flow condition and a neutral pressure condition is assigned to all other air boundaries. The heat transfer problem was solved by applying a constant temperature to the substrate, corona electrode surface, and air boundaries which had a net influx of air into the model. A convective flux boundary condition was applied to all other external air boundaries.

The numerical simulation space, shown in Figure 5.23 was descretized in approximately 15,000 to 50,000 triangular elements depending on separation gap distance, with the element density being highest in the region around the corona electrode due to the relative high space charge density and electric field intensity.

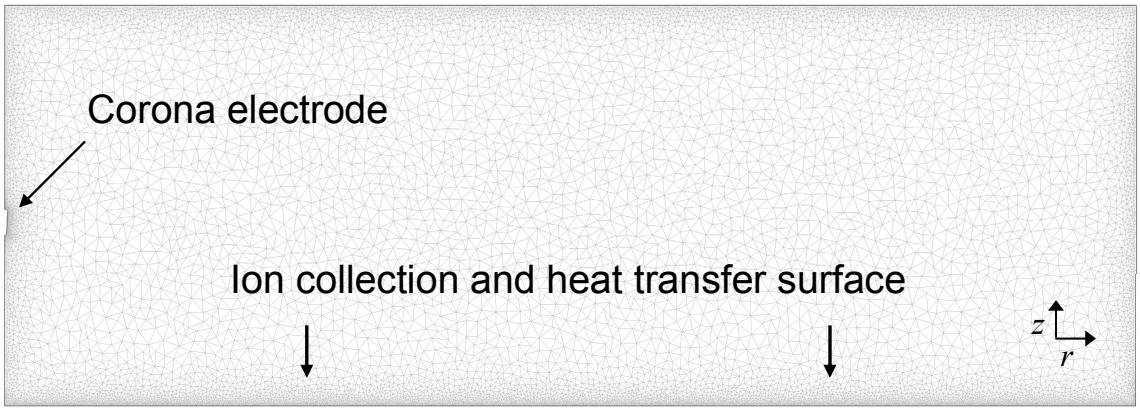

Figure 5.23. *Simulation domain space, showing geometry and location of corona electrode tip in relation to substrate, as well as the solution domain numerical mesh elements. The line of axial symmetry is on the left and bisects the corona electrode. The total simulation space is 2 cm long and 0.7 cm in height.*

Table 5.5. *Sub-domain modeling parameter values used in FEM modeling.*

Modeling parameter	**Value**
Relative dielectric permittivity of air	1
Charge diffusion coefficient	5.3×10^{-5}
Ion mobility coefficient	2.0×10^{-4} $m^2/(Vs)$
Density of air	1.2 kg/m^3
Kinematic viscosity of air	1.8×10^{-5} m^2/s
Heat capacity of air	1.007 kJ/(kgK)
Thermal conductivity of air	26.3×10^{-3} W/(mK)
Corona electrode to substrate separation	3 mm
Corona electrode tip radius (Bottom, Top)	25μm, 50 μm

Table 5.6. *Boundary conditions used in FEM modeling.*

Boundary	Electrostatics	Charge transport	Fluid dynamics	Heat transfer
Substrate	grounded	Zero diffusive flux	No-slip	Constant Temperature 60 C
Substrate	grounded	Zero diffusive flux	No-slip	Constant temperature 70 oC
Corona electrode	3, 3.5, 4, 4.5, and 5 kV	Surface charge density	No-slip	Constant temperature 28 oC
Upper air boundary	ABC	Zero diffusive flux	Normal flow with pressure prescribed by Bernoulli's equation	Constant temperature 25 oC
Side air boundary	ABC	Zero diffusive flux	Neutral pressure	Convective flux

5.6.4 Cantilever-to-plane numerical results

Numerical simulations results for the cantilever EHD blower design correlated well with the expected electric field profile, charge distribution, air jet velocity, jet shape, and the resulting heat transfer pattern. Surface plots of a cantilever EHD blower with a 3 mm separation are shown in Figure 5.24 through Figure 5.27. These plots display the solutions to the four coupled physical phenomena modeled: electrostatics, charge transport, fluid dynamics, and heat transfer shown respectively in Figure 5.24, Figure 5.25, Figure 5.26, and Figure 5.27. The plots were generated using modeling parameters in Table 5.5, Table 5.6, and a corona electrode to substrate electric potential difference of 5 kV.

The electric potential and corresponding electric field, Figure 5.24, fit the classical shape and profile of a corona based EHD system with the field strength and

charge density decreasing in magnitude from the edge of the corona electrode surface to the collecting electrode substrate. The space charge, generated from the corona discharge, is accelerated through the drift zone, and is distributed with high density near the corona electrode and decreasing slowly towards the collector, with the space charge density falling off faster in the r direction to the right of the corona electrode or in the positive z direction above the corona electrode. Thus, the ion stream has its largest component in the negative z direction directly below the corona electrode, traveling from corona to substrate, Figure 5.25. The traveling ion stream induces an air jet along its path that impinges on the substrate surface as seen in Figure 5.26, with the greatest z-directional air velocities centered directly below the corona electrode in the area of the highest space charge density and electric field magnitude. The impinging air jet decreases the fluid and thermal boundary layer thickness, producing the thermal boundary layer shown in Figure 5.27, which is thinnest at either side of the air jet and increases in thickness moving away from the center in the positive r direction.

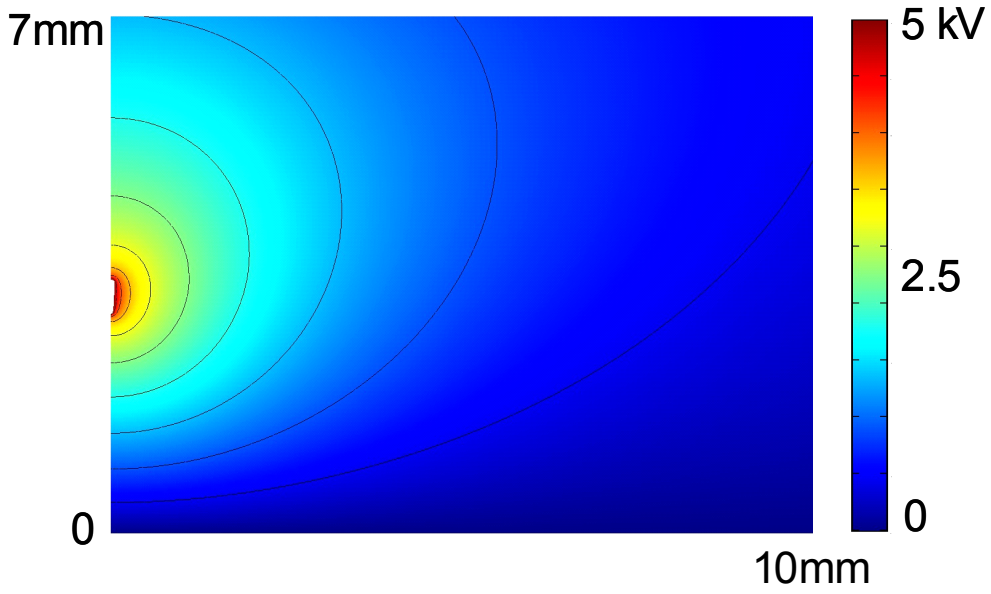

Figure 5.24. *EHD blower simulation results showing electric potential as colored surface map and equipotential contour lines.*

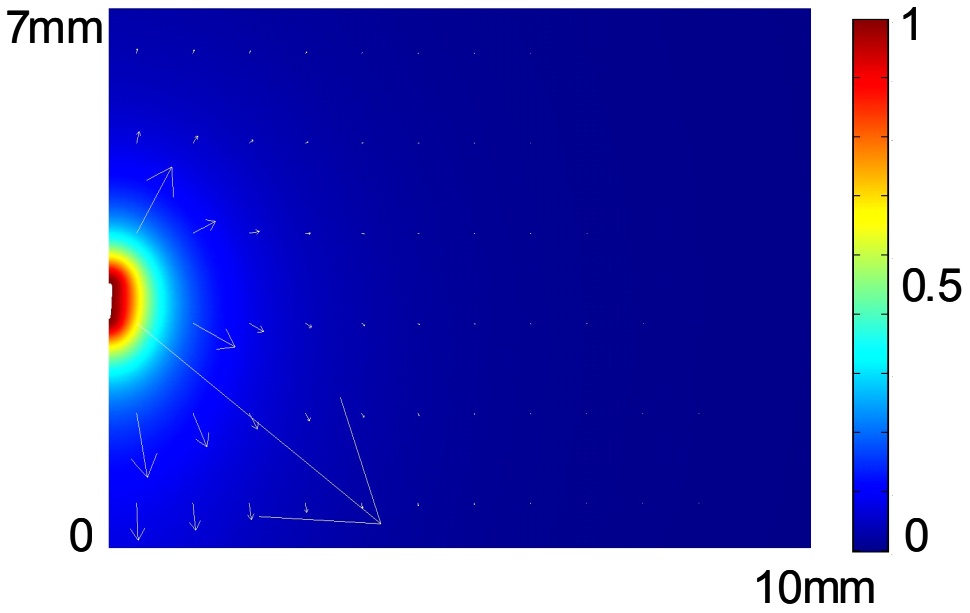

Figure 5.25. *EHD blower simulation results showing normalized space charge density as a colored surface map and relative coulombic force magnitudes as linear scaled arrows.*

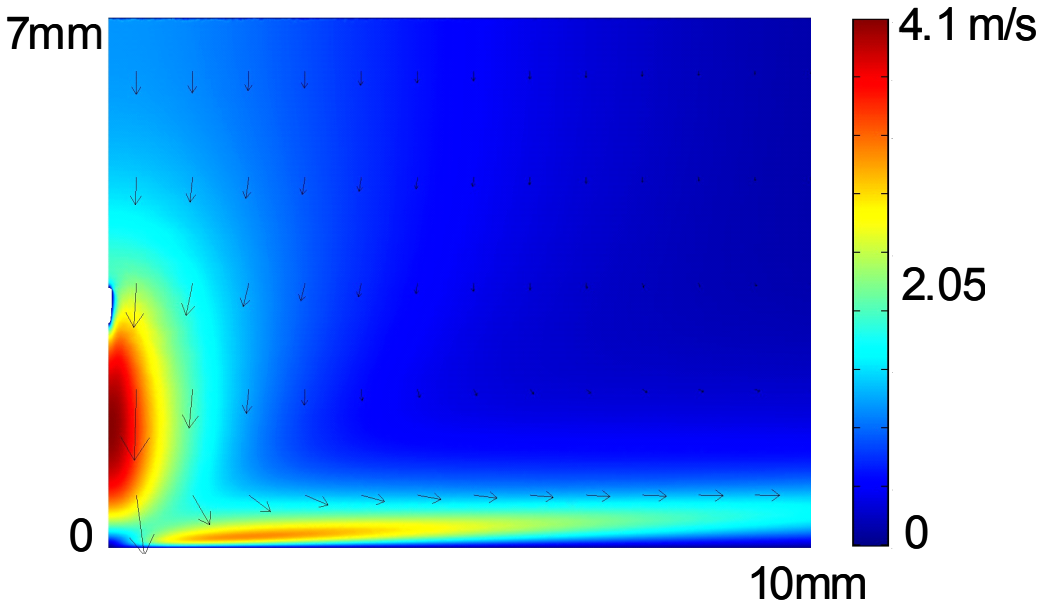

Figure 5.26. *EHD blower simulation results showing air velocity as a colored surface map and air velocity magnitudes as linearly scaled arrows.*

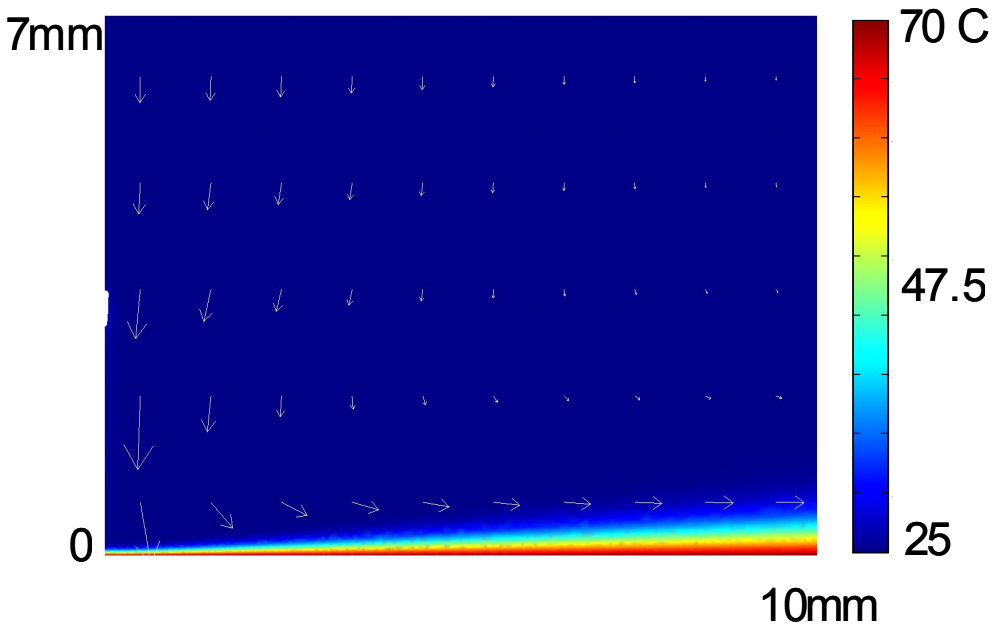

Figure 5.27. *EHD blower simulation results showing air temperature as a colored surface map and air velocity as linearly scaled arrows.*

The ion current, I_c, leaving the ionization zone can be calculated by integrating equation (5.3) over the area of the coronating zone surface with the electric field at the surface of the corona electrode. It was assumed for the cantilever structure that the coronating region of the corona electrode tip included the end face of the cantilever structure as well and seventy five micrometers length of the cantilever structure giving a total coronating region of 1.02×10-7 m^2. The assumption that the leading face of the tip was included as based on observation of a corona discharge glow around the entire front face of the cantilever electrode. The current-to-voltage characteristics of the cantilever EHD blower follow an exponential current dependence on the electric potential V_e between the corona electrode and substrate, as shown in Figure 5.28, with I_c increasing from 1.55×10-6 amperes to 1.98×10^{-5} amperes over a V_e range of 3 kV to 5 kV.

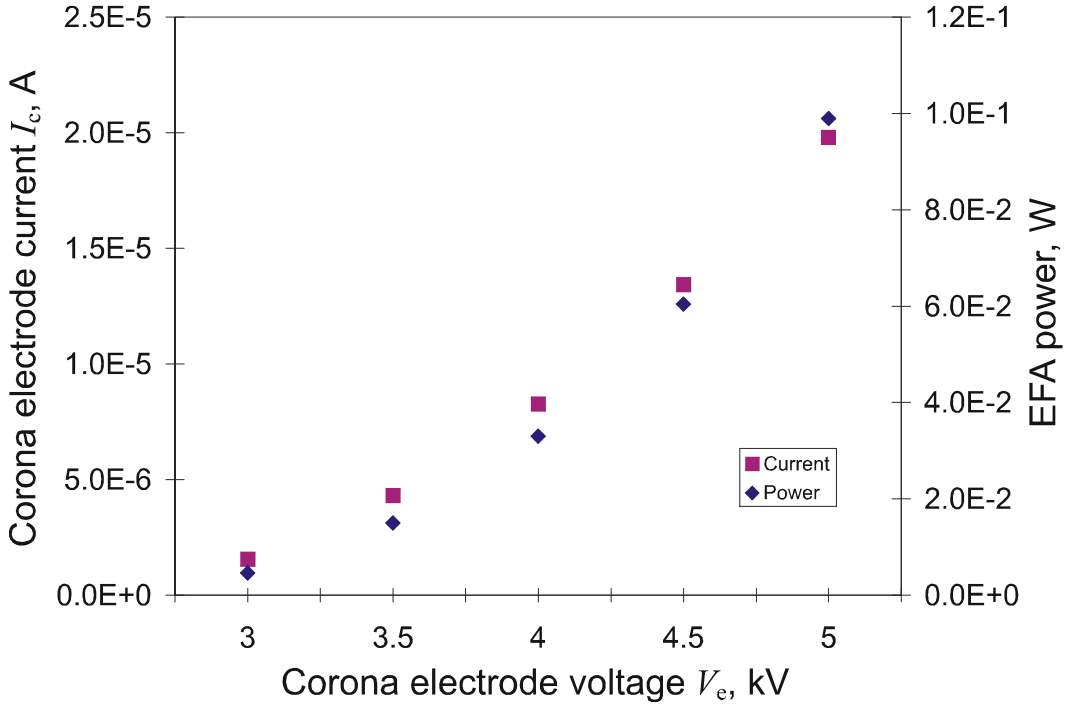

Figure 5.28. *Simulated EHD blower corona electrode current, I_c, vs. applied voltage V_e, plotted on the left vertical axis. EHD blower power vs. applied corona electrode voltage V_e plotted on the right vertical axis. Plot data corresponds to a corona electrode to collector electrode separation of 3 mm.*

The device power rises exponentially with the applied voltage due to the exponential increase in current with applied electric potential. A linear positive relationship was observed between EHD blower air jet velocity and V_e, as shown in Figure 5.29. Simulated air jet velocities fell within the range of velocity magnitudes reported from experimental findings [130], and velocity vs. applied voltage trends agree well qualitatively with experimental studies on macro scale EHD blowers [5].

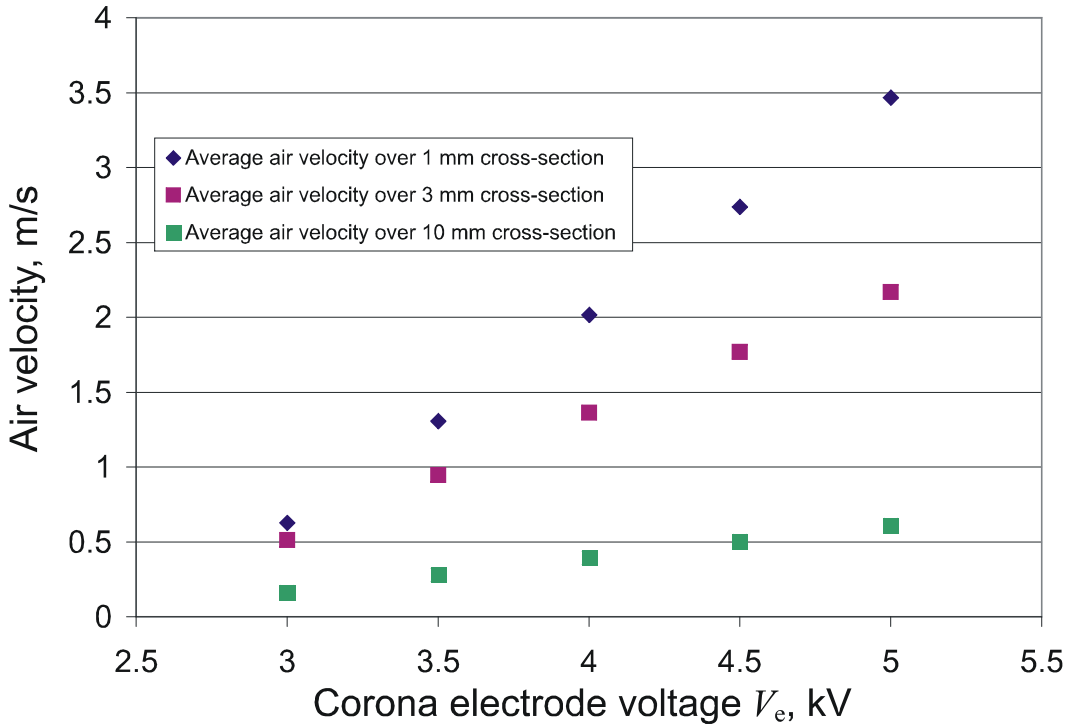

Figure 5.29. *Simulated EHD blower air jet z component velocity vs. applied voltage V_e averaged over three circular cross-section diameters 1 mm below the bottom surface of the corona electrode. Plot data corresponds to a corona electrode to collector electrode separation of 3 mm.*

The EHD blower air jet *z*-directional component velocity was averaged over three cross-sections, each centered below the corona electrode and positioned 1 mm below the bottom surface of the corona electrode in Figure 5.27. The three cross-section lengths chosen were 1 mm, 3 mm, and 10 mm. The average air velocity over the 1 mm cross-section ranged from approximately 0.6 m/s to 3.5 m/s with the highest velocity at a V_e of 5 kV. The EHD-induced air jet is focused around a 1 mm cross- section, with the average airflow for a 10 mm cross-section falling to 0.16 m/s and 0.61 m/s for an applied V_e of 3 kV and 5 kV respectively.

The average convection heat transfer coefficient h_{ave} can be calculated by

$$h_{ave} = Q/(A_s \Delta T_{sa}) \tag{5.13}$$

where Q is the thermal power in watts removed from a surface S, A_s is the area of surface S, and ΔT_{sa} is the temperature difference in degrees Kelvin between S and the ambient air. The average convection heat transfer coefficient along the substrate scaled

approximately linear with increasing applied voltage V_e, as shown in Figure 5.30. The average heat transfer coefficient was calculated at the surface of the substrate over four circular disk shaped areas, each centered above the corona electrode. Disk shaped surface areas with diameters of 1 mm, 5 mm, 10 mm, and 15 mm were used for the calculation. The highest h_{ave} of 280 W/(m^{2}K) was found to be over the 1 mm disk at the maximum applied voltage of 5 kV.

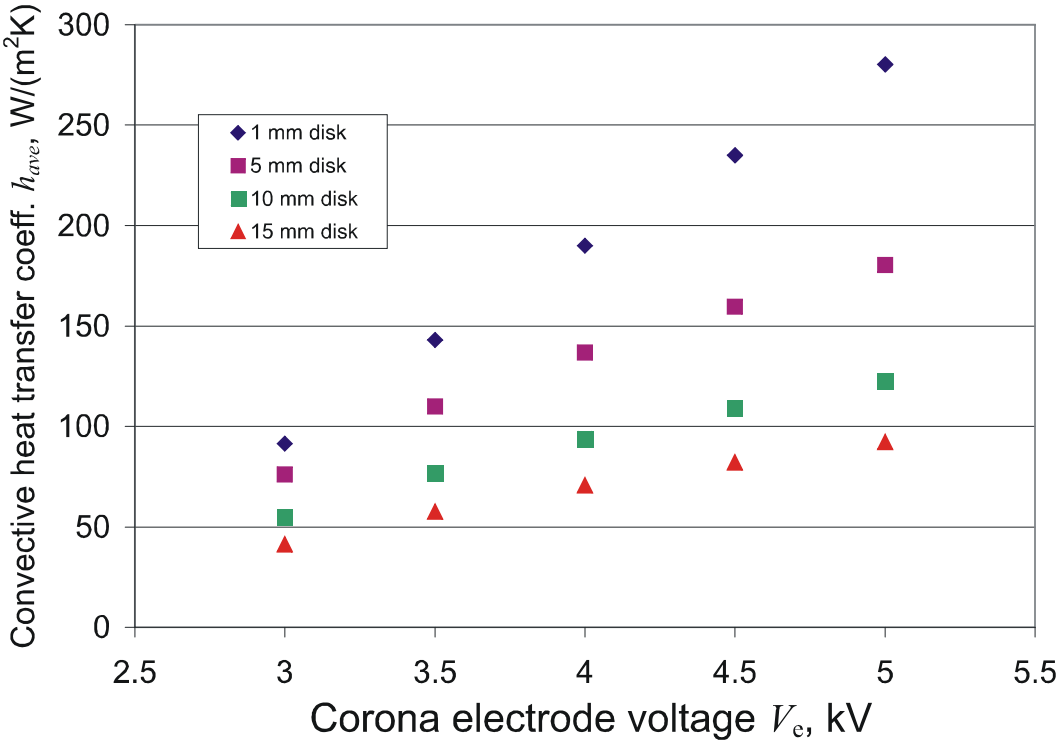

Figure 5.30. *Simulated convection heat transfer coefficient have vs. applied voltage V_e. have was calculated over four circular disk shaped areas on the substrate centered above the corona electrode. Disk diameters of 1 mm, 2 mm, 3 mm and 8 mm were used.*

The value of h_{ave} decreased with increasing distance from the impinging jet, dropping off up to 67 percent over the 15 mm disk at the highest V_e. Notably, these calculations assume a symmetric flow pattern about the disk axis, which would only be approximately true for the case of a cantilever corona electrode. However, experimentally it was shown that due to the electrical and fluidic impact of the entire cantilever structure, the air jet is angled out from the corona tip, rather than pointed directly down at the substrate. This creates a cooling zone area that is approximately circular and positioned

out in front of the cantilever as shown in Figure 6.12, making the disk assumption a fair approximation.

The EHD blower thermal cooling effectiveness can be calculated by dividing the thermal power removed by the EHD blower over a given area by the total power input to the system by EHD blower operation. The calculation was done over the same four discs described previously in the convection heat transfer coefficient calculation, and their thermal cooling effectiveness is shown in Figure 5.31. Cooling effectiveness ranged from 70.6 to 0.1, decreasing with decreasing thermal exchange area and increasing applied voltage V_e. Although the velocity and convection heat transfer coefficient increase linearly with increasing voltage, the EHD blower current and thus power increase exponentially with the increasing voltage, giving the highest airflow per watt and cooling effectiveness at the lowest operating voltages. Notably, heat generation from the corona discharge was taken into account in this analysis by applying a constant temperature to the corona electrode tip that was three degrees higher than ambient, which was the largest temperature rise seen on the corona electrode from experimental analysis with IR imaging.

However, heat generation will occur throughout the airgap and from ion bombardment on the substrate, which was not modeled in this investigation and would decrease the convection heat transfer coefficients and cooling effectiveness values presented here. These second order heating effects are likely only to have a significant effect when the EHD blower is operating at the edge of its breakdown electric potential.

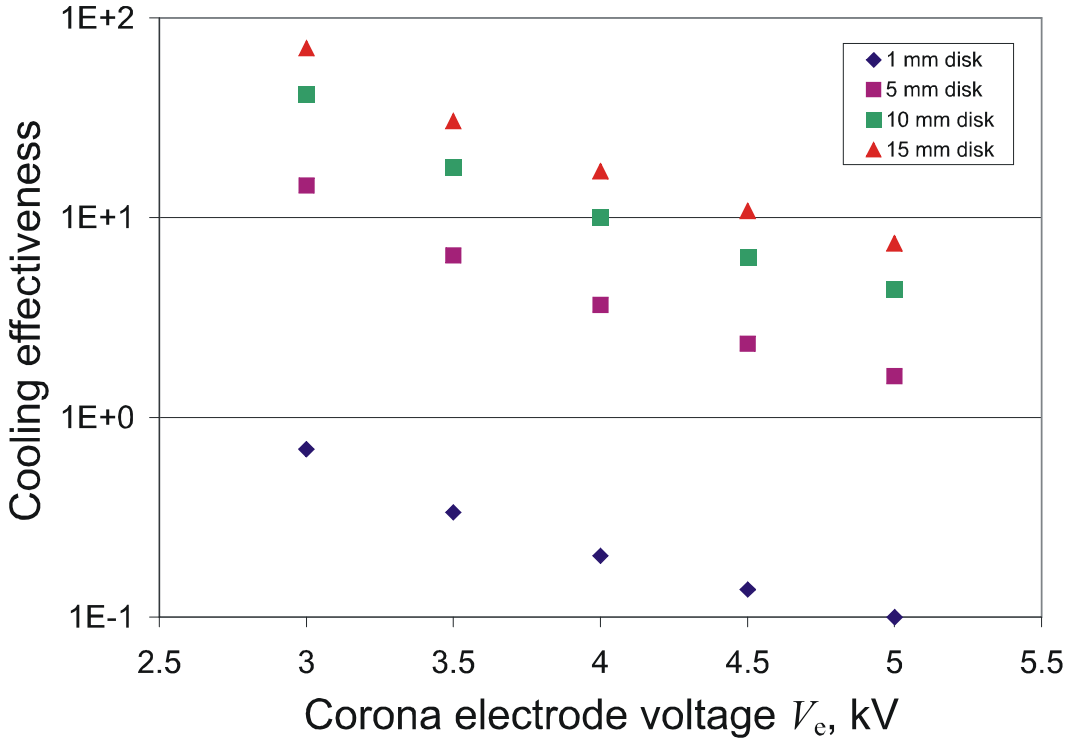

Figure 5.31. *Simulated cooling effectiveness in percent vs. applied voltage V_e. Cooling effectiveness calculated over four circular disk shaped areas on the substrate centered above the corona electrode. Disk diameters of 1 mm, 5 mm, 10 mm, and 15 mm were used.*

5.6.5 Heat transfer model verification using round nozzle jet impingement correlation

The heat transfer from a single EHD blower impinging jet can be approximated using the following correlation for a gas jet from a round nozzle.

$$\frac{\overline{\mathrm{Nu}}}{\mathrm{Pr}^{0.42}} = G\left(\frac{D}{r}, \frac{H}{D}\right) F_1(\mathrm{Re}) \tag{5.14}$$

where

$$F_1 = 2\,\mathrm{Re}^{1/2}\left(1 + 0.005\,\mathrm{Re}^{0.55}\right)^{1/2}, \tag{5.15}$$

and

$$G = 2\frac{D}{r}\frac{12 - 1.1D/r}{1 + 0.1(H/D - 6)D/r}. \tag{5.16}$$

where D, H, and r are respectively the diameter of the jet at the corona electrode, the distance from the substrate to the corona electrode, and the radius of the circular area of the substrate, over which the average Nusselt number, Nu, is calculated. The Nusselt, Reynolds, and Prandtl numbers are respectively defined as

$$\mathrm{Nu} = \frac{hD}{k_f}, \tag{5.17}$$

$$\mathrm{Re} = \frac{VD}{v}, \tag{5.18}$$

$$\mathrm{Pr} = \frac{v}{\alpha}. \tag{5.19}$$

where h, k_f, V, v, and α are respectively the convective heat coefficient, thermal conductivity of air, the velocity of the air jet just under the corona electrode, the kinematic viscosity of the air, and finally the thermal diffusivity of the air. Specific parameter values used for the correlation are shown in Table 5.7. Although the EHD blower is not perfectly representative of an air jet from a nozzle, it exhibits a similar confined air stream centered about the corona electrode. Having no exact nozzle diameter, since the airflow is induced by EHD forces rather than driven through a nozzle,

the nozzle diameter was estimated on the diameter of the high velocity region of the air jet. 1 mm was selected since the core of the EHD induced air jet was focused around that diameter. The velocity of the air jet used for the round nozzle correlation was calculated by averaging the air velocity across a 1 mm cross-section 1 mm downstream of the corona electrode. The corona electrode acts as a physical barrier to the air jet, causing the air jet to split around it and form a dead zone immediately downstream of it, as can be seen in Figure 5.26. Therefore, to better compare with the flow profile coming from an open nozzle air jet, the velocity was averaged over the 1 mm cross-section at a distance of 1 mm downstream from the center point of the corona electrode.

The forced convection heat transfer correlation for a gas jet from a round nozzle was shown to correlate well with the numerical results presented in subchapter 5.6.4 as shown in Figure 5.32. The correlation was shown to underestimate the numerical modeling results by less than five percent at the five mm disk very close to the impinging jet, and over estimate the heat transfer coefficient by less than ten percent over a 15 mm disk area. The good correlation suggesting that the heat transfer from meso-scale EHD cantilever-to-plane blower can be represented well by a round nozzle gas jet heat transfer correlation. The close correlation also suggest that the numerical model is predicting heat transfer rates within a reasonable range for the predicted EHD induced air jet velocities.

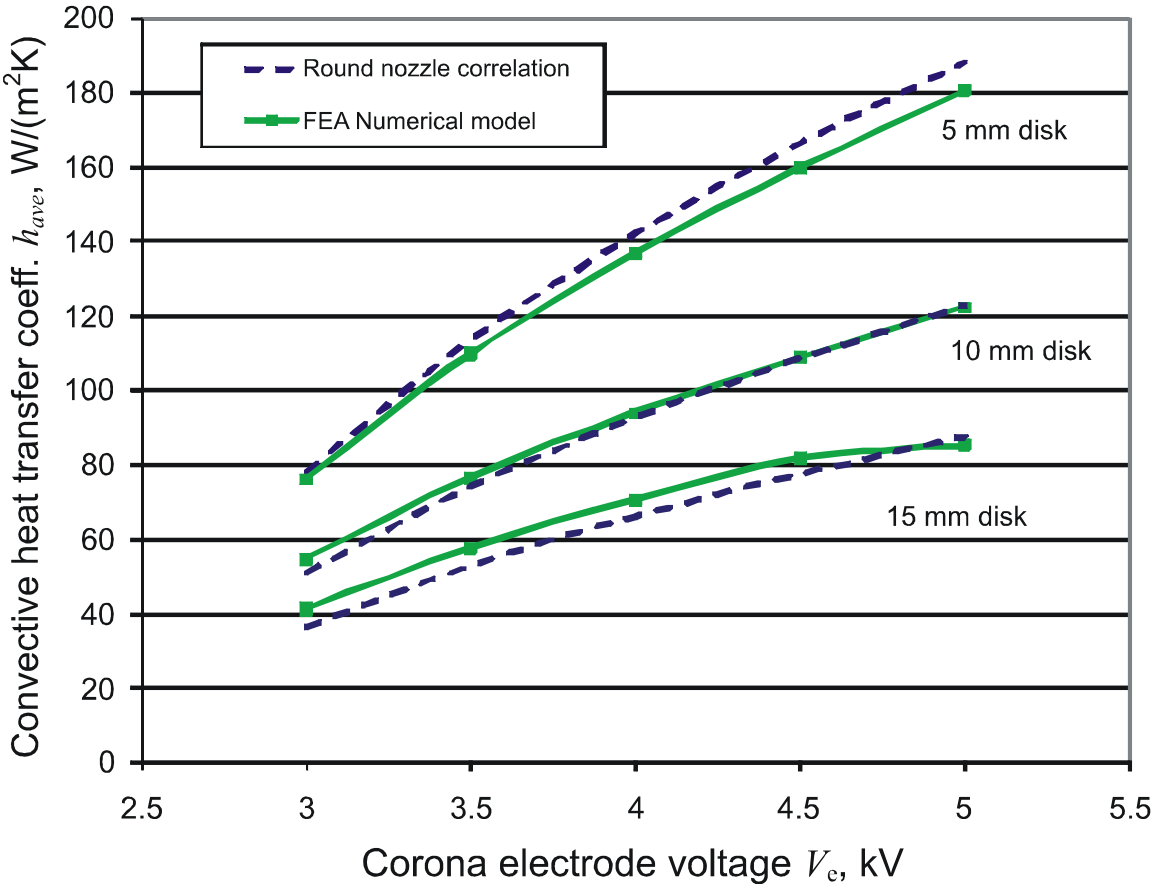

Figure 5.32. *Comparison between convection heat transfer coefficient estimation between FEA numeral modeling and round nozzle jet impingement correlation. The convection heat transfer coefficient was averaged over a 5 mm, 10 mm, and 15 mm disk centered about the jet nozzle for the shown values.*

Table 5.7. *Parameter values used in round nozzle gas jet impingement forced convection heat transfer correlation calculations*

Parameter	symbol	value
Diameter of air jet at corona electrode	D	1 mm
Distance between corona electrode and substrate	H	3 mm
Radius of disk over which h is averaged	r	2.5, 5, and 7.5 mm
Thermal conductivity of air at 300 K	k_f,	26.3×10^{-3} W/mK
Kinematic viscosity of the air at 300 K	v	15.89×10^{-6} m^2/s
Thermal diffusivity of the air at 300 K	α	22.5×10^{-6} m^2/s

5.6.6 Conclusions

The previous sub chapter presents a numerical coupled-physics modeling approach for EHD air movers for forced convection cooling that includes the full charge transport equation taking into account the effects of fluid dynamics and space charge diffusion. A cantilever EHD structure was analyzed using the coupled physics modeling approach. Numerical simulation results agreed well qualitatively with experimental results presented in literature for EHD blower performance characteristics including, velocity magnitude values, and velocity vs. operating voltage trends. Average simulated EHD blower air jet velocities ranged from 1 m/s to 3.5 m/s over a 1 mm cross-section. Maximum convection heat transfer coefficient was found to be 280 $W/(m^2K)$ over a disk-shaped surface area with a radius of 1 mm. Heat convection heat transfer coefficient were compared to a round nozzle impinging air jet heat transfer correlation showing good agreement with simulated values.

5.7 Chapter summary

A numerical model for EHD driven flow and heat transfer is presented. Limitations and assumption of the presented numerical model are discussed. Electrical and fluid dynamic predictions of the model are validated using a wire-to-grid EHD geometry showing good agreement of numerical and experimental EHD current and voltage results as well as total airflow and airflow velocity profile. A modeling study for meso-scale EHD blower forced convection cooling. Average simulated EHD blower air jet velocities ranged from 1 m/s to 3.5 m/s over a 1 mm cross-section. Maximum convection heat transfer coefficient was found to be 280 $W/(m^2K)$ over a disk-shaped surface area with a radius of 1 mm. Heat convection heat transfer coefficient were compared to a round nozzle impinging air jet heat transfer correlation showing good agreement with simulated values.

Chapter 6. Miniaturization of EHD blowers for thermal management

The miniaturization of electrostatic air pumps to the micro/meso-level offers several significant advantages over macro-scale designs. At the smaller scale, it is possible to generate a corona discharge at voltages on the order of a kilovolt rather than tens of kilovolts required at the macro-scale. The onset voltage reduction is made possible through small electrode separation gaps and high corona electrode tip curvature. The high tip curvature corona electrodes also increases the electric field gradient at the tip allowing for stable corona discharge over a larger operating range, enabling more flexible design and improved performance. Implementation at the micro/meso-scale also allows for the use of batch microfabrication technology enabling tighter device tolerances and greater reliability as well as potentially enabling low cost integration into electronics, micro electrical mechanical systems (MEMS), and other chip level devices for enhanced thermal dissipation.

6.1 Micro-scale planar EHD blower for boundary layer disruption based heat transfer

A micro-scale planar EHD design for boundary layer disruption based heat transfer was previously investigated by the author [14]. The purpose of the investigation was to develop an EHD that could operate on a thermal exchange surface, and by doing so break up the boundary layer and increase local heat transfer. The investigation was ultimately unsuccessful in creating a working prototype. However, the direction may still be viable, especially if alternating fields are used, which allow for discharges on the surface of dielectrics in the form of a dielectric barrier discharge (DBD), and would allow for the generation of miniature planar EHD structures that could be used for boundary layer modification. Although outside the scope of this dissertation, the author developed and tested several meso-scale DBD designs that functioned, and it seems reasonable that such systems could be scaled down to the micro scale. This section is included here to for

completeness, and further details regarding the micro-scale planar design can be found in [14].

6.2 Proof-of-concept meso-scale cantilever-to-plane EHD blower for jet impingement forced convection cooling

A proof-of-concept micro-fabricated EHD blower for jet impingement forced convection cooling is presented in this chapter. The design, fabrication, testing, and results are discussed for the micro-fabricated silicon cantilever-to-plane EHD blower design presented and modeled in Chapter 5.6.2 of this thesis.

6.2.1 Design

A high tip curvature cantilever corona electrode suspended over a flat conductive thermal exchange surface, shown in Figure 6.1, was chosen for this proof-of-concept microfabricated EHD-induced convection cooling study. DC voltage is applied between the cantilever corona electrode and conductive thermal exchange surface, creating ions at the tip of the cantilever. The ions are accelerated towards the thermal exchange surface, entraining an air jet along their path, resulting in forced convective thermal transfer from the surface. The cantilever-to-plane EHD blower design, although not necessarily optimal for cooling, was chosen due to its relative ease of fabrication and ease of experimental analysis with infrared imaging. For example, an EHD blower design embedded in a heatsink channel might enable greater heat transfer, but would have been difficult to image thermally, and therefore was not chosen. The cantilever electrode structure with high tip curvature allows for a high local field intensity to be generated at its tip at a minimum applied electric potential between corona and collector electrodes. The wide and flat collector electrode allows for a simple infrared analysis of cooling effects induced by EHD blowers.

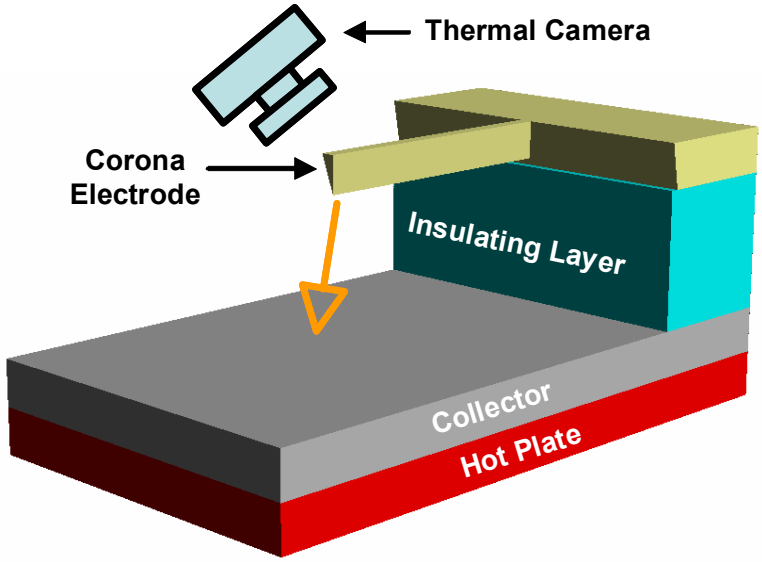

Figure 6.1. *Schematic diagram of the cantilever-to-plane EHD blower under test.*

6.2.2 Fabrication

A meso-scale high aspect ratio cantilever corona electrode with high tip curvature was fabricated in bulk silicon using the combination of Deep Reactive Ion Etch (DRIE) and Reactive Ion Etch (RIE). DRIE was chosen for its high aspect ratio etching capability and negative etching profile. RIE was used for further corona electrode sharpening after DRIE. The negative etching profile from DRIE was exploited to create a high tip curvature blade along the bottom surface of the cantilever structure, as shown in Figure 6.1. A negative etching profile creates vertical sidewalls that taper inward to the structure from top to bottom, as shown in Figure 6.2. This sidewall profile angle has a strong correlation to the exposed area and etched depth around the structure, with the angle increasing with the exposed area and etched depth [131]. The cantilever corona electrode was fabricated on a four-inch Silicon On Insulator (SOI) wafer with (100) orientation. In order to make high aspect ratio electrodes, the thicker side of the wafer, usually used for handling rather than fabrication, was used for the device layer. Detailed SOI wafer specification is listed in Table 6.1. Figure 6.3 shows the process flow for the cantilever corona electrode fabrication. First, in order to etch 350 μm thick silicon, a double-layer photoresist AZ4620 was spin coated and patterned, as described in Table 6.2. Subsequently, the wafer was placed in the DRIE chamber to etch the silicon and form the

cantilever corona electrode. A cantilever length of 8 mm with a top side width of 100 μm was fabricated resulting in a bottom side radius of tip curvature of 25 μm assuming a five degree negative taper. A picture of a completed wafer with multiple microfabricated devices before dicing is shown in Figure 6.4**.**

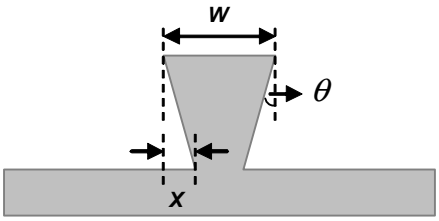

Figure 6.2. *Schematic diagram of the negative sidewall profile in DRIE.*

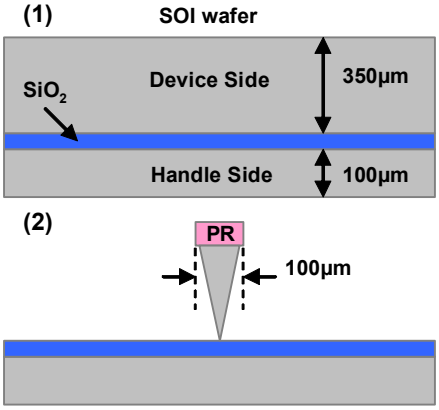

Figure 6.3. *Schematic diagram of process flow showing a cross-section taken along the plane orthogonal to the cantilever corona electrode 1) SOI wafer, 2) photolithography and anisotropic silicon etching by DRIE.*

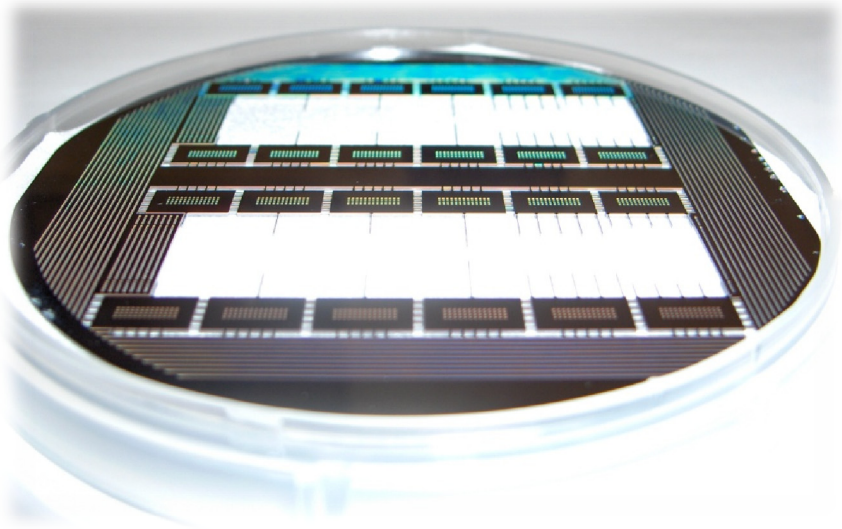

Figure 6.4. *Picture of completed wafer with multiple Microfabricated EHD devices prior to dicing.*

Figure 6.5 shows SEM images of a microfabricated cantilever corona electrode with length of 8 mm from substrate to tip. The corona electrode was patterned by coating a double-layer photoresist AZ4620 and etched by using the combination of DRIE and RIE as described above. Rather than using a SOI wafer, two double polished silicon wafers, stacked together by using photoresist AZ4620, were used in the fabrication. The top wafer was used for cantilever corona electrode fabrication and the bottom wafer was used as a carrier for wafer loading/unloading in DRIE system. Although the SOI wafer was adequate for fabrication, two double polished was used in place of an SOI wafer for all following device fabrication to reduce fabrication cost. Detailed wafer specification for the double side polished wafer is listed in Table 6.3. The blade is 448 μm tall, with a width w of 85.23 μm, and has an undercut x of approximately 16 μm, resulting in a negative taper angle θ of approximately two degrees, shown in Figure 6.5 (a). In order to achieve higher tip curvature for lower corona onset voltage, an extra sharpening process using RIE was performed. Experimental results shows that the RIE etching rate in vertical and lateral directions are approximately 0.63 μm and 0.55 μm per minute, respectively. A cantilever tip diameter of approximately 1.5 μm was achieved after the RIE sharpening process, as shown in Figure 6.5 (b).

Table 6.1. *Wafer specification for SOI silicon wafer.*

Type	Orientation	ρ, Ω-cm	T_{ox}, µm	D, µm	H, µm
N/Ph	1-0-0	1-10	2	350	100

Table 6.2. *Photolithography process steps for DRIE.*

Resist Polarity	**Positive**	**Material**	**Clariant AZ4620**
Process Steps:			
1st photoresist spin coat		Rest period, 45 min	
1st soft bake on the hot plate, 100°C, 3 min		Exposure, 80 sec	
2nd photoresist spin coat		Develop, 7 min	
2nd soft bake on the hot plate, 100°C, 5 min		Hard bake in the oven, 110°C, 30 min	

Table 6.3. *Wafer specification for double-side polished silicon wafer.*

Type	Orientation	ρ, Ω-cm	*Thickness*, µm
N/Sb	1-0-0	0.005-0.025	445-455

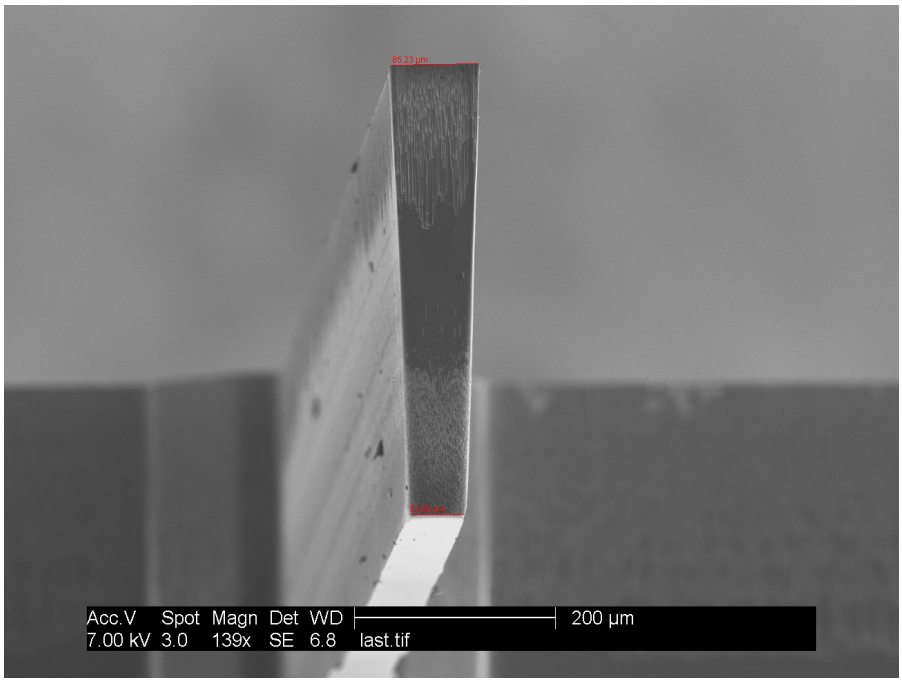

(a) SEM image of a microfabricated cantilever tip after DRIE without a RIE sharpening process, with a beam width and tip diameter of 83 µm and 54 µm respectively.

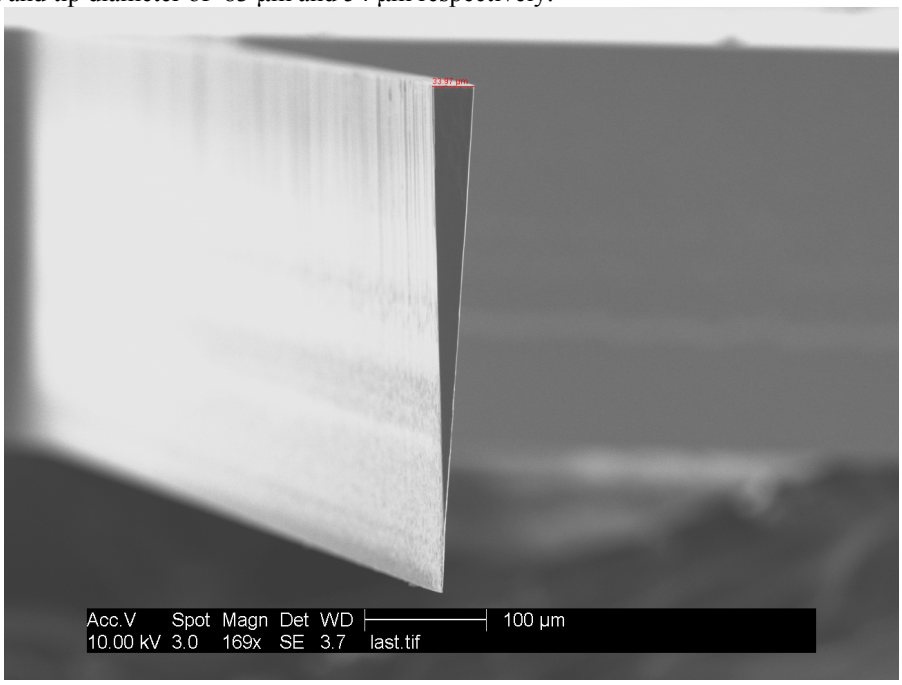

(b) SEM image of a microfabricated cantilever tip after DIRE with a RIE sharpening process, with a beam width and tip diameter of 34 µm and 1.5 µm respectively.

Figure 6.5. *SEM micrographs of 5 mm-long microfabricated cantilever corona electrodes.*

6.2.3 Experiment procedure and results

6.2.3.1 Current vs. voltage measurement procedure

Current-voltage measurements for the microfabricated silicon cantilever-to-plane EHD blower prototype were conducted using the experimental test setup shown in Figure 6.6.

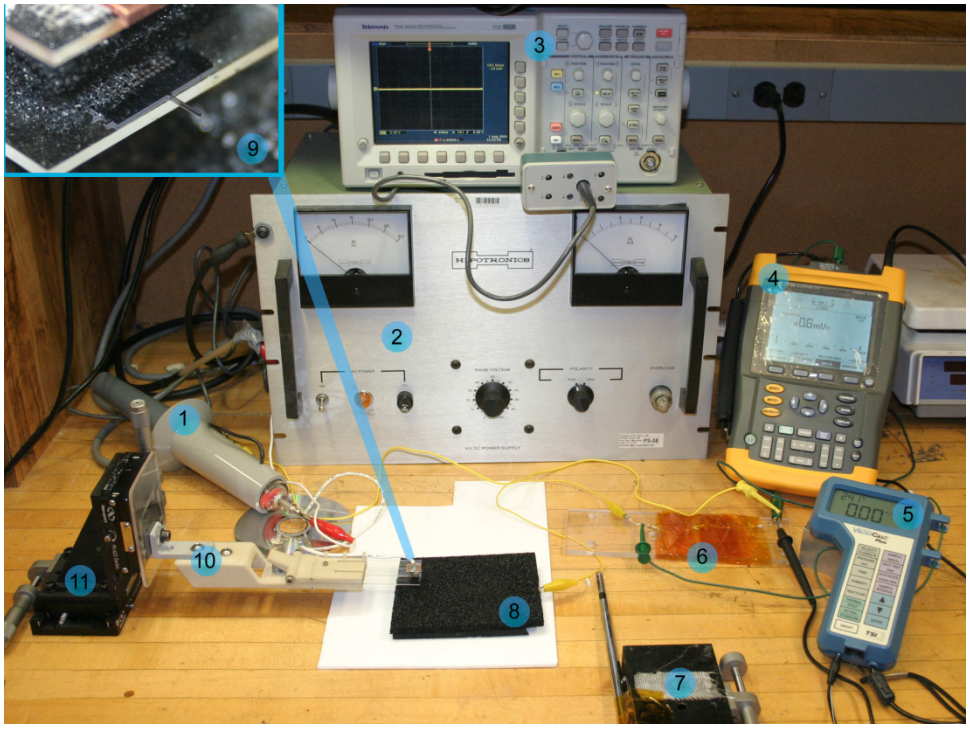

Figure 6.6. *(1) High voltage probe; (2) High voltage power supply; (3) Digital oscilloscope (Voltage); (4) Digital oscilloscope (Current); (5) Hot wire anemometer DAQ; (6) Voltage divider; (7) Hot wire anemometer probe; (8) Foam collector electrode; (9) EHD emitter under test; (10) Dielectric EHD mounting platform; (11) Micro-positioning x-z Stage.*

The EHD emitter under test was mounted in a custom designed mounting platform, Figure 6.6 (10), that enabled high voltage application to the silicon EHD EMITTER prototype while simultaneously maintaining mechanical connection but electrical isolation from the micro-positioning optical x-z stage that was used to accurately position the device under test at a desired location. The mounting platform used two glass substrates with a slab of semiconductive foam attached to the upper glass substrate, which clamped onto the silicon substrate portion of the device under test,

Figure 6.6 (9) and Figure 6.7. The conductive foam secured and created the electrical connection to the device under test. The prototype was positioned over a flat plane of conductive foam that was connected through two one half watt 100 k Ohm resisters to ground. During operation, the device current was measured by measuring the voltage drop over one of the series resisters. The voltage drop over the resister was measured using a Fluke digital multimeter. The high positive voltage was generated using a Hipotronics model R30B HV DC Power Supply, and voltage levels were monitored using a Tektronix P6015 high voltage probe connected to a Tektronix digital oscilloscope. A hot wire anemometer based VELOCICALC PLUS 8386 airflow sensor was used to measure the wall-jet air velocity four centimeters downstream from the device under test. The velocity probe was kept at four centimeters to ensure that it would create no significant electrical or fluid dynamic disturbance. Notably, due to the small size of the air-jet and low total air flow the hot wire anemometer is only useful for qualitative airflow measurements, but was used to show presence of EHD induced airflow. Airflow was detected at all air gap separation distances tested.

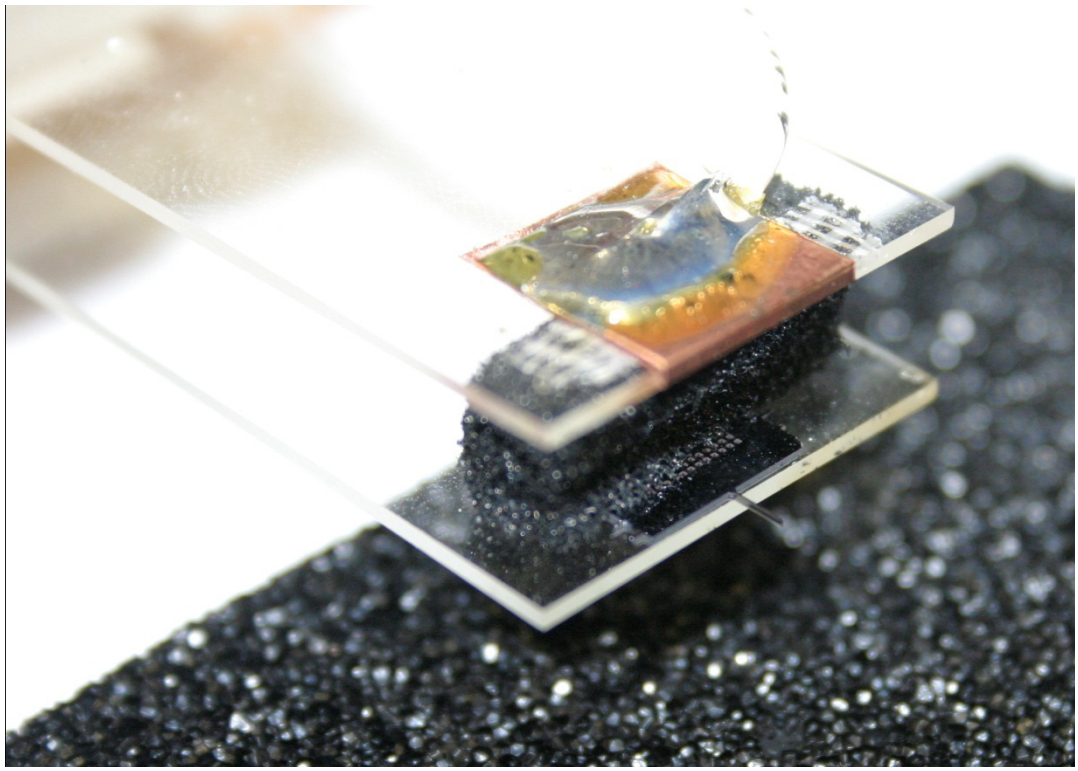

Figure 6.7. *Photograph of microfabricated EHD blower test setup showing an EHD emitter positioned 5 mm above the conductive plane.*

6.2.3.2 Current vs. voltage measurement results

Current and voltage characteristic of the microfabricated cantilever-to-plane ED blower, Figure 6.5 (a)**,** is shown in Figure 6.9 for four different air gap separation distances. The operation range of cantilever-to-plane EHD blower shown is between the corona onset voltage and the air breakdown voltage. In order to maintain tip integrity for all measurement gap separations, the voltage applied between the corona and collector electrodes was never allowed to reach the breakdown voltage since arcing may damage the corona electrode tip thus affecting the performance for future measurements. A photograph of a microfabricated EHD blower in operation is shown in Figure 6.8. The figure shows the corona discharge region around the end of the microfabricated EHD cantilever blower. The image was captured using a thirty-second exposure time in a nearly dark room, with the device operating approximately 3 mm above the collector electrode.

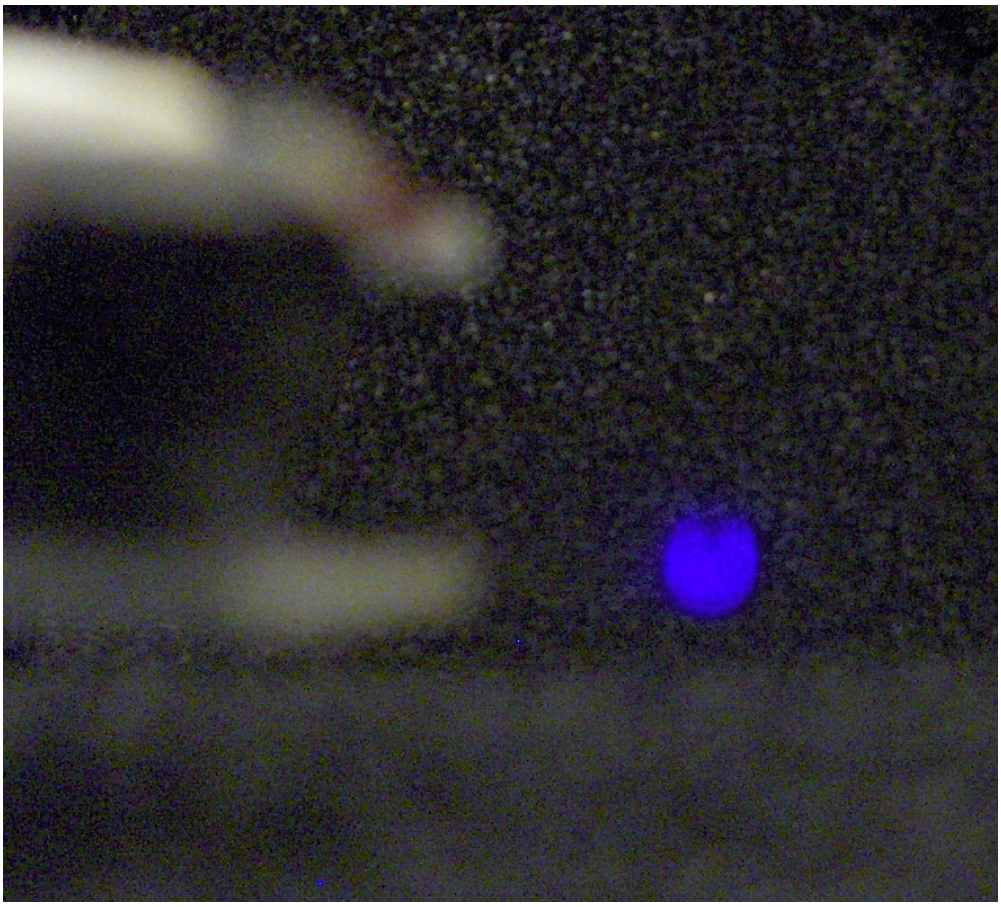

Figure 6.8. *Photograph of microfabricated EHD blower in operation with 30 second shutter exposure in near dark room. Blue purple glow from corona discharge at the end of the microfabricated EHD cantilever emitter. EHD emitter positioned 3 mm above the conductive plane.*

The maximum test voltages were chosen by first testing a similar microfabricated device at each separation distance to determine breakdown thresholds and then maintaining a margin of safety of approximately 10% to 20% below the breakdown threshold during testing. Therefore, the data does not necessarily display the maximum corona current achievable. Figure 6.9 shows that the corona onset voltage of the smallest to the largest separation distances ranges from 2.8 kV to 3.7 kV as expected, and the maximum power consumption was about 181 mW at 8.8 kV for the largest air gap separation of 5 mm. Although precise airflow measurements were not obtained for reasons explained previously, airflow was measured for all separation distances, with the highest velocity of 1.6 m/s at a separation of 5 mm and 7.8 kV.

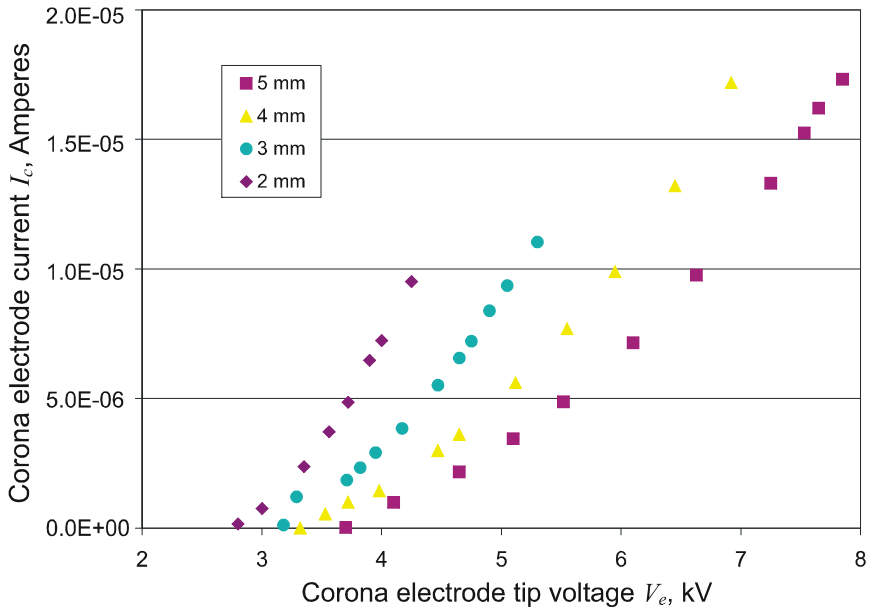

Figure 6.9. *Experimental corona current Ic vs. applied voltage Ve between corona and collector electrodes for the 5 mm cantilever prototype without the RIE sharpening process, Figure 6.5 (a). Data for air gap distances of 2 mm, 3 mm, 4 mm, and 5 mm are shown.*

6.2.3.3 Infrared imaging test setup and analysis

In this section, the cantilever-to-plane EHD blower prototype used for demonstration of forced convection cooling, Figure 6.10, was fabricated from a SOI wafer with a 350 μm silicon device thickness. Two experimental setups were used in this study. One was to determine the active region of the cantilever corona electrode, and another was to demonstrate the forced convection cooling effect of the cantilever-to-plane EHD blower. Figure 6.10 shows the experimental setup used for determining the active region of the corona electrode. In the picture, the black background is a 5 mm thick slab of black semiconductive foam that serves as the collector electrode. An electrically insulating layer of 7 mm thick Teflon was placed on top of the collector surface. A rectangular silicon substrate was secured to the top of the Teflon with the cantilever corona electrode protruding out from the edge of the silicon substrate and over the collector surface. A piece of semiconductive foam was placed over the silicon substrate and taped in place to provide an electrical connection to the cantilever corona electrode. A standard alligator clip was attached to the semiconductive foam atop the silicon substrate to create an electrical connection from the high voltage DC power supply to the

silicon substrate. Application of voltage between the corona and the collector electrode induces corona discharge. The corona discharge was found to occur only at the tip of the cantilever corona electrode, creating an ion stream traveling out and down from the tip as shown in Figure 6.11. Figure 6.11 was taken in low light conditions with an applied voltage near the breakdown threshold, so that the corona glow and pre-breakdown streamer could be observed.

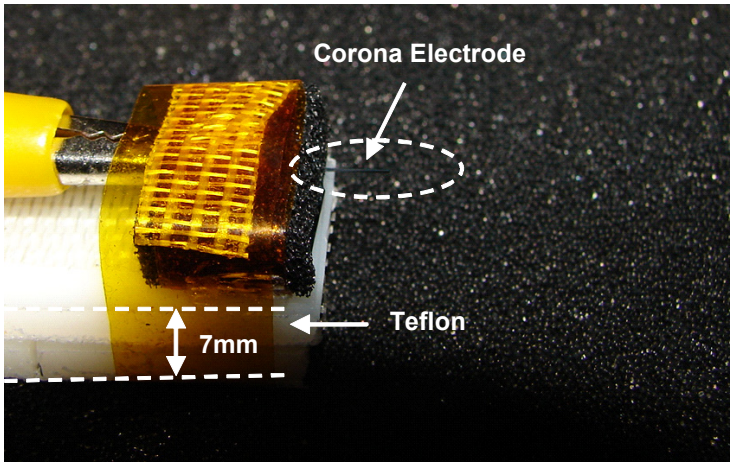

Figure 6.10. *Picture of experimental setup for determining corona electrode active region of a single cantilever-to-plane EHD blower.*

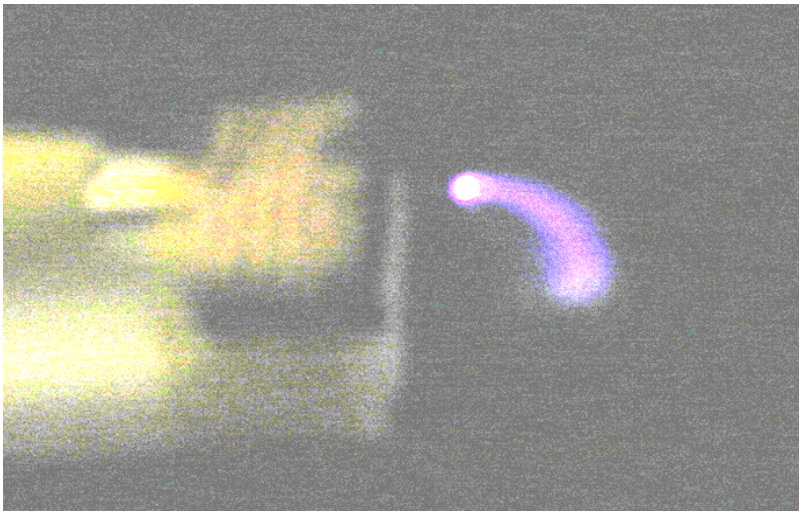

Figure 6.11. *Picture taken in low light condition showing active corona discharge region of cantilever corona electrode and resulting ion stream.*

The experimental setup for EHD driven forced convection heat transfer, shown schematically in Figure 6.1, was identical to the setup explained previously with two alterations. The insulating Teflon layer was replaced with a thinner slab of 4 mm

insulating foam, and the whole EHD blower assembly including collector, was placed on the surface of a digitally controlled hot plate. During the experiment, the hot plate was kept at a constant temperature of approximately 60°C. The experiment was conducted under ambient air conditions with an ambient air temperature of approximately 20°C. Semiconductive foam was chosen as a collector electrode due to its low reflectivity compared to other conductive surfaces, making it a good candidate for infrared imaging. Figure 6.12 and Figure 6.13 show five different stages of the experiment. All images were taken with a FLIR ThermCAM S series camera at approximately 200 frames per second at a resolution of 230×320. The scale on the right of each image shows temperature in °C and a corresponding color (shade in the black and white version). Orange color (lighter shade in b/w) corresponds to high temperatures, and blue color (darker shade in b/w) corresponds to low temperatures. The purple (light) and orange (light) rectangular objects at the bottom in Figure 6.12 and Figure 6.13 is the heated collector electrode, an equivalent of a thermal exchange surface. The blue (dark) object above is the silicon substrate, covered with semiconductive foam, from which the cantilever corona electrode is protruding. The corona electrode is small and near ambient temperature, and therefore is difficult to see at this resolution in Figure 6.12.

Figure 6.13 shows the setup with a hot plate on and in steady-state regime at a voltage above the breakdown threshold, which resulted in arching between the corona electrode tip and the collector surface. The corona electrode can be easily observed in this case due to a large temperature contrast between it and the surrounding environment. Both the corona electrode and a portion of the collector surface were heated to over 100°C due to the current-induced self-heating from the arching.

Figure 6.12 (a) shows the setup same as in Figure 6.13, but with the EHD blower turned off. Figure 6.12 (b) shows how the spot directly under the corona electrode cools slightly when the EHD blower was operating with low air velocity at an applied voltage of 5 kV. Figure 6.12 (c) shows the maximum cooling effect for this setup at an applied voltage of 8.5 kV. At this voltage the maximum substrate surface temperature reduction of 25°C was achieved at an operating current and power of approximately 70 μA and 0.6 W. Figure 6.12 (d) was taken at the end of the experiment, when the EHD blower was

turned off and the heat distribution returned to steady-state. This experiment demonstrates that even a setup unoptimized for thermal management can produce a significant cooling effect. Numerically modeled EHD blower performance characteristics for the experimental cantilever EHD blower are presented in Chapter 5.

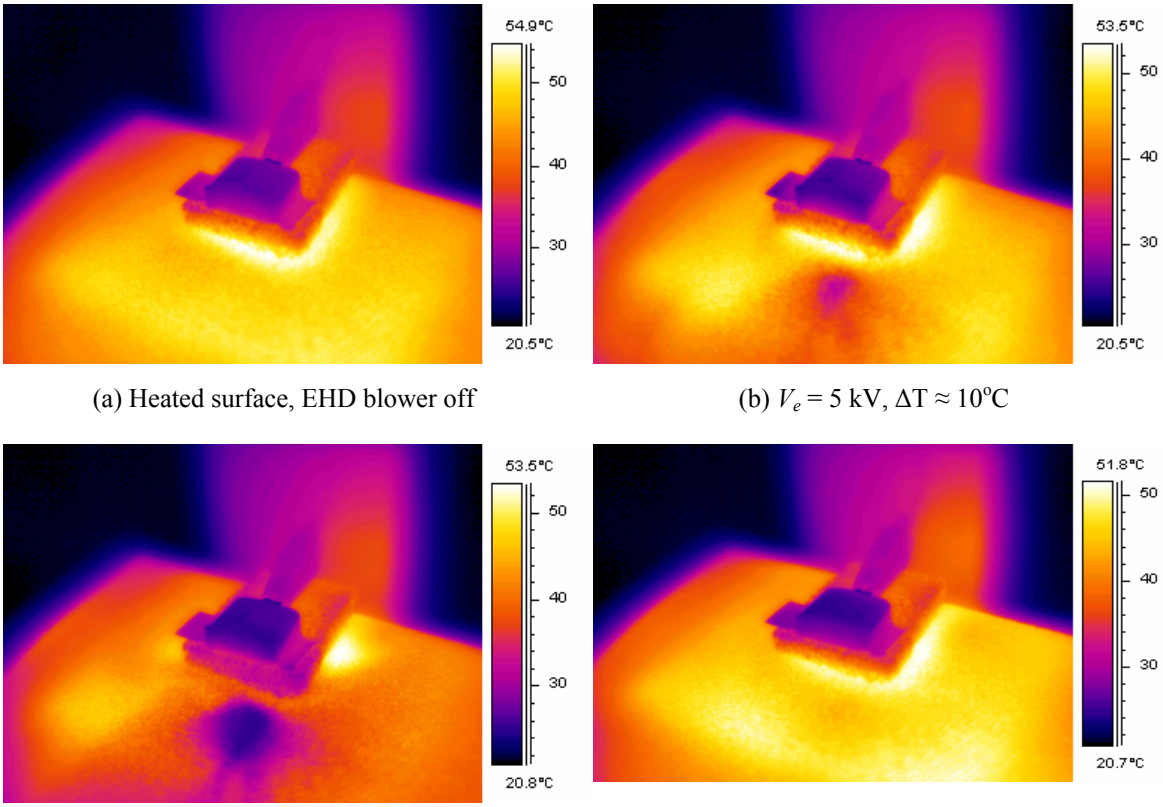

(a) Heated surface, EHD blower off

(b) V_e = 5 kV, $\Delta T \approx 10^{o}C$

(c) V_e = 8.5 kV, $\Delta T \approx 25^{o}C$

(d) Re-heated surface, EHD blower off

Figure 6.12. *Experimental demonstration of cooling effect with a microfabricated cantilever-to-plane EHD blower.*

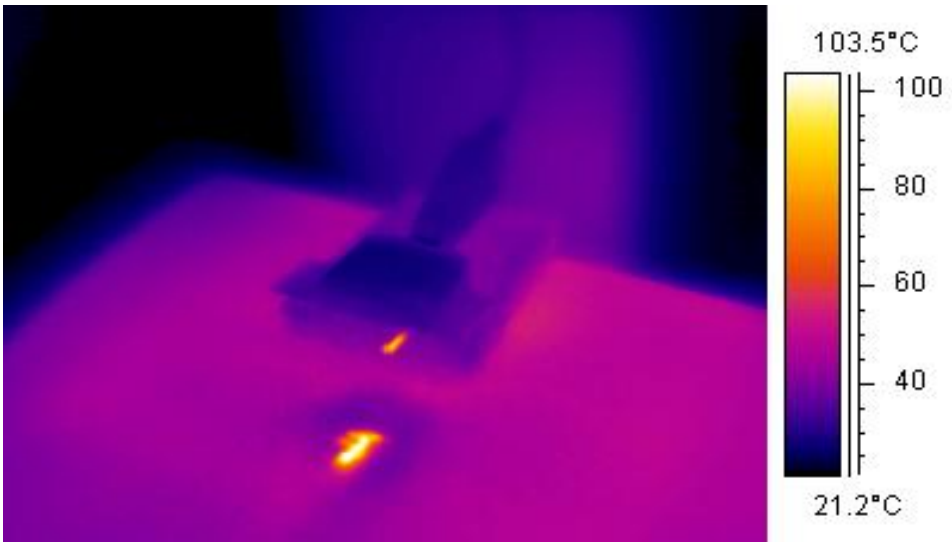

Figure 6.13. *Arcing caused by over voltage leading to corona electrode and substrate heating. Ve ≈ 9 kV.*

6.2.4 Summary

In this section, the design, fabrication, and testing of a proof of concept meso-scale EHD blower is discussed. A novel fabrication process for achieving high tip curvature and aspect ratio silicon corona tips has been demonstrated and multiple EHD blowers were fabricated. Current-voltage curves were measured for multiple air gap separations and compared to numerical results. The concept of meso-scale EHD-enhanced forced convection impingement cooling has been demonstrated using a microfabricated cantilever based EHD blower. Experimental results show that even an EHD blower unoptimized for forced convection enhancement can result in significant surface cooling. A 25^{o}C surface temperature reduction over an actively heated substrate was achieved at an applied voltage of 8.5 kV, with an operating current and power of 70 μA and 0.6 W, respectively.

6.3 Heat transfer measurement for meso-scale microfabricated EHD devices

6.3.1 Introduction

At present, most previous work of meso-scale EHD blower cooling focused on modeling efforts [22, 132] or basic proof-of-concept heat transfer enhancement experimental studies [2, 10, 11, 133]. Reported modeling results suggest local heat transfer rates of 200 W/m^2K are possible in a jet impingement regime [132] and heat transfer augmentation of over 200% can be achieved from boundary layer disruption over a flat plate [133].

In a previous chapter, the successful demonstration of a proof-of-concept microfabricated EHD cooling device was demonstrated. This chapter is a continuation of that study with an improved EHD design and focus on heat transfer measurements for the EHD system. The EHD blower investigated in this study consists of a microfabricated AFM-cantilever corona electrode and a flat collecting electrode that doubles as the thermal exchange surface. The fabrication results as well as electrical and thermal performance characterization of microfabricated EHD air movers are presented in this chapter. Air gap separation distances of 2 mm, 3 mm, 4 mm, and 5 mm between the corona electrode and the thermal exchange were examined under constant surface-to-ambient temperature difference of approximately 40^oC.

6.3.2 Background

The operating voltage range of EHD blowers lies between the corona discharge onset and the complete air gap breakdown voltages [59]. In thermal management of microelectronics, the air speed, operation voltage, and the ozone production are the three critical parameters for adopting EHD AIR MOVER technology. For a given electrode separation distance, it has been shown that the corona onset voltage as well as ozone production can be reduced by using a high aspect-ratio corona electrode [105, 134]. Lower ozone production and greater discharge uniformity can be achieved by selecting positive corona discharge over negative corona discharge [66, 135]. Because of the

aforementioned design criteria, the EHD blowers investigated in this study were designed to operate with positive corona discharge.

6.3.3 Corona electrode design and fabrication

6.3.3.1 Design

Figure 6.14 shows the schematic diagram of the proposed EHD air mover configuration for the EHD-enhanced forced convection cooling study. The microfabricated AFM-cantilever corona electrode is suspended over a flat collecting electrode, which doubles as the thermal exchange surface for the heat transfer enhancement measurements. During operation, a DC voltage is applied between the corona electrode and the collecting electrode, which creates a high electric field intensity and gradient at the corona tip, ionizing surrounding air molecules. The ions are then accelerated towards the collecting electrode, exchanging momentum with neutral air molecules along their path, thus resulting in bulk air movement for forced convection cooling from the hot surface. The EHD blower design in this chapter, although not necessarily optimal for cooling, was chosen because of its relative ease of fabrication and ease of experimental analysis. In addition, the design allows for higher local electric field intensity and gradient to be generated at the corona tip at a reduced applied voltage in comparison with the EHD blower design in [10] where a blade like corona emitter was formed along the bottom edge of a cantilever structure.

In order to fabricate a high aspect-ratio tip at the end of the cantilever structure, a fabrication process to exploit both negative and vertical sidewall etching profiles of deep reactive ion etch (DRIE) was adapted from [131], which had developed a nearly identical process to fabricate high aspect silicon needles for use in in-vitro neuron electrical potential measurements. For a given recipe, the sidewall etching profile for DRIE has been shown to depend on the exposed area and the etching depth around the structure [131], as shown in Figure 6.15. The negative sidewall angle θ increases as the exposed area increases for a given etching depth. In order to fabricate a solitary high aspect ratio pillar, and avoid the undercutting of the base of the pillar, a circle of sacrificial silicon poles are patterned and formed close to the enclosed corona tip shaft.

The sacrificial poles protect that center pillar maintaining its vertical sidewall etching profile, as shown in Figure 6.16 (c).

During the tip-sharpening step, the height of the corona tip shaft was maintained by a pre-deposited silicon dioxide masking layer. During the RIE tip sharpening step the sacrificial silicon poles etch away, leaving a high aspect-ratio silicon tip at the end of the cantilever structure, Figure 6.16 (d).

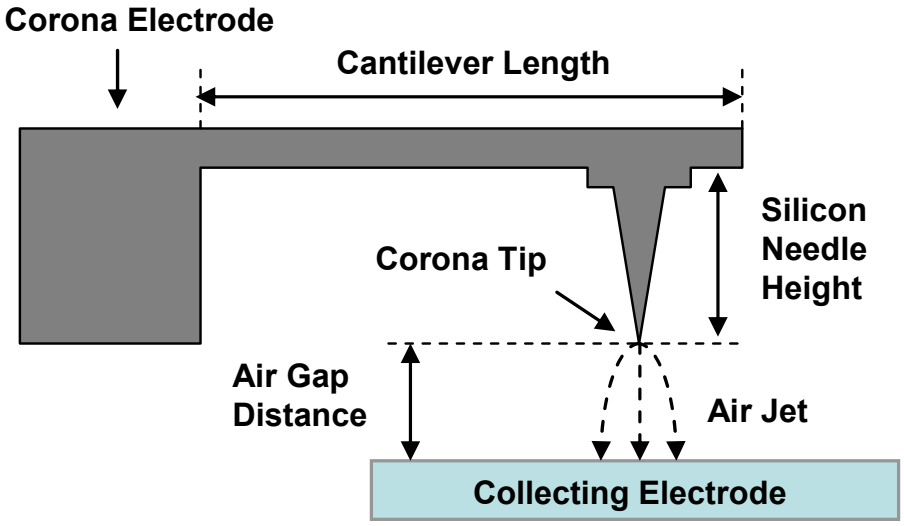

Figure 6.14. *Concept diagram for EHD-enhanced forced convection cooling. The EHD blower shown in the picture consists of a microfabricated AFM-cantilever corona electrode and a flat collecting electrode.*

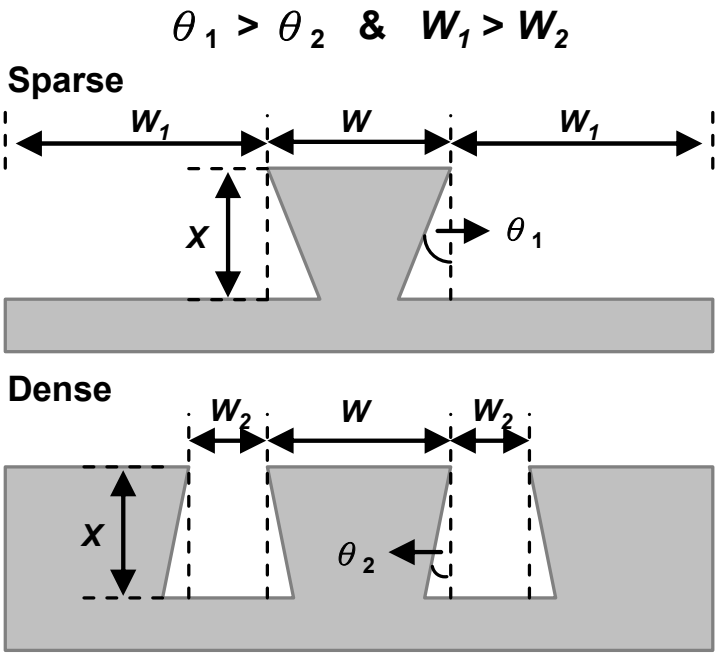

Figure 6.15. *Schematic diagrams of the negative sidewall etching profiles achievable in DRIE through proper pattern design for the given process parameters.*

6.3.3.2 Fabrication

Figure 6.16 shows the simplified fabrication procedure of the AFM-cantilever corona electrode structure. The process consists of three photolithography steps, including the definitions of the cantilever structure, the corona tip, and the corona tip shaft. First, the buried masking layer for forming corona tips, SiO2, was thermally grown, followed by an isotropic silicon dioxide etching on the top side of the wafer using reactive ion etching (RIE). Next, the cantilever structures of corona electrodes were defined using a standard photolithography procedure, Figure 6.16**.** A 10 μm thick photoresist AZ4620 was chosen as the masking layer for the later anisotropic silicon etching using DRIE. Subsequently, the corona tip patterns were created on the bottom side of the wafer using the aforementioned photolithography procedure and the isotropic silicon dioxide etching, Figure 6.16 (b). After the corona tip patterning, the corona tip shafts and their sacrificial silicon poles were patterned and formed using DRIE, Figure 6.16 (c). Prior to the final tip sharpening process using RIE, the photoresist was stripped off, leaving only the silicon dioxide as the masking layer during the tip sharpening

process. Finally, the corona emitter tips were sharpened and the sacrificial silicon poles were etched away with RIE, as shown Figure 6.16 (d).

Figure 6.17 shows the SEM images of a microfabricated AFM-cantilever corona electrode with a length of 8 mm from the substrate to the end of cantilever before and after the tip sharpening process. The resulting negative sidewall angles of the outer sidewalls of sacrificial silicon poles range approximately from 3 to 6 degrees, as shown in Figure 6.17 (a). After final tip sharpening, a high aspect-ratio silicon tip of 413.22 μm in height was formed, Figure 6.17 (b). In this study, both fabrication and testing results of 5 mm and 8 mm long AFM-cantilever corona electrodes were reported. A detailed wafer specification is listed in Table 6.4.

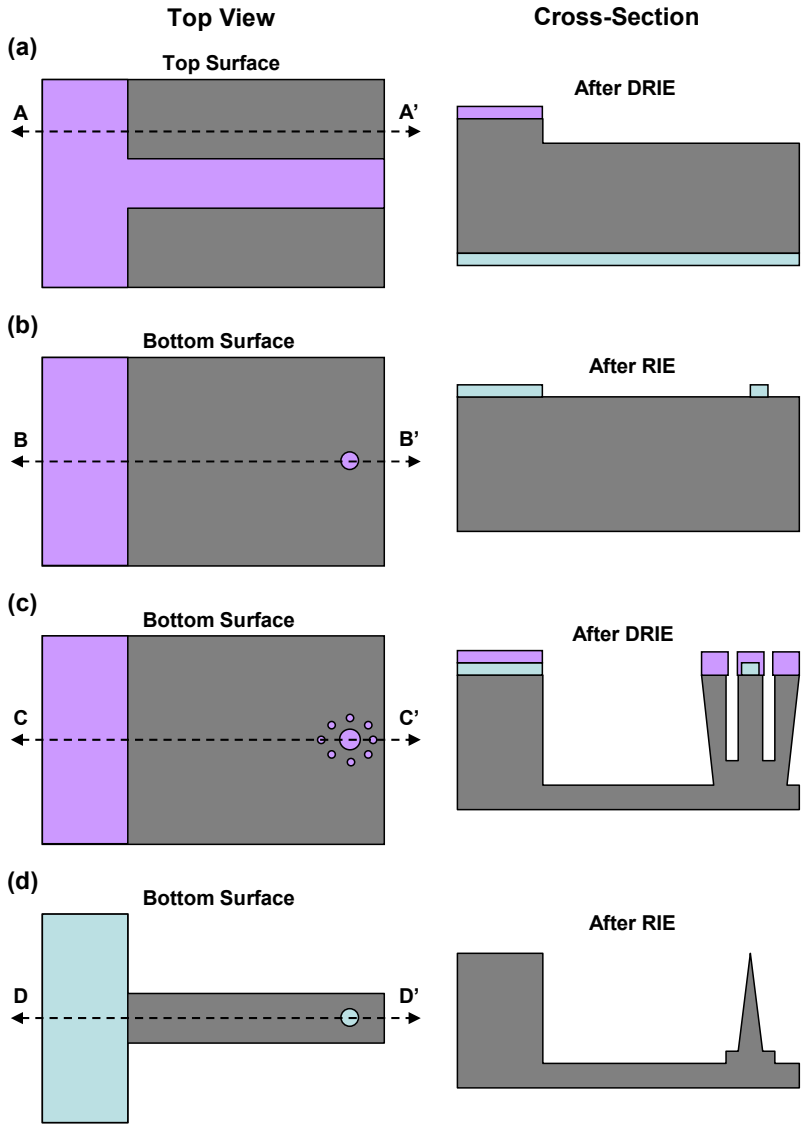

Figure 6.16. *Schematic diagrams of the process flow for the fabrication of AFM-cantilever corona electrode. In the diagrams, gray, purple, and light blue areas represent silicon substrate, photoresist AZ4620, and silicon dioxide, respectively. a) cantilever structure patterning, b) corona tip patterning, c) corona tip shaft patterning and formation, d) tip sharpening.*

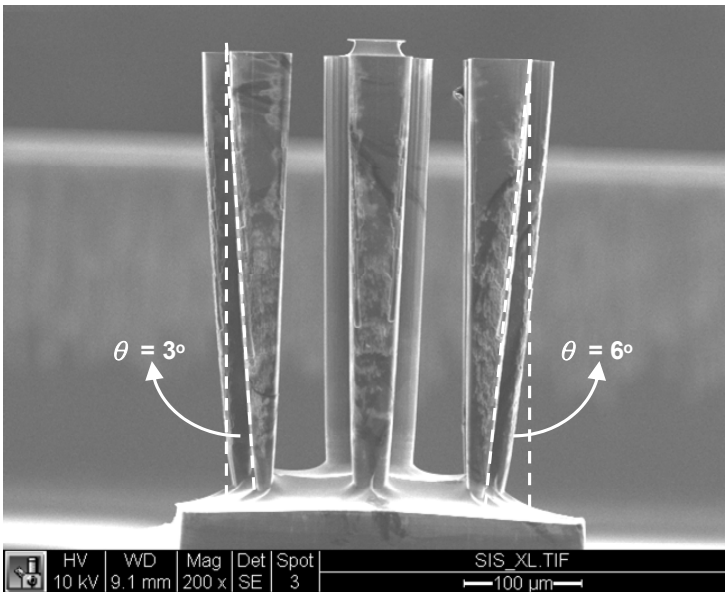

(a) SEM image of the microfabricated AFM-cantilever corona electrode before the tip sharpening process.

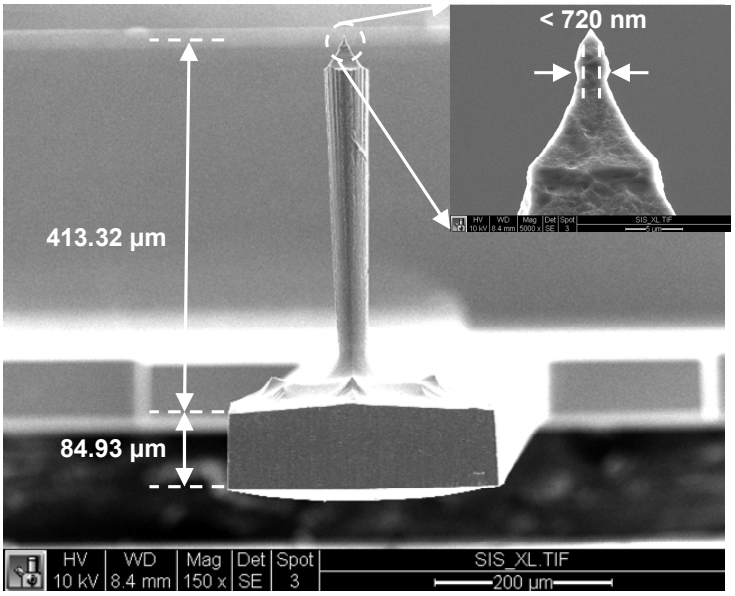

(b) SEM image of the microfabricated AFM-cantilever corona electrode after the tip sharpening process.

Figure 6.17. *SEM micrographs of an 8 mm long microfabricated AFM-cantilever corona electrode before and after the tip sharpening process. The resulting radius corona tip curvature is less than approximately 360nm.*

TABLE 6.4. *Silicon wafer specification for corona electrode fabrication.*

Type	Orientation	ρ, Ω-cm	Thickness, μm
N/As	1-0-0	0.001-0.004	500-550

6.3.4 Heat transfer enhancement measurement setup, procedure, calculations, and results

6.3.4.1 Experimental setup

The experimental setup for heat transfer enhancement measurement of microfabricated EHD blowers used a customized designed testing platform, as shown schematically in Figure 6.18. The platform consists of a thermal insulation block, electrical heater (1 X 1 in^2), thermal interface material (TIM), a 3 mm thick copper collecting electrode (1 X 1 in^2), four plastic screws, and four K-type thermocouples. In order to minimize the heat loss from the peripheral surfaces of collecting electrode, the electrode was clamped in place using plastic screws. Only the top surface of electrode was exposed to surrounding air. The remaining surfaces were enclosed by the thermal insulation block. Four holes were drilled into the sidewalls of both the collecting electrode and the thermal insulation block to position the thermocouples, Figure 6.18. The thermocouples were placed 5 mm deep inside the collecting electrode from each side wall. All thermocouples were electrically insulated with Kapton tape. In addition, a TIM was placed between the collecting electrode and the electrical heater to ensure that no electrical conduction path exists between them, as well as to minimize the interface thermal resistance. The collecting electrode surface temperature was defined by averaging the readings of four thermocouples.

In order to precisely control the air gap distance between the corona and the collecting electrodes, an optical xyz stage was used. To measure corona current, the corona electrode was connected to the positive polarity of high voltage DC power supply and the collecting electrode was placed in series with a 100 kΩ resistor to the ground. The corona current was then measured by monitoring the voltage drop across the resistor.

The power delivered to the heat elements was similarly measured by adding a 1.2-Ω resistor in series with the AC electrical heater. Figure 6.19 shows the experimental setup for heat-transfer enhancement measurement.

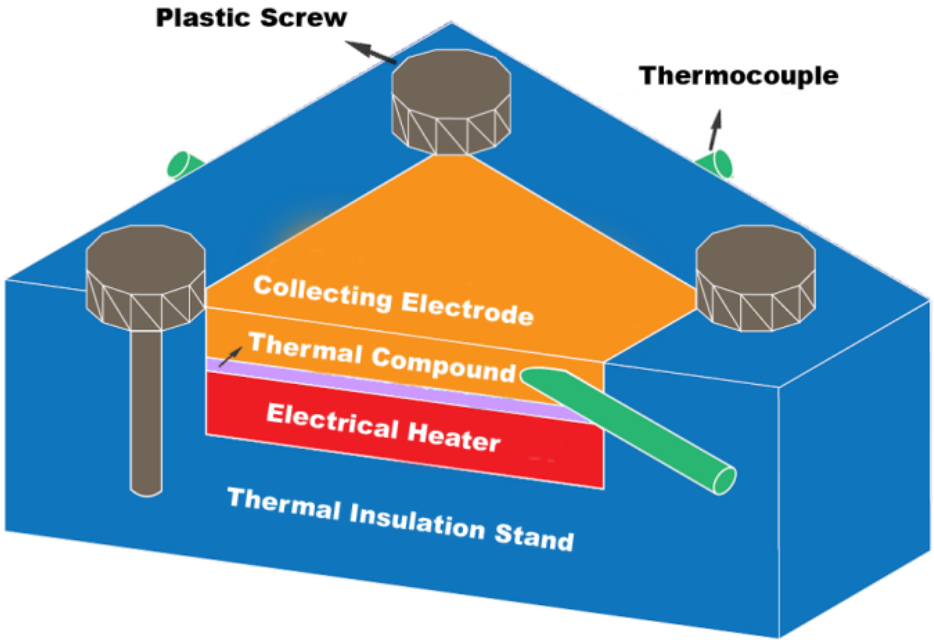

Figure 6.18. *Schematic diagram showing the cross-section of the thermal test platform for heat transfer enhancement measurement of microfabricated EHD blowers. The platform consists of an electrical and thermal insulation block (blue), AC electrical heater (red), ceramic-based TIM layer (purple), copper collecting electrode (orange), four plastic screws (brown), and four electrically insulated K-type thermocouples (green).*

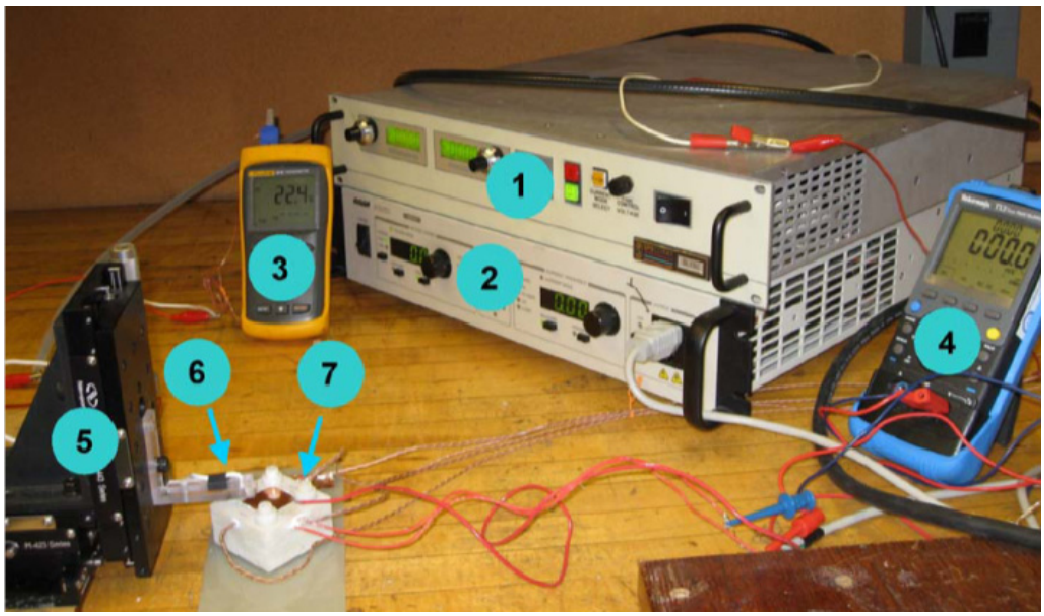

Figure 6.19. *Picture of the experimental setup. (1) High-voltage dc power supply. (2) Heat-source power supply. (3) Thermocouple reader for ambient temperature measurement. (4) Multimeter. (5) Micropositioning xyz stage. (6) Dielectric EHD emitter-mounting platform. (7) Thermal-insulation stand.*

6.3.4.2 Procedure

All measurements were conducted in ambient conditions. The ambient temperature, T_{air}, varied from 21.1°C to 22.3°C. Through all measurements, the microfabricated corona electrodes were fixed parallel to the collecting electrode with air gap separation distances of 2 mm, 3 mm, 4 mm and 5 mm. In addition, the collecting electrode surface temperature T_s was controlled to have a fixed temperature difference ΔT between the ambient temperature of 38.3°C. The heat transfer rate due to free convection and conduction, Q_{t0}, was obtained by calculating the heating power to maintain a delta T from ambient of 38.3°C with the EHD off. Then, the forced convection heat transfer rate with corona wind, Q_t, was obtained at different operating voltage levels for the given air gap separation distance by adjusting the AC input power to the heater to maintain the constant surface-to-ambient temperature difference.

6.3.5 Calculations

The total heat transfer rate in free convection was calculated using

$$Q_{t0} = Q_{c0} + Q_{r0} + Q_{loss0} \tag{6.1}$$

where Q_{c0} is the free convection heat transfer rate, Q_{r0} is the radiation heat transfer rate of the collecting electrode surface in free convection, and Q_{loss0} is the heat loss from the peripheral sides of the collecting electrode and the electrical heater in the free convection measurement. With corona wind present, the total heat transfer rate Q_t can be described in a similar form

$$Q_t = Q_c + Q_r + Q_{loss} \tag{6.2}$$

where Q_c, Q_r, and Q_{loss} are aforementioned terms but in the forced convection conditions.

Because the surface-to-ambient temperature difference ΔT was maintained constant, it is reasonable to assume that the radiation heat transfer rate and the heat loss terms in (6.1) and (6.2) were constant. By rearranging (6.1) and (6.2), the increase of average convective heat transfer coefficient, and the heat transfer enhancement due to the microfabricated EHD induced air jet can be calculated

$$\Delta\bar{h} = \bar{h} - \bar{h}_0 = \frac{\Delta Q_t}{A\Delta T} \tag{6.3}$$

$$\frac{\bar{h}}{\bar{h}_0} = 1 + \frac{\Delta Q_t}{Q_{c0}} \tag{6.4}$$

where $\bar{h}$ is the average forced convective heat transfer coefficient, h_0 is the average free convective heat transfer coefficient ΔQ_t, is the heating power difference, and A is surface area of the collecting electrode.

In all experiments, since the free convection heat transfer term was not measured, an average free convection heat transfer coefficient of approximately 10 W/m^2K calculated from published data [27, 33] was used for the calculation of heat transfer enhancement in (6.4).

6.3.5.1 Experimental results

From Figure 6.20 to Figure 6.25, the experimental results of the corona current and heat transfer enhancement measurements are presented using 8 mm and 5 mm long microfabricated silicon AFM-cantilever corona electrodes. Four air gap separation distances between the corona and the collecting electrodes were examined. The tested 8 mm long AFM-cantilever electrodes have an average silicon needle height of approximately 412 μm and the tested 5 mm long AFM-cantilever electrodes have an average silicon needle height of approximately 422μm. The radii of corona tip curvature are less than 500 nm for all tested electrodes.

Figure 6.20 and Figure 6.21 show the corona current measurement results using 8 mm long AFM-cantilever corona electrodes and the resulting increases of average convective heat transfer coefficient at different levels of EHD blower operating voltages. As expected, higher applied voltage led to increased corona current under a given air gap separation distance. The slope of current curve was greater as the air gap separation distance decreased, implying that the operation voltage range of EHD blower is narrower in smaller air gap separation distance, Figure 6.20. This effect is described in depth in previous chapters. In Figure 6.21, experimental results show that the increase of average convective heat transfer coefficient $\Delta\bar{h}$ is linearly proportional to the applied voltage. This is because the velocity of EHD-induced air flow is proportional to cubed root of the power, and in this geometry the corona current increases approximately with the square of the voltage. This creates a linear relationship between the voltage and flow rate [136], resulting in a near linear increase of the average forced convective heat transfer coefficient with voltage above corona onset.

However, although the EHD power was greater for a given applied voltage at the smaller air-gap separation distance, the heat-transfer enhancement was observed to be

less. This is likely due to the fact that the smaller distance created a more focused ion stream and thus a more focused air jet, reducing the surface area on the heating plate that received a high velocity jet flow. In addition, the reduce distance would also reduce the amount of airflow entrained by the jet onto the surface further reducing the heat removal. The results are consistent with other experimental observations presented in [29].

Figure 6.22 and Figure 6.23 show similar experimental result trends and magnitudes acquired by using the 5 mm long AFM-cantilever corona electrodes. As the distance between the cantilever base anchor and the tip increases, the field interference from the base also decreases, resulting in a higher gradient electric field around emitter tip. As expected the higher tip gradient and field strength at the tip of the 8 mm device, as compared to the 5 mm device, resulted in a higher current for a given voltage and a higher maximum observed increase in average convective heat transfer coefficient. A maximum average heat transfer convection coefficient of 53.7 W/m^{2}K was achieved at 7 kV for the largest tested air gap separation distance with the 8 mm device.

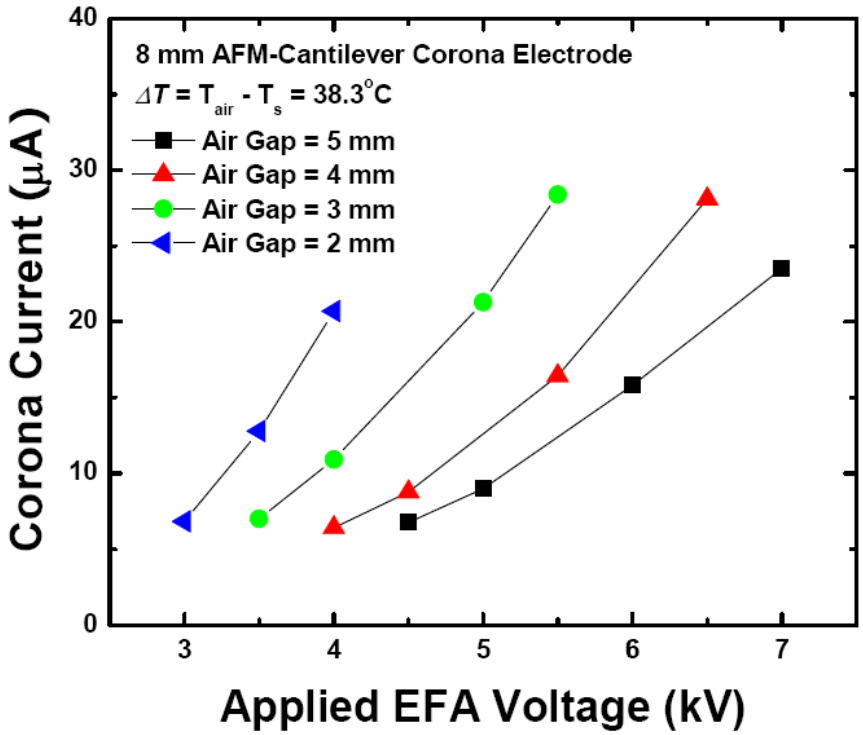

Figure 6.20. *Measurement results of corona current for using 8 mm long AFM-cantilever corona electrodes.*

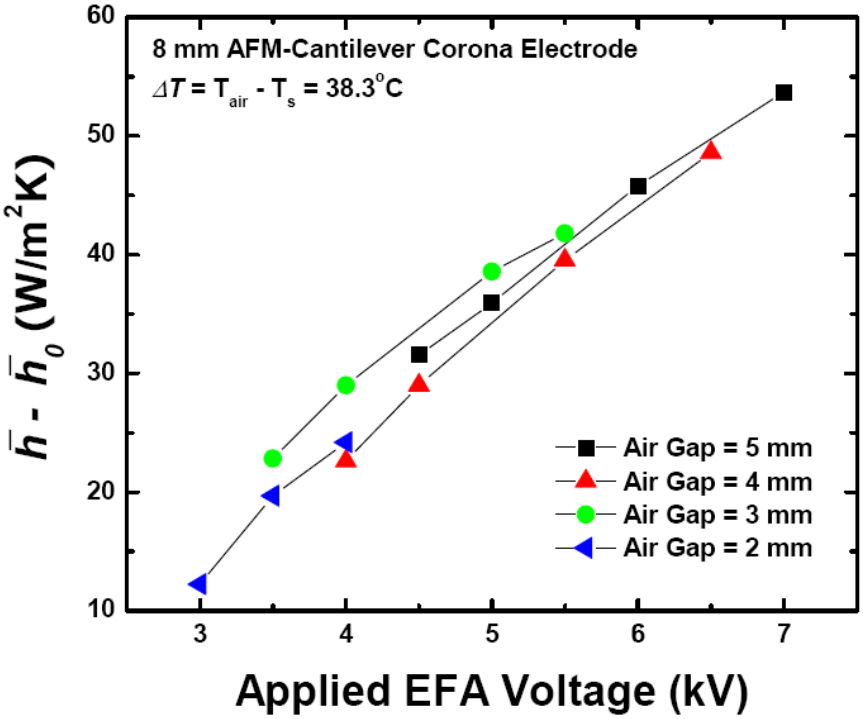

Figure 6.21. *Measurement results of the difference in average heat transfer coefficient for forced and free convections using 8mm long AFM-cantilever corona electrodes.*

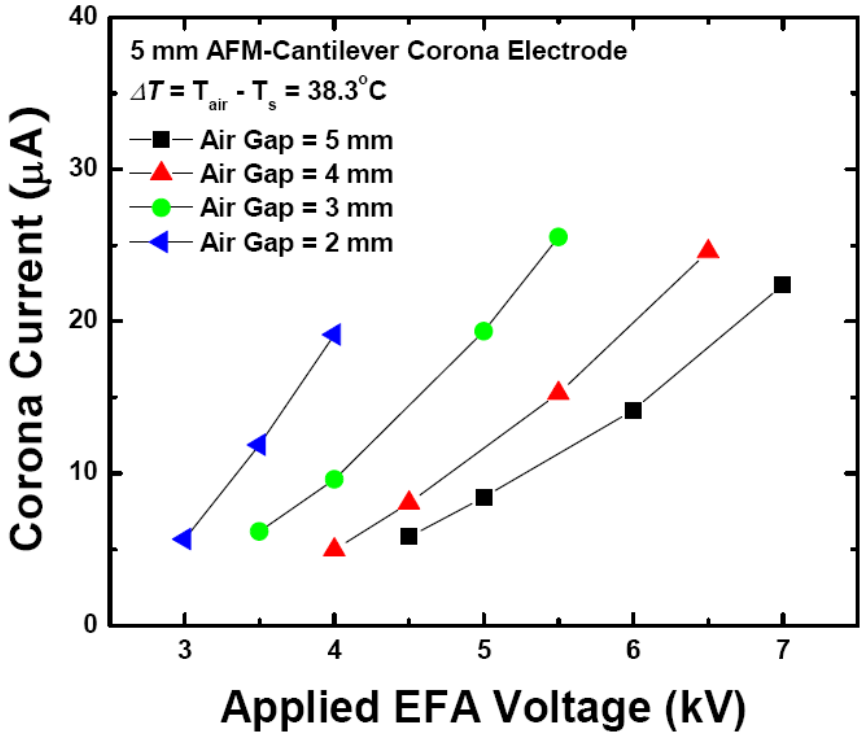

Figure 6.22. *Measurement results of corona current for using 5 mm long AFM-cantilever corona electrodes.*

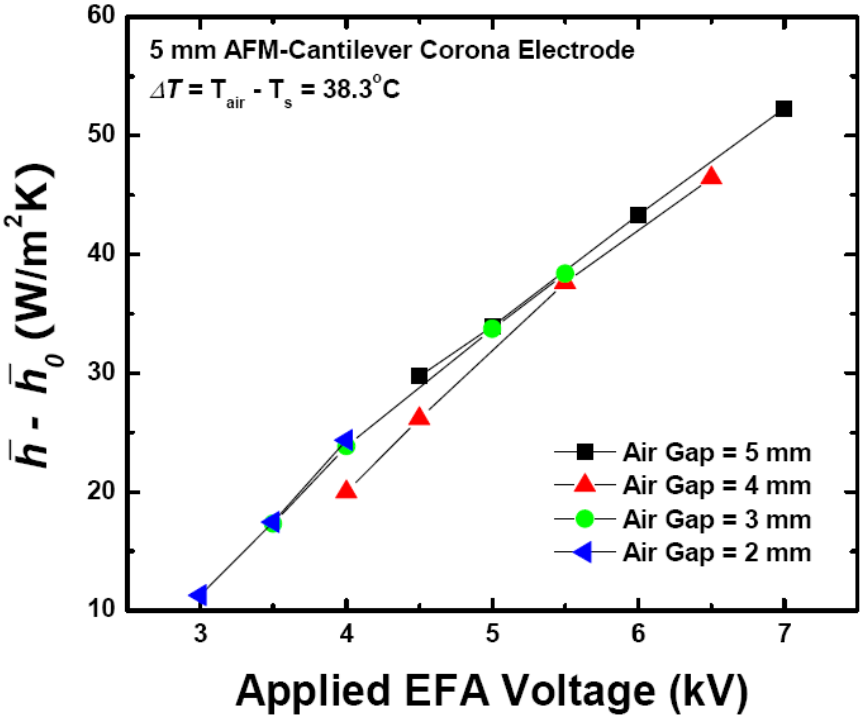

Figure 6.23. *Measurement results of the difference in average heat transfer coefficient for forced and free convections using 5 mm long AFM-cantilever corona electrodes.*

Figure 6.24 and Figure 6.25 show the measurement results of the total heat being removed by the EHD-induced air flow using 8 mm and 5 mm long AFM-cantilever corona electrodes. As shown in the results, as the EHD power increased, the speed of induced airflow jet increased, creating greater heat transfer from the heated surface. Since the heat transfer rate cannot increase faster than the increase in flow rate, and the flow rate increases at the cubed root of the power, the ratio of heat power removed vs. electrical power consumed by the EHD system will decrease with increasing power. The reader should be reminded that this is true of all air movers, EHD or otherwise. The greatest thermal power removed was achieved by the 8 mm long AFM-cantilever corona electrode of approximately 1.33 W at 7 kV at the largest tested air gap separation distance. The resulting EHD blower power consumption was approximately 165 mW.

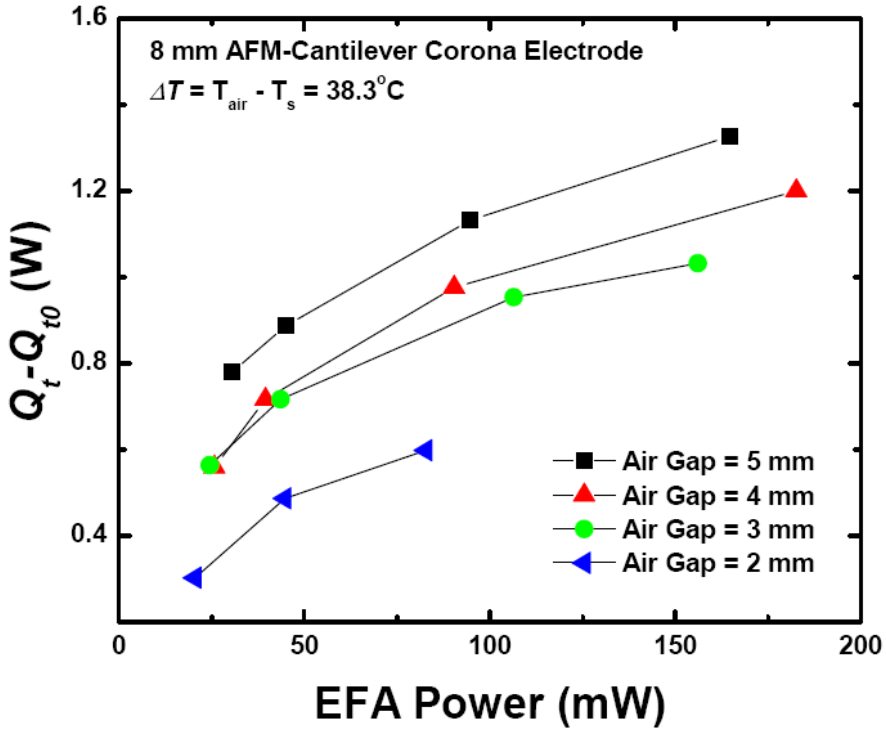

Figure 6.24. *Effects of EHD blower power on heat transfer enhancement for using 8 mm long AFM-cantilever corona electrodes.*

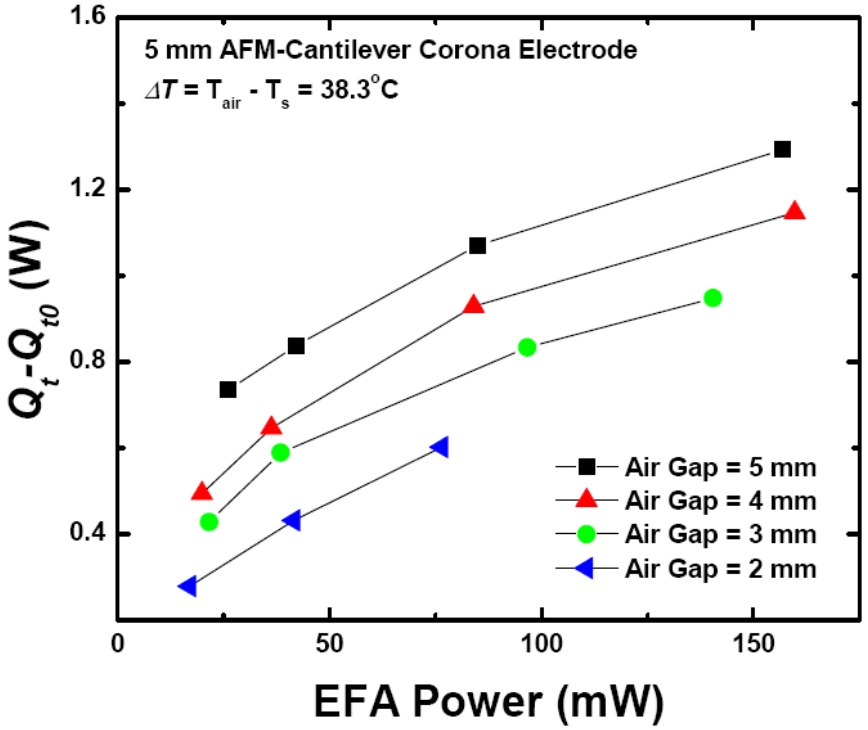

Figure 6.25. *Effects of EHD blower power on heat transfer enhancement for using 5 mm long AFM-cantilever corona electrodes.*

In this study, no special treatment was done to improve the corona electrode longevity, thus, in order to maintain the integrity of corona tips, maximum allowable applied voltages for each air gap separation distance were not pursued. Therefore, the maximum achievable increase of average convective heat transfer coefficient and the power removed by EHD blower are not presented.

Figure 6.26 and Figure 6.27 show the heat transfer enhancement results of the tested devices. Free convection heat transfer coefficient of 10 W/m^2K was used to calculate the enhancement using (6.4). Experimental results show that the heat transfer enhancements are similar for the 8 mm and 5 mm long electrodes. The maximum augmentations are approximately 6.37 and 6.23 at 7 kV at the largest tested separation distance, respectively. Since the augmentations shown in Figure 6.26 and Figure 6.27 are average values over the entire collecting electrode surface, significantly greater heat transfer augmentations are expected to have been present towards the center area of the surface.

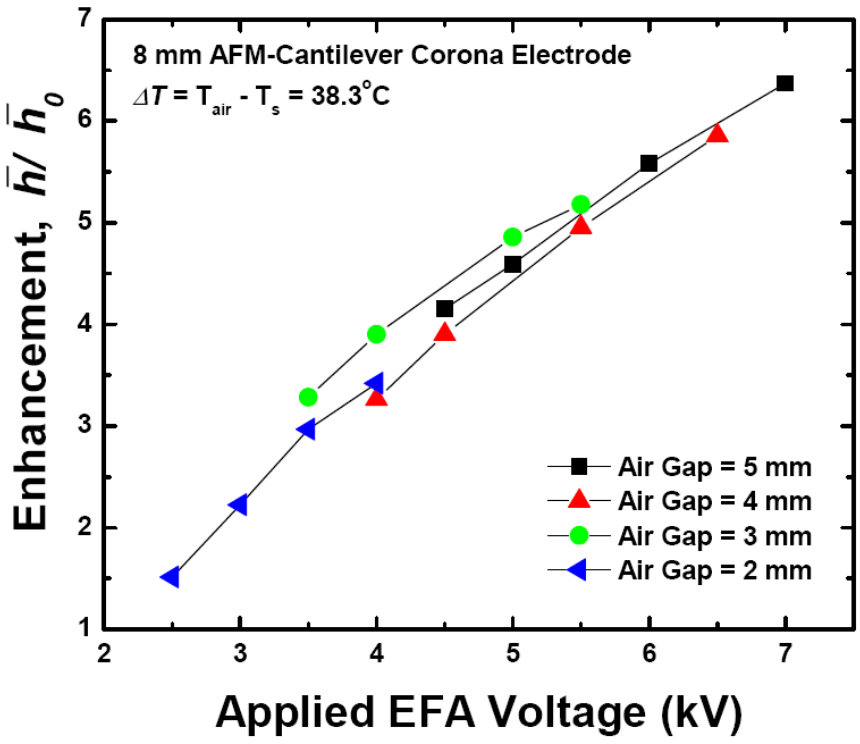

Figure 6.26. *Measurement results of the heat transfer enhancement for using 8 mm long AFM-cantilever corona electrodes.*

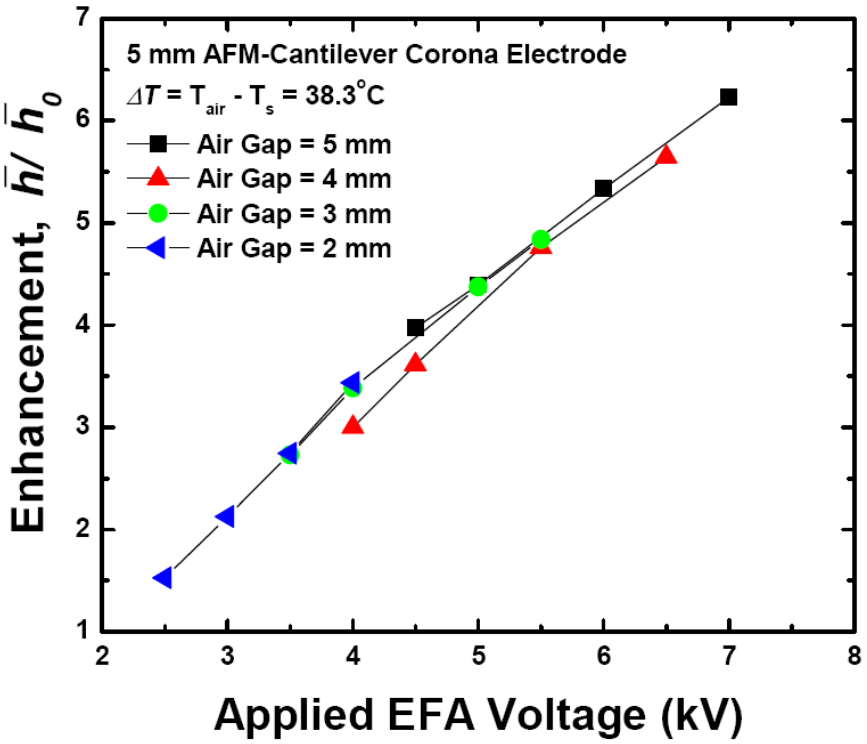

Figure 6.27. *Measurement results of the heat transfer enhancement for using 5 mm long AFM-cantilever corona electrodes.*

6.3.6 Summary

In this study, a microfabricated EHD blower was constructed, tested, and electrical and thermal results analyzed, demonstrating the heat removal magnitudes and values for a meso-scale EHD blower device. The experimental results are similar for both 8 mm- and 5 mm-long devices at all tested air gap separation distances. A maximum average convection heat transfer coefficient increase of 53.7 W/m^{2}K was achieved using an 8 mm-long AFM-cantilever corona electrode for an applied voltage of 7 kV at the largest tested air gap separation distance. The resulting EHD blower power consumption was approximately 165 mW, which represented one-eighth of the total heating power removed. The maximum average heat transfer enhancement ratio was 6.37, however greater heat transfer augmentations are expected to have been present towards the center area of the heat transfer surface in the region of highest impinging air jet velocity.

6.4 Experimental vs. numerical predicted heat transfer measurements for meso-scale cantilever-to-plane EHD devices

This subchapter presents a comparison of numerical and experimental electrical and thermal measurements of a meso-scale cantilever-to-plane EHD used for jet impingement forced convection heat transfer. EHD blower thermal measurements for simulated and experimental meso-scale devices have been presented in previous subchapters. Direct comparison of the simulated and experimental results is possible, though limited to the aspects that a 3D axial symmetric numerical model can predict accurately of an inherently non axial-symmetric cantilever-to-plane EHD structure. In this light, direct comparison are made where axial-symmetric assumptions are valid, and where they are shown to be invalid, scaling calculations are proposed based on experimentally observed cantilever-to-plane EHD performance characteristics.

6.4.1 Comparison of numerical and axial-symmetric model geometries

A top view comparison of the effective axial-symmetric numerical model geometry and the experimental testing setup geometry in schematic form are shown in Figure 6.28. In both cases, the active area of the EHD blower is positioned over the center for the flat collector-electrode/heat-transfer surface, and the size of the collector electrode is large compared to the emitter to collector distance making it look like an infinite plane to the corona emitter. The cross section of the emitter tip are similar in both cases with a sharp bottom towards the collector surface and a blunt top side. The numerical and experimental geometries are shown in previous sub chapters in Figure 5.23 and Figure 6.14, respectively. Thus, the current and voltage relationship for the numerical and experimental device should be similar.

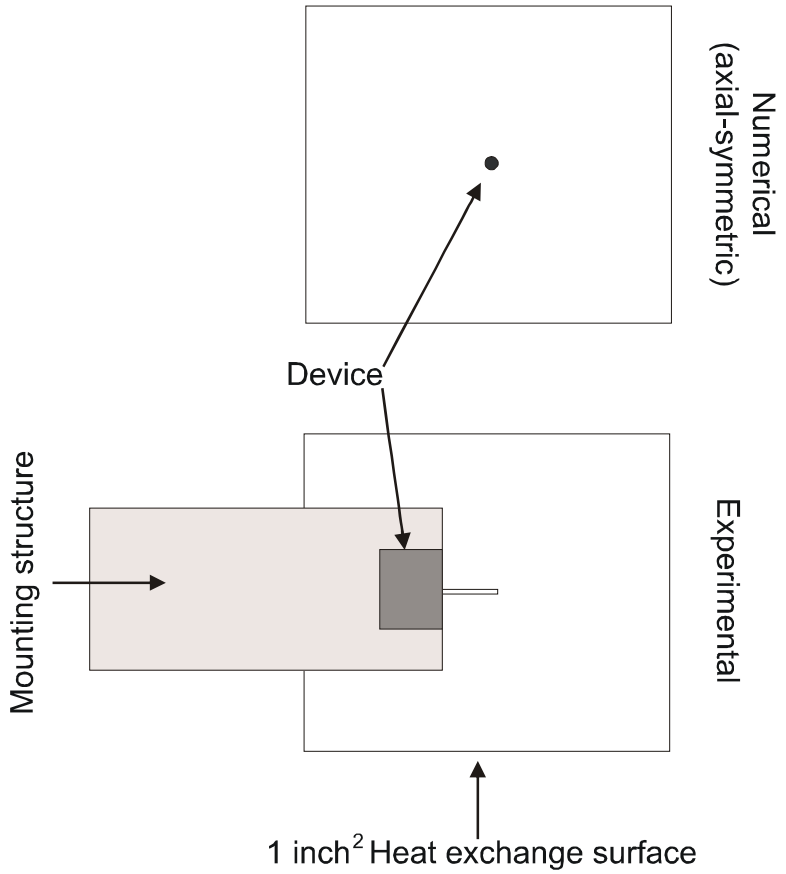

Figure 6.28. *Top view of cantilever-to-plane EHD blower heat transfer measurement setup for the axial-symmetric numerical model and experimental model geometry, shown on top and bottom respectively.*

However, differences do exist. The axial symmetric model does not take into account the electrical effect of the cantilever beam or that of the mounting structure. As described in previous chapters, the electrical field impact of the beam and mounting structure prevent the ion flow from impinging down symmetric around the emitter tip, as is the case in the axial symmetric model, but instead cause the ion stream to be projected out and away from the beam and mount structure. Since the air jet is entrained by the ion stream, the air jet trajectory is similarly moved to the right as is shown in Figure 6.29. In addition to the electrical impact on the air jet trajectory, the device mounting structure creates a physical barrier to the flow on one side of the heat transfer surface, which further changes the flow pattern. The solid obstacle of the mount prevents airflow from

moving under it and tends to baffle flow away from the end of the mount, adding to the trajectory change.

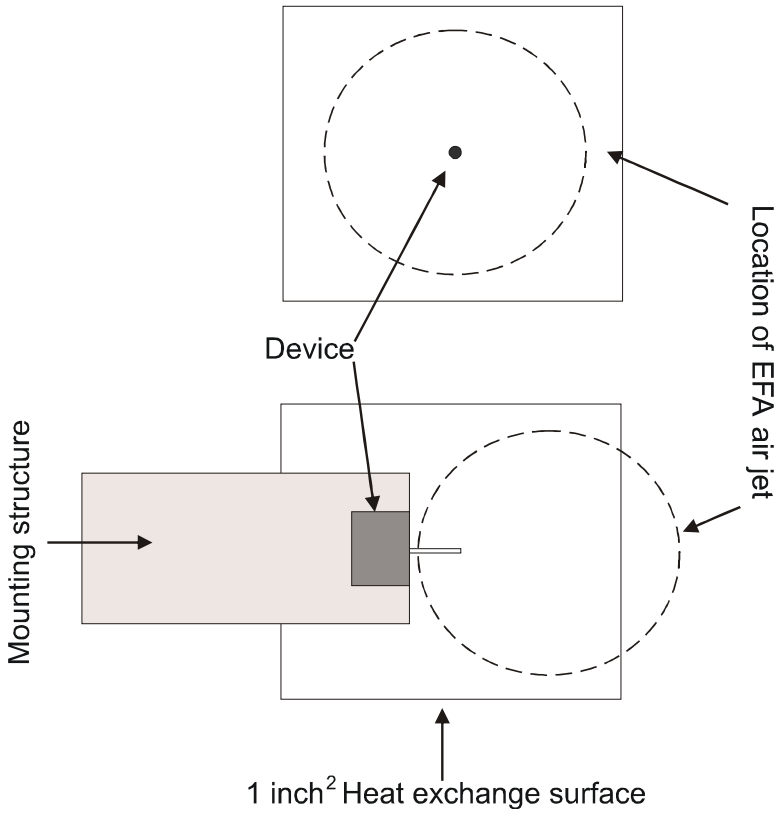

Figure 6.29. *Top view of cantilever-to-plane EHD blower heat transfer measurement setup showing location of EHD blower air jet for both the axial symmetric numerical model and experimental model, shown on top and bottom respectively.*

The change in location of the air jet will influence the total heat removed from the surface and therefore affect the average convection heat transfer coefficient from the surface. Compared to the numerical case, where the air jet impinges on the center of the heat exchanger and then radiates outward in all directions increasing the heat transfer across the entire surface, the experimental case will only increase the heat transfer over a portion of the surface. The region of the surface not affected by the air jet can be assumed to be at or near free convection heat transfer rates, thus reducing the total heat transfer from the surface compared to the numerical case.

6.4.2 Electrical and thermal result comparison

A 3 mm emitter to collector electrode distance was used for both numerical and experimental studies, and an 8 mm AFM tip EHD blower cantilever was used for the experimental results compared in this section. The data presented is taken from numerical and experimental models described in detail in chapters 5.6.2 and 6.3 respectively.

6.4.2.1 Electrical

A comparison between numerical and actual current versus voltage results shows good agreement between simulated and experimental models. The lower numerical emitter current is likely due to the difference in emitter geometry used in the model, which was without the high tip curvature regions at the very tip of the emitter.

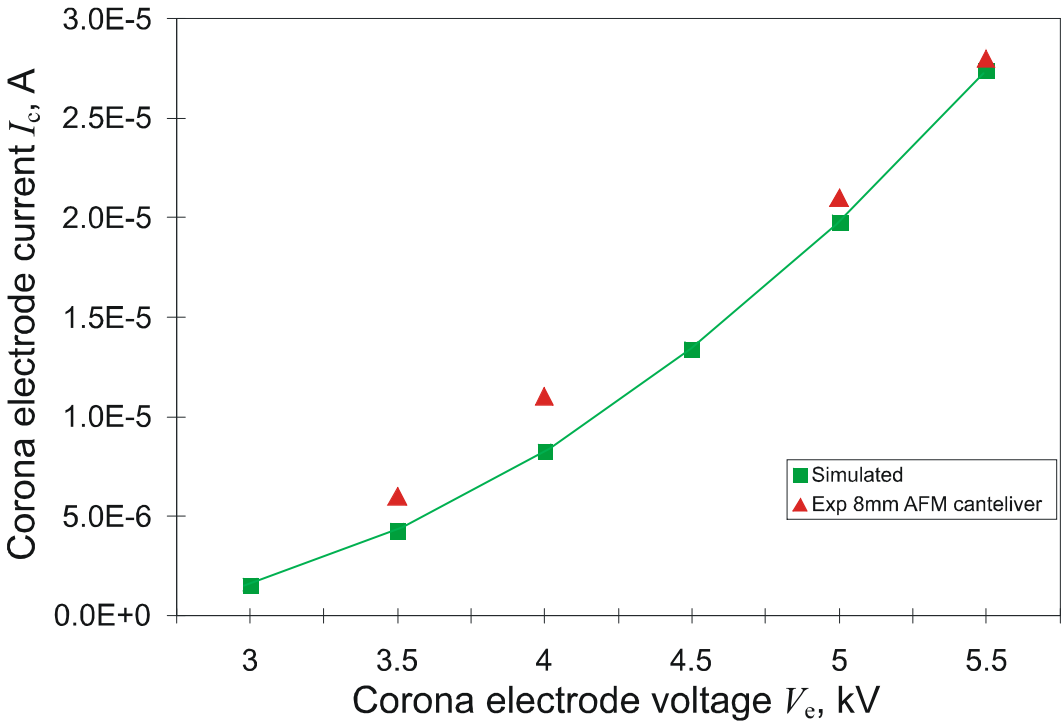

Figure 6.30. *Simulated vs. experimental corona current and voltage for a 3 mm air gap.*

6.4.2.2 Thermal

A summary of the numerical and experimental heat transfer measurement procedures are as follows. The numerical heat transfer rates were calculated and averaged over a constant radius circular disk over the heat transfer surface and centered under the corona electrode, in the same manner described in Chapter 5.6.2. The radius of the disk was increased or decreased to change the area over which the measurement was taken.

The experimental heat transfer measurements were taken using the experimental setup described in Chapter 6.3, which consisted of a constant temperature controlled heat transfer surface made of a 1 in^2copper plate.

For the reasons described in the previous section, a direct comparison of average heat transfer rates over a one square inch area for the numerical and experimental study will result in experimentally measured average convective heat transfer coefficient being less than numerical results, which is confirmed in Figure 6.31.

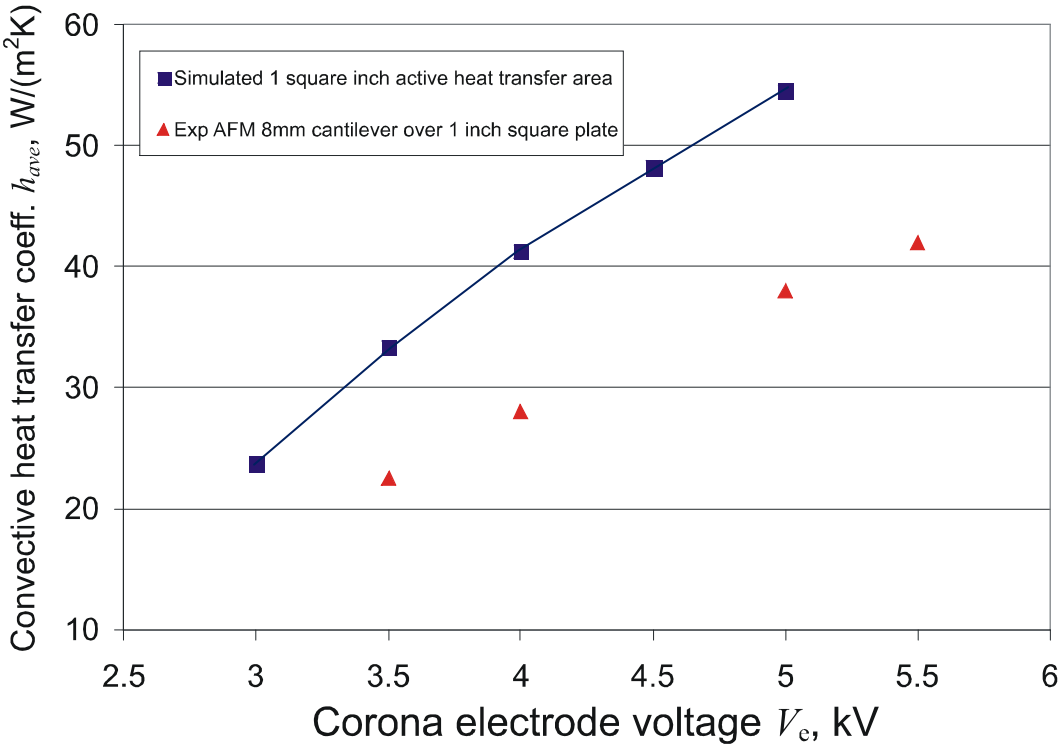

Figure 6.31. *Simulated vs. experimental average convective heat transfer results, with simulated results assuming EHD air jet is centered under corona electrode.*

When the numerical results assume the EHD air jet is centered on the heat transfer surface the predicted average heat transfer rate over a 1 in^2area is larger than the measured value, as shown in Figure 6.31., . However, if the EHD induced air jet is assumed to be offset from the center, as depicted in the bottom half of Figure 6.29 and seen experimentally in Figure 6.12 (c), a good correlation is seen between modeled and measured results, Figure 6.32. For the results shown in Figure 6.32, it was assumed that the air jet was focused over one third of the 1 in^2 plate. The remaining two thirds of the surface area not in the flow path were set to a free convection heat transfer rate of 10 W/m^2K, the same value used for the heat transfer calculations in Chapter 6.3. The convective heat transfer rates for the free and forced convection areas were averaged based on their respective areas, two thirds and one third respectively, and plotted against the experimental measurements in Figure 6.32.

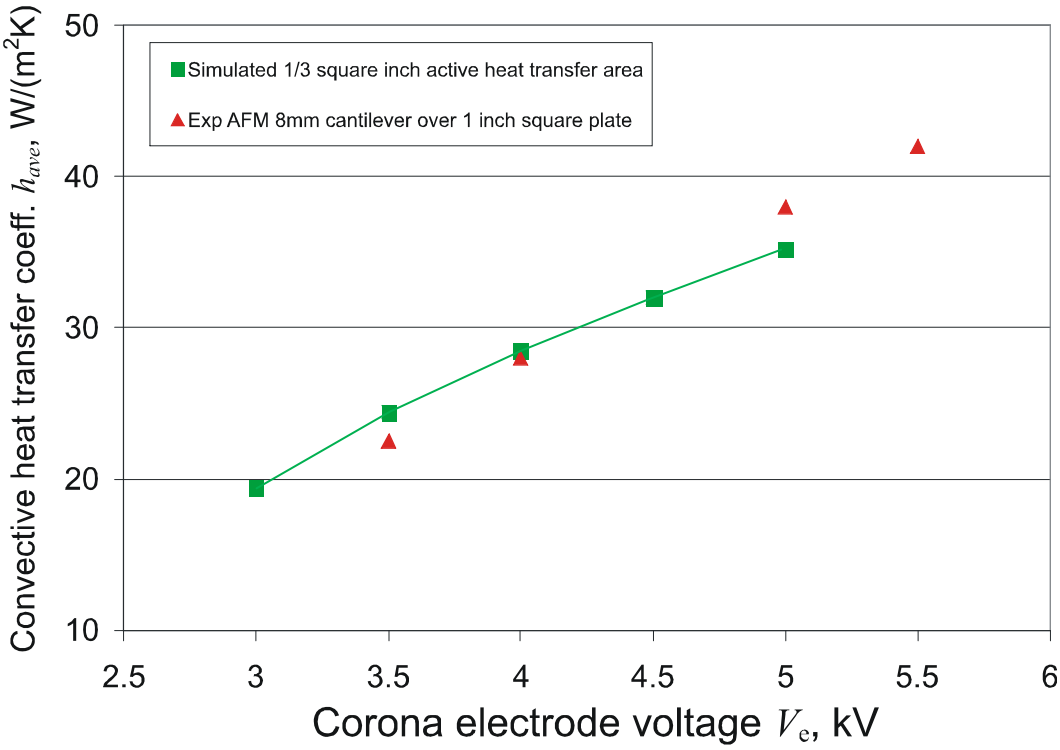

Figure 6.32. *Simulated vs. experimental average convective heat transfer results, with simulated results assuming the EHD blower air jet is located to the right side of the corona electrode tip as shown in the bottom half of Figure 6.29.*

Notably, the one third active area and free convection heat transfer rate assumptions are not rigorously defendable to high precision due to the difficulty in directly measuring the EHD flow profile near the corona electrode and lack of localized heat transfer rate measurements over the cooled surface. However, the assumptions are reasonable based on infrared images of cantilever-to-plane heat transfer experiments, Figure 6.12, and a good correlation between numerical and experimental results in previous chapters in predicting flow fields, voltage, and current relationships..

6.4.3 Summary

Numerical and experimental results are compared for an AFM tip cantilever-to-plane jet impingement forced convection device. Comparison of convective heat transfer rates between numerical and experimental results required modification of the predicted jet impingement location given by the axial-symmetric model to simulate properly the experimentally observed flow profile and heat transfer rates. An axial symmetric model is inherently unable to take into account asymmetries in a system, and future numerical modeling work should focus on the development of a full 3D model in order to minimize simulation error by accounting for system mechanical and electrical asymmetries that exist in the cantilever-to-plane EHD structure.

6.5 Demonstration of EHD blower thermal management in laptop application

Forced air cooling with rotary fans is the most popular cooling solution for electronic products. However, increasing heat generation in microelectronics and the demand for ever smaller portable devices has resulted in heat fluxes and form-factors that push the limits of conventional rotary fan-based air cooling technology. EHD air movers offer a potential alternative to rotary fans in cooling thin applications.

Significant developments over the last half century have been made in the EHD field as a whole [81, 137-139]. However, investigation into meso-scale EHD cooling has been limited, with most previous work focused on modeling efforts [4, 84] or basic proof-of-concept heat transfer enhancement experimental studies [2, 10, 133]. The lack of many real-world EHD based applications to date is due mainly to technical challenges such as device miniaturization, efficient high voltage generation, electromagnetic interference (EMI), ozone management, and reliability. This chapter focuses on the practical implementation of EHD technology in a compact consumer electronic product. The stock rotary blowers in a laptop computer were retrofitted with EHD-blowers and their associated power supplies and control electronics. The thermal performance and laptop functionality are discussed.

A laptop with a total design power (TDP) of approximately 60 W was used as a vehicle to demonstrate a proof-of-concept EHD based cooling system in a laptop computer. To integrate the EHD system, the two 65 mm diameter rotary fans in the laptop were removed and directly replaced with two EHD blower systems and their associated power supplies and control electronics. For simplicity, the EHD system in this study was constrained to the footprint of the stock rotary blowers and the laptop computer remained stock with the exception of the blowers. As such, the performance for the EHD thermal solution does not represent the full capabilities of the technology. Rather this study focused primarily on demonstrating the integration of EHD technology into a laptop computer application.

6.5.1 Integrated EHD laptop computer design

The EHD blower and power supply were designed to fit within the quasi circular ~26 cm^2 by 1 cm tall cavity intended for the stock rotary blower. A multistage EHD blower was used to maximize airflow within the existing system. As with axial fans, EHD blowers can operate in multiple stages to increase pressure and flow rate. In an ideal case without resistance or electric field interference, an N stage device has N times the static pressure of a single device, and $N^{1/2}$ times the flow rate. Figure 6.33 shows the measured pressure head vs. flow rate (P-Q) curve of a single stage, two stage, and three stage EHD device, at the same input voltage. The pressure head and flow rate are normalized by the static pressure and free flow rate of a single device. A three stage device was chosen for this study to enable greater airflow at a minimum operating voltage, and is shown within the laptop in Figure 6.34.

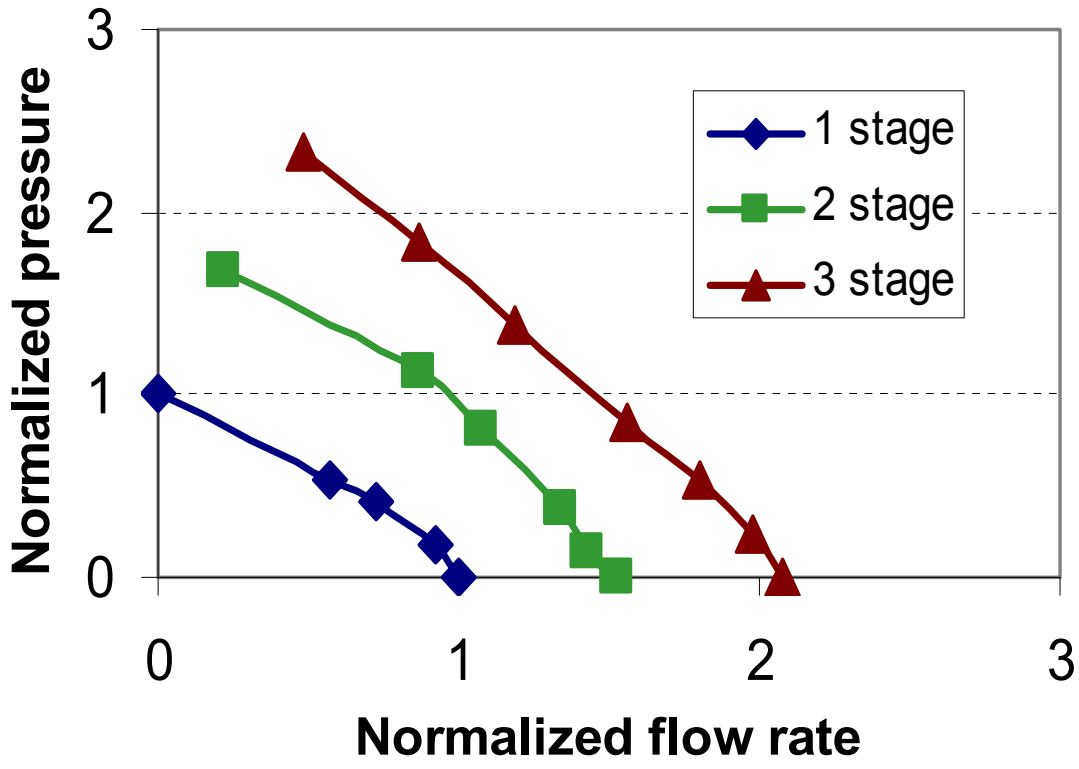

Figure 6.33. *Measured flow rate vs. pressure head, normalized to a single stage device.*

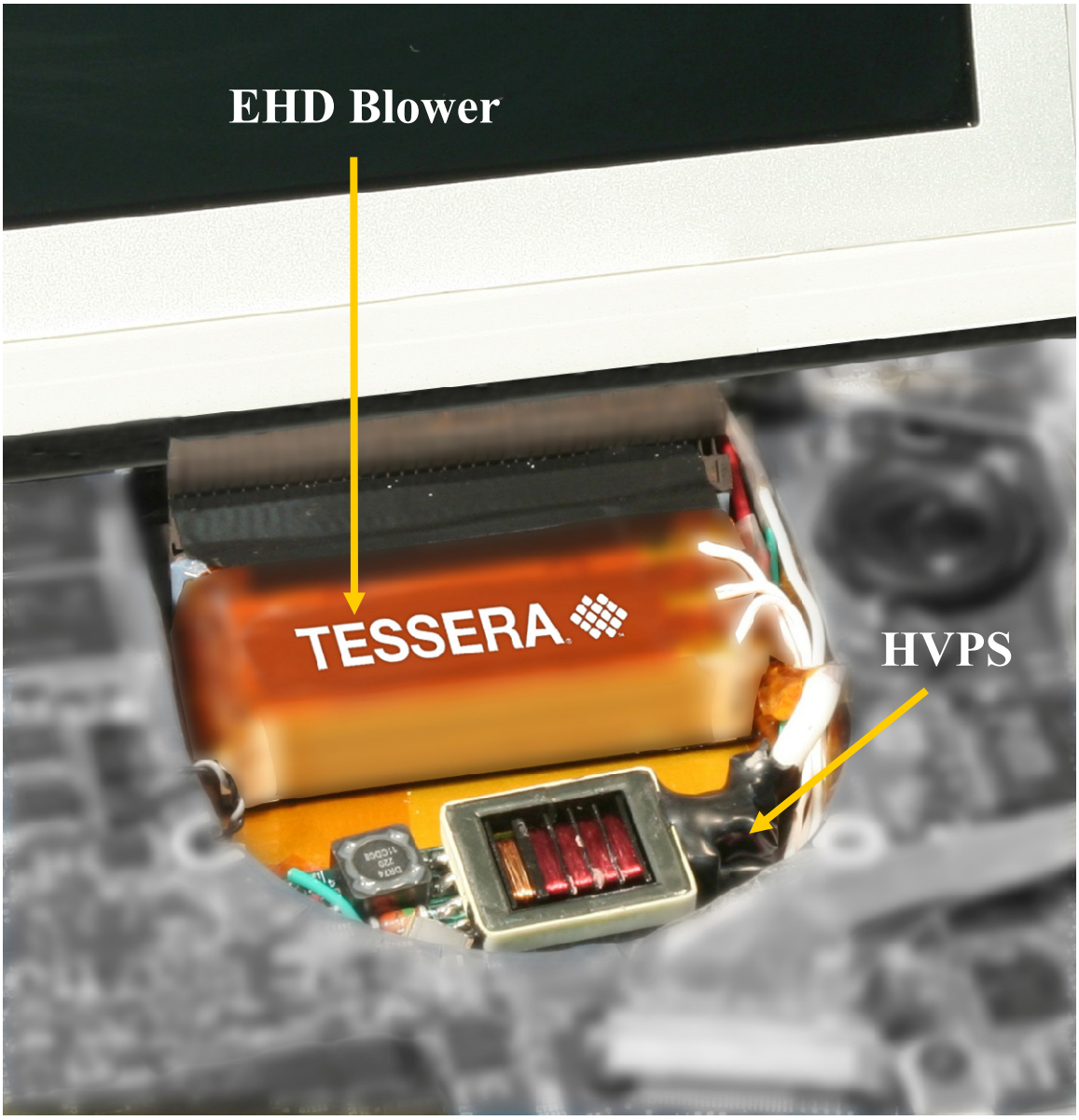

Figure 6.34. *Picture of EHD thermal system integrated into an operational laptop, showing both EHD blower and miniature high voltage power supply (HVPS) built into the stock rotary blower cavity. Partial view of laptop monitor at top of picture.*

One of the integration challenges of this technology lies in the design of a compact voltage converter capable of converting the 12V DC voltage of the laptop battery to approximately 3,000 volts required to operate the EHD blower. A Royer switching power supply topology, commonly used to power cold cathode florescent lamp (CCFL) laptop backlights, with a voltage multiplier at the output was used and is shown in schematic form in Figure 6.35. The power supply had an approximate footprint and

power output of 3 cm^2 and 1.5 watts respectively, and is shown within the laptop with the keyboard removed in Figure 6.34. Newer versions are significantly more compact.

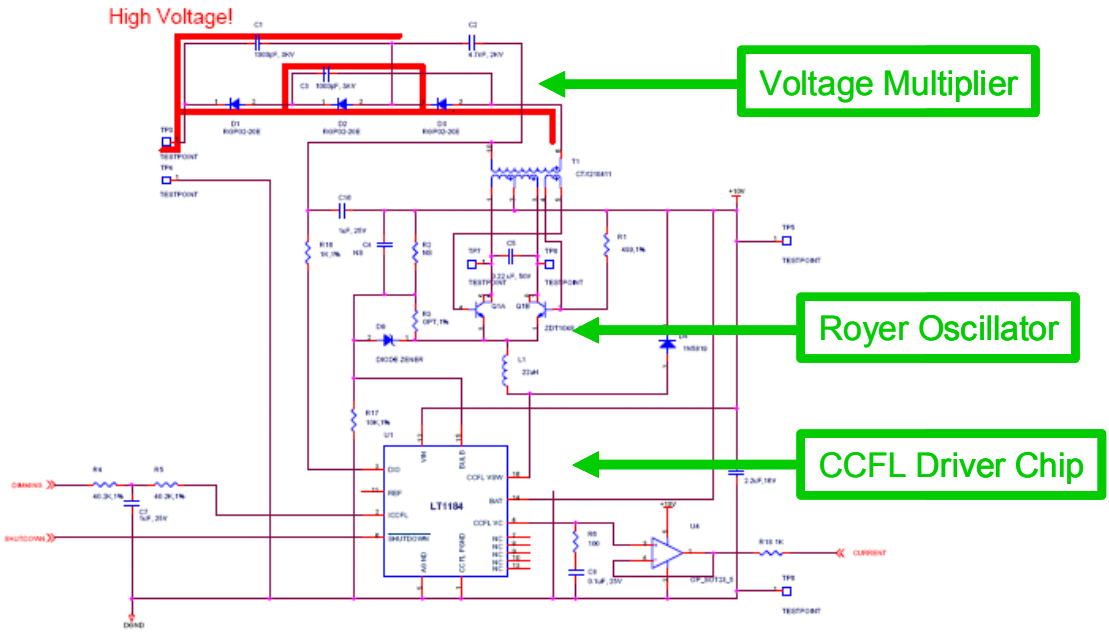

Figure 6.35. *Schematics of first generation miniature high voltage power supply.*

6.5.2 EHD-cooled laptop operation and performance comparison with stock mechanical blowers

The retrofitted laptop was tested with a closed case and with no modifications other than direct replacement of the stock rotary blowers with the EHD blowers. In all tests the retrofitted laptop was compared against a stock version of the same model, which had no modifications and was cooled using the two stock blowers. The major heat sources of the laptop are an Intel Core2Duo CPU, GPU, and the chipset.

In operation, the retrofitted laptop performed similarly to the stock unit with no impact on laptop functionality. There was no discernable effect on electrically sensitive systems, such as wireless communication and track pad human interfaces.

Thermal performance of the prototype system was measured by running several benchmark programs, including Geekbench™, and a looped 1080P movie trailer. Hardware Monitor™, an off the shelf system utility application, was used to monitor the real time temperature of major components, such as the CPU, GPU and the heatsinks.

Figure 6.36 shows the steady state CPU and GPU temperature while playing a high definition (HD) movie in full screen mode. The CPU and GPU temperature of the retrofitted EHD cooled laptop was found to be approximately 10^{o}C higher than the stock laptop, with an overall temperature rise of approximately 60^{o}C. Benchmark results demonstrated comparable overall performance scores, with a variation of less than one percent between stock and EHD retrofitted laptops while running at an 1800 MHz clock speed. Figure 6.37 shows the comparison of skin temperature for both the keyboard and bottom surface of the laptop, showing a temperature difference less than 5^{o}C.

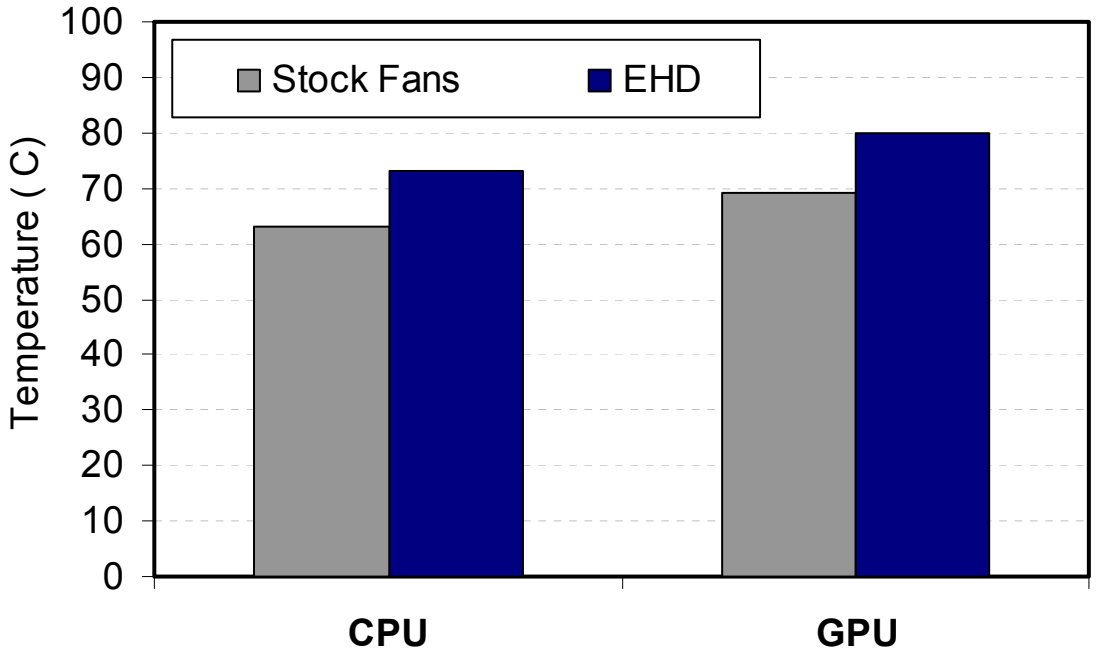

Figure 6.36. *Steady state temperature while looping a 1080p movie trailer.*

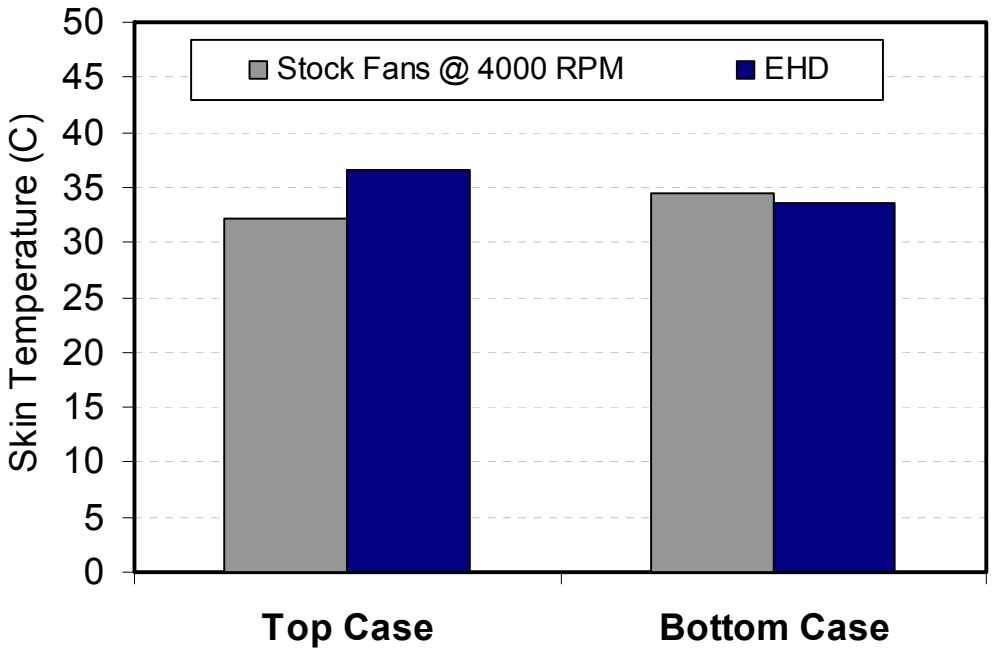

Figure 6.37. *Skin temperature comparison.*

6.5.3 Path towards improved device and system performance

The first generation cooling solution merely replaced the stock rotary fans with EHD blowers and a HVPS. This approach achieved promising results and proved that the technology could function within a realistic laptop environment. However, because the EHD blowers were force fit into a cooling system optimized for rotary blowers and not EHD blowers, they did not demonstrate the technology's full potential.

The design and testing of a second generation prototype has been undertaken. For this prototype, the constraints of fitting within an existing fan footprint and using an off-the-shelf spreader, heatpipe, and heatsink, have been removed. The second generation solution dramatically increases heat transfer but still manages to reduce overall size. Two of the ways in which it does this are by using the collector as the heat removal surface and by increasing its total area. Air blowing across a surface forms a boundary layer that limits heat transfer. Figure 6.38 shows the idealized velocity profiles of air in a channel. The black curve shows a classic parabolic profile due to a pressure differential from a conventional fan blower, the blue curve plots a non-parabolic profile due to EHD driven

flow, with higher velocity near the boundary. The altered profile reduces boundary layer thickness and enhances heat transfer. In this case the channel walls are acting as collector electrodes.

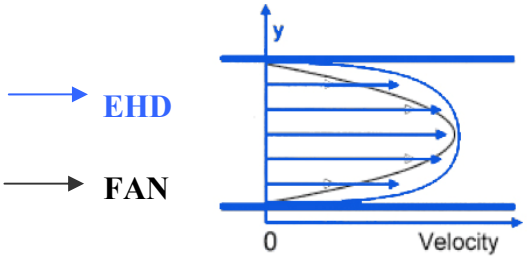

Figure 6.38. *Air velocity profile between two parallel plates.*

Using a reference fin geometry, heat removal was measured using EHD and conventional fan-driven flows. For a given flow rate and the same sink to ambient temperature drop, EHD generated airflow removed up to 38% more heat than a fan, as illustrated in Figure 6.39. Another advantage of using the collector as the heat transfer surface is that there is no additional pressure drop, weight or volume associated with a separate heatsink, as is the case with a fan.

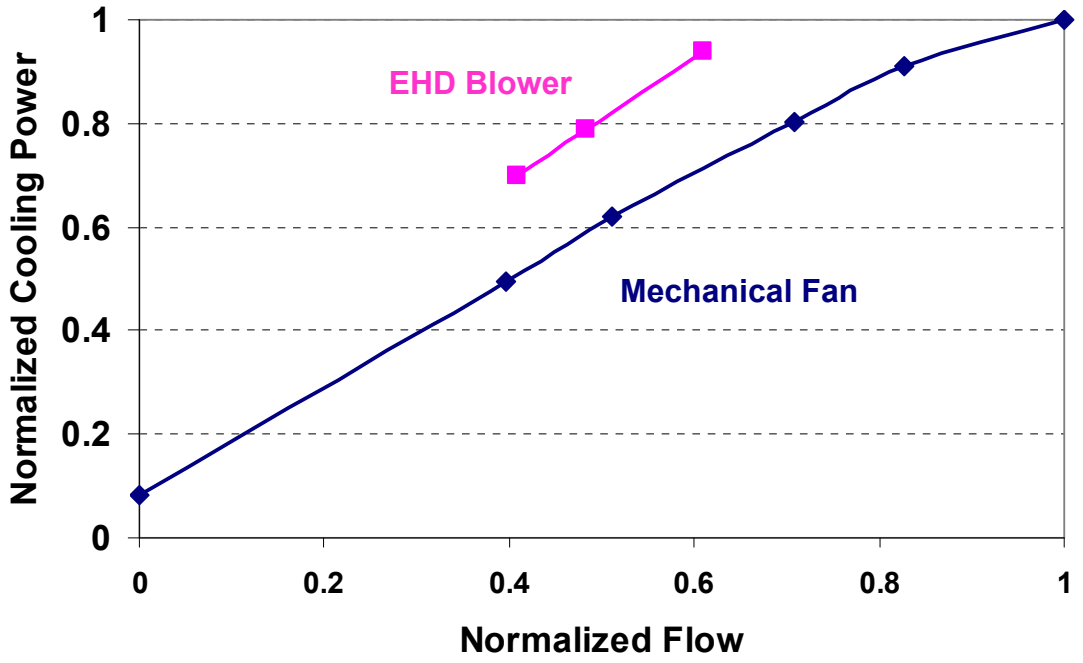

Figure 6.39. *Cooling power of a heatsink when the air flow was generated by an EHD device as compared with a conventional fan.*

In an EHD blower, static pressure P and air velocity V are functions of power density per unit length of emitter wire W. To first order, pressure (P) is proportional to $W^{2/3}$ and velocity (V) is proportional to $W^{1/3}$. Figure 6.40 shows the change of static pressure and total flow rate, the product of air velocity and total device area, as a function of total emitter length. The total power to the EHD device was held constant in each case. The figure shows that it is possible to adjust the P-Q curve of the EHD blower to emphasize either static pressure or maximum flow rate by adjusting the total emitter length. However, favoring flow rate over pressure is advantageous. When the collector is used at the heat removal surface, increased emitter length corresponds to an increased flow rate, a larger surface area, and more heat removal capability. The pressure and flow values in Figure 6.40 were normalized against the point or case of highest pressure and flow respectively in each plot.

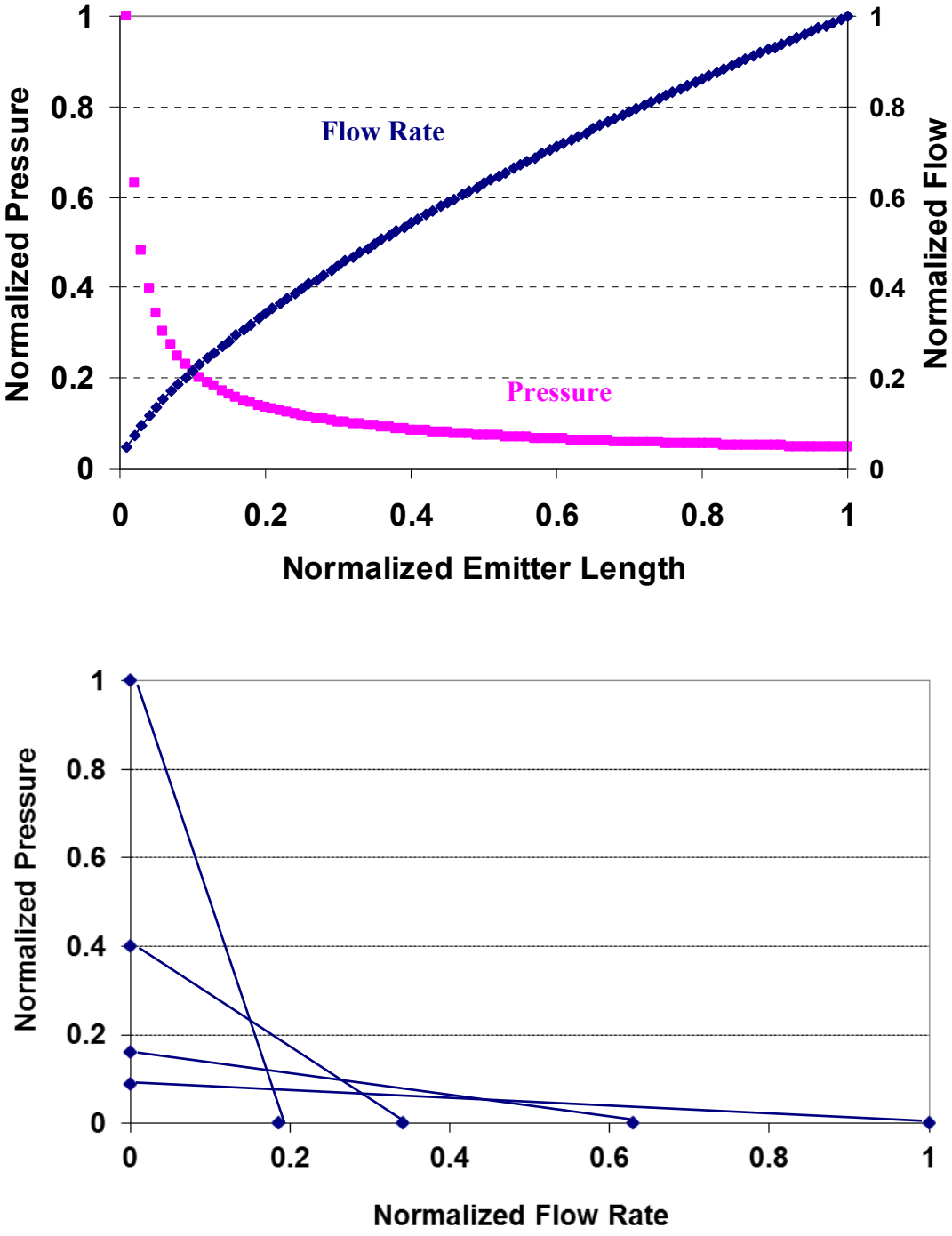

Figure 6.40. *(top) static pressure and flow rate as a function of total wire length, with fixed power consumption; (bottom), change of fan curves as wire length increase.*

The COP of the second generation EHD cooling system is improved by a factor of five over the first generation in free air. The performance of the improved EHD system

exceeded that of the laptop stock cooling system, fan and heatsink/heatpipe, in free air. In addition, the total footprint of the cooling system is more than 50% smaller with an overall thickness of less than 6 mm. These characteristics give EHD cooling significant advantages in thin laptop applications where low overall flow impedance exists.

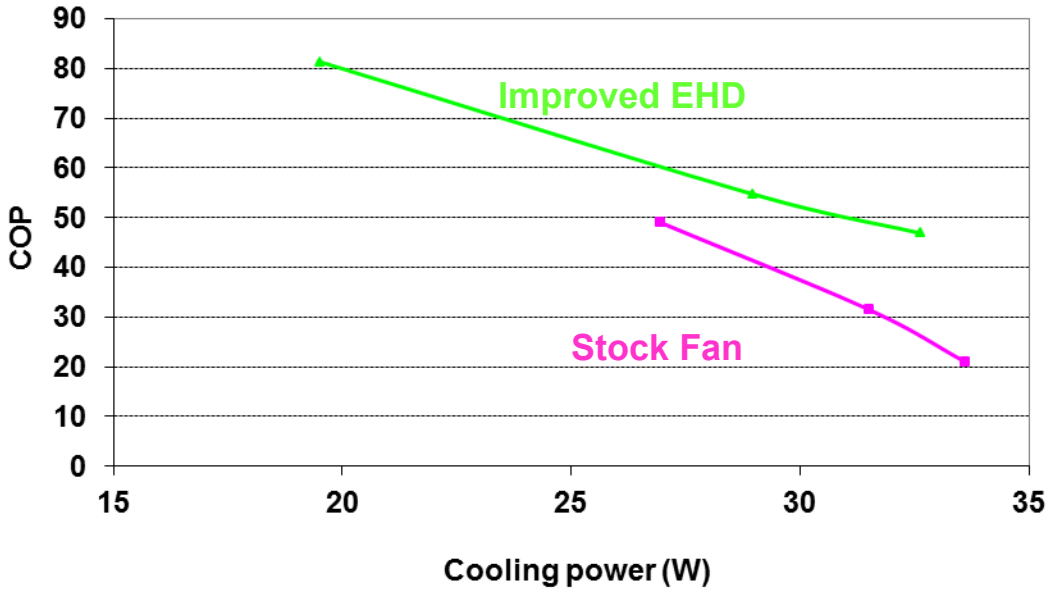

Figure 6.41. *Comparison of COP between improved EHD cooling system and the existing stock fan solution.*

6.5.4 Chapter summary

An EHD cooling system with compact blower and power supply was successfully integrated into the existing cooling system of a performance laptop, replacing the conventional mechanical fan blowers. The retrofitted laptop was found to operate with no apparent effect on system functionality, including subsystems, such as wireless communication and touchpad human interfaces. The performance of the laptop was compared with an unmodified stock laptop of the same model. Even with an un-optimized design, the EHD system shows promising cooling performance with reduced thermal solution volume and acoustics. By further design optimization and modification of the existing cooling solution, the performance can be further improved to meet or exceed that of laptop rotary blowers.

In addition to performance gains, EHD blowers offer other benefits such as:

- Silent operation
- Flexible form factor able to fit around electronics
- Reduced thermal solution height and volume

These advantages among others make EHD cooling an intriguing technology for forced air cooling in space constrained or acoustically limited applications.

Chapter 7. Investigation of Dust in EHD systems

7.1 Chapter summary

A previous chapter discussed the successful integration of an EHD cooling system in a notebook computer. It demonstrated the benefits of EHD cooling technology including silence, high coefficient of performance and flexible form factor, and discussed key technical challenges for commercialization. In this chapter, we focus on a concern shared by both mechanical fan and EHD cooling systems: the accumulation of dust particles, which can result in performance loss. The fundamental mechanisms of particle collection within an EHD system are discussed, and a numerical model for predicting dust deposition is presented and verified using experimental results.

7.2 Introduction

All electronic devices consume power and generate heat. Ultimately, all waste heat in portable electronic devices is transferred to the air, making the heatsink-to-air heat transfer path critical to system performance. Traditionally, forced airflow has been provided by various forms of mechanical fans with rotating blades. However, the mechanical fan has many fundamental limitations such as thickness, form factor, noise, etc.

Electrohydrodynamic (EHD) ionic wind pumps have the potential of becoming a critical element of electronic thermal management solutions [1, 3, 6, 8, 14, 22, 25, 29, 92, 94, 140]. EHD-based solid state devices offer silent operation, dynamic airflow profiles, high cooling efficiency, and a thin flexible form factor.

As an emerging technology, reliability of EHD systems is not as well documented as mature fan-heatsink technology. Although rotary fan and EHD-based thermal systems have some unique longevity challenges, such as bearing wear in rotary fans, and emitter electrode wear in EHD blowers, dust fouling is a challenge shared by both technologies. However, dust fouling exhibits differently in fan-based and EHD systems, leading to different types of effects on the system and thus different arenas of solutions.

To better understand the problem, experiment facilities were developed to evaluate the effects of airborne contaminates on the performance of EHD cooling systems and comparable rotary fan-based cooling systems.

This chapter focuses on verification of the simulation tool developed to predict particle motion and capture within an EHD system. The mechanism of charging aerosol particles in EHD air pumps and the applied force field on the charged particle is discussed. Following, a numerical model to predict aerosol particle charging and flow trajectory is presented. Finally, the numerical results are compared with experimental observations and measurements.

7.3 Challenge of dust in thermal management systems

Dust is the root cause of several reliability issues in electronics, and specifically in notebook computers [141-143], including shorting between electrical contacts of components on PCBs, fouling of heatsinks, damage to fan bearings, etc. In particular, as heatsink fin pitch becomes finer, dust accumulation on the heatsink increases flow impedance, leading to significant reduction in cooling efficiency and capacity over time [141].

Dust, in urban environments, commonly consists of mineral particles, human/animal skin fragments and hairs, textile and paper fibers, etc. These particulates can be separated into two general categories: particulate and fibrous. Fine particulates are sub-micron to micron sized with low aspect ratio geometry. Fibrous dust can be tens of microns to millimeters in size with high aspect ratio geometry.

Generally, fibrous dust is the major cause of dust-related issues in electronics. The fibers get caught between heatsink fins and form a matrix. The fibrous matrix then works as a filter to collect smaller particles, resulting in further dust collection and performance loss of the cooling system [142].

The impact of dust on EHD- and rotary fan-based cooling systems is different due to their different mechanism of air propulsion. In a DC positive corona-induced ionic wind device, application of voltage between a high tip-curvature corona electrode and a low tip-curvature collecting electrode creates a high electric field gradient at the corona

electrode, ionizing its surrounding air molecules. Particles in the air become charged from collision with the ions. The charged particles are then electrostatically attracted to nearby surfaces. The particles move along a trajectory influenced by the electric field, gravitational field, and airflow drag among other forces. In rotary fan-based systems, electrostatic forces are largely absent, leading to different particle trajectories and thus collection areas and characteristics. In addition to differences in collection characteristics, there are differences in the cause of performance loss. Dust degrades rotary fan mechanical operation while dust on the collector surface of the EHD blower increases electrical resistance, reducing output current and performance. The degree to which dust is collected within an EHD system and to what degree the collected dust impacts performance is geometry and operation dependent. This makes the development of a model able to predict dust behavior in an EHD system an important design tool.

7.4 EHD and dust deposition modeling procedure

Modeling was conducted using a coupled physics EHD model and solved with COMSOL multiphysics, a commercial software package that performs equation-based multiphysics modeling for different physical processes by applying the finite element method to the system of partial differential equations. The EHD model used for this study was adapted from the authors' previously published modeling work [4] and described in earlier chapters that focused on EHD induced flows and heat transfer. The modeling presented in this paper extends the previous model capabilities to include particle collection behavior. To demonstrate this, a simplified EHD reference platform, Figure 7.1, was created to test and validate a particle charging and trajectory-tracking model.

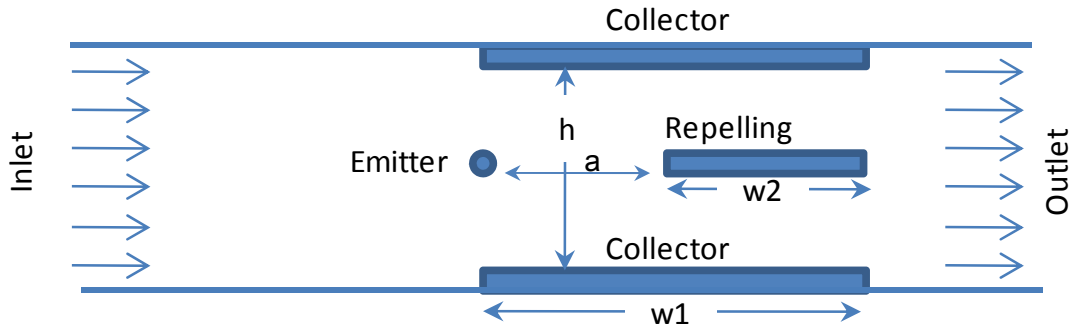

Figure 7.1. *Schematic of the simplified 2D model. The model includes a corona wire with diameter d. The collectors are two grounded parallel plates of length w1. Distance between the plates is h. The EHD device is in a dielectric enclosure, with the inlet and outlet at the left and right respectively.*

The reference platform consists of an emitter wire electrode and three plate electrodes downstream of the emitter wire that forming the basic structure of an electrostatic precipitator (ESP). In this configuration, the top and bottom plates are held at ground potential and act as collecting electrodes, while the center plate is held at a potential similar to the emitter wire and acts to deflect the incoming charged particles towards the collecting plates where they are captured. The ESP reference design was selected because it allows for rapid particle collection and thus quick experimental verification of the model. In addition, the ESP configuration is symmetric about the x-axis enabling numerical simulation of only half the ESP domain, which minimized simulation time.

The geometric dimensions used in the model are as follows: the diameter of the emitter wire is twenty five micrometers with the emitter positioned flush with the input of the collector plates. The length of the collector and repelling electrodes are 5 mm, 2 mm and 0.5 mm respectively, with a thickness for all plates of 0.5 mm. The distance between collector electrodes and between the emitter and repelling electrode is 5 mm, 2 mm, and 0.5 mm respectively. The ESP is located within a dielectric channel comprised of two Plexiglas plates. The inlet to the channel is positioned three centimeters upstream of the emitter. Critical geometric dimensions and boundary conditions for the ESP are summarized in Table 7.1.

Numerical simulations results for electric potential, charge density and charge flux streamlines, and velocity field are shown in Figure 7.2, Figure 7.3, and Figure 7.4 respectively, all of which used a repelling voltage of 3.5 kV.

Table 7.1. *Critical EHD model parameters and boundary conditions.*

Geometric parameter	**Value**
Emitter diameter, d	25 μm
Distance between emitter and repelling electrode, a	2.5 mm
Distance between collector electrode, h	5 mm
Collector electrode length, w1	5 mm
Repelling electrode length, w2	2.5 mm
Electrostatic boundary conditions	
Emitter electrode	3.1 kV
Collector electrode	0 V
Repelling electrode	2.5kV, 3.5kV
All dielectric channel and air surfaces	Symmetry
inlet	Symmetry
Outlet	0 V
Charge transport boundary conditions	**See [4]**
Emitter current	20 μA
Navier Stokes boundary conditions	
All solid surfaces	Non slip
Inlet boundary	Prescribed velocity
Outlet boundary	Normal flow, zero pressure

For dust particles traveling in the vicinity of an EHD device, there are two dominating forces acting on the particle that determine its trajectory: electrostatic forces produced by interaction of the electric field with the particle charge, and the drag force produced by relative motion of the particle with respect to the fluid. All other forces, such as gravity and buoyancy, have little effect on particle motion and can be neglected with minimal error.

The charging rate of a particle moving in the vicinity of a corona electrode depends on the ion concentration, electric field strength, and the difference in magnitude between the charge residing on the particle and the particle saturation charge. Particle saturation charge is defined as the maximum charge a particle can accumulate and is a function of the electric field strength around the particle. The particle charging rate can be modeled by [144]

$$\frac{\partial q}{\partial t} = 3\pi n(t)\mu E(t) r^2 \frac{\varepsilon_r}{\varepsilon_r + 2}\left[1 - \frac{q(t)(\varepsilon_r + 2)}{12\pi\varepsilon_0 E(t) r^2 \varepsilon_r}\right]^2 \tag{7.1}$$

where r is the aerosol particle radius, ε_r the relative particle permittivity, μ the ion mobility, and n the charge density in the charging zone. Dust particles for this paper were assumed to be spherically shaped and have a density of 1000 kg/m3 and relative electric permittivity of 10. The particle accumulates charge as it moves within the charging space, until it reaches the saturation charge, which is given by Pauthenier equation [59].

$$q_s = 12\pi\varepsilon_0 r^2 E_m \frac{\varepsilon_r}{\varepsilon_r + 2} \tag{7.2}$$

where E_m is the amplitude of the electric field at the particle.

Since the size of dust particles is small, on the order of microns, and the relative motion of particles with respect to the fluid is slow, the expression for the drag force is obtained from assumption of Stokes flow with a correction factor that depends on the ratio of the mean free path of air molecules to the particle radius [144].

During particle motion, the expression for charging rate was integrated over time to obtain the particle's current charge magnitude and the resultant electrostatic force.

7.5 Modeling results

Particle trajectories were obtained by integrating the particle's equations of motion over time. Particle trajectories for two different repelling electrode voltages 3.5 kV and 2.5 kV were calculated to show the effect of repelling voltage on capture efficiency. Trajectories for particles with radii of 0.3, 1, 5, 15, and 30 μm with a repelling voltage of 2.5 kV and 3.5 kV are shown respectively in Figure 7.5 and Figure 7.6. Figure 7.7 shows a full domain view of the trajectories within the ESP.

The electrostatic force is dominant for larger particles while drag force rules for smaller particles. Larger particles therefore are readily attracted to a collecting surface, while smaller particles tend to follow air flow stream lines as seen in Figure 7.5 and Figure 7.6. The highest electric field seen by the particles is found between the emitter and collector electrodes and the repelling and collector electrodes. This causes the

sharpest transitions in the particle trajectories in these regions and is responsible for the sharp edge of collection just upstream or downstream of the repelling electrode leading edge as seen in Figure 7.5 and Figure 7.6. Larger particles generally accumulate higher charges and are expected to be more impacted in these regions.

Estimation of the dust loading distribution along the collecting electrode surface was achieved using the following assumptions and process. The particles within the air were assumed to be uniformly distributed within the airflow and the airflow velocity at the inlet of the channel that holds the EHD device is assumed to be uniform. The relative distribution of particle sizes was taken from experimental measurements of the particle size distribution using a particle counter for particles of five microns and less and estimated for larger particles as described in the following section.

The dust loading distribution along the 5 mm length of the collector surface was broken into twenty 0.25 mm discrete zones from the leading to trailing edge.

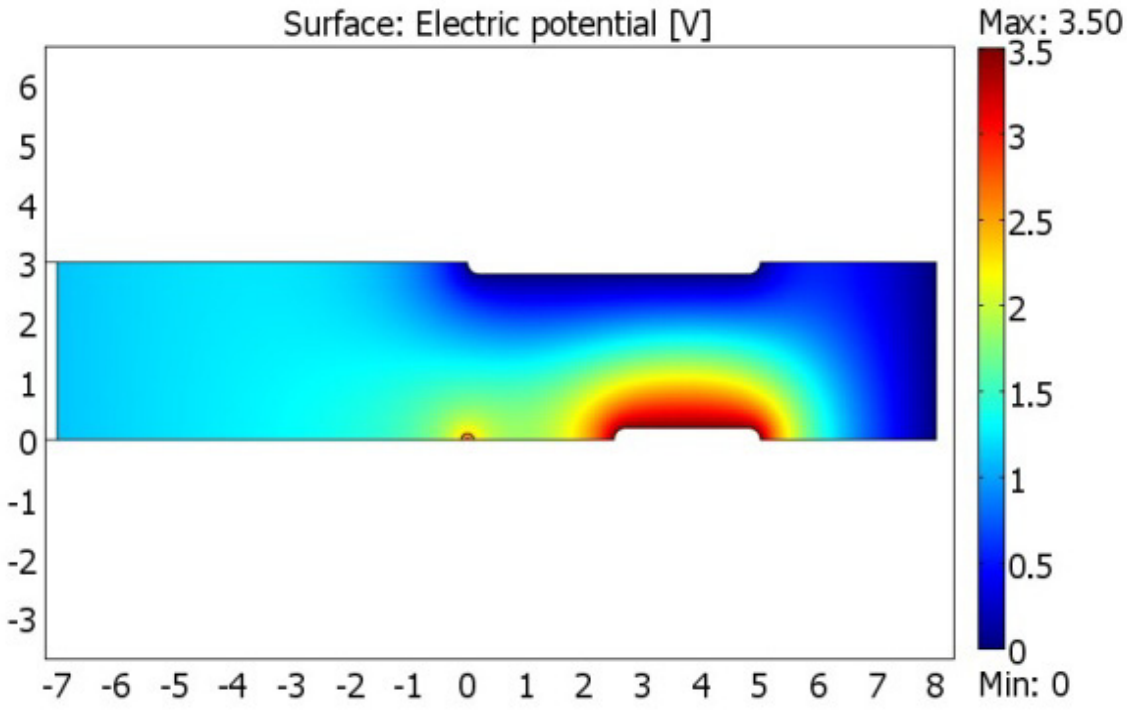

Figure 7.2. *Electric potential surface map of EHD device.*

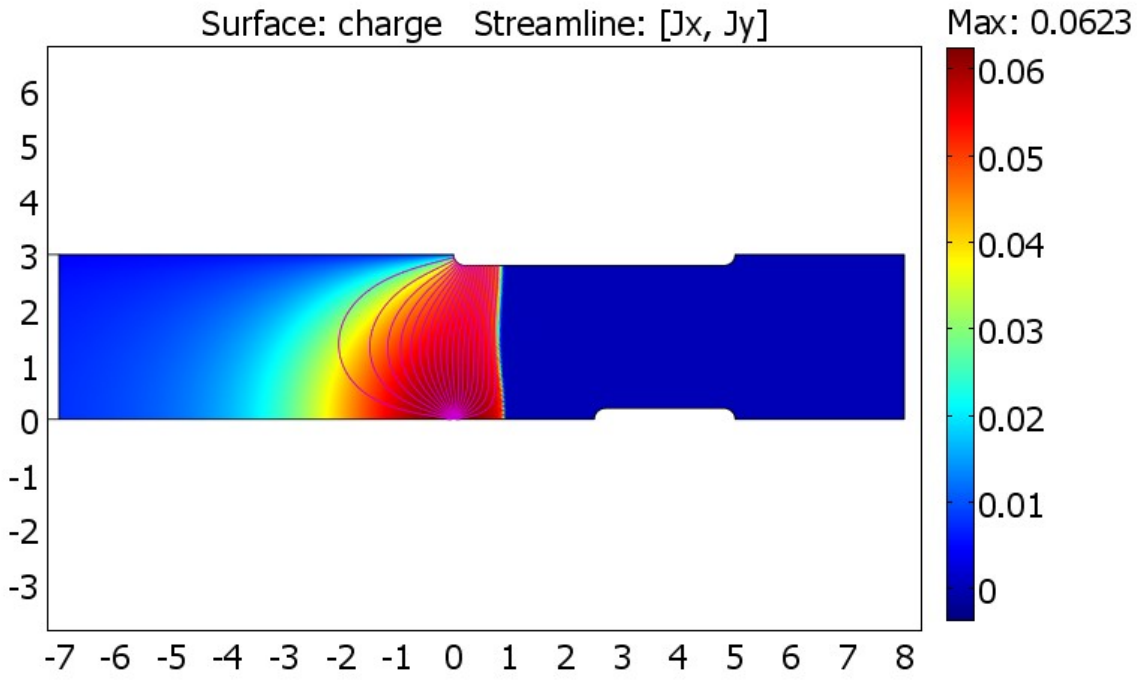

Figure 7.3. *Charge density surface map and charge flux streamlines of EHD device.*

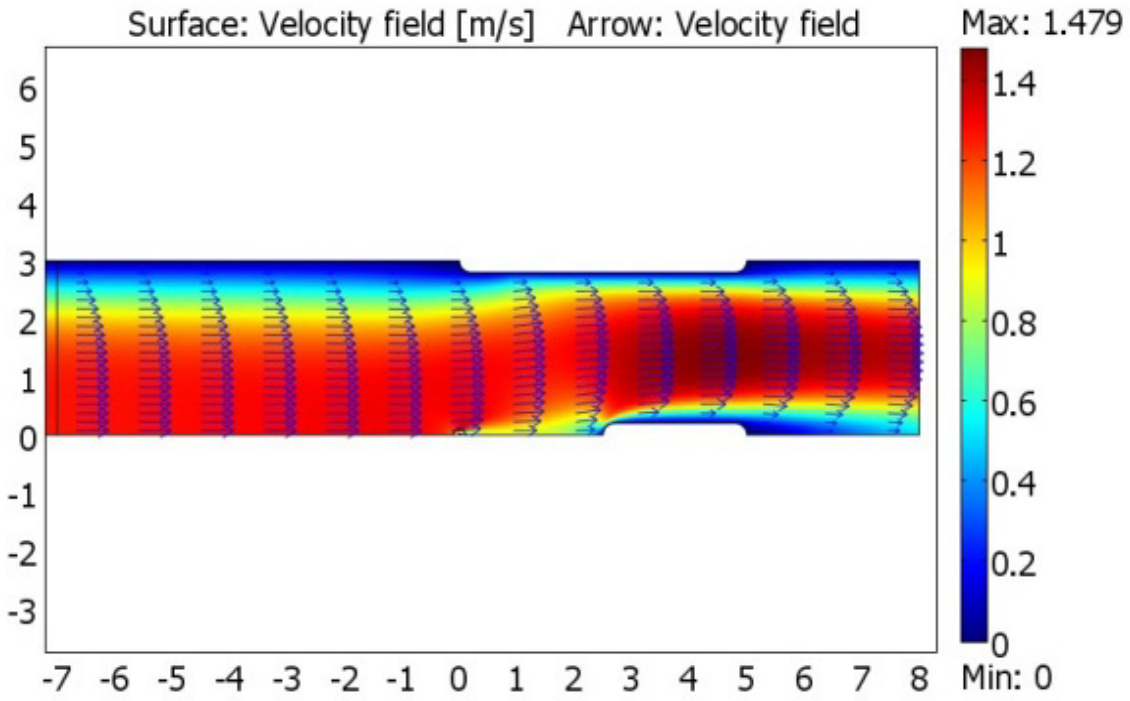

Figure 7.4. *Air flow velocity field surface map and arrows of EHD device.*

For each model, fifteen particles paths were calculated starting at the inlet of the channel and spaced evenly along the channel inlet. The number of particles terminating on each of the twenty discrete zones on the collector was counted. This process was repeated for each particle size giving an overall particle capture distribution map. The captured particulate volume for each zone was estimated by taking the product of the measured particle size distribution, the relative volume for each particle size, and the number of trajectories terminating in each zone for each particle size. The particles were assumed to be densely packed.

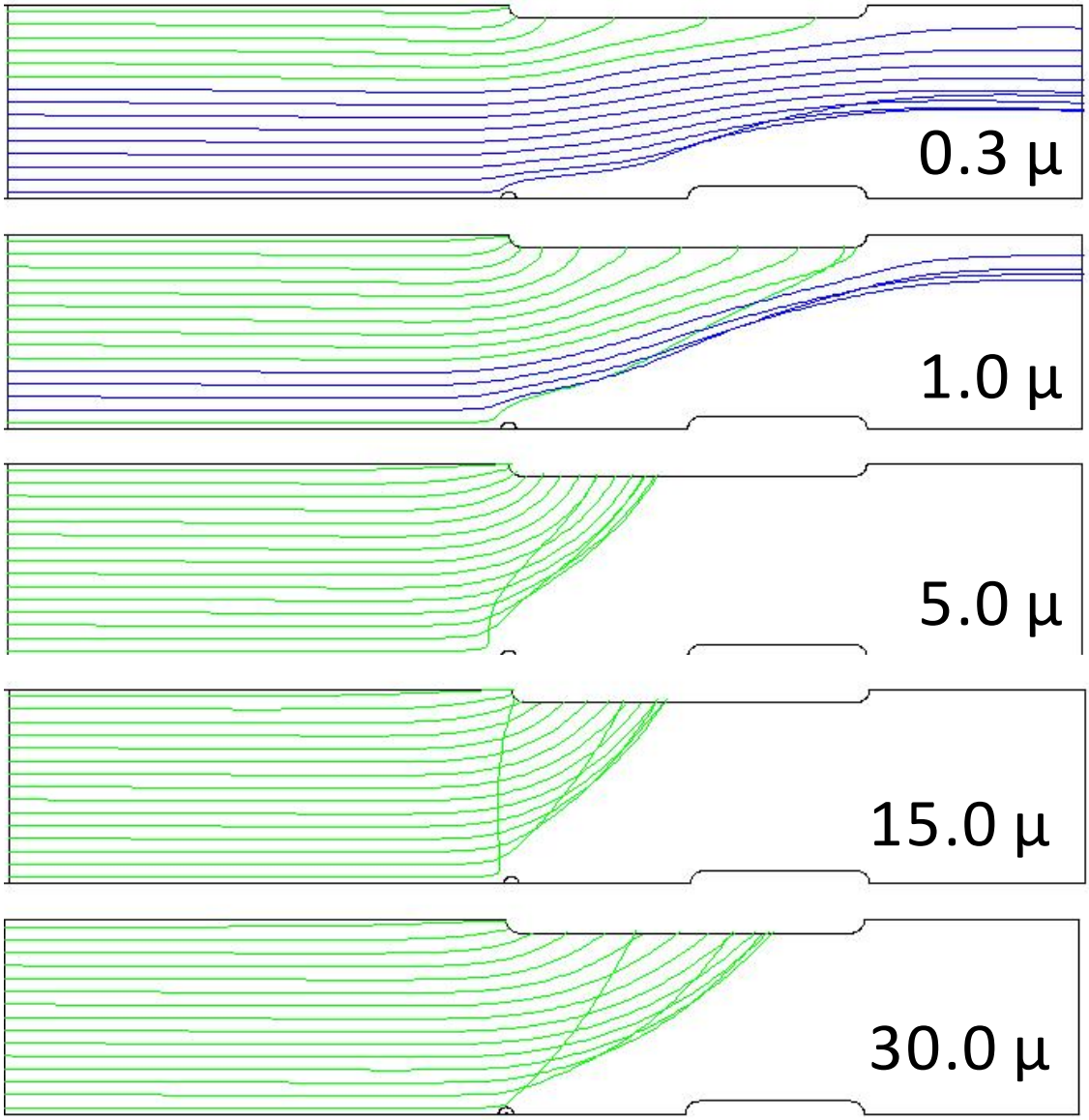

Figure 7.5. *Trajectories of dust particles with radii of 0.3, 1, 5, 15, and 30 μm for a repelling electrode voltage of 2.5 kV. Escaped particles are shown by blue curves, while captured particles are shown by green curves.*

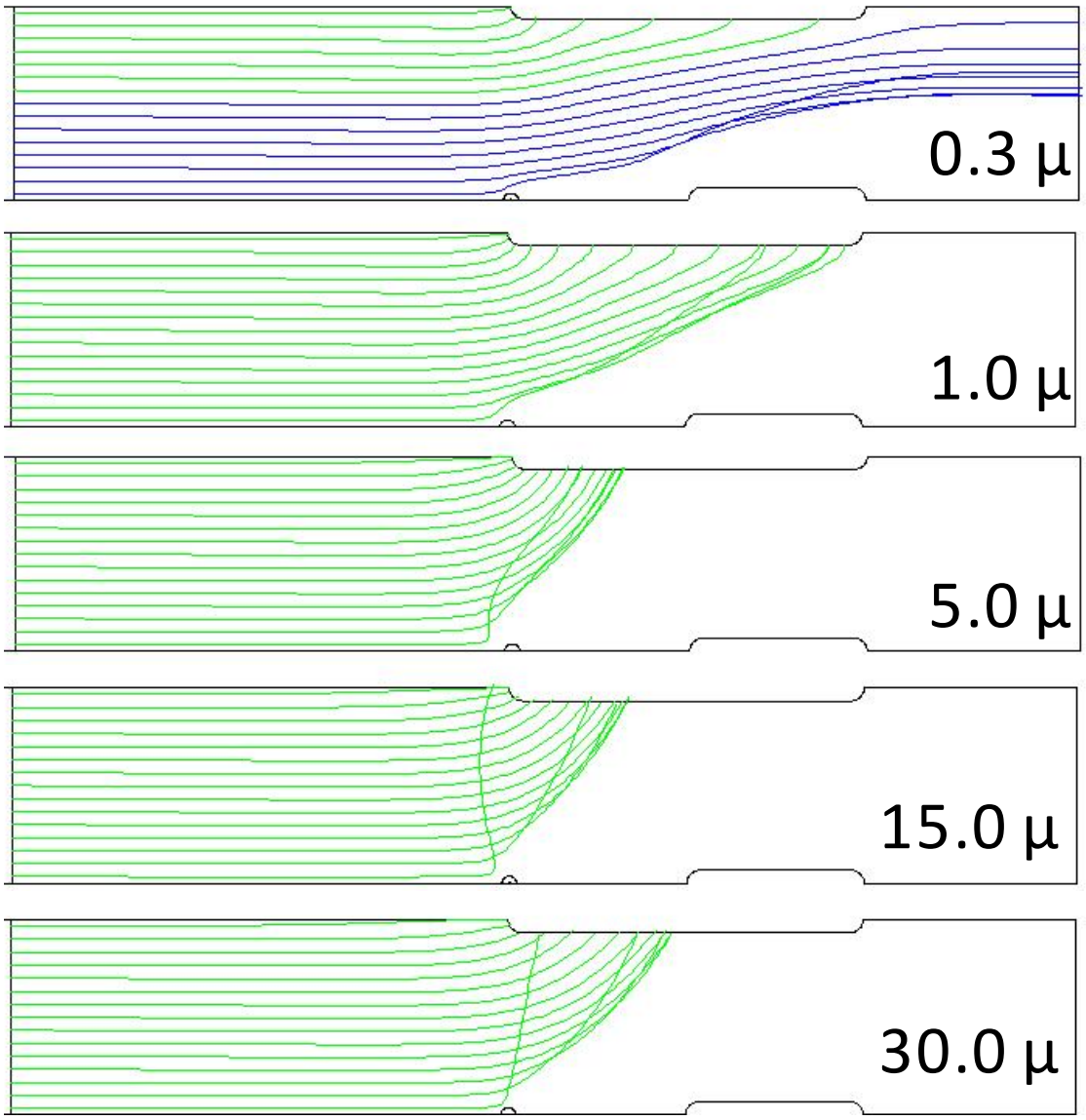

Figure 7.6. *Trajectories of dust particles with radii of 0.3, 1, 5, 15, and 30 µm for a repelling electrode voltage of 3.5 kV. Escaped particles are shown by blue curves, while captured particles are shown by green curves. The higher repelling electrode voltage collects more of the 1.0 and 0.3 micron particles.*

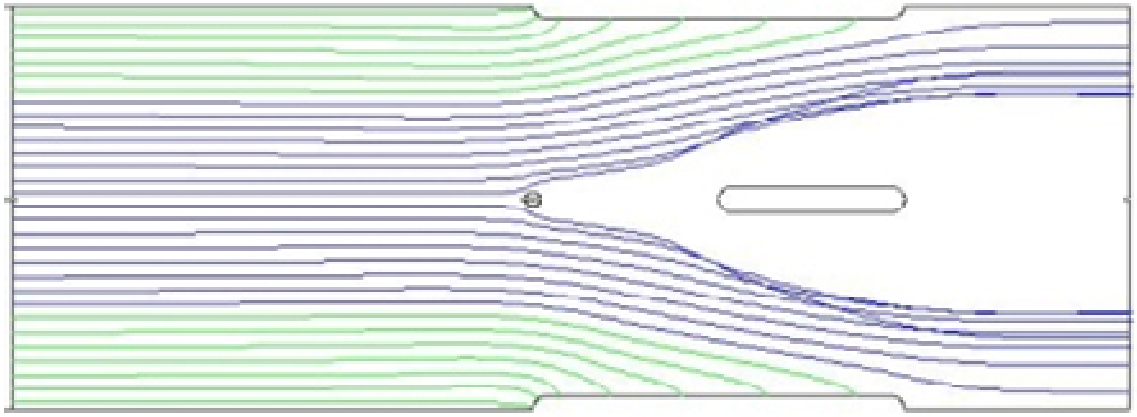

Figure 7.7. *Trajectories of dust particles with radii of 0.3 µm shown in a full model view with a repelling electrode voltage of 3.5 kV. Escaped particles are shown by blue curves, while captured particles are shown by green curves.*

7.6 Experimental methods and procedure

IEC (International Electrotechnical Commission) standards are widely used for environmental reliability of electronics equipment and devices. The IEC 60068-2-68 standard addresses dust- and sand-related reliability testing methods. However, it only addresses issues related to particulate mineral dust. Currently there is no industry-wide consensus over dust reliability testing methods, especially for mobile computing devices such as notebooks, netbooks, and handheld smart phones and tablets As described previously, it is commonly observed that realistic dust includes not only particulate mineral dust but also airborne fibrous dust [142]. In light of these facts, a custom dust test system was developed to experimentally investigate the effects of both particulate and fibrous dust on EHD device operation and facilitate validation of the modeling results.

The experimental set-up shown in Figure 7.8 was built to test small form factor thermal solutions found in present day mobile computing systems such as notebooks. The set-up consists of a closed forced air circulation circuit with a blower fan. The circuit consists of a main square x-section dust chamber of 24” length and 6” x 6” cross section dimension. The test chamber is made of clear acrylic plastic in order to observe dust input during the test as well as dust collection on the device under test. Using a blower fan, air speeds of 0.25 to 8 m/s seconds can be achieved. The test system is designed to accommodate both particulate and fibrous types of dust. ISO 12103-1, A2 Fine Test Dust

was used as particulate dust and Kleenex brand paper tissues were used to generate fibrous dust. Particulate dust is introduced in the system by a pipette tube and fibrous dust is introduced using a top mounted, modified flour sifter, in a controlled manner by timing turns of the sifter.

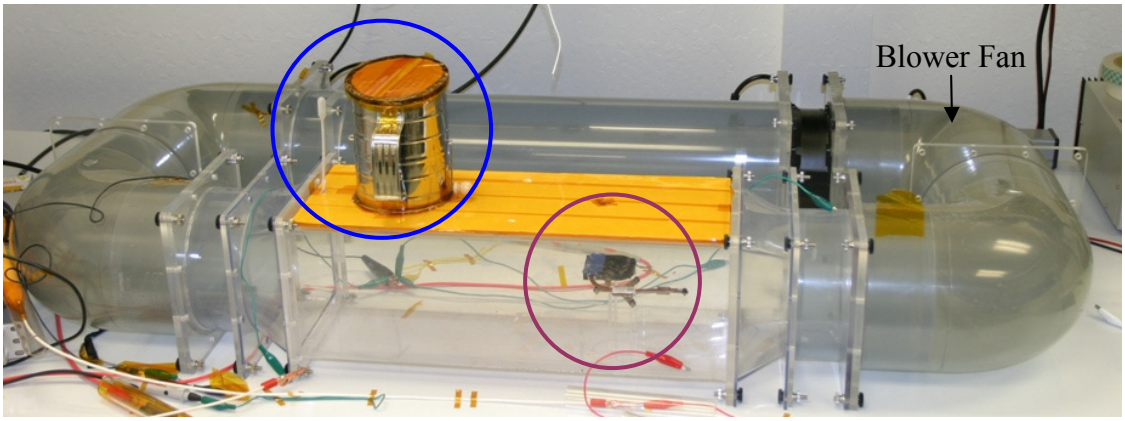

Figure 7.8. *Dust test set-up showing test chamber, dust input methods (blue circle), and a sample thermal system under test (red circle).*

The experimental procedure was as follows: the DUT (Device Under Test) is secured at the center of the chamber cross section on a low drag support structure. The blower fan is set to the desired air speed and then particulate and fibrous dust is introduced upstream of the DUT. A typical dust test in this study uses 1.5 m/s air speed measured at the location of the DUT and injections of 0.5 grams of ISO A2 fine test dust followed by two sifter turns of fibrous dust. Dust was added multiple times during the test until there was visible accumulation.

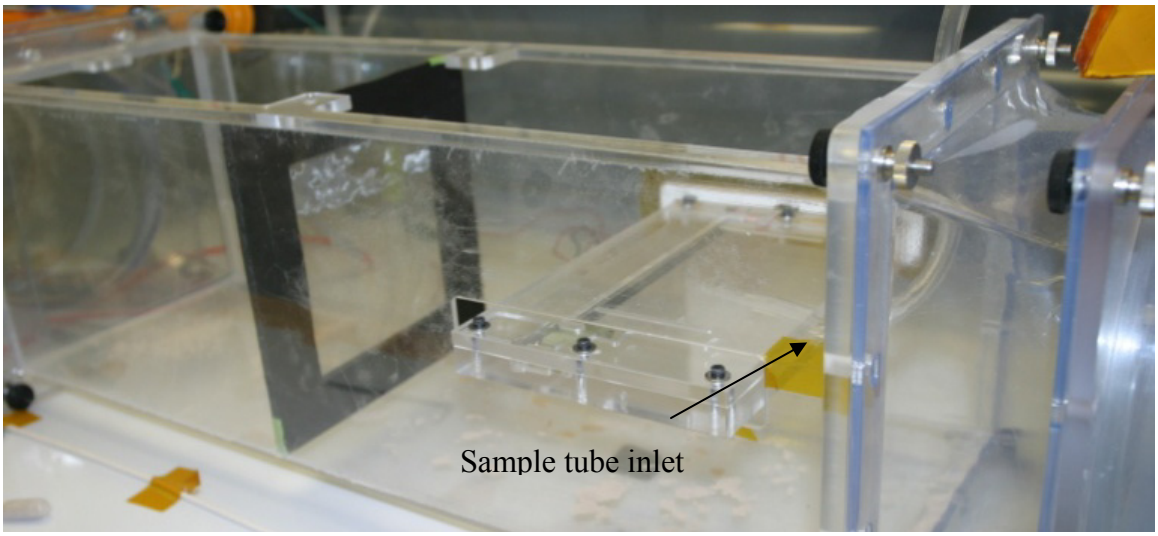

Figure 7.9. *Close up view of the device in the test chamber. The dust sampling tube is inserted between two Plexiglas plates bounding the electrostatic precipitator.*

The particle size distribution of the dust reaching the electrostatic precipitator was measured using a Solair 3100+ portable particle counter (Lighthouse World Wide, Fremont, CA). A sample tube was inserted between the plexiglass plates defining the top and bottom of the air channel for the precipitator,Figure 7.9. Measurements were taken for 0.3, 0.5, 1, 3, 5 and 10 μm particles (the maximum range for the instrument). Each scan was repeated at least three times, alternating between having the device on and having it off, and the results were averaged.

7.7 Experimental results and comparison with numerical results

Figure 7.10 shows that the electrostatic precipitator preferentially collected particles greater than 1 micron. The 10 μm particle counts were deemed too low to be reliable and are excluded from the graph below.

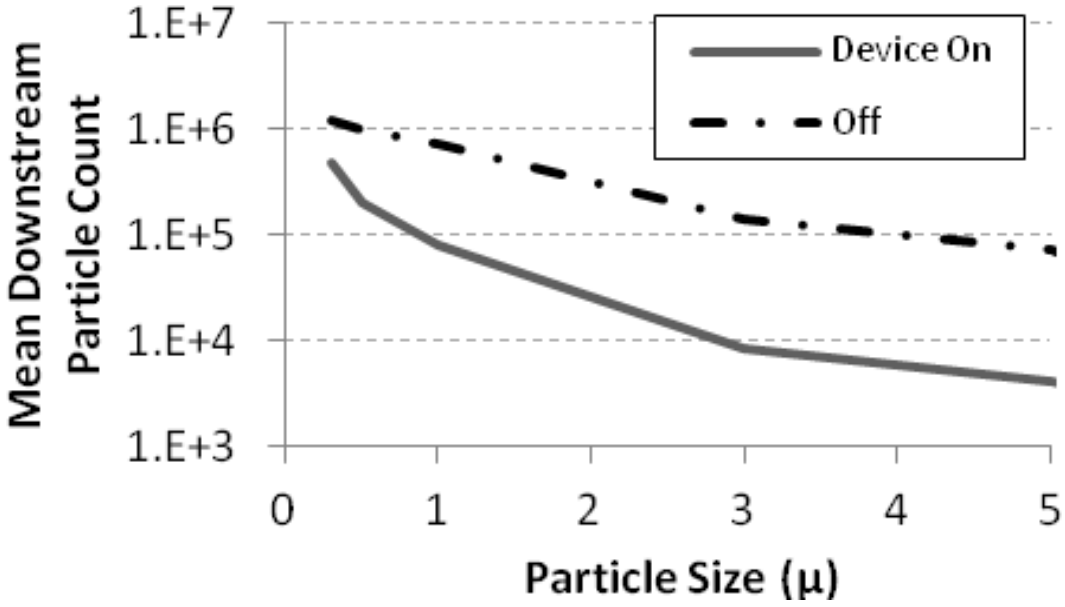

Figure 7.10. *Average particle counts with the electrostatic precipitator on and off. The precipitator is most effective at removing particles above 1 µm in diameter.*

The collection plates from the precipitator were examined using a scanning electron microscope (SEM). As can be seen in Figure 7.11, the leading portion of the collector electrode accumulated many large particles and fibers (>10µ). The area that had been immediately above or below the repelling electrode was virtually free of large particles, consistent with the models predictions.

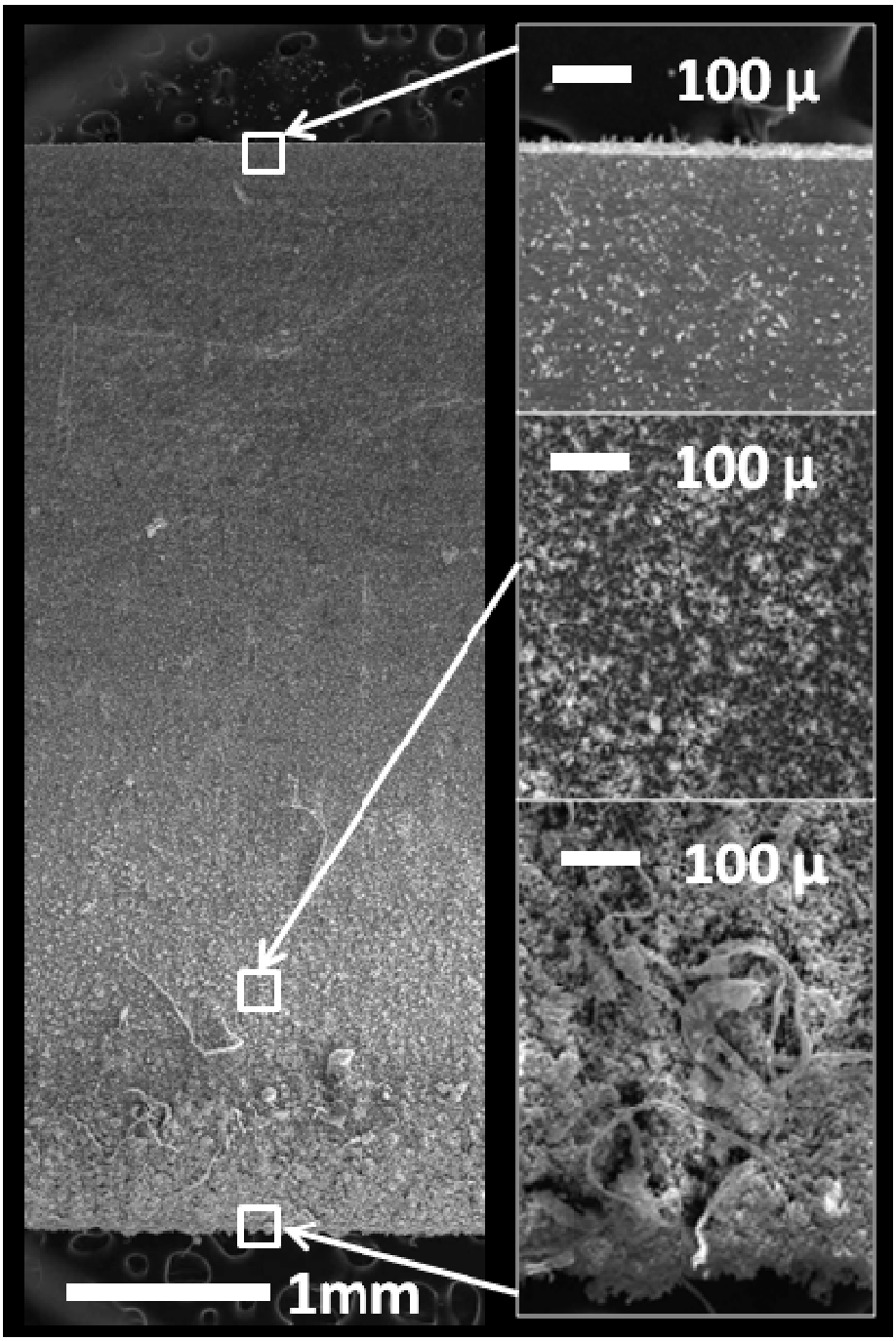

Figure 7.11. *SEM image of the lower collecting electrode after dust exposure. The leading portion (bottom of the image) accumulated most of the large particles. The trailing half of the collector, which was directly beneath the repelling electrode, accumulated very few large particles, which is consistent with the simulation results. Boxes on the left half of the image accurately indicate the distance from the leading edge of the images on the right, but not the exact location.*

The amount of dust buildup at various locations on the collector was quantitatively determined using an optical microscope with a digital stage readout with 0.4 micron resolution. The collecting electrode was secured to the microscope stage and the height of the dust was determined by adjusting the z-axis until the image was in focus when viewed under 200X magnification. The location of the x, y and z stages, were read using the digital readout every 0.25-0.50 mm from the leading edge of the collector. The sample was then wiped clean of dust using a Q-tip and the profile of the bare collector was measured. The dust height was calculated by taking the difference between the two measurements.

The measured results were compared to the predicted values, Figure 7.12. Because particles larger than 5 μm were very clearly present in the SEM image, the model was updated to include 15 and 30 μm particles. The particle concentrations at these sizes were estimated using a log-normal fit [145] to the measured concentrations for particles between 0.3 and 5 μm.

The simulation results were scaled to account for the actual concentration of dust introduced into the precipitator. Both the simulation and measured results show a large accumulation of predominately larger particles at the leading edge, followed by a dip in accumulation, a second area of accumulation located at approximately 1.5-2.0 mm from the leading edge of the collector, and relatively low accumulation beyond 2.5 mm from the leading edge.

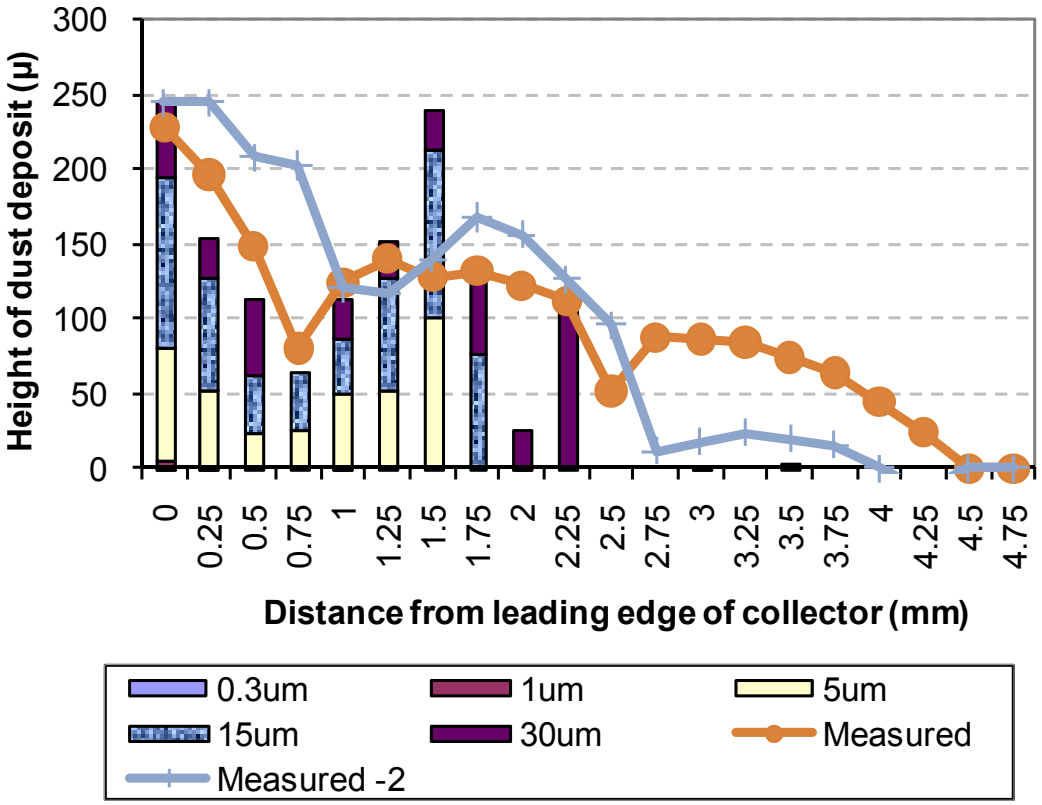

Figure 7.12. *Estimated particle capture distribution along collector surface compared to measured distribution. Both simulation and model predict accumulation zones at the leading edge of the collector and between 1.5 and 2.0 mm from the leading edge.*

7.8 Chapter summary

One of the identified potential issues with EHD technology is the collection of dust, which could have adverse effects on performance, which is an issue shared with fan based systems as dust landing on the inlet face of a heatsink can occlude flow for both EHD and regular fan-based systems.

To better understand how to design an EHD system that is robust to dust, a simulation model to map where particles were collected in a reference geometry designed to collect dust. The model was verified by operating the reference electrostatic precipitator in a custom dust testing system and measuring the deposition thickness and particulate size of the dust collected.

Even though much of the dust was fibrous and the model was based on spherical particles, the simulation predicted the salient feature of the dust accumulation. The majority of the dust was collected in two locations on the collector plate. Large dust particles were preferentially collected and deposited on the first half of the collector.

Larger particles are the most detrimental to thermal performance as they are more likely to block the openings in a heatsink and can form a scaffolding that increases the collection of smaller dust particles, which do not otherwise present as much of a threat.

The simulation developed herein is a valuable tool in increasing the robustness of electrohydrodynamic cooling systems.

Chapter 8. EHD in other applications

8.1 Potential emerging EHD technologies

A laundry list of possible applications outside of thermal management exist that may take advantage of EHD transducers, however, two general areas of application seem most likely at the time of this writing due to their maturity and potential interest in the market place. The first is a combined air conditioning/movement system and the second is loud speakers.

EHD based air condition/movement is not new and many products have been sold using EHD based airflow and air filtration, such as The Sharper Image Ionic Breeze product line, which were purposed to remove particulates from the air and create a better living environment. Unfortunately, the Ionic Breeze products and many of their imitators had products that were plagued with high ozone generation, low clean air delivery rates (CADR), and poor air cleaning efficiency. These limitations ultimately reduced the market for such devices, and relatively few of them are being sold at the time of this writing, even though air quality concerns and awareness continues to increase. A detailed comparison of electrostatic and barrier based air purifiers is outside the scope of this dissertation. However, some of the key benefits of EHD based air purifiers compared to their fan/barrier-filter counterparts include the ability to operate silently, high particle collection efficiency with low pressure drop, high CADR per watt, possibility to kill or render inert captured pathogens, destruction of some volatile organic compounds (VOC), and flexible form factors for unique product design among others. With recent developments in the EHD thermal management space to mitigate ozone production and improve transduction efficiency, this author believes that a new generation of EHD based air condition systems are likely to evolve, which greatly reduce or eliminate the problems that plagued the previous generation systems. The next generation systems may be designed for more than particulate filtration from air, but also on enhanced VOC reduction, air cooling and/or heating, and exist in hybrid systems including barrier filtration, UV, and catalyst technologies.

The EHD based loudspeaker has been investigated to a much lesser extent than electrostatic precipitation, but offers a unique loudspeaker technology that may be applied to a new generation speaker systems. An introduction to the technology and summary of findings for an EHD based loud speaker developed at Kronos Air Technologies with the help of the author is given in the following sub chapters.

8.2 Introduction to EHD driven loud speakers

A loudspeaker is a device that converts electrical signal to acoustic waves, i.e. sound. There are different types of loudspeaker. The most popular and widely used is a moving coil type. This type itself has many variations such as electrodynamic, permanent magnet, horn speakers, among others. A coil is attached to a diaphragm or cone and is placed in a magnetic field created by an electro- or permanent magnet. An electric current through the coil forces the diaphragm to move back and forth generating pressure waves in the fluid, which create sound. Speakers can also be created using non-coil transducers such as electrostatic speakers, which use a thin charged membrane placed between two conductive stationary panels to generate sound rather than a coil and diaphragm. In operation, an electric potential proportional to the acoustic signal is applied between the panels and membrane, creating electrostatic forces that induce movement in the membrane. Advantages of electrostatic speakers include a low mass membrane and the resulting flat frequency response, especially at high frequencies [146]. A planar-magnetic type speaker can be made similar to the electrostatic speakers but uses a thin metal ribbon placed between two magnets where magnetic forces between the ribbon and magnets are controlled by electric current through the ribbon.

All of the above loudspeaker technologies described above have fundamental limitations related to their method of electrical to acoustic energy transduction. One common limitation is the presence of a diaphragm or membrane that has non-zero mass, limited maximum displacement, and suspension stiffness. These traits result in limited dynamic range, poor transient response, non-uniform frequency response, and acoustic distortion.

In contrast, plasma loudspeakers do not have a membrane or moving parts. In plasma speakers, acoustic waves are excited by partially ionized gas that works as a transducer. The ionization is created by a gas discharge, which is generally produced by application of high voltage between electrodes with different curvatures. A good review of plasma loudspeakers as well as principles of operation and applications can be found in [146, 147].

Plasma loudspeakers can be divided into two classes: “hot-plasma” and “cold-plasma” [147]. Hot-plasma loudspeakers use heat as an acoustic source and are based on thermal expansion of the gas surrounding the plasma to produce acoustic waves. The plasma induced heat is generated by the interaction of ions with neutral molecules, allowing for rapid heating of the gas. High voltage varying with radio frequency is applied between electrodes and modulated with an acoustic frequency signal. The gas temperature changes with time according to the acoustic signal, leading to changes in gas pressure and thus generating acoustic waves. One of the first loudspeakers based on this operational principle was developed by S. Klein in 1954 [148]. Originally it was called “Ionophone”, later it was commercially produced and sold as the “Ionovac” [149]. Ackerman *et. al.* built “hot-plasma” speakers for animal research that could generate sound pressure levels up to 132 dB at 3 kW power [150].

Cold-plasma speakers use Coulombic force as an acoustic source and are based on momentum transfer between ions and the fluid medium. Their principle of operation is the same as one of electrostatic fluid accelerators [81]. In the case of cold-plasma speakers, also known as EHD or ionic wind speakers, dc high voltage is applied between electrodes arranged such that resulting corona discharge creates ions moving from the high curvature corona electrode to the low curvature collecting electrode. As the ions transit the two electrodes the ions collide with neutral gas molecules creating a pressure head that can result in net gas flow in some particular direction or so-called “ionic wind”. Modulation of high voltage with acoustic frequency creates forces changing with the applied frequency, which act on neutral gas molecules and generate acoustic waves. Although the cold-plasma loudspeaker has been investigated more intensively than the hot-plasma loudspeaker [36] with many different models describing its operation [36,

147, 151-154] the author is not aware of an EHD loudspeaker being produced commercially to date.

The main advantage of plasma loudspeakers is the absence of membrane and moving parts, which makes them essentially inertia-free. This results in a near-perfect transient response, i.e. the ability to instantaneously respond to an infinitesimally short pulse, and frequency response free of resonance. The former allows creating acoustic generators that can produce very short impulses with wide spectrum [155], and the later allows creating acoustic generators with high fidelity output up to 150 kHz [152] and higher. In addition, plasma speakers can be made very small in size and can work as true acoustic point-source with uniform directivity curve [152, 156, 157]. However, there are also some difficulties associated with plasma loudspeakers that limit their wide exploitation. The main problems are the following: poor signal output at lower frequencies from devices produced to date, ozone production as a byproduct of corona discharge, longevity of high curvature electrodes, and low electric to kinetic transduction efficiency. The purpose of this paper is to present a model of EHD loudspeakers that overcomes many problems mentioned above while keeping all advantages of plasma loudspeakers.

8.3 EHD loud speaker design

Schematic representation of the EHD driven acoustic system using EHD loudspeakers is shown in Figure 8.1. The stereo system consists of two EHD driven loudspeakers powered by a proprietary Kronos Air Technologies switching high voltage power supply (HVPS) connected through an amplifier to an acoustic signal source such as CD player or IPod.

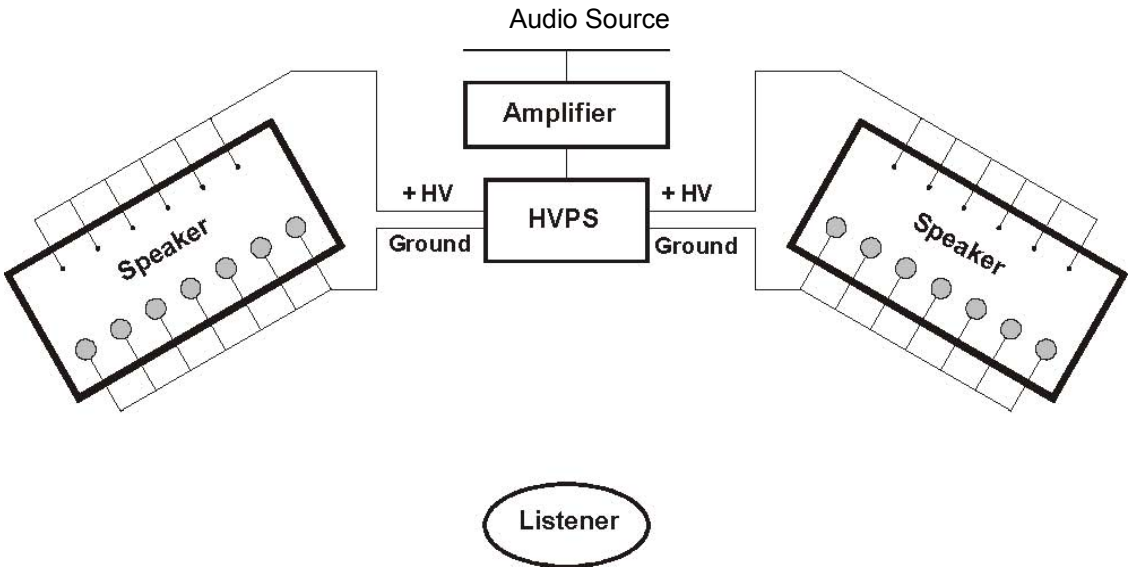

Figure 8.1. *Schematic representation of Kronos acoustic system that uses two EHD loudspeakers.*

EHD loudspeakers developed at Kronos are shown in Figure 8.2 and Figure 8.3. High curvature corona electrodes consisting of an array of metallic wires are placed parallel to an array of attracting electrodes made of hollow aluminum rods. High electric potential is applied at wires while aluminum rods are kept at ground potential. Similar to other conventional speaker technologies, the assembly of emitter wires and collector rods can be wrapped in speaker fabric and or put in a box enclosure.

Dimensions of the EHD loudspeaker shown in Figure 8.2 are 14" by 22" by 2". The geometry and the material choice of the loudspeaker have several advantages. First of all, the loudspeaker is very light, weighting only 1.6 lb, and is comparatively thin. This allows for flexible mounting options such as hanging it on a wall or to a ceiling. Second, the loudspeaker has a high transparency, so it can be installed, for example, in a window where both sun and air may come through the window, or through a window between rooms in a house. Third, the EHD loudspeaker can work simultaneously as an air purifier and/or an EHD fluid accelerator, i.e. fan, as their geometry and principle of operation are similar. In addition, the loudspeaker geometry makes it possible to change its directivity by controlling magnitude and phase of high voltage applied to each wire according to concept of wave field synthesis that is based on a Huygens principle on wave propagation.

Figure 8.2. *Single Kronos EHD loudspeaker shown without an enclosure, fabricated from two parallel arrays of collector and emitter electrodes made from thin Al rods and 100 um diameter W wires respectively.*

Figure 8.3. *A pair of Kronos EHD loudspeakers installed in a box and wrapped in speaker fabric.*

One of the main concerns associated with plasma loudspeakers is ozone generation as a byproduct of corona discharge. Although the EHD loudspeakers produce a small amount of ozone, it is possible to reduce the ozone level at the exterior of the speaker to natural background levels. For example, the EHD loudspeakers shown in Figure 8.3 retain the majority of ozone produced within their enclosure, where the ozone (O_3) is allowed to naturally decay back to O_2. In addition, ozone destructive materials can be placed within the speaker enclosure to enhance the decay rate further minimizing ozone.

8.4 EHD loud speaker results and discussion

For the following experimental results a high electric potential of 14 kV was applied to the corona electrodes and a time dependent acoustic modulated HV signal was applied to the collecting electrodes with a maximum amplitude of approximately 3 kV.

During operation of an EHD loudspeaker, the electric potential difference between arrays is bounded by the corona onset voltage and corona breakdown voltage.

The EHD loudspeakers produce high fidelity crisp sound. It is currently possible to achieve a sound level of 130 dB measured in the near field without audible distortion or spark evens. The acoustic signal from each speaker has a maximum intensity along its centerline.

Frequency response of the EHD loudspeaker is shown in Figure 8.4. The acoustic signal was measured at a distance of 1 ft from the speaker. One can see that frequency response is relatively flat over a full range up to 24 kHz.

Frequency response of a waterfall test is shown in Figure 8.5. Again, one can see an almost abrupt decay of the signal, when compared with results from the same test conducted with a generic moving coil-type speaker. This is expected due to the lack of membrane inertia from the EHD loudspeaker.

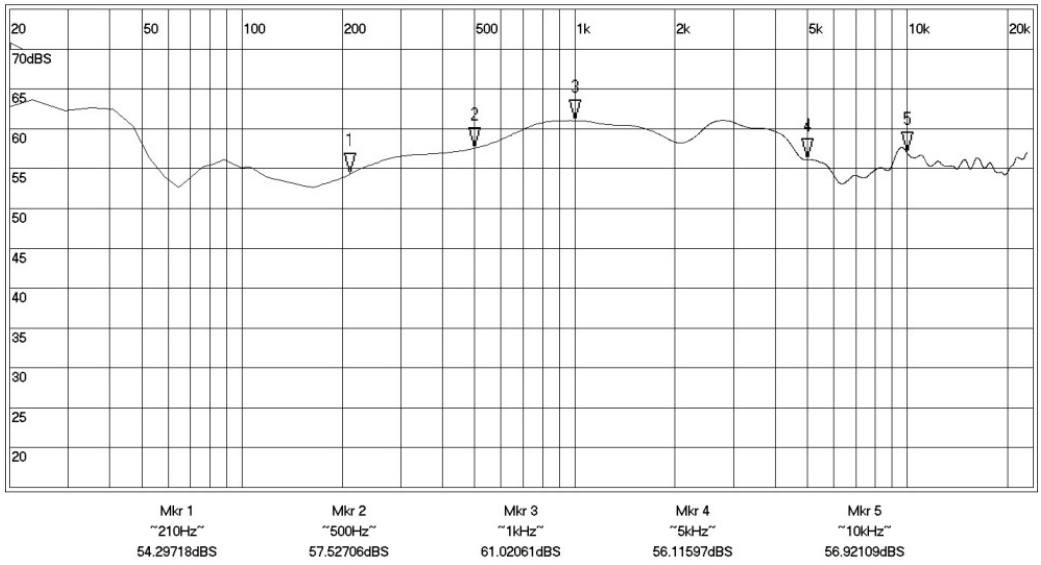

Figure 8.4. *Frequency response of EHD loudspeaker.*

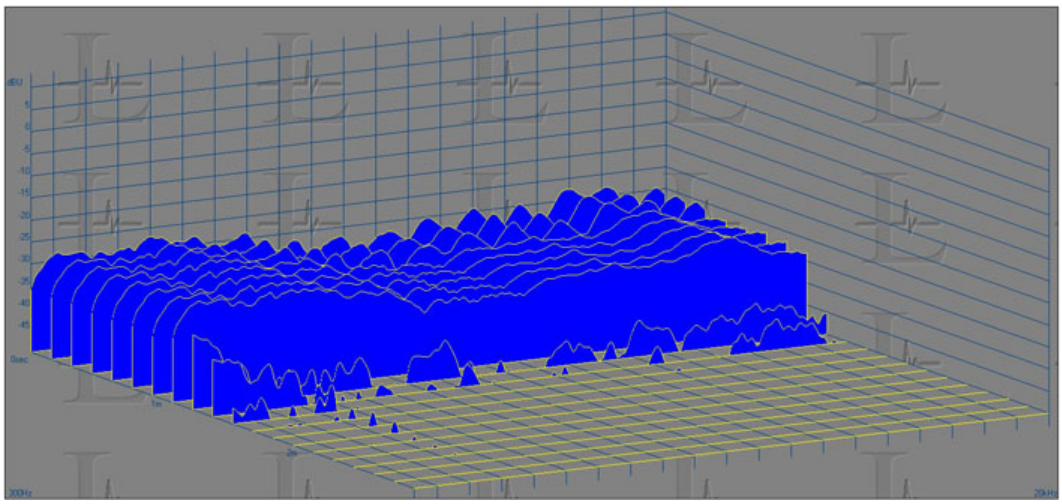

(a)

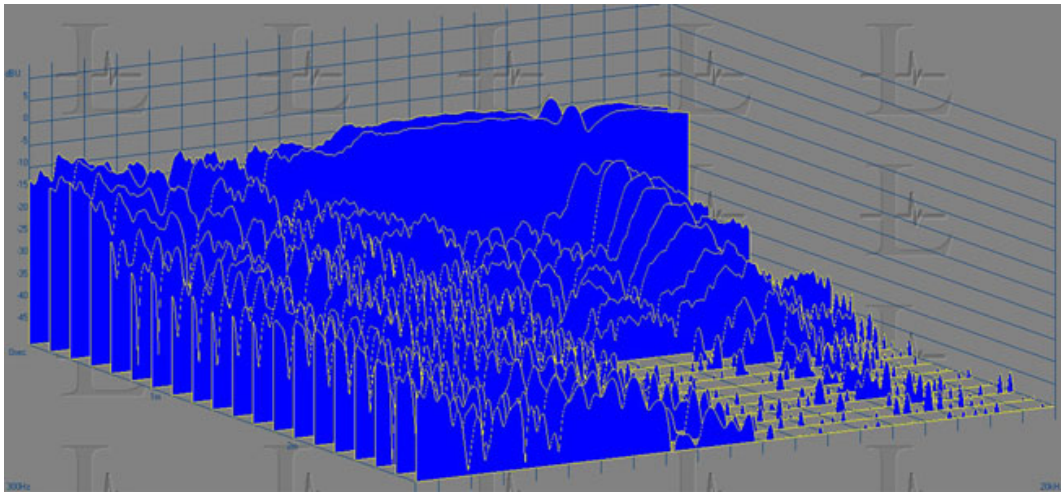

(b)

Figure 8.5. *Waterfall test: (a) EHD loudspeaker and (b) generic moving coil-type speaker.*

In addition, The EHD loudspeaker was investigated for the potential application of active noise cancellation device. Experimental setup for active noise cancellation tests is shown in Figure 8.6. A box with walls covered by sound absorption foam imitates a closed volume where noise is to be eliminated. The dimensions of the box used were 3 ft by 2 ft by 2 ft. One wall of the box was replaced by EHD speaker 2, which was used to cancel sound generated by EHD speaker 1 placed outside of the box. Both speakers were oriented such that generated airflow was directed into the box. The distance between speakers was approximately 24 inches.

Both speakers were driven by a HVPS connected through a Yamaha amplifier to an acoustic signal generator. The amplitude of the acoustic signal for both speakers was independently controlled by the Yamaha amplifier. The time delay of the signal for the second speaker was controlled by an AD 22d Audio Delay device. Sound level at different locations inside the box was measured using a Sound Level meter. The background noise level was approximately 40 dB.

Cancellation of a simple sinusoidal wave was investigated for three individual frequencies, 1, 2, and 3 kHz. The signal of the second speaker had an opposite phase with respect to the first speaker. It was found that at all three frequencies proper time delay and amplitude adjustment of the acoustic signal of the second speaker decreased sound level by 20 dB, 27 dB, and 24 dB, at any point inside the acoustically insulated box. By adjusting the time delay while maintaining the same amplitude of both speakers, it was possible to provide sound level reduction by 14 dB at any point inside the box for all three frequencies.

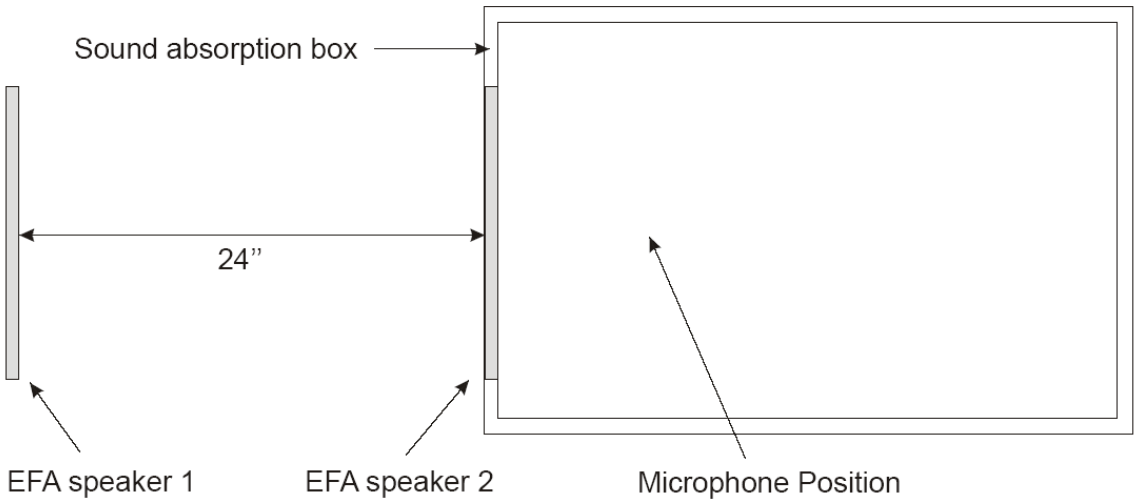

Figure 8.6. *Experimental setup for active noise cancellation tests.*

8.5 Chapter summary

A proof of concept full range EHD loudspeaker has been built and demonstrated with near flat frequency response up to 24 kHz, and a maximum acoustic output of 130 dB. Future work should further characterize the Kronos EHD loudspeaker including

directivity curve and signal destruction analysis. Further work should also investigate the developments in active noise cancellation and dynamic magnitude and phase to ray directivity control for various applications including, air movers, EHD based thermal solutions, air purifiers, or more generally other applications that use EHD based airflow generation or particulate charging.

Chapter 9. Future work

This chapter is focused on future efforts required to bring EHD thermal management technology to a successful commercial application and possible paths forward. This chapter includes areas focused on scientific development as well as industrial development, since both are required for commercialization.

9.1 Improved modeling tools

The models presented in this dissertation provide a step forward in the modeling ability for EHD systems for performance prediction, but further development efforts would be beneficial. As computation costs come down, models that better represent the inner workings of the corona plasma would be beneficial from a number of perspectives including performance modeling; being able to more accurately model a wide range of non symmetric and geometrically complex emitter geometries; reliability modeling, being able to better understand the impact of geometry, current density, and environment on plasma chemistry and material compatibility for long term operation; ozone modeling, being able to optimize geometry and optimization for minimum ozone production and maximum destruction.

Although a full plasma model would be the holy grail of corona plasma EHD models, and may be possible at a future time, progress can be made without it. Although it is difficult to use peek's equations to estimate corona onset for asymmetric and irregular shaped emitter surfaces, improvements can be made on several thrusts.

First, most modeling methods today use the emitter physical geometry as the basis to calculate the critical field in Peeks equation. Although this works well for wire type and spherical type emitter geometries, it will fail to accurately predict more complex shapes, because it is not the physical geometry that is fundamental to the corona discharge, rather it is the field profile and gradient that the geometry generates that is critical. Using a critical electric field gradient method, where corona onset is defined based on a critical electric field gradient given by the effective radius of the emitter structure, peeks empirical correlations should be able to be extended to more complex emitter geometries.

Second, in addition to using an effective emitter curvature method to predict onset, it will be necessary for irregular emitter surfaces where the electric field is not equal on all surfaces to have an adaptive plasma region boundary condition that updates the region of coronating emitter surface based on the applied voltage. If one imagines a saw tooth blade used as an emitter electrode the tip of the saw tooth will form a corona discharge at a much lower emitter to collector electric potential than the side of the sawtooth. Therefore, there needs to be an adaptive boundary condition to deal with the changing coronating surface area.

Beyond charge generation, ozone modeling can also be done through empirical correlations. It is known that ozone generation for a given corona EHD system will scale approximately linear with emitter current. Even such rough correlations can be useful in EHD, catalyst structure, and system design, if integrated with a performance and heat transfer predictive model such as presented earlier in this dissertation.

In addition models that are able to more accurately predict surface charging of dielectric surfaces around the emitter and collector electrode, as well as surface charge currents that can reduce real world efficiency but are generally missing from most modeling efforts to date.

9.2 Ozone mitigation

EHD air movers most often utilize corona discharge for ion generation, and ozone is created as a byproduct of the ion generation process in an oxygen environment. Ozone can be an irritant at high concentrations and damaging to some materials, and therefore solutions aimed at reducing the ozone generation at point of generation around the emitter as well as those that increase the destruction of ozone before it leaves the system are important for real world applications. Future improvements in ozone mitigation are likely to take one of several forms as follows:

- Improved EHD design to reduce the plasma size and or reduce the total current while maintaining performance.

- Research into emitter materials to catalyze the ozone as it is generated and reduce the ozone leaving the plasma region.
- Investigation of airborne reactants that can be used to attack ozone both within the plasma region where it is formed and downstream.
- Development of improved catalyst materials that can be used downstream of the emitter for ozone destruction.
- Exploration of novel methods of using catalyst material to maximize ozone destruction while minimizing flow restriction.

9.3 Reliability

The absence of high speed rotating parts removes many of the reliability issues that plague long term operation of mechanical fans. However, both mechanical fans and EHD blowers share the issue of dust ingress, where dust buildup in the air mover and thermal exchange surfaces reduces blower performance and heat transfer. EHD blowers however, will capture particulates at a higher rate and must devote extra design effort to deal with it. EHD blowers also have unique reliability challenges relating to their unique mode of operation. Development of improved EHD reliability solutions will include the following key areas:

- Design optimization for minimizing dust and debris collection and the removal of dust and debris that does collect and deposit on the collector electrode and surrounding surfaces.
- Investigation into emitter and collector materials that offer long-term operation in the corona discharge environment in the full spectrum of real world environments that the products will be expected to operate.
- Methods to minimize the deposit of silica on the emitter surface through decomposition of siloxanes in the air and the subsequent chemical vapor deposition onto the emitter. Methods to remove or deal with deposits that do form may also be required.

- Optimization of geometry and materials for the emitter, collector, and surrounding surfaces to reduce the probability of arc discharge events, and minimize damage from them.
- Development of smart algorithms and systems that manage the power supply to adjust voltage based on device and environmental characteristics to improve lifetime.

9.4 High voltage power supply miniaturization

To initiate and sustain a corona discharge process to generate ions in an EHD blower, the electric field in the area of ion creation must exceed the dielectric strength of air, which at standard conditions is approximately three kilovolts per millimeter. For most practical devices, this requires an operating voltage greater than a kilovolt and often multiple kilovolts. As most electronic applications do not have an existing power source suitable to directly power an EHD air mover, a compact high voltage power supply must be included as part of the EHD system design.

For compact applications, such as many consumer electronics, the development of small, efficient, and low cost high voltage power supplies is critical. Compact high voltage power supplies have been used in the notebook space for some time as the power source for the cold cathode florescent lamps used as monitor backlights. Similar power supply architectures are likely feasible for commercial EHD applications to start with, but further miniaturization may require the development of new high voltage silicon processes, use of advanced packaging technologies to miniaturize high voltage multipliers, and / or a move towards piezo-transformers.

9.5 Design for high volume production

From the EHD blower module to the control and power electronics, the entire EHD thermal management system will be required to be designed for low cost high volume manufacturing. Although significant work is involved in taking a lab prototype to a cost effective high volume design, there is no obvious reason why a low cost design cannot be achieved. As mentioned before, the power supply can resemble power supplies that are

found in notebooks today for the cold cathode florescent lamp backlights, which can be produced today for several dollars. The EHD blower itself, although complex in design theory, can be quite simple to fabricate. In one embodiment the device may consist of an emitter made of a thin diameter wire, collecting electrodes made from formed metal, and a dielectric body made by injection modeled plastic, similar in construction methods used in the Sharper Image Ionic Breeze product line and found in a vast number of high volume products made today.

9.6 System design and integration

Just as EHD air movers offer a new method of generating airflow for system cooling, new thermal management designs including venting, heatsink design, and system air plenum structure are also required. The PQ curves of EHD blowers are shallower than those of mechanical centrifugal fans, offering a fraction of the pressure. However, the intrinsic air resistance of an EHD blower can be made to be little more than the duct that it resides, allowing for the potential of low flow resistance air paths, and high flow and cooling performance. To achieve optimum performance, the thermal system needs to be designed around the EHD air mover and its specific performance characteristics, which will be different from current thermal systems designed around mechanical fans.

In addition to system level performance optimization, innovative methods of designing in the EHD control and power electronics should also be developed, perhaps eventually being built into the motherboard itself in the case of a notebook or other mobile computing application.

Although EMI shielding for normal operation is not required when using a DC voltage driven EHD blower, in the event of an arc discharge event, the application of embedded EMI shielding may be required.

Proper design of the EHD blower will include design efforts to prevent ion leakage through the air inlets and outlets, so as to avoid chassis or component charging and the resulting ESD events. Such design is not difficult, but will be necessary.

Finally, applications that would benefit from the flexible form factor, silent operation, thin profile, rapid switching or changing of pressure head, low sensitivity to rapid x-y-z acceleration should be developed, and extreme temperature operation, which are not possible with mechanical fan thermal management systems today. Industrial and system design should look to the unique features and capabilities of EHD blowers to create new offerings that meet the demand of mobile computing in ways not possible with current technologies.

9.7 Hybrid technology development

This dissertation has mainly focused on the development of EHD air movers for primary air movers in thermal management systems. It is also possible that EHD air movers be used in concert with other air movement technologies such as mechanical fans, synthetic jets, piezo fans, or others. The relative strengths of one or more technologies may be used, and perhaps optimized together to develop compelling thermal management solutions not feasible for any one by itself.

Beyond integration with other air mover technologies, adoption of EHD technology may make other technologies more attractive, such as those requiring high voltage for operation. For example, the tandem use of a high voltage for electrospray based evaporative cooling, and an EHD air mover, may be applicable to niche applications where very high heat flux removal is required. EHD forces in liquids may also be used to enhance the capacity of ultra thin heat pipes, by improving liquid transport between the condenser and evaporator. Further, a high voltage rail might be shared with devices outside of the thermal management solution, to enable a new class of sensors, actuators, loud speakers or other devices not currently practical due to lack of an intelligent onboard high voltage source.

In addition, the creation of a robust, compact, and low cost EHD driven air mover may find a number of possible applications outside of thermal management, where the unique EHD air mover properties are useful. Such unique properties include uniform and non pulsing flow, the lack of gyroscopic and vibration forces, extreme high or low

temperature operation, or sampling of airborne particles for sensing, high frequency or broad band loud speakers, and so on.

Chapter 10. Conclusions

In recent years, the quest for shrinking and ever more capable consumer electronics has created an environment where mechanical fan based cooling solutions are struggling to meet market demands. The lack of adequate forced convection thermal management from mature technologies has brought forth significant research and development efforts into alternative air movement technologies for ultra thin and silent thermal solutions, including electrohydrodynamic (EHD) based air movers.

This dissertation has attempted to bring EHD air movers a step closer to commercial application by bringing together and helping to develop a body of knowledge relevant to EHD air mover design, miniaturization, and commercial application.

Design: A numerical model is presented and validated against experimental results that allows for accurate prediction of current and voltage relationships as well as the resulting EHD driven airflows and pressures. The model is shown to predict electrical properties of the EHD system including corona onset voltages and current-voltage curves with an error of less than five percent, and predict fluid dynamic properties including outlet airflow profiles and average velocities within an error of about ten percent. A figure-of-merit optimization technique based on electric field profile is also presented.

In addition to model development to aid in design, an investigation into the scaling laws of EHD air movers shows that the static pressure in an ideal EHD air mover, scales as the power density raised to the two-thirds power. In addition, the open-air flow rate in an ideal EHD air mover scales as the product of the outlet area and the power density raised to the one-third power. The pressure and flow of a practical EHD blower geometry was shown to scale similarly to the ideal case, and it was shown that an EHD air mover within a duct could be modeled reasonably well by considering the device to be an ideal pressure source. This is because the EHD air mover can be designed to have minimal flow impedance of its own by virtue of its straight-through flow path and lack of flow resistive elements.

Miniaturization: A microfabricated EHD air mover was modeled, fabricated, and analyzed, demonstrating the heat removal magnitudes for a meso-scale EHD air mover in a jet impingement configuration. A maximum average convection heat transfer coefficient increase of 53.7 W/m^2K was achieved using a microfabricated EHD device. Local heat transfer rates up to 280 $W/(m^2K)$ were predicted by numerical modeling to have been present in the region of highest impinging air jet velocity. The resulting EHD blower power consumption was approximately 165 mW, which represented one-eighth of the total active thermal power removed.

Small-scale EHD air movers optimized for bulk air movement were also investigated, resulting in the successful demonstration of EHD air movers with a total active thicknesses of 2 mm and flow rates and pressures over 40 l/min and 15 Pa respectively with 1.5 W input power.

Commercial application: An EHD cooling system with compact blower and power supply was integrated into the existing cooling system of a high performance commercial laptop, replacing the conventional mechanical fan blowers. The EHD system showed promising cooling performance with reduced thermal solution volumetric size and acoustics.

Ultimately, the long term success or failure of EHD based thermal management will lie in the value placed on the technologies key advantages including silent operation, thinness, and flexible form factor; and balanced against the development efforts still required to develop high performance systems with long term reliability and acceptable ozone generation. If EHD based air movers do find a place in electronics thermal management, it is likely that they will spread to other applications that can take advantage of their novel merits.

REFERENCES

[1] N. E. Jewell-Larsen, C. P. Hsu, I. A. Krichtafovitch, S. W. Montgomery, J. T. Dibene, and A. V. Mamishev, "CFD Analysis of Electrostatic Fluid Accelerators for Forced Convection Cooling," *IEEE Transactions on Dielectrics and Electrical Insulation,* vol. 15, no. 6, pp. 1745-1753, Dec, 2008.

[2] C. P. Hsu, C. Sticht, N. E. Jewell-Larsen, M. Fox, I. A. Krichtafovitch, and A. V. Mamishev, "Characterization of Microfabricated Cantilever-to-Plane Electrostatic Fluid Accelerators for Cooling in Electronics." ASME International Mechanical Engineering Congress and Exposition, Seattle, Washington, November 11-15, 2007, pp. 121-127.

[3] F. Yang, N. E. Jewell-Larsen, D. L. Brown, K. Pendergrass, D. A. Parker, I. A. Krichtafovitch, and A. V. Mamishev, "Corona Driven Air Propulsion for Cooling of Electronics," in XIIIth International Symposium on High Voltage Engineering, Netherlands, 2003, pp. 155.

[4] N. E. Jewell-Larsen, P. Q. Zhang, C. P. Hsu, I. A. Krichtafovitch, and A. V. Mamishev, "Coupled-Physics Modeling of Electrostatic Fluid Accelerators for Forced Convection Cooling," in 9th AIAA/ASME Joint Thermophysics and Heat Transfer Conference, San Francisco, California USA, 2006, pp. 2038-2047.

[5] N. E. Jewell-Larsen, E. Tran, I. A. Krichtafovitch, and A. V. Mamishev, "Design and Optimization of Electrostatic Fluid Accelerators," *IEEE Transactions on Dielectrics and Electrical Insulation,* vol. 13, no. 1, pp. 191-203, 2006.

[6] N. E. Jewell-Larsen, H. Ran, Y. Zhang, M. Schwiebert, K. Honer, and A. V. Mamishev, "Electrohydrodynamic (EHD) Cooled Laptop," in 26nd IEEE SEMI-THERM Symposium, San Jose, CA, 2009.

[7] H. Ran, N. E. Jewell-Larsen, Y. Zhang, and K. A. Honer, "Emerging Technologies in Forced Convection Air Cooling," *Thermal News*, 11/1/2008, 2008.

[8] C. P. Hsu, N. E. Jewell-Larsen, I. A. Krichtafovitch, and A. V. Mamishev, "Heat-Transfer-Enhancement Measurement for Microfabricated Electrostatic Fluid Accelerators," *Journal of Microelectromechanical Systems,* vol. 18, no. 1, pp. 111-118, Feb, 2009.

[9] N. E. Jewell-Larsen, S. V. Karpov, H. Ran, P. Savalia, and K. A. Honer, "Investigation of dust in electrohydrodynamic (EHD) systems." Semiconductor Thermal Measurement and Management Symposium, 2010. SEMI-THERM 2010. 26th Annual IEEE, Santa Clara, CA, Feburary 21-25, 2010, pp. 249-255.

[10] C. P. Hsu, N. E. Jewell-Larsen, I. A. Krichtafovitch, S. W. Montgomery, J. T. Dibene, and A. V. Mamishev, "Miniaturization of electrostatic fluid accelerators," *Journal of Microelectromechanical Systems,* vol. 16, no. 4, pp. 809-815, Aug, 2007.

[11] C. P. Hsu, N. E. Jewell-Larsen, A. C. Rollins, I. A. Krichtafovitch, S. W. Montgomery, J. T. Dibene II, and A. V. Mamishev, "Miniaturization of electrostatic fluid accelerators," in ASME International Mechanical Engineering Congress and Exposition, IMECE2006, Chicago, IL, United States, 2006, pp. 165-170.

[12] N. E. Jewell-Larsen, S. V. Karpov, I. A. Krichtafovitch, V. Jayanty, C. P. Hsu, and A. V. Mamishev, "Modeling of Electrohydrodynamic Flow with COMSOL." ESA Annual Meeting on Electrostatics, Minneapolis, MN, 06/17/2008, 2008, pp. E1.

[13] N. E. Jewell-Larsen, D. A. Parker, I. A. Krichtafovitch, and A. V. Mamishev, "Numerical Simulation and Optimization of Electrostatic Air Pumps." 2004 Annual Report Conference on Electrical Insulation and Dielectric Phenomena, Boulder, CO, Oct, 2004, pp. 106-109.

[14] N. E. Jewell-Larsen, "Optimization and Miniaturization of Electrostatic Air Pumps for Thermal Management," Master of Science, University of Washington, Seattle, 2004.

[15] N. E. Jewell-Larsen, G. G. Joseph, and K. A. Honer, "Scaling Laws for Electrohydrodynamic Air Movers," *ASME Conference Proceedings,* vol. 2011, no. 38921, pp. T10109-T10109-9, 2011.

[16] J. E. Bryan, and J. Seyedyagoobi, "Experimental-Study of Ion-Drag Pumping Using Various Working Fluids," *IEEE Transactions on Electrical Insulation,* vol. 26, no. 4, pp. 647-655, Aug, 1991.

[17] C. A. Belhadj, Shwehdi, M.H., and Farag, A.S., "Corona Wind Velocity: Parametric Approach," *IEEE*, pp. 489-492, 1998.

[18] G. M. Colver, and S. El-Khabiry, "Modeling of DC Corona Discharge Along an Electrically Conductive Flat Plate with Gas Flow," *IEEE Transactions on Industry Applications,* vol. 35, no. 2, pp. 387-394, Mar-Apr, 1999.

[19] J. R. Roth, D. M. Sherman, and S. P. Wilkinson, "Electrohydrodynamic Flow Control with a Glow-Discharge Surface Plasma," *AIAA Journal,* vol. 38, no. 7, pp. 1166-1172, Jul, 2000.

[20] J. R. Roth, "Aerodynamic Flow Acceleration Using Paraelectric and Peristaltic Electrohydrodynamic Effects of a One Atmosphere Uniform Glow Discharge Plasma," *Physics of Plasmas,* vol. 10, no. 5, pp. 2117-2126, May, 2003.

[21] A. Labergue, L. Leger, E. Moreau, G. Touchard, and J. P. Bonnet, "Experimental Study of the Detachment and the Reattachment of an Airflow Along an Inclined Wall Controlled by a Surface Corona Discharge - Application to a Plane Turbulent Mixing Layer," *IEEE Transactions on Industry Applications,* vol. 40, no. 5, pp. 1205-1214, Sep-Oct, 2004.

[22] D. Schilitz, S. Garimella, and T. Fisher, "Numerical Simulation of Microscale Ion-Driven Air Flow," in ASME International Mechanical Engineering Congress, Washington, DC, United States, 2003, pp. 303-310.

[23] L. Leger, E. Moreau, and G. G. Touchard, "Effect of a DC Corona Electrical Discharge on the Airflow Along a Flat Plate," *IEEE Transactions on Industry Applications,* vol. 38, no. 6, pp. 1478-1485, 2002.

[24] E. Moreau, L. Leger, and G. Touchard, "Effect of a DC Surface-Corona Discharge on a Flat Plate Boundary Layer for Air Flow Velocity up to 25 m/s," *Journal of Electrostatics,* vol. 64, no. 3-4, pp. 215-225, Mar, 2006.

[25] D. J. Schlitz, S. V. Garimella, and T. S. Fisher, "Microscale Ion-Driven Air Flow Over a Flat Plate," in Proceedings of the ASME Heat Transfer/Fluids Engineering Summer Conference, Charlotte, NC, United States, 2004, pp. 463-468.

[26] J. A. Cross, "Electrostatically Assisted Heat Transfer." International Electrostatics Conference, UK, 1975, pp. 191-199.

[27] M. E. Franke, and L. E. Hogue, “Electrostatic Cooling of a Horizontal Cylinder,” *Journal of Heat Transfer-Transactions of the ASME,* vol. 113, no. 3, pp. 544-548, Aug, 1991.

[28] J. Mathew, and F. C. Lai, “Enhanced Heat Transfer in a Horizontal Channel With Double Electrodes,” *IEEE*, pp. 1472-1479, 1995.

[29] B. L. Owsenek, J. Seyedyagoobi, and R. H. Page, “Experimental Investigation of Corona Wind Heat-Transfer Enhancement with a Heated Horizontal Flat-Plate,” *Journal of Heat Transfer-Transactions of the ASME,* vol. 117, no. 2, pp. 309-315, May, 1995.

[30] M. Molki, and K. L. Bhamidipati, “Enhancement of Convective Heat Transfer in the Developing Region of Circular Tubes Using Corona Wind,” *International Journal of Heat and Mass Transfer,* vol. 47, no. 19-20, pp. 4301-4314, Sep, 2004.

[31] Y. Tada, A. Takimoto, and Y. Hayashi, “Heat Transfer Enhancement in a Convective Field by Applying Ionic Wind,” *Journal of Enhanced Heat Transfer,* vol. 4, no. 2, pp. 71-86, 1997.

[32] C. P. Hsu, N. E. Jewell-Larson, A. C. Rollins, I. A. Krichtafovitch, S. W. Montgomery, J. T. D. II, and A. V. Mamishev, "Electrostatic Fluid Accelerators Miniaturization Using Microfabrication Technology." ASME International Mechanical Engineering Congress and Exposition, Chicago, IL, Nov. 5-10, 2006.

[33] H. Kalman, and E. Sher, “Enhancement of Heat Transfer by Means of a Corona Wind Created by a Wire Electrode and Confined Wings Assembly,” *Applied Thermal Engineering,* vol. 21, no. 3, pp. 265-282, Feb, 2001.

[34] F. Bastien, “Acoustics and Gas Discharges: Applications to Loudspeakers,” *Journal of Physics D: Applied Physics,* vol. 8, no. 20, pp. 1547-1557, 1987.

[35] P. Bequin, V. Montembault, and P. Herzog, “Modeling of Negative Point-to-Plane Corona Loudspeaker,” *The European Physical Journal Applied Physics,* vol. 15, pp. 57-67, 2001.

[36] M. S. Mazzola, and G. M. Molen, “Modeling of a Dc Glow Plasma Loudspeaker,” *Journal of the Acoustical Society of America,* vol. 81, no. 6, pp. 1972-1978, 1987.

[37] S. A. Hoenig, “New Applications of Electrostatic Technology to Control of Dust, Fumes, Smokes, and Aerosols,” *IEEE Transactions on Industry Applications,* vol. 17, no. 4, pp. 386-391, 1981.

[38] S. A. Hoenig, "New Technology for Detection and Removal of Surface Contamination Involving Particulates or Water/Organic Materials." 42nd Annual Frequency Control Symposium, Baltimore, MD, Jun. 1-3, 1988, pp. 189-201.

[39] M. Jyumonji, and H. Uchiyama, “Field Experiment on the Abatement of Stock-Raising Odors by an Electrostatic Fog-Liquefier.,” *Journal of Electrostatics,* vol. 40-1, pp. 645-650, Jun, 1997.

[40] H. Uchiyama, and M. Jyumonji, “Field Experiments of an Electrostatic Fog-Liquefier,” *Journal of Electrostatics,* vol. 35, no. 1, pp. 133-143, Jul, 1995.

[41] C. J. M. Lasance. "Technical Data: Thermal Conductivity of Leadfram Materials (W/mK)," 2011; http://www.electronics-cooling.com/1997/01/technical-data/: Updated Jan 1, 1997.

[42] O. A. Leon, G. De Mey, E. Dick, and J. Vierendeels, "Staggered Heat Sinks with Aerodynamic Cooling Fins," *Microelectronics Reliability,* vol. 44, no. 7, pp. 1181-1187, Jul, 2004.

[43] E. A. Silk, "Investigation of Enhanced Surface Spray Cooling," Ph.D., University of Maryland, 2006.

[44] R. J. Moffat, "Modeling Air-Cooled Heat Sinks as Heat Exchangers." Proceedings of SEMI-THERM, San Jose, CA, March 18-22, 2007, pp. 200-207.

[45] S. B. White, N. C. Gallego, D. D. Johnson, K. Pipe, A. Shih, and E. Jih, "Graphite Foam for Cooling of Automotive Power Electronics," *Power Electronics in Transportation*, pp. 61-65, Oct. 21-22, 2004.

[46] http://www.k-technology.com/products.html.

[47] http://www.graftechaet.com/Home/Brands/eGRAF.aspx.

[48] S. V. Garimella, "Advances in Mesoscale Thermal Management Technologies for Microelectronics," *Microelectronics Journal,* vol. 37, pp. 1165-1185, 2006.

[49] C. J. M. Lasance, and R. E. Simons. "Advances In High-Performance Cooling For Electronics," Electronics Cooling Magazine; http://www.electronics-cooling.com/2005/11/advances-in-high-performance-cooling-for-electronics/: Updated Nov 1, 2005.

[50] T. Acikalin, S. M. Wait, S. V. Garimella, and A. Raman, "Experimental Investigation of the Thermal Performance of Piezoelectric Fans," *Heat Transfer Engineering,* vol. 25, no. 1, pp. 4-14, Jan-Feb, 2004.

[51] I. Sauciuc, "Piezo Actuators for Electronics Cooling," *Electronics Cooling Magazine*, Feb, 2007.

[52] A. Glezer, and M. Amitay, "Synthetic Jets," *Annual Review of Fluid Mechanics,* vol. 34, pp. 503-529, 2002.

[53] R. Grimes, P. Walsh, E. Walsh, and V. Egan, "The Effects of Diameter and Rotational Speed on the Aerodynamic Performance of Low Profile Miniature Radial Flow Fans," in Proceedings of the Fifth International Conference on Nanochannels, Microchannels and Minichannels, Puebla, Mexico, 2007, pp. ICNMM2007-30185.

[54] P. A. Walsh, V. Egan, R. Grimes, and E. Walsh, "Scaling of Flow Characteristics and Power Consumption with Profile Height for Miniature Centrigugal Fans." Proceedings of the Fifth International Conference on Nanochannels, Microchannels and Minichannel, Puebla, Mexico, 2007, pp. 237-243.

[55] E. J. Walsh, P. A. Walsh, R. Grimes, and J. Punch, "Acoustic Emissions from Active Cooling Solutions for Portable Devices," in Thermal and Thermomechanical Phenomena in Electronic Systems, ITHERM Orlando, FL, 2008.

[56] R. Mahalingam, S. Heffington, L. Jones, and R. Williams, "Synthetic Jets for Forced Air Cooling of Electronics," *Electronics Cooling,* vol. 13, no. 2, http://www.nuventix.com/files/uploaded_files/Electonics%20Cooling%20Magazine%20Nuventix%20Article%20Reprint.pdf, 2007.

[57] M. M. Schwickert, *IEEE Reliability Society Annual Technical Report*, IEEE Reliability Society, , 2009.
[58] I. Sancinc, M. Mochizuki, M. Ikeda, and G. Kamitain, "Non-Conventional Cooling Solutions for Low-Power Components," Intel Developer Forum, 2008.
[59] F. W. Peek, *Dielectric Phenomena in High Voltage Engineering*, New York: McGraw-Hill, 1929.
[60] L. B. Loeb, *Basic Processes of Gaseous Electronics*, Berkeley: University of California Press, 1955.
[61] L. B. Loeb, *Fundamental Processes of Electrical Discharge in Gases*, New York: John Wiley & Sons Inc., 1939.
[62] L. B. Loeb, *Electrical Coronas: Their Basic Physical Mechanisms*, New York: John Wiley & Sons Inc., 1965.
[63] R. Morrow, "Theory of Positive Corona in SF_6 Due to a Voltage Impulse," *IEEE Transactions on Plasma Science,* vol. 19, no. 2, pp. 86-94, Apr, 1991.
[64] J. D. Cobine, *Gaseous Conductors*: Dover Publications, 1958.
[65] R. Morrow, "The Theory of Positive Glow Corona," *Journal of Physics D: Applied Physics,* vol. 30, no. 22, pp. 3099-3114, Nov 21, 1997.
[66] J. Chen, "Direct Current Corona-Enhanced Chemical Reactions," PhD, University of Minnesota, 2002.
[67] J. Zeleny, "On Discharges From Points in Gases, With Special Regard to So-Called Dark Discharges," *Physical Review*, no. 3, 1924.
[68] G. N. Aleksandrov, "Physical Conditions for the Formation of an Alternating-Current Corona Discharge," *Soviet Physics-Technical Physics,* vol. 1, no. 8, pp. 1714-1726, 1956.
[69] R. Morrow, "Theory of Negative Corona in Oxygen," *Physical Review A,* vol. 3, no. 32, pp. 1799-1809, 1985.
[70] H. J. White, *Industrial Electrostatic Precipitation*: Addison-Wesley, 1963.
[71] C. Kenty, "Photoelectric Yields in the Extreme Ultraviolet," *Physical Review,* vol. 11, no. 44, pp. 891-897, 1933.
[72] K. Boetler, "Ozone Generation of Indoor, Electronic Air Cleaners," Masters, Mechanical Engineering, University of Minnesota, 1966.
[73] G. W. Trichel, "The Mechanism of the Negative Point to Plane Corona Near Onset," *Physical Review,* vol. 54, pp. 1078-1086, December 15, 1938.
[74] J. S. Townsend, *Electricity in Gases*, Oxford England: Oxford University Press, 1915.
[75] J. H. Jeans, *Electricity and Magnetism*, 5th ed., New York: Cambridge University Press, 1927.
[76] F. Hauksbee, *Physico-Mechanical Experiments on Various Subjects*, p.^pp. 46-47, London, England, 1709.
[77] I. Newton, *Opticks*, p.^pp. 315-316, London, 1718.
[78] M. Faraday, *Experimental Researches in Electricity*, p.^pp. 665, 1443-1444, 1535, 1592, 1595, London, 1839.
[79] J. C. Maxwell, *Treatise on Electricity and Magnetism*, p.^pp. 52-54, London, 1873.

[80] O. M. Stuetzer, “Ion Drag Pressure Generation,” *Journal of Applied Physics,* vol. 30, no. 7, pp. 984-994, 1959.
[81] M. Robinson, “Movement of Air in the Electric Wind of Corona Discharge,” *AIEE Transactions,* vol. 80, pp. 143-150, 1961.
[82] A. Shooshtari, M.Ohadi, and F. H. R. Franca, “Experimental and Numerical Analysis of Electrohydrodynamic Enhancement of Heat Transfer in Air Laminar Channel Flow,” in 19th IEEE SEMI-THERM Symposium, San Jose, CA, 2003, pp. 48-52.
[83] A. Takimoto, Y. Tada, Y. Hayashi, and K. Yamada, “Convective Heat-Transfer Enhancement by a Corona Discharge,” *Heat Transfer - Japanese Research,* vol. 20, no. 1, pp. 18-35, 1991.
[84] D. Schilitz, S. Garimella, and T. Fisher, "Numerical Simulation of Microscale Ion Driven Air Flow." ASME 2003 International Mechanical Engineering Congress and Exposition, Washington DC, Nov. 15-21, 2003, pp. 303-310.
[85] K. Kelly-Wintenberg, A. Hodge, T. C. Montie, L. Deleanu, D. Sherman, J. R. Roth, P. Tsai, and L. Wadsworth, “Use of a One Atmosphere Uniform Glow Discharge Plasma to Kill a Broad Spectrum of Microorganisms,” *Journal of Vacuum Science & Technology a-Vacuum Surfaces and Films,* vol. 17, no. 4, pp. 1539-1544, Jul-Aug, 1999.
[86] H. Uchiyama, Jyumonji, M. , “Development of an Electrostatic Fogliquefier and Its Field Experiments,” *Japanese Journal of Applied Physics,* vol. 28, no. 11, pp. 2319-2320, 1989.
[87] S. P. Burke, *Heat transfer*, New York/USA 1835557, 1931.
[88] H. R. Velkoff, “Investigation of the Effects of Electrostatic Fields on Heat Transfer and Boundary Layers,” Wright-Patterson Air Force Base, 1962.
[89] M. Robinson, *Corona discharge heat transfer*, New Jersey/USA 3526268, 1970.
[90] T. Mizushina, H. Ueda, T. Matsumoto, and K. Waga, “Effect of Electrically Induced Convection on Heat Transfer of Air Flow in an Annulus,” *Journal of Chemical Engineering of Japan,* vol. 9, no. 2, pp. 97-102, 1976.
[91] H. R. Velkoff, and R. Godfrey, “Low-Velocity Heat-Transfer to a Flat-Plate in the Presence of a Corona Discharge in Air,” *Journal of Heat Transfer-Transactions of the ASME,* vol. 101, no. 1, pp. 157-163, 1979.
[92] M. M. Ohadi, D. A. Nelson, and S. Zia, “Heat-Transfer Enhancement of Laminar and Turbulent Pipe-Flow Via Corona Discharge,” *International Journal of Heat and Mass Transfer,* vol. 34, no. 4-5, pp. 1175-1187, Apr-May, 1991.
[93] M. Molki, M. M. Ohadi, B. Baumgarten, M. Hasegawa, and A. Yabe, “Heat Transfer Enhancement of Airflow in a Channel Using Corona Discharge,” *Journal of Enhanced Heat Transfer,* vol. 7, no. 6, pp. 411-425, 2000.
[94] B. L. Owsenek, and J. SeyedYagoobi, “Theoretical and Experimental Study of Electrohydrodynamic Heat Transfer Enhancement Through Wire-Plate Corona Discharge,” *Journal of Heat Transfer-Transactions of the ASME,* vol. 119, no. 3, pp. 604-610, Aug, 1997.
[95] H. Bondar, and F. Bastien, “Effect of Neutral Fluid Velocity on Direct Conversion from Electrical to Fluid Kinetic-Energy in an Electro-Fluid-Dynamics

(Efd) Device," *Journal of Physics D: Applied Physics,* vol. 19, no. 9, pp. 1657-1663, Sep 14, 1986.
[96] H. Kawamoto, H. Yasuda, and S. Umezu, "Flow Distribution and Pressure of Air Due to Ionic Wind in Pin-to-Plate Corona Discharge System," *Journal of Electrostatics,* vol. 64, no. 6, pp. 400-407, Jun, 2006.
[97] E. Moreau, and G. Touchard, "About the Kinetic Power Induced by AC and DC Discharges," in 2005 Annual Report Conference on Electrical Insulation and Dielectric Phenomena, 2005, pp. 469-473.
[98] J. Q. Feng, "An Analysis of Corona Currents Between Two Concentric Cylindrical Electrodes," *Journal of Electrostatics,* vol. 46, no. 1, pp. 37-48, Mar, 1999.
[99] J. R. Mcdonald, W. B. Smith, H. W. Spencer, and L. E. Sparks, "Mathematical-Model for Calculating Electrical Conditions in Wire-Duct Electrostatic Precipitation Devices," *Journal of Applied Physics,* vol. 48, no. 6, pp. 2231-2243, 1977.
[100] J. L. Davis, and J. F. Hoburg, "Wire-Duct Precipitator Field and Charge Computation Using Finite-Element and Characteristics Methods," *Journal of Electrostatics,* vol. 14, no. 2, pp. 187-199, 1983.
[101] K. Adamiak, "Simulation of Corona in Wire-Duct Electrostatic Precipitator by Means of the Boundary-Element Method," *IEEE Transactions on Industry Applications,* vol. 30, no. 2, pp. 381-386, Mar-Apr, 1994.
[102] J. Q. Feng, "Application of Galerkin Finite-Element Method With Newton Iterations in Computing Steady-State Solutions of Unipolar Charge Currents in Corona Devices," *Journal of Computational Physics,* vol. 151, no. 2, pp. 969-989, May 20, 1999.
[103] J. H. Chen, and P. X. Wang, "Effect of Relative Humidity on Electron Distribution and Ozone Production by DC Coronas in Air," *IEEE Transactions on Plasma Science,* vol. 33, no. 2, pp. 808-812, Apr, 2005.
[104] J. H. Chen, and J. H. Davidson, "Electron Density and Energy Distributions in the Positive DC Corona: Interpretation for Corona-Enhanced Chemical Reactions," *Plasma Chemistry and Plasma Processing,* vol. 22, no. 2, pp. 199-224, Jun, 2002.
[105] J. H. Chen, and J. H. Davidson, "Ozone production in the positive DC corona discharge: Model and comparison to experiments," *Plasma Chemistry and Plasma Processing,* vol. 22, no. 4, pp. 495-522, Dec, 2002.
[106] I. A. Krichtafovitch, V. L. Gorobets, S. V. Karpov, and A. V. Mamishev, "Electrostatic Fluid Accelerator and Air Purifier – The Second Wind." Annual Meeting of the Electrostatics Society of America, Edmonton, Canada, 2005, pp. 1-13.
[107] L. Zhao, and K. Adamiak, "EHD Flow in Air Produced by Electric Corona Discharge in Pin-Plate Configuration," *Journal of Electrostatics,* vol. 63, no. 3-4, pp. 337-350, Mar, 2005.
[108] N. Kasayapanand, "Numerical Study of Electrode Bank Enhanced Heat Transfer," *Applied Thermal Engineering,* vol. 26, no. 14-15, pp. 1471-1480, Oct, 2006.
[109] N. Kasayapanand, J. Tiansuwan, W. Asvapoositkul, N. Vorayos, and T. Kiatsiriroat, "Effect of the Electrode Arrangements in a Tube Bank on the

Characteristic of Electrohydrodynamic Heat Transfer Enhancement: Low Reynolds Number," *Journal of Enhanced Heat Transfer,* vol. 9, no. 5-6, pp. 229-242, 2002.

[110] F. Yang, "Corona-Driven Air Propulsion for Cooling of Microelectronics," University of Washington, Seattle, WA, 2002.

[111] M. S. Peterson, T. S. Fisher, S. V. Garimella, and D. J. Schlitz, "Experimental Characterization of Low Voltage Field Emission From Carbon-Based Cathodes in Atmospheric Air," in ASME International Mechanical Engineering Congress, Washington, DC., United States, 2003, pp. 199-203.

[112] W. Zhang, T. S. Fisher, and S. V. Garimella, "Simulation of Ion Generation and Breakdown in Atmospheric Air," *Journal of Applied Physics,* vol. 96, no. 11, pp. 6066-6072, Dec 1, 2004.

[113] K. A. Dean, and B. R. Chalamala, "The Environmental Stability of Field Emission from Single-Walled Carbon Nanotubes," *Applied Physics Letters,* vol. 75, no. 19, pp. 3017-3019, Nov 8, 1999.

[114] J. M. Bonard, C. Klinke, K. A. Dean, and B. F. Coll, "Degradation and Failure of Carbon Nanotube Field Emitters," *Physical Review B,* vol. 67, no. 11, Mar 15, 2003.

[115] P. G. Slade, and E. D. Taylor, "Electrical Breakdown in Atmospheric Air Between Closely Spaced (0.2 μm – 40 μm) Electrical Contacts," *IEEE Transactions on Components and Packaging Technologies,* vol. 25, no. 3, pp. 390-396, 2002.

[116] H. Bondar, "Plasma Propulsion," http://members.lycos.fr/plasmapropulsion/Basic%20_&_models/, 2004.

[117] A. Rashkovan, E. Sher, and H. Kalman, "Experimental optimization of an electric blower by corona wind," *Applied Thermal Engineering,* vol. 22, no. 14, pp. 1587-1599, 2002.

[118] I.-D.-E. T. Comm., "Recommended international standard for dimensionless parameters used in electrohydrodynamics," *IEEE Transactions on Dielectrics and Electrical Insulation,* vol. 10, no. 1, pp. 3-6, Feb, 2003.

[119] T. Yamamoto, and H. R. Velkoff, "Electrohydrodynamics in an Electrostatic Precipitator," *Journal of Fluid Mechanics,* vol. 108, pp. 1-18, 1981.

[120] P. Atten, F. M. J. Mccluskey, and A. C. Lahjomri, "The Electrohydrodynamic Origin of Turbulence in Electrostatic Precipitators," *IEEE Transactions on Industry Applications,* vol. 23, no. 4, pp. 705-711, 1987.

[121] E. Bonjour, J. Verdier, and L. Well, "Electroconvection Effects on Heat Transfer," *Chemical Engineering Progress,* vol. 58, pp. 63-66, 1962.

[122] T. Ohkubo, S. Hamasaki, Y. Nomoto, J. S. Chang, and T. Adachi, "The Effect of Corona Wire Heating on the Downstream Ozone Concentration Profiles in an Air-Cleaning Wire-Duct Electrostatic Precipitator," *IEEE Transactions on Industry Applications,* vol. 26, no. 3, pp. 542-549, May-Jun, 1990.

[123] *Ansoft Maxwell 2D User Guide*, Ansoft Corp. , 2001.

[124] *Rotary Fan Efficiency for Intel Processor Fans*, PC Power & Cooling, Inc., www.pcpowercooling.com/products/cooling/cooling.htm, 2002.

[125] Wikipedia. "Electric Motor," 8/31/2010; http://en.wikipedia.org/wiki/Electric_motor#Efficiency.
[126] N. A. Kaptsov, *Elektricheskie Yavvleniya Gazakh i Vakuume*, Moscow, 1947.
[127] M. Abdel-Salam, and N. L. Allen, "Current-Voltage Characteristics of Corona in Rod-Plane Gaps as Influenced by Temperature," *IEE Proceedings-Science Measurement and Technology,* vol. 150, no. 3, pp. 135-139, May, 2003.
[128] J. S. Chang, P. A. Lawless, and T. Yamamoto, "Corona Discharge Processes," *IEEE Transactions on Plasma Science,* vol. 19, no. 6, pp. 1152-1166, 1991.
[129] J. Q. Feng, "Electrohydrodynamic Flow Associated with Unipolar Charge Current due to Corona Discharge from a Wire Enclosed in a Rectangular Shield," *Journal of Applied Physics,* vol. 86, no. 5, pp. 2412-2418, Sep 1, 1999.
[130] C. A. Belhadj, M. H. Shwehdi, A. S. Farag, F. M. Zedan, and U. K. A. Klein, "Experimental Measurement of Corona Discharge Using Laser Doppler Velocimetry." Conference Record of the 1998 IEEE International Symposium on Electrical Insulation, Arlington, VA, June 7-10, 1998, pp. 503-506.
[131] Y. Hanein, C. G. J. Schabmueller, G. Holman, P. Lucke, D. D. Denton, and K. F. Bohringer, "High-Aspect Ratio Submicrometer Needles for Intracellular Applications," *Journal of Micromechanics and Microengineering,* vol. 13, no. 4, pp. S91-S95, Jul, 2003.
[132] N. E. Jewell-Larsen, Zhang, P. Q., Hsu, C. P., Krichtafovitch, I. A., and Mamishev, A. V., "Coupled-Physics Modeling of Electrostatic Fluid Accelerators for Forced Convection Cooling," in 9th AIAA/ASME Joint Thermophysics and Heat Transfer Conference, San Francisco, California, 2006, pp. 1.
[133] D. B. Go, S. V. Garimella, T. S. Fisher, and R. K. Mongia, "Ionic Winds for Locally Enhanced Cooling," *Journal of Applied Physics,* vol. 102, no. 5, Sep 1, 2007.
[134] A. Bendaoud, A. Tilmatine, K. Medles, M. Rahli, M. Huzau, and L. Dascalesu, "Characterisation of Dual Corona Electrodes for Electrostatic Processes Applications," in 2004 IEEE Industry Applications Conference, Seattle, 2004, pp. 1552-1558.
[135] E. Sher, G. Pinhasi, A. Pokryvailo, and R. Bar-on, "Extinction of Pool Flames by Means of a DC Electric Field," *Combustion and Flame*, pp. 244-252, 1994.
[136] M. Robinson, "Movement of Air in the Electronic Wind of Corona Discharge," *AIEE Transactions,* vol. 80, pp. 143-150, May 1961.
[137] M. Huang, and F. C. Lai, "Effects of Joule Heating on Electrohydrodynamic-Enhanced Natural Convection in an Enclosure," *Journal of Thermophysics and Heat Transfer,* vol. 20, no. 4, pp. 939-945, 2006.
[138] S. Moghaddam, K. T. Kiger, and M. Ohadi, "Measurement of Corona Wind Velocity and Calculation of Energy Conversion Efficiency for Air-Side Heat Transfer Enhancement in Compact Heat Exchangers," *HVAC&R Research,* vol. 12, pp. 57-68, 2006.
[139] Y. Yue, Hou,J., Ai, Z., Yang, L., and Zhang, Q., "Experimental Studies of the Enhanced Heat Transfer from a Heating Vertical Flat Plate by Ionic Wind," *Plasma Science & Technology,* vol. 8, no. 6, pp. 697-700, November 2006, 2006.

[140] D. B. Go, S. V. Garimella, T. S. Fisher, and R. K. Mongia, “Ionic winds for locally enhanced cooling,” *Journal of Applied Physics,* vol. 102, no. 5, pp. -, Sep 1, 2007.
[141] D. A. Moore, “The Dust Threat,” in IMAPS Advanced Technology Workshop (ATW) on Thermal Management for High-Performance Computing and Wireless Applications, Palo Alto, CA, 2003.
[142] D. A. Moore, “Characterization of Fiber Accumulation Fauling in Fine Pitched Heat Sinks,” in 25th IEEE SEMI-THERM Symposium, San Jose, CA, 2009.
[143] A. Nabi, P. Rodgers, and A. Bar-Cohen, “Prediction of Thermal Performance Degradation of Air-Cooled Fine-Pitch Fin Array Heat Sinks due to Fouling,” in 22nd IEEE SEMI-THERM Symposium, San Jose, CA, 2006.
[144] M. Lackowski, “Unipolar Charging of Aerosol Particles in Alternating Electric Field,” *Journal of Electrostatics,* vol. 51, pp. 225-231.
[145] E. Limpert, W. A. Stahel, and M. Abbt, “Log-Normal Distributions Across the Sciences: Keys and Clues,” *Bioscience,* vol. 51, no. 5, pp. 341-352, May, 2001.
[146] "Quad ESL-989 Electrostatic Loudspeaker: Specifications," 2002.
[147] P. Bequin, K. Castor, P. Herzog, and V. Montembault, “Modeling plasma loudspeakers,” *Journal of the Acoustical Society of America,* vol. 121, pp. 1960-1970, 2007.
[148] S. Klein, *Acustica,* vol. 4, 1954.
[149] J. Podplesky. "Ionovac, Replacement Quartz Cells, DuKane Ionovac, Replacement Quartz Cells, Original DuKane Documents," http://www.ionovac.com.
[150] E. Ackerman, A. Anthony, and F. Oda, “Corona-Type Loudspeaker for Animal Studies,” *Journal of Acoustical Society of America,* vol. 33, no. 12, pp. 1708-1712, 1961.
[151] D. M. Tombs, “Corona Wind Loudspeaker,” *Nature (London),* vol. 176, no. 4489, pp. 923, 1955.
[152] F. J. Fransson, and E. V. Jansson, “The STL-Ionophone: Transducer Properties and Construction,” *Journal of Acoustical Society of America,* vol. 58, no. 4, pp. 910-915, 1975.
[153] G. Shirley, “The Corona Wind Loudspeaker,” *Journal of Audio Engineering Society,* vol. 5, pp. 29-37, 1957.
[154] K. Matsuzawa, “Sound Sources with Corona Discharges,” *Journal of Acoustical Society of America,* vol. 54, no. 2, pp. 494-489, 1973.
[155] R. J. Wyber, “The Design of a Spark Discharge Acoustic Impulse Generator,” *IEEE Transactions on Acoustics, Speech, and Processing,* vol. 23, no. 2, pp. 157-162, 1975.
[156] S. Klein, *Transducer for the transformation of electrical modulations into vibratory modulations*, United States 4482788, 1984.
[157] M. K. Lim, “Corona-Type Point Source for Model Studies in Acoustics,” *Applied Acoustics,* vol. 14, no. 4, pp. 245-252, 1981.